Volcanic arc island flank collapse emplacement:

The complex interplay of depositional processes and long-term deposit stability

Dissertation

zur Erlangung des Doktorgrades

der Mathematisch-Naturwissenschaftlichen Fakultät

der Christian-Albrechts-Universität zu Kiel

vorgelegt von

Michel Kühn

Kiel, 2024

Erster Gutachter:	Prof. Dr. Christian Berndt
Zweite Gutachterin:	Prof. Dr. Morelia Urlaub
Tag der mündlichen Prüfung:	13.09.2024
Zum Druck genehmigt am:	13.09.2024

…….

Der Dekan

Erklärung

Hiermit erkläre ich, dass ich die vorliegende Doktorarbeit, abgesehen von der Beratung durch die Betreuer, selbständig und ohne Zuhilfenahme unerlaubter Hilfsmittel erstellt habe. Weder diese Arbeit noch eine ähnliche Arbeit wurde im Rahmen eines Prüfungsverfahrens veröffentlicht und/oder zur Veröffentlichung vorgelegt. Ferner versichere ich, dass die Arbeit unter Einhaltung der Regeln guter wissenschaftlicher Praxis der Deutschen Forschungsgemeinschaft angefertigt wurde. Des Weiteren wurde mir kein akademischer Grad entzogen.

_____

Kiel, den Michel Kühn

Summary

Volcanic island flank collapses are the most voluminous mass movements on Earth and can trigger devastating tsunamis. With nine major events and more than 15000 casualties over the last 400 years, they pose a serious geohazard on a non-geological time scale. Hazard assessments for volcanic flank collapses require a detailed understanding of pre-condition, failure and emplacement mechanisms. However, the different processes during emplacement, the controls on the dynamics of the associated landslides, and the potential consequences of emplacement for the stability of the slope sediments are poorly constrained. Studies on ancient volcanic flank collapse deposits using high-resolution seismic data combined with drilling operations provide insight into these processes and their complex interplay.

This cumulative doctoral thesis shows that the emplacement of volcanic flank collapse is an interplay of different processes over multiple phases, including initial failure of the volcanic flank and versatile interaction of the failure mass with seafloor sediments. This work also shows that the slope topography and the nature of the substrate sediment are major controls on slide dynamics and morphology, and that once a slope failure occurred on a slope, the propensity for subsequent failure is enhanced.

One study of in thesis of previously unknown volcanic flank collapse deposits offshore Sakar, Papua New Guinea, reveals that where the slide substrate is dominated by homogeneous hemipelagic sediments, a volcaniclastic slide mass may incise and erode into the substrate, leading to widespread disaggregation and deformation of seafloor sediments, and an elongated outline of the deposits margins. Where the slide substrate is dominated by previously deposited volcaniclastic mass transport deposits, a subsequent volcaniclastic slide is unlikely to incise and rather spreads freely along the volcanic slope creating a sub-circular-shaped deposit outline. The potential consequences of this for landslide velocities and thus tsunami magnitude have not been recognized before.

Another study in this thesis of volcanic flank collapse deposits offshore Montserrat, Lesser Antilles, aims to analyze the geological processes involved in the emplacement of an ancient volcanic flank collapse deposit, Deposit 2, by combining high-resolution 2D and 3D seismic data with MeBo70 drill data. The analysis reveals that Deposit 2 (subdivided in Deposit 2a and Deposit 2b) was not formed by one, but by at least two major - likely tsunamigenic - volcanic flank collapse events. The first flank collapse resulted in a volcaniclastic landslide that triggered secondary seafloor failure in an adjacent graben, and incised into the substrate, deforming

surrounding sediments. This was preceded by a late-stage erosive density current that incised a channel system into the surface of the main slide mass, followed by a second volcaniclastic landslide due to a second volcanic flank collapse. The runout and shape of the associated sub-deposits is strongly controlled by a narrow topography, formed by either the tectonic graben or previously emplaced mass transport deposits. These key insights can serve as input parameters for landslide and tsunami simulations that will improve volcanic flank collapse hazard assessment in volcanic island settings.

A heat flow study using temperature data collected offshore Montserrat reveals isothermal zones of elevated temperature within Deposit 2a that cannot be explained by diffusive heat flow. Instead, advection appears to be the dominating heat flux mechanism, indicating fluid flow and thus elevated pore pressure within the deposit. This elevated pressure is evident in cone penetrations tests on Deposit 2a. A numerical pore pressure study shows that loading due to the rapid emplacement of a volcanic flank collapse (Deposit 2b) can lead to excess pore pressure in the sediments below and adjacent to the loaded deposit for up to hundreds of thousands of years, increasing the risk for subsequent slope failure events.

Failure of a volcanic flank and the emplacement of the associated landslides are complex interplays of different geological and physical processes. However, this thesis - using the exceptional opportunity to combine high-resolution 2D and 3D seismic with drilling data from volcanic flank collapse deposits - provides new insights into this complexity.

Zusammenfassung

Flankenkollapse an vulkanischen Inseln zählen zu den massereichsten Umlagerungsprozessen der Welt. Neun solcher Einstürze in den letzten 400 Jahren und über 15000 Todesopfern dokumentieren eine ernst zu nehmende geologische Gefahr auf einer nicht-geologischen Zeitskala. Gefahrenabschätzungen für vulkanische Flankenkollapsereignisse erfordern ein detailliertes Verständnis der aktiven Mechanismen, während und nach dem Kollaps, sowie der resultierenden Hangrutschungen. Die verschiedenen Prozesse, die während der Rutschung und der Ablagerung der Rutschmasse wirken, sowie die möglichen Auswirkungen auf die Stabilität der submarinen Hangsedimente sind jedoch nur unzureichend erforscht. Die Untersuchung alter vulkanischer Hangrutschungssablagerungen mit Hilfe von hochauflösenden seismischen Daten kombiniert mit Bohrungen, gewährt Einblicke in diese Prozesse und ihr komplexes Zusammenspiel.

Diese kumulative Doktorarbeit zeigt, dass die Ablagerung von vulkanischen Hangrutschungen ein Zusammenspiel verschiedener Prozesse über mehrere Phasen hinweg ist, beginnend mit dem anfänglichen Versagen der Vulkanflanke bis zu den vielseitigen Wechselwirkungen der resultierenden Hangrutschungen mit den Sedimenten des Meeresbodens. Diese Arbeit zeigt auch, dass die Topografie des Vulkanhangs und die Beschaffenheit des Substrats die Dynamik und Morphologie der Rutschung maßgeblich beeinflussen und dass ein erstmaliges Versagen eines Vulkanhangs die Wahrscheinlichkeit eines weiteren Flankenkollapses erhöht.

Eine der Studien dieser Arbeit befasst sich mit bisher unbekannten, prä-historischen Hangrutschungen vor der Küste der Insel Sakar, Papua-Neuguinea. Die Ergebnisse dieser Arbeit zeigen, dass die Beschaffenheit der Meeresbodensedimente, über die sich eine vulkanische Hangrutschung bewegt, maßgeblich reguliert, ob sich die Hangrutschung in die Meeresbodensedimente eingräbt und so eine umfassende Deformation des Meeresbodens verursacht, oder sich frei über den Meeresboden hinwegbewegt. Dort wo größtenteils hemipelagische Meeresbodensedimente vorliegen, neigt eine Hangrutschung dazu in diese hinein zu erodieren, während dort wo zuvor abgelagerte vulkanische Hangrutschungen den Meeresboden dominieren, die freie Ausbreitung der Rutschmasse entlang des Meeresbodens begünstigt wird.

Ein weiterer Teil dieser Arbeit untersucht die geologischen Prozesse die während der Ablagerung von prä-historischen Hangrutschungen vor der Insel Montserrat in den Kleinen Antillen stattgefunden haben. Die Studie kombiniert hochauflösende seismische Daten mit

Bohrdaten und zeigt das eine vulkanische Hangrutschungsablagerung von mindesten zwei großen, zeitlich voneinander getrennten, Flankenkollapsen erzeugt wurde – die vermutliche beide ein großes tsunamigenes Potential hatten. Der erste Flankenkollaps führte zu einer Hangrutschung, die eine weitere, sedimentär geprägte Hangrutschung ausgelöst hat, dann in die unterliegenden Meeresbodensedimente erodiert ist und eine großflächige Deformation des Meeresbodens ausgelöst hat. Auf diese Ereignisse folgte eine hoch-erosiver Dichtestrom, der tiefe Kanalstrukturen in die Hangrutschungsablagerung hineingeschnitten hat. Anschließend erfolgte ein zweiter vulkanischer Flankenkollaps. Die vorherrschende, verengte Topographie des Ablagerungsgebiets (hervorgerufen durch einen tektonischen Graben und die Ablagerung des vorangegangenen Kollapses) hat dabei zu einer langgestreckten Form der Ablagerung geführt. Diese gewonnen Erkenntnisse können als Parameter für nachfolgende Hangrutschungs- und Tsunamisimulationen verwendet werden und werden damit zu einer verbesserten Gefahrenabschätzung beitragen.

Eine Studie zum Wärmestrom in den Sedimenten vor der Küste Montserrats deutet auf isothermale Zonen von erhöhter Temperatur in einer Hangrutschungsablagerung hin, die nur mit Advektion und Fluidfluss und damit folglich Überdruck im Sediment erklärt werden kann. Direkte Druckmessungen bestätigen diese Interpretation. Numerischen Porendruck Simulationen zeigen, dass die Auflast, die durch Ablagerung einer Hangrutschung auf die darunterliegenden Sedimente wirkt, zu Überdruck im sedimentären Porenraum führt. Dieser Überdruck kann über mehrere hunderttausend Jahre anhalten.

Das Abrutschen einer Vulkanflanke und die Ablagerung der damit verbundenen Rutschmassen sind ein komplexes Zusammenspiel verschiedener geologischer und physikalischer Prozesse. Diese Arbeit nutzt die außergewöhnliche Gelegenheit, hochauflösende 2D- und 3D-Seismik mit Bohrdaten von vulkanischen Hangrutschungsablagerungen zu kombinieren und gewährt neue Einblicke in ebenjene Komplexität.

Table of Contents

Abbreviations

2D	Two-dimensional
3D	Three-dimensional
AAA	Anomalous amplitude attenuation
CCTV	Closed Circuit Television
D/V	Drilling Vessel
FD	Finite-Differences
GI Gun	Generator-Injector Air Gun
GNSS	Gloval Navigation Satellite System
GPS	Global Positioning System
HyLO	Hybrid Lister-Outrigger (Probe)
InSAR	Interferometric Synthetic Aperture Radar
IODP	International Ocean Discovery Program
M1 - M6	Model 1 – Model 6
Mbsf	Meters below seafloor
MCS	Multi-channel seismic
MeBo	*Meeresbodenbohrgerät* (Seafloor drilling device)
MTD	Mass transport deposit
NMO	Normal moveout
OBS	Ocean bottom seismometer
RNA	Random noise attenuation
R/V	Research Vessel
SLD1	Sakar Landslide Deposit 1
SLD2	Sakar Landslide Deposit 2
T_{adapt}	Temperature adaption rate
T_{va}	Average stationary stage temperature
TWT	Two-way travel time
V_p	P (primary, compressional) wave velocity

1. Introduction

1.1 Motivation

Volcanic flank collapses – large-scale slope failure events of volcanic flanks – can generate large and destructive landslides that have the potential to trigger devastating tsunamis. These events appear to be a common process within the life-cycle of a volcano, as indications for large-scale edifice collapses have been found at more than 400 volcanoes worldwide in variable tectonic settings (Siebert et al., 2006), including 61 on volcanic arcs (Watt et al., 2021). The destructive potential of such events was once more demonstrated by the lateral collapse of the Indonesian Volcano Anak Krakatau in December 2018 that triggered a tsunami with run-up heights of up to 13 m at the coasts of the Sunda Strait and caused more than 400 casualties (Grilli et al., 2019; Walter et al., 2019). Historical records and recent studies indicate at least nine tsunamigenic volcanic flank collapses over the last 400 years (Figure 1.1) with more than 15,000 casualties (Day, 2015; Furst et al., 2023; Grilli et al., 2019).

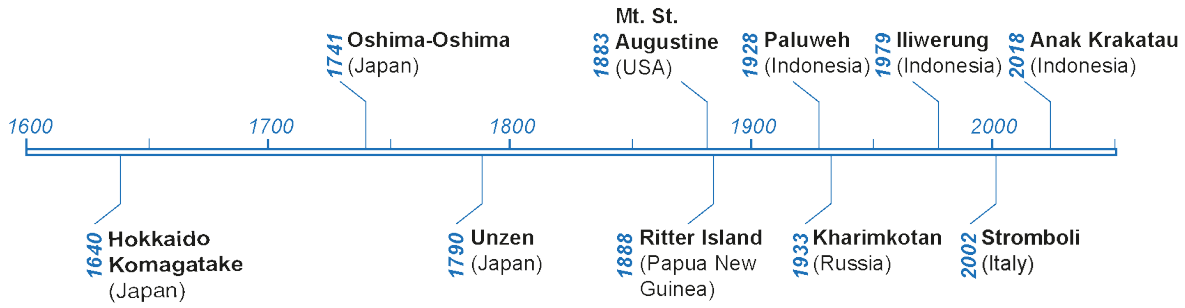

Figure 1.1: *Historic tsunamigenic volcanic flank collapse events over the last 400 years based on Day (2015); Furst et al. (2023), and Grilli et al. (2019).*

The historic events in Figure 1.1 have in common, that they all occurred in volcanic arc island settings. There is, however, evidence for ancient flank collapse events at many intraplate ocean island volcanoes as well, e.g., Cape Verde (Barrett et al., 2020; Day et al., 1999; Le Bas et al., 2007), the Canary Islands (Krastel et al., 2001; Masson et al., 2002, 1998), or Hawaii (Moore et al., 1989; Moore and Normark, 1994). These ancient flank collapse deposits are the most voluminous rapid mass movements on Earth, with deposit volumes reaching up to several thousand km^3 (Moore and Normark, 1994). The tsunamigenic potential of such intraplate ocean

island flank collapses is exemplified at the Cape Verde Islands, where megaclasts of a flank collapse at Fogo were transported over a vertical distance of more than 200 m on the neighbouring island Santiago (Ramalho et al., 2015) (Figure 1.2).

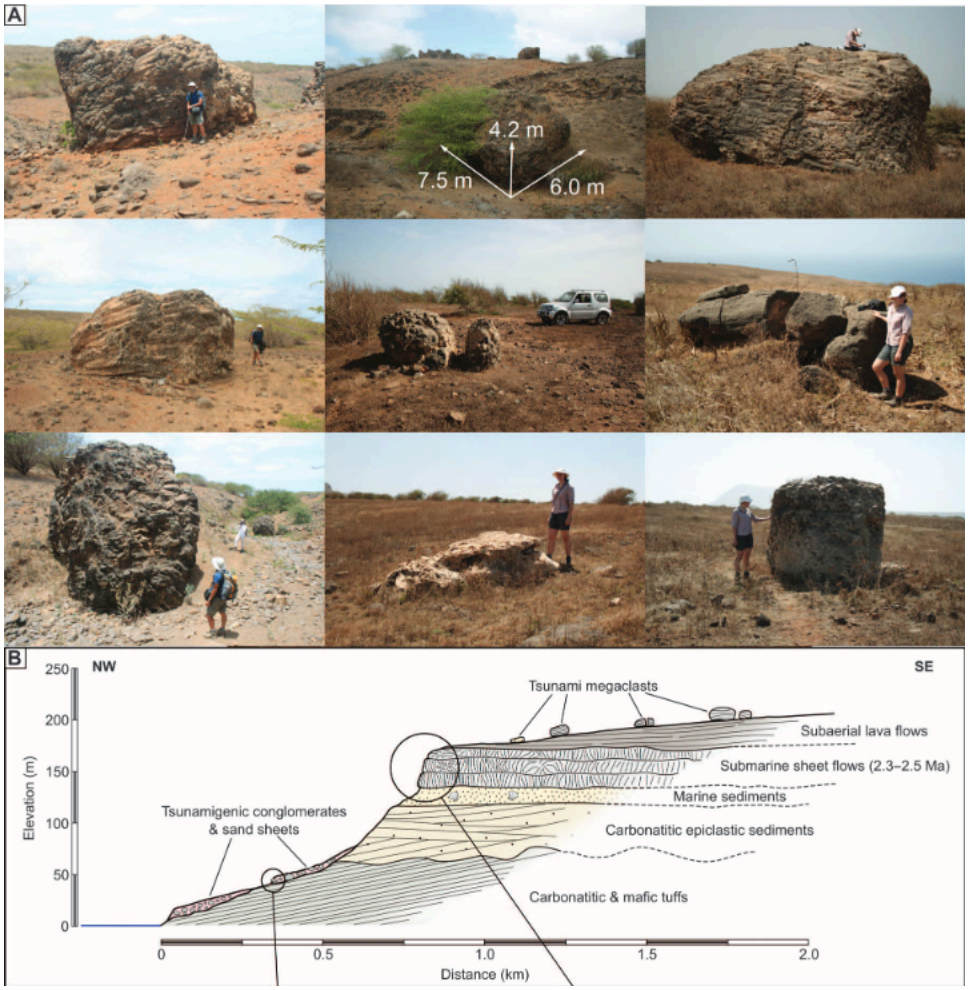

Figure 1.2: *Tsunami megaclasts found on Santiago > 200 m above the sea surface, originating from a volcanic flank collapse at Fogo (from Ramalho et al., 2015).*

The volumes of arc-island flank collapse deposits usually vary between 1 and 50 km^3 (Watt et al., 2021). Aside the tsunamigenic potential, flank collapse-derived landslides can be accompanied or followed by fast-travelling turbidity currents or debris flows (e.g., Hunt et al., 2014; Karstens et al., 2019; Watt et al., 2019). Such highly-mobile flows have the potential to damage marine infrastructure such as ocean cables pipelines, and other seafloor installations, as well as marine ecosystems (Clare et al., 2020, 2023; Clarke et al., 1990; Kvalstad et al., 2001).

The frequency of historic events in Figure 1.1., the consequential economic damages, and most importantly the large number of casualties emphasize that volcanic flank collapses pose a serious geohazard on a non-geological time scale. Yet, no tsunami warning preceded the catastrophic flank collapse of Anak Krakatau in 2018, because the tsunami early warning system in the area was designed for earthquake-generated tsunamis (Zorn et al., 2023). Assessing the tsunamic hazard of a volcanic flank collapse requires a detailed understanding of the failure and emplacement processes and dynamics. However, failure and emplacement are complex interplays of different geological processes (i.e., preconditioning factors, triggers, flow dynamics, and emplacement characteristics). Robust hazard assessments require a detailed understanding of these processes and their individual influence on tsunami generation. This thesis combines geophysical data, i.e., high-resolution 2D and 3D multichannel seismic (MCS), sediment echosounder, and bathymetry data, with drill core data and physical property measurements from MeBo70 and International Ocean Discovery Program (IODP) drilling campaigns to reconstruct the emplacement processes during volcanic flank collapse deposition and its consequences.

1.2 Controls on volcano flank instability

The stability or instability of a volcanic flank in a marine environment is controlled by a combination of internal and external factors that precondition and/or trigger failure either by increasing the stress operating on the edifice or weakening its mechanical strength (Keating and McGuire, 2000; McGuire, 2006). During the failure-preconditioning phase of a marine volcanic flank or edifice a critical threshold might be reached once the driving force on the rock mass exceeds the resisting force of the zone of weakness (Furst et al., 2023). Keating and McGuire (2000) identify several internal (intra-edifice) and external (extra-edifice) processes as preconditioning factors for volcanic flank instability. Internal or endogenic preconditions include decollement surfaces linked to intrusions or dykes, unstable foundations within the edifice (e.g., clay or pebble), (hydro-)thermal alteration, changes in edifice pore fluid pressure, and faults (Furst et al., 2023; Keating and McGuire, 2000; references therein). External or exogenic precondition factors include: mechanically weak zones (caused by e.g., hydrothermal alteration), steep slopes, (un-)loading of flanks, earthquakes, tilting, uplift, ice/snow coverage, extreme climatic events and rapid climate change, as well as weathering (Furst et al., 2023; Keating and McGuire, 2000; and references therein). Watt et al. (2021) point out that erosional processes at the submarine part of a volcanic flank might also play an important role in destabilizing the flank of a volcanic island. The long-term destabilization of a volcanic structure

may take up to several thousands of years, but could also be achieved in relative short time span of several months (McGuire, 2003; Roverato et al., 2021). However, preconditions should be clearly distinguished from short-term trigger processes that initiate failure (Watt et al., 2021). Potential triggers for volcano collapse are rapid stress changes due to propagating magma bodies and increased ground acceleration by volcanic or tectonic earthquakes (Keating and McGuire, 2000). Also, extreme weather events like heavy rainfalls due to rapid climate change are considered to be potential triggers for volcanic flank failure (Aubry et al., 2022; Farquharson and Amelung, 2022).

1.3 Flank collapse depositional processes and tsunami implications

The emplacement of volcanic flank collapse deposits can be a complex interplay of different geological processes, including, but not limited to the initial failure (Karstens et al., 2019; Watt et al., 2021), secondary seafloor failure (Brunet et al., 2016; Crutchley et al., 2013; Watt et al., 2019, 2012b), interactions of the slide mass with the pre-existing topography (Karstens et al., 2019; Tost et al., 2014; Watt et al., 2019), substrate incorporation and deformation (Brunet et al., 2016; Sobiesiak et al., 2018; Watt et al., 2012a, 2012b), and the transformation of debris avalanches into more mobile slide phases such as debris flows and turbidity currents (Capra et al., 2002; Janda et al., 1981; Watt et al., 2019). An example were all of these processes came together is the historic collapse of Ritter Island, Papua New Guinea: In March 1888, Ritter Island catastrophically collapsed and triggered a tsunami with reported heights of up to 15 m (Johnson et al., 1987; Silver et al., 2009; Ward and Day, 2003). Karstens et al. (2019) could show (based on 3D MCS data) that the catastrophic collapse of the island was preceded by deep-seated gradual deformation of the volcanic flank and that the collapse triggered secondary failure of seafloor sediments. These secondarily failed seafloor sediments are also evident in distal debris flow deposits associated to the Ritter Island collapse (Watt et al., 2019). The Ritter Island collapse was likely followed by an eruption that produced an erosive, channel-forming turbidity current (Watt et al., 2019). A similar highly-mobile and erosive flow has been produced as a consequence of an explosive eruption of the Hunga Tonga volcano in 2022, where a pyroclastic flow transitioned into a turbidity current that reached a velocity of um to 130 km/h and destroyed marine infrastructure (Clare et al., 2023).

Using tsunami simulations of historic flank collapses for hazard assessment requires eyewitness accounts of tsunami heights and arrival times, which are only available for a few historic volcanic flank collapse events (Day, 2015; Karstens et al., 2020). Tsunami simulations of the

Ritter Island collapse are broadly consistent with historic eyewitness observations (Karstens et al., 2020) and show - in consistence with earlier studies (e.g., Løvholt et al., 2015) - that the most important landslide parameters for tsunami generation are the volume and the velocity of the initial failure mass as it enters the sea. At volcanic islands where a large fraction of a volcano is submerged, collapse deposits may be entirely submarine and onshore collapse scars yield the only accessible evidence for a collapse event (Watt et al., 2021). But such collapse scars can be quickly obscured and overprinted by subsequent volcanism (e.g., Grilli et al., 2019) or erosion (e.g., Lipman et al., 2002). These settings require offshore (3D) high-resolution seismic surveys and geological sampling to map deposits from past volcanic flank collapses and use their internal seismic and lithological character to differentiate the initial slide volume from the overall deposit volume.

1.4 Research Areas

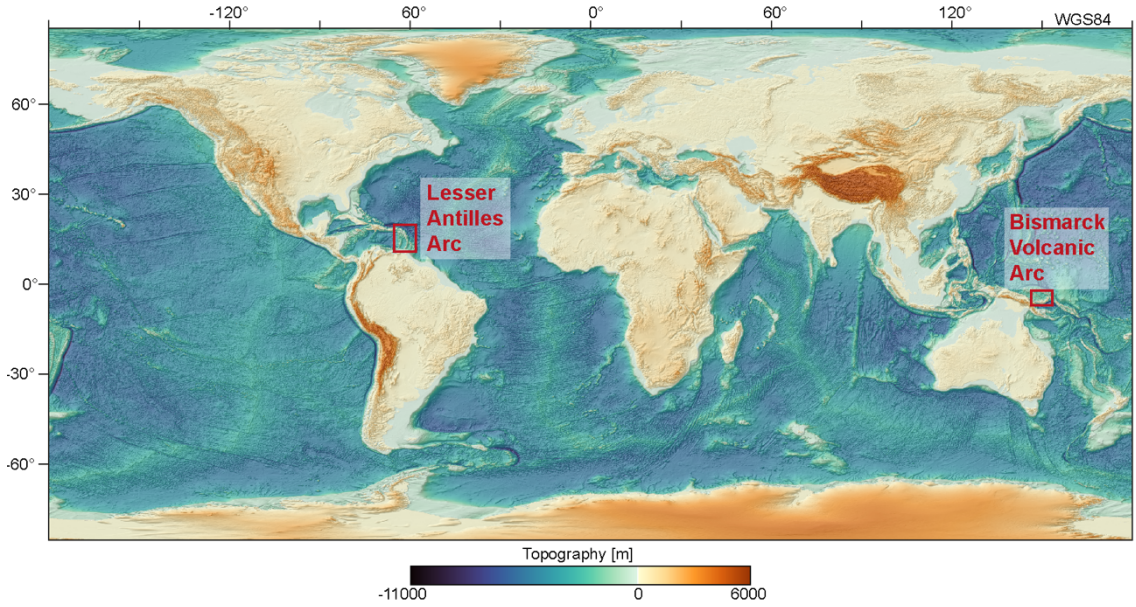

Figure 1.3: *Topographic map of the world based on a GMRT digital elevation model* (Ryan et al., 2009). *Red rectangles indicate the location of the research areas of this thesis on the globe.*

The research areas of this thesis are two volcanic arc islands: Sakar Island, Papua New Guinea, and Montserrat, Lesser Antilles. Sakar Island is part of the Western Bismarck Volcanic Arc (Figure 1.3) formed by northward subduction of the Solomon microplate beneath the Bismarck microplate (Baldwin et al., 2012; Taylor, 1979). A detailed tectonic and geological background of the regions is provided in Chapter 3. The seafloor around the volcanoes of the Western Bismarck Volcanic Arc has been surveyed by two research expeditions: In 2004, the crew of

R/V Kilo Moana mapped 12 submarine landslide deposits around the islands of the western Bismarck Volcanic Arc, including Umboi, Sakar, and Ritter Island (Silver et al., 2009). In 2016, a research expedition on R/V Sonne (SO252, Berndt et al., 2017) carried out intensive geophysical surveys, including a 3D MCS volume, and geological sampling targeting deposits associated with the 1888 collapse of Ritter Island (Karstens et al., 2019; Watt et al., 2019). However, the seismic data acquired during SO252 did not only provide insight into the Ritter Island collapse and emplacement – they also revealed two previously unknown landslides deposits offshore Sakar Island. These landslide deposits are analysed in Chapter 3 of this thesis.

Montserrat is a volcanic island on the Lesser Antilles Arc (Figure 1.3), southwest of Antigua and northwest of Guadeloupe. The Lesser Antilles Arc is formed by southward subduction of the North American plate beneath the Caribbean plate (Davis, 1924; Feuillet et al., 2010). Montserrat has been the subject of several geophysical and geological research expeditions (Crutchley et al., 2013; Feuillet et al., 2010; Karstens et al., 2013; Le Friant et al., 2015, 2004; Lebas et al., 2011; Watt et al., 2012b). Lebas et al. (2011) mapped at least 12 buried or surficial mass transport deposits at the flanks of Montserrat and within in the adjacent Montserrat-Bouillante-Graben based on MCS data from the expeditions AQUADOMAR (1999), CARAVAL (2002), GWADASEIS (2009), and JC45/46 (2010). Additional work on marine pyroclastic flow deposits has been caried out with data from an expedition with the vessel Seapony (1998) (Hart et al., 2004), the expeditions JCR123 (2005) and JC18 (2007) (Trofimovs et al., 2008), and 3D MCS data from JC45 (Karstens et al., 2013). Mass transport deposits offshore Montserrat and Martinique have also been the target of drilling operations during IODP Expedition 340 (Expedition 340 Scientists, 2013; Le Friant et al., 2015). In 2019, two research cruises on R/V Meteor – M154-1 (Berndt et al., 2019) and M154-2 (Huhn et al., 2019) acquired new 2D and 3D MCS, bathymetry, and Parasound sediment echosounder data, and conducted a drilling campaign with the robotic seafloor drill rig MeBo70. Parts of the data acquired on these cruises are analysed in the chapters 4 to 6 of this thesis.

1.5 Aims of this thesis

The hazard assessment of tsunamigenic volcanic flank collapses requires a detailed understanding of the geological processes that are active during failure and emplacement of the associated landslides and their role in tsunami generation. This thesis aims to analyse these processes and their interplay by answering the following questions:

1. Which processes are involved in volcanic flank collapse emplacement?

2. How do these processes interact with each other?
3. What are the controls on emplacement characteristics and deposit morphology?
4. How does each process affect tsunami magnitudes?
5. How does rapid loading by a volcanic mass transport deposit affect subsurface pore fluid pressure and what are the consequences for the stability of the sediments on the volcanic flank?

1.6 Outline of this thesis

This thesis consists of seven chapters. Four of these chapters are scientific articles or manuscripts which are either published, in review, or in preparation. Chapter 1 provides an introduction to the topic of volcanic island flank collapses, associated geological processes, and their consequences, gives an overview of the research areas, and defines the aims and the outline of this thesis.

Chapter 2 gives an overview of the different datasets analyzed in this thesis. It summarizes how the geophysical data were acquired and processed, as well as where they have been archived for public access. The processing of multi-channel 2D and 3D seismic data is focused here, as seismic data is the data basis for all four scientific articles in chapters 3 to 6. This chapter also describes how temperature was measured with two different approaches, a hybrid lister-outrigger probe attached to a gravity corer and via logging-while-tripping during a MeBo70 drilling campaign, and how subsurface pore fluid pressure was modelled based on permeability measurements from IODP Expedition 340 with a finite-difference approach.

Chapter 3 is a publication titled '*Seismic reconstruction of seafloor sediment deformation during volcanic debris avalanche emplacement offshore Sakar, Papua New Guinea*' (Kühn et al., 2021) that has been published in the journal '*Marine Geology*'. In this study we analyze the role of the substrate in the emplacement of submarine landslide deposits by studying the emplacement characteristics of two previously unknown landslide deposits offshore Sakar Island. Full reference: *Kühn, M., Karstens, J., Berndt, C., Watt, S.F.L., 2021. Seismic reconstruction of seafloor sediment deformation during volcanic debris avalanche emplacement offshore Sakar, Papua New Guinea. Marine Geology 439. https://doi.org/10.1016/j.margeo.2021.106563*

Chapter 4 is a publication titled '*Volcanic flank collapse, secondary sediment failure and flow-transition: multi-stage landslide emplacement offshore Montserrat, Lesser Antilles*' which is

published in the journal '*Geochemistry, Geophysics, Geosystems*'. This study reconstructs the geological processes that formed mass transport deposits offshore Montserrat, including at least two major volcanic flank collapses, secondary seafloor failure, substrate incorporation and deformation, as well as a late-stage erosive density current. Full reference: *Kühn, M., Berndt, C., Watt, S.F.L., Hornbach, M.J., Krastel, S., Sass, K., Kutterolf, S., Freudenthal, T., Huhn, K., Karstens, J., Schramm, B., Elger, J., Böttner, C., Klaeschen, D., 2024. Volcanic flank collapse, secondary sediment failure and flow-transition: Multi-stage landslide emplacement offshore Montserrat, Lesser Antilles. Geochemistry, Geophysics, Geosystems, 25, e2024GC011564. https://doi.org/10.1029/2024GC011564*

Chapter 5 is a manuscript titled '*New Heat Flow Measurements Offshore Montserrat: Advective Heat Flow Detected via MeBo Borehole Temperature Logging*' which is submitted the '*Journal of Geophysical Research - Solid Earth*'. This study analyses shallow temperature measurements and drill hole temperature data from a drilling campaign offshore Montserrat and finds indications for previously undetected advective heat flow in buried mass transport deposits.

Chapter 6 is a manuscript titled '*Loaded to fail - Critical pore fluid pressure by stacking of mass transport deposits offshore Montserrat*' which is in preparation for submission to a letter-style scientific journal. In this study we use permeability measurements from IODP Expedition 340 offshore Montserrat and seismic data from cruise M154-1 to model the evolution of pore pressure within the subsurface after rapid loading by a mass transport deposit.

Chapter 7 draws conclusions of the research done within the framework of this thesis and gives an outlook how future research and further studies might contribute to a better understanding of volcanic flank collapses and towards robust hazard assessments. This thesis closes with acknowledgements, curriculum vitae, and a publication list.

References

Aubry, T.J., Farquharson, J.I., Rowell, C.R., Watt, S.F.L., Pinel, V., Beckett, F., Fasullo, J., Hopcroft, P.O., Pyle, D.M., Schmidt, A., Sykes, J.S., 2022. Impact of climate change on volcanic processes: current understanding and future challenges. Bull Volcanol 84. https://doi.org/10.1007/s00445-022-01562-8

Baldwin, S.L., Fitzgerald, P.G., Webb, L.E., 2012. Tectonics of the New Guinea Region. Annu Rev Earth Planet Sci 40, 495–520. https://doi.org/10.1146/annurev-earth-040809-152540

Barrett, R., Lebas, E., Ramalho, R., Klaucke, I., Kutterolf, S., Klügel, A., Lindhorst, K., Gross, F., Krastel, S., 2020. Revisiting the tsunamigenic volcanic flank collapse of fogo island in the cape verdes, offshore West Africa, in: Geological Society Special Publication. Geological Society of London, pp. 13–26. https://doi.org/10.1144/SP500-2019-187

Berndt, C., Böttner, C., Elger, J., Kontradowitz, S., Kühn, M., Müller, S., Schramm, B., Stelzner, M., 2019. Sector collapse kinematics and tsunami implications - SEKT, Cruise No. M154/1, April 3 - April 25, 2019, Mindelo (Cape Verde) - Point-á-Pitre (Guadeloupe). METEOR-Berichte, M154/1. Gutachterpanel Forschungsschiffe, Bonn, 47 pp.

Berndt, C., Muff, S., Klaucke, I., Watt, S., Böttner, C., Schramm, B., Völsch, A., Bennecke, S., Elger, J., Chi, W.-C., 2017. RV SONNE 252 Cruise Report/Fahrtbericht, Yokohama: 05.11. 2016-Nouméa: 18.12. 2016. SO252: RITTER ISLAND Tsunami potential of volcanic flank collapses.

Brunet, M., Le Friant, A., Boudon, G., Lafuerza, S., Talling, P., Hornbach, M., Ishizuka, O., Lebas, E., Guyard, H., 2016. Composition, geometry, and emplacement dynamics of a large volcanic island landslide offshore Martinique: From volcano flank-collapse to seafloor sediment failure? Geochemistry, Geophysics, Geosystems 17, 699–724. https://doi.org/10.1002/2015GC006034

Capra, L., Macıas, J.L., Scott, K.M., Abrams, M., Garduño-Monroy, V.H., 2002. Debris avalanches and debris flows transformed from collapses in the Trans-Mexican Volcanic Belt, Mexico–behavior, and implications for hazard assessment. Journal of Volcanology and Geothermal Research 113, 81–110.

Clare, M., Lintern, D.G., Rosenberger, K., Clarke, J.E.H., Paull, C., Gwiazda, R., Cartigny, M.J.B., Talling, P.J., Perara, D., Xu, J., Parsons, D., Jacinto, R.S., Apprioual, R., 2020. Lessons learned from the monitoring of turbidity currents and guidance for future platform designs, in: Geological Society Special Publication. Geological Society of London, pp. 605–634. https://doi.org/10.1144/SP500-2019-173

Clare, M.A., Yeo, I.A., Watson, S., Wysoczanski, R., Seabrook, S., Mackay, K., Hunt, J.E., Lane, E., Talling, P.J., Pope, E., Cronin, S., Ribó, M., Kula, T., Tappin, D., Henrys, S., de Ronde, C., Urlaub, M., Kutterolf, S., Fonua, S., Panuve, S., Veverka, D., Rapp, R., Kamalov, V., Williams, M., 2023. Fast and destructive density currents created by ocean-entering volcanic eruptions. Science (1979)

381, 1085–1092. https://doi.org/10.1126/science.adi3038

Clarke, J.E.H., Shor, A.N., Piper, D.J.W., Mayer, L.A., 1990. Large-scale current-induced erosion and deposition in the path of the 1929 Grand Banks turbidity current. Sedimentology 37, 613–629.

Crutchley, G.J., Karstens, J., Berndt, C., Talling, P.J., Watt, S.F.L., Vardy, M.E., Hühnerbach, V., Urlaub, M., Sarkar, S., Klaeschen, D., Paulatto, M., Le Friant, A., Lebas, E., Maeno, F., 2013. Insights into the emplacement dynamics of volcanic landslides from high-resolution 3D seismic data acquired offshore Montserrat, Lesser Antilles. Mar Geol 335, 1–15. https://doi.org/10.1016/j.margeo.2012.10.004

Davis, W.M., 1924. The formation of the Lesser Antilles. Proceedings of the National Academy of Sciences 10, 205–211.

Day, S.J., 2015. Volcanic Tsunamis, in: The Encyclopedia of Volcanoes. Elsevier, pp. 993–1009. https://doi.org/10.1016/B978-0-12-385938-9.00058-4

Day, S.J., Heleno Da Silva, S.I.N., Fonseca, J.F.B.D., 1999. A past giant lateral collapse and present-day flank instability of Fogo, Cape Verde Islands. Journal of Volcanology and Geothermal Research 94, 191–218. https://doi.org/10.1016/S0377-0273(99)00103-1

Expedition 340 Scientists, 2013. Expedition 340 summary, in: Le Friant, A., Ishizuka, O., Stroncik, N.A., and the Expedition 340 Scientists, Proc. IODP, 340: Tokyo (Integrated Ocean Drilling Program Management International, Inc.). https://doi.org/10.2204/iodp.proc.340.101.2013

Farquharson, J.I., Amelung, F., 2022. Volcanic hazard exacerbated by future global warming-driven increase in heavy rainfall. R Soc Open Sci 9. https://doi.org/10.1098/rsos.220275

Feuillet, N., Leclerc, F., Tapponnier, P., Beauducel, F., Boudon, G., Le Friant, A., Deplus, C., Lebrun, J.F., Nercessian, A., Saurel, J.M., Clément, V., 2010. Active faulting induced by slip partitioning in montserrat and link with volcanic activity: New insights from the 2009 GWADASEIS marine cruise data. Geophys Res Lett 37, 1–6. https://doi.org/10.1029/2010GL042556

Furst, S., Urlaub, M., Klein, E., Bonanati, C., 2023. Are eruptions reliable precursors to marine volcano collapses? Front Earth Sci (Lausanne) 11. https://doi.org/10.3389/feart.2023.1130561

Grilli, S.T., Tappin, D.R., Carey, S., Watt, S.F.L., Ward, S.N., Grilli, A.R., Engwell, S.L., Zhang, C., Kirby, J.T., Schambach, L., Muin, M., 2019. Modelling of the tsunami from the December 22, 2018 lateral collapse of Anak Krakatau volcano in the Sunda Straits, Indonesia. Sci Rep 9, 1–13. https://doi.org/10.1038/s41598-019-48327-6

Hart, K., Carey, S., Sigurdsson, H., Sparks, R.S.J., Robertson, R.E.A., 2004. Discharge of pyroclastic flows into the sea during the 1996-1998 eruptions of the Soufrière Hills volcano, Montserrat. Bull Volcanol 66, 599–614. https://doi.org/10.1007/s00445-004-0342-1

Huhn, K., Freudenthal, T., Dehning, K., Gatter, R., Hilgenfeldt, C., Hönekopp, L., Hornbach, M., Kühn, M., Kuhlmann, J., Kutterolf, S., Meyer-Schack, B., Pallapies, K., Rapp, S.K., Sievers, C., Watt, S.,

Stelzner, M., 2019. Sector collapse kinematics and tsunami implications - SEKT, Cruise No. M154-2, April 29 - Mai 23, 2019, Pointe-à-Pitre (Guadeloupe) - Pointe-à-Pitre (Guadeloupe).

Hunt, J.E., Talling, P.J., Clare, M.A., Jarvis, I., Wynn, R.B., 2014. Long-term (17 Ma) turbidite record of the timing and frequency of large flank collapses of the Canary Islands. Geochemistry, Geophysics, Geosystems 15, 3322–3345. https://doi.org/10.1002/2014GC005232

Janda, R.J., Scott, K.M., Nolan, K.M., 1981. The 1980 eruptions of Mount St. Helens, Washington. Geological Survey Professional Paper 1250, 461.

Johnson, R., Kitts, S., Indies, W., Roobol, M.J., I, A.L.S., Wright, J. V, 1987. Large-scale volcanic cone collapse: the 1888 slope failure of Ritter volcano, and other examples from Papua New Guinea. Bull Volcanol 49, 669–679.

Karstens, J., Berndt, C., Urlaub, M., Watt, S.F.L., Micallef, A., Ray, M., Klaucke, I., Muff, S., Klaeschen, D., Kühn, M., Roth, T., Böttner, C., Schramm, B., Elger, J., Brune, S., 2019. From gradual spreading to catastrophic collapse – Reconstruction of the 1888 Ritter Island volcanic sector collapse from high-resolution 3D seismic data. Earth Planet Sci Lett 517. https://doi.org/10.1016/j.epsl.2019.04.009

Karstens, J., Crutchley, G.J., Berndt, C., Talling, P.J., Watt, S.F.L., Hühnerbach, V., Friant, A. Le, Lebas, E., Trofimovs, J., 2013. Emplacement of pyroclastic deposits offshore Montserrat: Insights from 3D seismic data. Journal of Volcanology and Geothermal Research 257, 1–11. https://doi.org/10.1016/j.jvolgeores.2013.03.004

Karstens, J., Kelfoun, K., Watt, S.F.L., Berndt, C., 2020. Combining 3D seismics, eyewitness accounts and numerical simulations to reconstruct the 1888 Ritter Island sector collapse and tsunami. International Journal of Earth Sciences. https://doi.org/10.1007/s00531-020-01854-4

Keating, B.H., McGuire, W.J., 2000. Island Edifice Failures and Associated Tsunami Hazards, Pure appl. geophys.

Krastel, S., Schmincke, H.U., Jacobs, C.L., Rihm, R., Le Bas, T.P., Alibés, B., 2001. Submarine landslides around the Canary Islands. J Geophys Res Solid Earth 106, 3977–3997. https://doi.org/10.1029/2000jb900413

Kühn, M., Karstens, J., Berndt, C., Watt, S.F.L., 2021. Seismic reconstruction of seafloor sediment deformation during volcanic debris avalanche emplacement offshore Sakar, Papua New Guinea. Mar Geol 439. https://doi.org/10.1016/j.margeo.2021.106563

Kvalstad, T.J., Nadim, F., Arbitz, C.B., 2001. Deepwater geohazards: Geotechnical concerns and solutions, in: Offshore Technology Conference. OTC, p. OTC-12958.

Le Bas, T.P., Masson, D.G., Holtom, R.T., Grevemeyer, I., 2007. Slope failures of the flanks of the southern Cape Verde Islands. Submarine Mass Movements and Their Consequences, 3rd International Symposium 337–345. https://doi.org/10.1007/978-1-4020-6512-5_35

Le Friant, A., Harford, C.L., Deplus, C., Boudon, G., Sparks, R.S.J., Herd, R.A., Komorowski, J.C., 2004. Geomorphological evolution of Montserrat (West Indies): importance of flank collapse and erosional processes. J Geol Soc London 161, 147–160. https://doi.org/10.1144/0016-764903-017

Le Friant, A., Ishizuka, O., Boudon, G., Palmer, M.R., Talling, P.J., Villemant, B., Adachi, T., Aljahdali, M., Breitkreuz, C., Brunet, M., Caron, B., Coussens, M., Deplus, C., Endo, D., Feuillet, N., Fraas, A.J., Fujinawa, A., Hart, M.B., Hatfield, R.G., Hornbach, M., Jutzeler, M., Kataoka, K.S., Komorowski, J.C., Lebas, E., Lafuerza, S., Maeno, F., Manga, M., Martínez-Colõn, M., McCanta, M., Morgan, S., Saito, T., Slagle, A., Sparks, S., Stinton, A., Stroncik, N., Subramanyam, K.S.V., Tamura, Y., Trofimovs, J., Voight, B., Wall-Palmer, D., Wang, F., Watt, S.F.L., 2015. Submarine record of volcanic island construction and collapse in the Lesser Antilles arc: First scientific drilling of submarine volcanic island landslides by IODP Expedition 340. Geochemistry, Geophysics, Geosystems 16, 420–442. https://doi.org/10.1002/2014GC005652

Lebas, E., Le Friant, A., Boudon, G., Watt, S.F.L., Talling, P.J., Feuillet, N., Deplus, C., Berndt, C., Vardy, M.E., 2011. Multiple widespread landslides during the long-term evolution of a volcanic island: Insights from high-resolution seismic data, Montserrat, Lesser Antilles. Geochemistry, Geophysics, Geosystems 12. https://doi.org/10.1029/2010GC003451

Lipman, P.W., Sisson, T.W., Ui, T., Naka, J., Smith, J.R., 2002. Ancestral submarine growth of Kilauea volcano and instability of its south flank. Hawaiian volcanoes: deep underwater perspectives 128, 161–191.

Løvholt, F., Pedersen, G., Harbitz, C.B., Glimsdal, S., Kim, J., 2015. On the characteristics of landslide tsunamis. Philosophical Transactions of the Royal Society A: Mathematical, Physical and Engineering Sciences 373. https://doi.org/10.1098/rsta.2014.0376

Masson, D.G., Canals, M., Alonso, B., Urgeles, R., Huhnerbach, V., 1998. The Canary Debris Flow: Source area morphology and failure mechanisms. Sedimentology 45, 411–432. https://doi.org/10.1046/j.1365-3091.1998.0165f.x

Masson, D.G., Watts, A.B., Gee, M.J.R., Urgeles, R., Mitchell, N.C., Le Bas, T.P., Canals, M., 2002. Slope failures on the flanks of the western Canary Islands. Earth Sci Rev 57, 1–35. https://doi.org/10.1016/S0012-8252(01)00069-1

McGuire, W.J., 2006. Lateral collapse and tsunamigenic potential of marine volcanoes. Geol Soc Spec Publ 269, 121–140. https://doi.org/10.1144/GSL.SP.2006.269.01.08

McGuire, W.J., 2003. Volcano instability and lateral collapse, Revista.

Moore, J.G., Clague, D. a., Holcomb, R.T., Lipman, P.W., Normark, W.R., Torresan, M.E., 1989. Prodigious submarine landslides on the Hawaiian Ridge. J Geophys Res 94, 17465. https://doi.org/10.1029/JB094iB12p17465

Moore, J.G., Normark, W.R., 1994. Giant Hawaiian Landslides. Annu Rev Earth Planet Sci 22, 119–

144.

Ramalho, R. S., Winckler, G., Madeira, J., Helffrich, G. R., Hipólito, A., Quartau, R., Adena, K., & Schaefer, J. M. (2015). Hazard potential of volcanic flank collapses raised by new megatsunami evidence. *Science Advances*, *1*(9). https://doi.org/10.1126/sciadv.1500456

Roverato, M., Di Traglia, F., Procter, J., Paguican, E., Dufresne, A., 2021. Factors contributing to volcano lateral collapse. Volcanic Debris Avalanches: From collapse to hazard 91–119.

Ryan, W.B.F., Carbotte, S.M., Coplan, J.O., O'Hara, S., Melkonian, A., Arko, R., Weissel, R.A., Ferrini, V., Goodwillie, A., Nitsche, F., Bonczkowski, J., Zemsky, R., 2009. Global multi-resolution topography synthesis. Geochemistry, Geophysics, Geosystems 10. https://doi.org/10.1029/2008GC002332

Siebert, L., Alvarado, G.E., Vallance, J.W., Van Wyk De Vries, B., 2006. Large-volume volcanic edifice failures in Central America and associated hazards. Special Paper of the Geological Society of America 412, 1–26. https://doi.org/10.1130/2006.2412(01)

Silver, E., Day, S., Ward, S., Hoffmann, G., Llanes, P., Driscoll, N., Appelgate, B., Saunders, S., 2009. Volcano collapse and tsunami generation in the Bismarck Volcanic Arc, Papua New Guinea. Journal of Volcanology and Geothermal Research 186, 210–222. https://doi.org/10.1016/j.jvolgeores.2009.06.013

Sobiesiak, M.S., Kneller, B., Alsop, G.I., Milana, J.P., 2018. Styles of basal interaction beneath mass transport deposits. Mar Pet Geol 98, 629–639. https://doi.org/10.1016/j.marpetgeo.2018.08.028

Taylor, B., 1979. Bismarck Sea: Evolution of a back-arc basin. Geology 7, 171–174. https://doi.org/10.1130/0091-7613(1979)7<171:BSEOAB>2.0.CO;2

Tost, M., Cronin, S.J., Procter, J.N., 2014. Transport and emplacement mechanisms of channelised long-runout debris avalanches, Ruapehu volcano, New Zealand. Bull Volcanol 76, 1–14. https://doi.org/10.1007/s00445-014-0881-z

Trofimovs, J., Sparks, R.S.J., Talling, P.J., 2008. Anatomy of a submarine pyroclastic flow and associated turbidity current: July 2003 dome collapse, Soufri??re Hills volcano, Montserrat, West Indies. Sedimentology 55, 617–634. https://doi.org/10.1111/j.1365-3091.2007.00914.x

Walter, T.R., Haghshenas Haghighi, M., Schneider, F.M., Coppola, D., Motagh, M., Saul, J., Babeyko, A., Dahm, T., Troll, V.R., Tilmann, F., Heimann, S., Valade, S., Triyono, R., Khomarudin, R., Kartadinata, N., Laiolo, M., Massimetti, F., Gaebler, P., 2019. Complex hazard cascade culminating in the Anak Krakatau sector collapse. Nat Commun 10. https://doi.org/10.1038/s41467-019-12284-5

Ward, S.N., Day, S., 2003. Ritter Island Volcano - Lateral collapse and the tsunami of 1888. Geophys J Int 154, 891–902. https://doi.org/10.1046/j.1365-246X.2003.02016.x

Watt, S.F.L., Karstens, J., Berndt, C., 2021. Volcanic-Island Lateral Collapses and Their Submarine

Deposits, Advances in Volcanology. Springer International Publishing. https://doi.org/10.1007/978-3-030-57411-6_10

Watt, S.F.L., Karstens, J., Micallef, A., Berndt, C., Urlaub, M., Ray, M., Desai, A., Sammartini, M., Klaucke, I., Böttner, C., Day, S., Downes, H., Kühn, M., Elger, J., 2019. From catastrophic collapse to multi-phase deposition: Flow transformation, seafloor interaction and triggered eruption following a volcanic-island landslide. Earth Planet Sci Lett 517. https://doi.org/10.1016/j.epsl.2019.04.024

Watt, S.F.L., Talling, P.J., Vardy, M.E., Heller, V., Hühnerbach, V., Urlaub, M., Sarkar, S., Masson, D.G., Henstock, T.J., Minshull, T.A., Paulatto, M., Le Friant, A., Lebas, E., Berndt, C., Crutchley, G.J., Karstens, J., Stinton, A.J., Maeno, F., 2012a. Combinations of volcanic-flank and seafloor-sediment failure offshore Montserrat, and their implications for tsunami generation. Earth Planet Sci Lett 319–320, 228–240. https://doi.org/10.1016/j.epsl.2011.11.032

Watt, S.F.L., Talling, P.J., Vardy, M.E., Masson, D.G., Henstock, T.J., H??hnerbach, V., Minshull, T.A., Urlaub, M., Lebas, E., Le Friant, A., Berndt, C., Crutchley, G.J., Karstens, J., 2012b. Widespread and progressive seafloor-sediment failure following volcanic debris avalanche emplacement: Landslide dynamics and timing offshore Montserrat, Lesser Antilles. Mar Geol 323–325, 69–94. https://doi.org/10.1016/j.margeo.2012.08.002

Zorn, E.U., Vassileva, M., Walter, T.R., Darmawan, H., Röhler, L., Amelung, F., 2023. Interactions of magmatic intrusions with the multiyear flank instability at Anak Krakatau volcano, Indonesia: Insights from InSAR and analogue modeling. Geology 51, 340–344. https://doi.org/10.1130/G50693.1

2. Methodology

2.1 Active seismic experiments

The Chapters 3 to 6 of this thesis present and analyze 2D and 3D multi-channel seismic (MCS) data that was acquired during the research expeditions SO252 on R/V SONNE in 2016 (Ritter/Sakar Island, Berndt et al., 2021) and M154-1 on R/V METEOR in 2019 (Montserrat, Kühn et al., 2023a, 2023b). While the 2D MCS data that has been collected during expedition SO252 was already processed and ready for interpretation, the 2D and 3D MCS data from M154-1 was processed within the framework of this thesis. The following subsections give a brief overview of the general acquisition parameters and processing steps of each data set and report the 2D and 3D seismic processing of the M154-1 seismic data in detail.

2.1.1 Seismic survey parameters and seismic processing SO252 data (Sakar Island)

The scientific party of research expedition SO252 on R/V SONNE acquired 680 km of 2D MCS profiles in a survey area between the islands of Umboi, Sakar, and Ritter in the Bismarck Sea (Berndt et al., 2017; Kühn et al., 2021). Berndt et al. (2017) provide the seismic experiment parameters as follows: Two Generator-Injector (GI) airguns (105/105 I^3 chamber volumes) generated the source signal during the acquisition with a time-controlled shot rate of 5 s and a nominal air pressure of 210 bar (produced by a shipboard compressor). A streamer system with a total length of 335.5 m (total active length: 250.5 m) recorded the seismic signal with a sample rate of 0.5 ms and 4 s record length. The streamer system consisted of 20 12.5 m long active sections with a channel spacing of 1.56 m, a 25 m stretch section, and a 60 m long tow-cable. The processing of the data included bandpass filtering (10, 45, 250, 500 Hz corner frequencies), normal moveout (NMO) correction with a constant velocity of 1495 m/s and a post-stack 2D-Stolt-migration with a constant velocity of 1500 m/s. The acquisition geometry given in Berndt et al. (2017) is illustrated in Figure 2.1. An overview of the locations of the seismic profiles is given in Chapter 3. The data is accessible via Berndt et al. (2021).

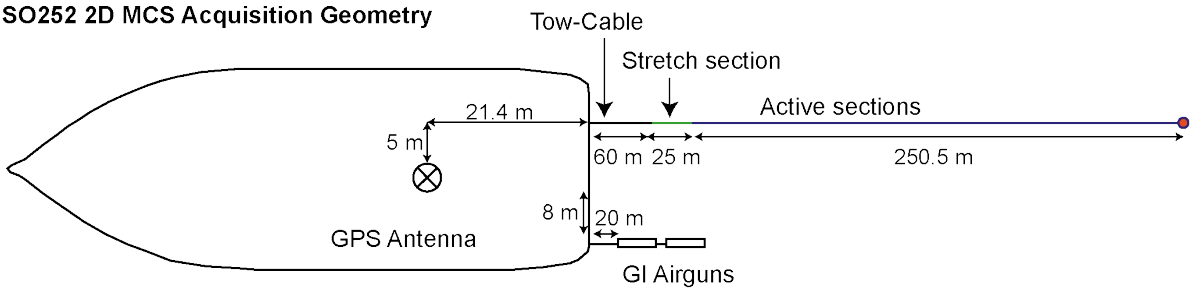

Figure 2.1: *Acquisition geometry for the 2D seismic experiment during research expedition SO252 adapted from Berndt et al. (2017).*

2.1.2 Seismic survey parameters M154-1 (Montserrat)

The seismic experiments offshore Montserrat during research expedition M154-1 on R/V METEOR include three 2D MCS surveys that acquired ~600 km of 2D MCS profiles and a 3D P-Cable MCS survey that acquired a 3.3 x 13 km 3D seismic data volume (Berndt et al., 2019). Berndt et al. (2019) provide the following acquisition parameters: Two GI airguns (105/105 I^3 chamber volumes) produced the source signal with a time-controlled shot rate of 5 s and an air pressure of 160 bar (produced by an offshore compressor container) at a nominal ship's speed of ~4.5 kn. During the 2D MCS survey the streamer system consisted of 2 to 7 12.5 m long active sections with a channel increment of 1.56 m (8 channels per section), a 25 m long stretch section, and a tow-cable length between 31 and 40 m. Fig. 3.2 illustrates the acquisition geometries from Berndt et al. (2019). An overview of the locations of the seismic profiles is given in Chapter 4.

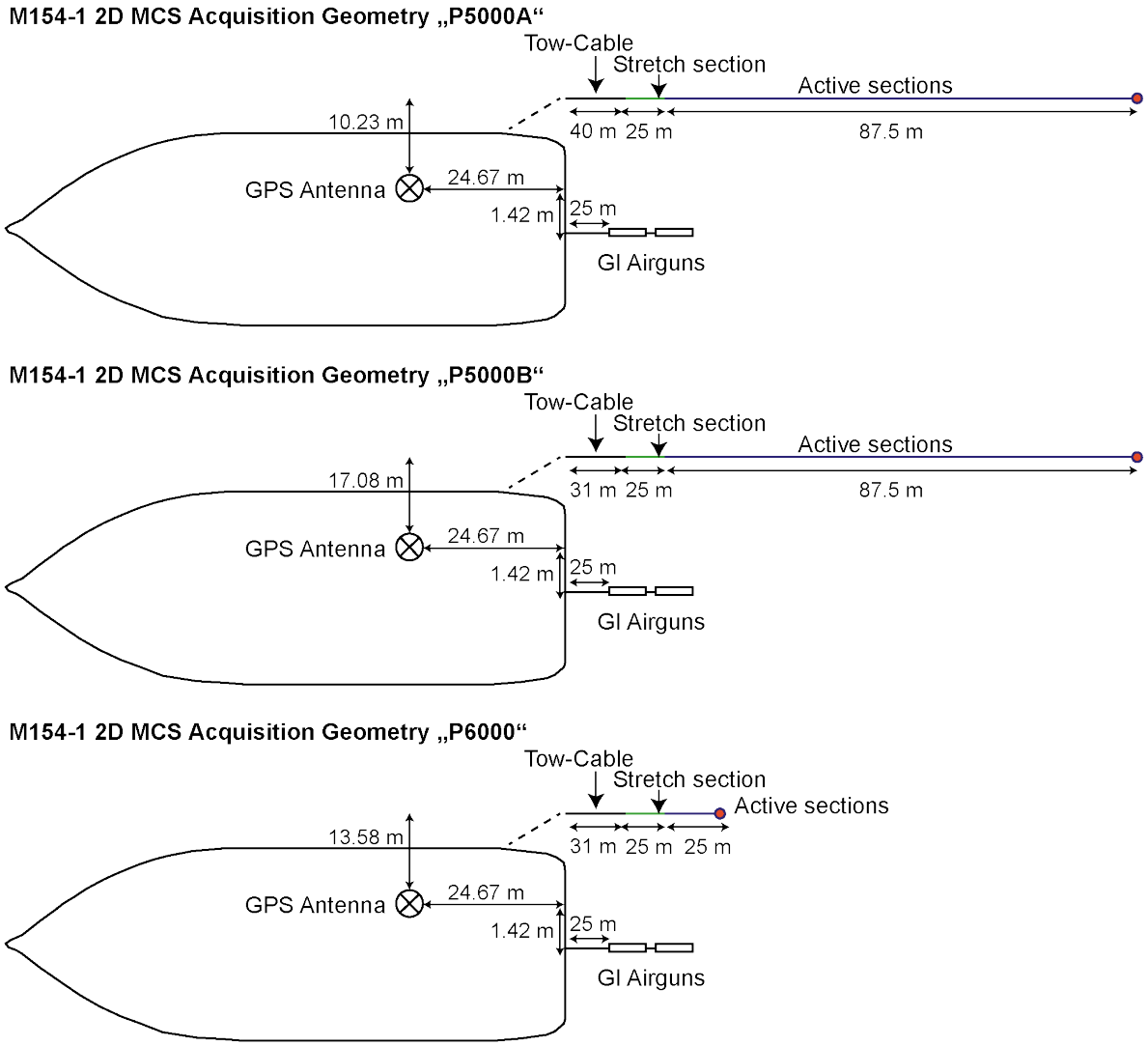

Figure 2.2: *Acquisition geometries for the 2D seismic experiment during research expedition M154-1 adapted from Berndt et al. (2019).*

This thesis does not include 2D MCS data acquired with the acquisition geometry “P1000” that is listed in Berndt et al. (2019) due to technical problems with the raw data files. The processed dataset is downloadable via Kühn et al. (2023a). During the 3D P-Cable MCS survey the streamer system consisted of 14 to 16 12.5 m long active streamer segments (8 channels per segment, channel increment 1.54 m) parallelly attached to a 199 m long cross-cable towed behind the vessel’s stern at a nominal speed of ~3.5 kn (Berndt et al., 2019). Figure 2.3 illustrates the 3D P-Cable MCS acquisition geometry. The processed dataset is downloadable via Kühn et al. (2023a).

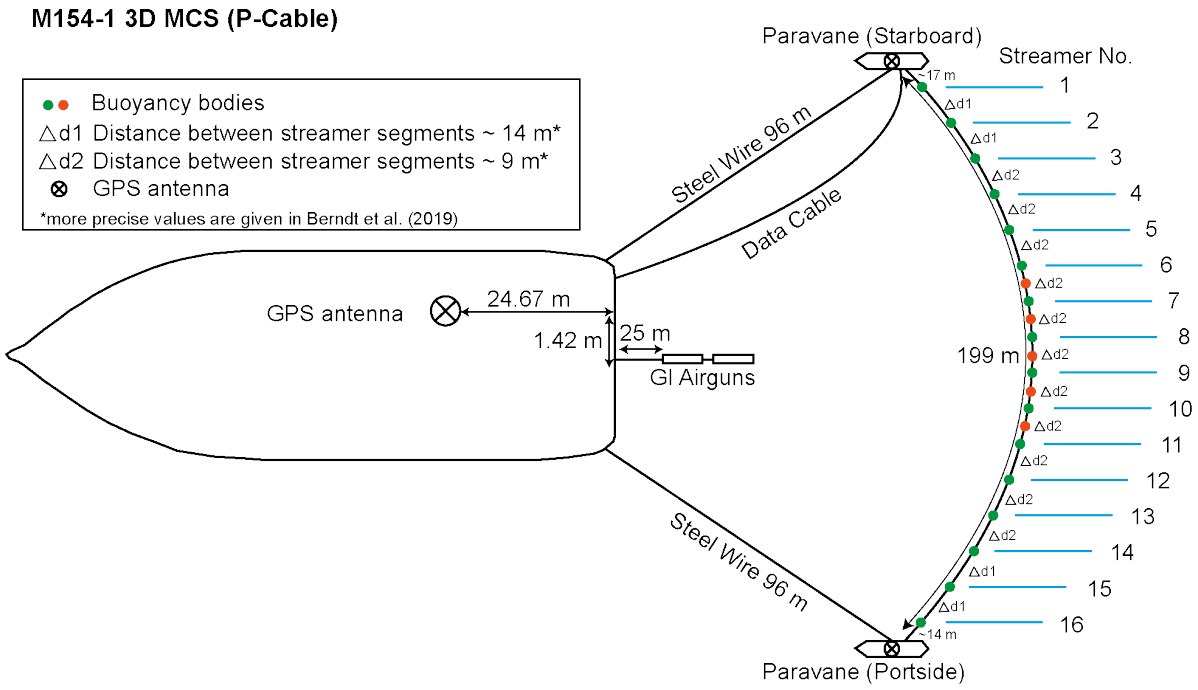

Figure 2.3: *Acquisition geometries for the 3D seismic experiment during research expedition M154-1 adapted from Berndt et al. (2019). Note that for parts of the survey the streamer geometry slightly changed: For the shots 22000 to 55000 streamers 2 and 8 did not collect data. The length of the steel wires towing the system was reduced to 85 m for shots 57000 to 75000. After shot 55000 parts of the cross cable were replaced and the streamer distances changed slightly. Berndt et al. (2019) provide distances on a cm scale.*

2.1.3 Processing of the M154-1 2D and 3D MCS data

The processing of the 2D and 3D MCS data collected during M154-1 was carried out with the seismic processing software “Omega” by Schlumberger. Pre-processing steps including geometry setup (1.5625 m bin size for the 2D data, 3.125 m bin size for the 3D data), quality control and 3D geometry corrections were performed with the Unix-based software packages Generic Mapping Tools version 5 (Wessel et al., 2013) and Seismic Unix (Stockwell Jr, 1999). Figure 2.4 shows the processing flow for the 2D MCS dataset that includes noise attenuation, multiple attenuation, NMO correction, stacking, post-stack denoising and a finite-difference migration. The noise attenuation segment of the processing flow combines six different methods of noise attenuation, trace manipulation, and interpolation with the aim to increase the signal-to-noise ratio of the data in a shot gather domain:

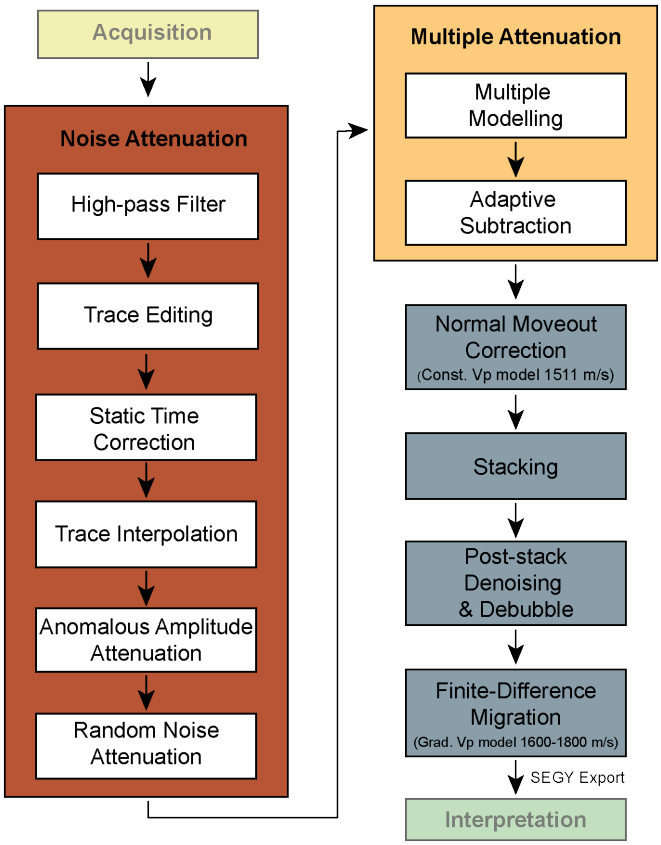

***Figure 2.4**: The seismic processing flow used for the M154-1 2D MCS dataset.*

(1) A zero-phase high-pass filter filtered out frequencies below 15 Hz (Figure 2.5A) and attenuated frequencies between 15 and 38 Hz with an upwardly decreasing intensity gradient (Figure 2.5B). The technical background of frequency filters in seismic data processing is discussed elsewhere (Yilmaz, 2001). (2) Extremely noisy (and likely malfunctional) channels (Figure 2.5B) required to be removed and interpolated in a later step. (3) Berndt et al. (2019) determined a trigger-shot-delay of 0.02 s in the data. A static time shift of 0.02 s (in negative direction) corrected this delay (Figure 2.5C). (4) Gaps in the shot gather that resulted from trace removal were interpolated between neighboring traces (Figure 2.5C) with a "Compact Fourier Interpolation"-algorithm (Moore et al., 2008; Yen, 1956). (5) Anomalous amplitude attenuation (AAA; e.g., Tian et al., 2022) reduced high amplitude noise in individual frequency bands by scaling the anomalously high amplitude traces to the median energy of neighboring traces within a defined spatial window of 21 traces in the frequency domain (Figure 2.5D). (6) Remaining patches of random noise were removed with a predictive deconvolution after Fourier transformation (Yilmaz, 2001) of the data from time-offset-domain to frequency-offset-

domain (Figure 2.5E). This method is commonly referred to as random noise attenuation (RNA; (Canales, 1984; Xia et al., 2021).

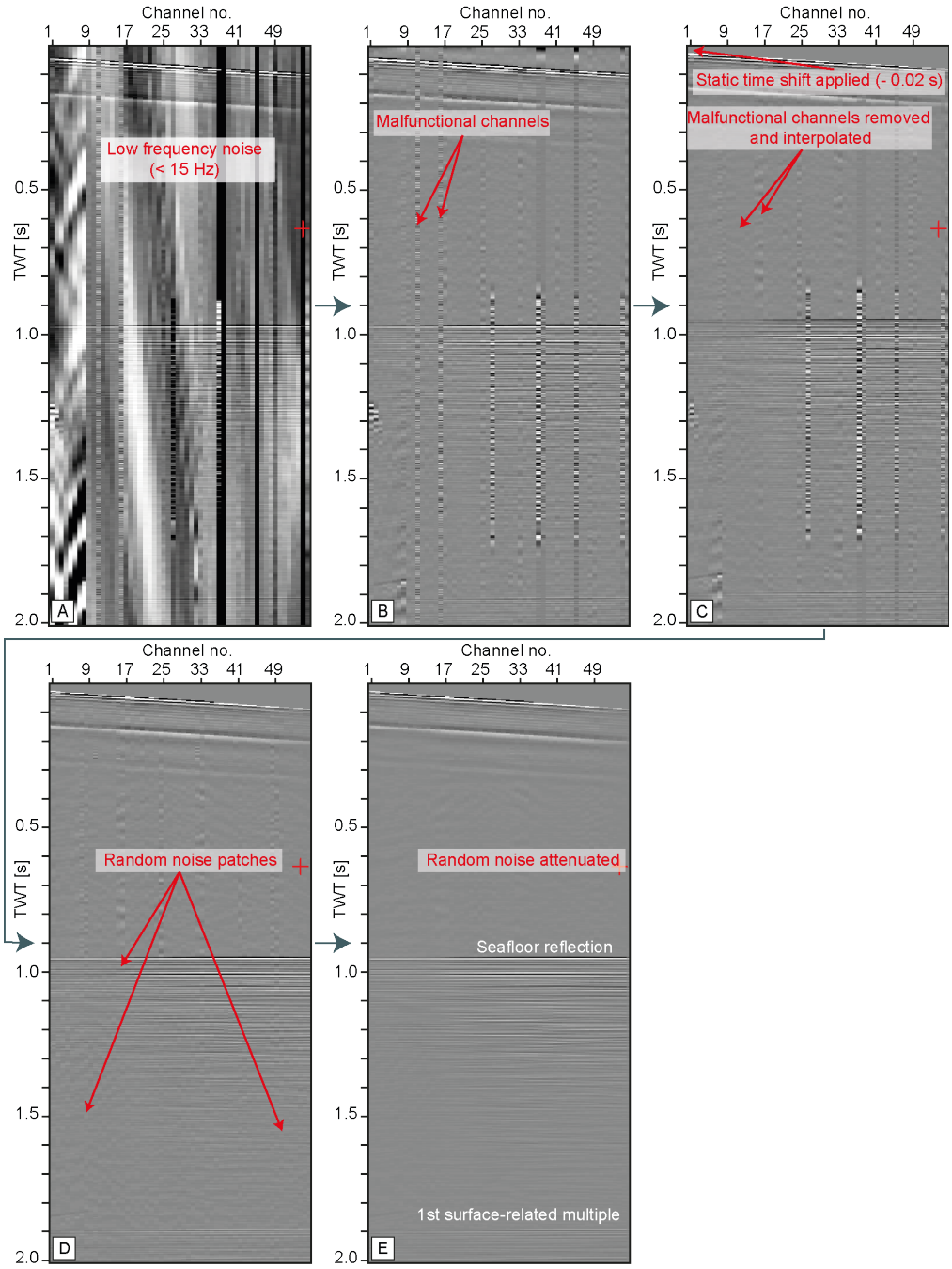

Figure 2.5: *Trace editing sequence within the 2D seismic processing workflow. A: Raw shot gather with low frequency noise overlaying the desired signal. B: Low frequency noise removed. C: Malfunctional channels are removed and interpolated, static time shift of 0.02 s is applied. High-amplitude noise is still visible. D: High amplitude noise reduced with AAA. Patches of random noise are still visible. E: Random noise reduced with RNA.*

Figure 2.6 shows surface-related multiples overlaying the primary data. A common approach of multiple attenuation in seismic data is the subtraction of a multiple model from the original data (Weglein et al., 2011). The adaptive subtraction method advances this approach by iteratively optimizing the input multiple models to the multiples in the original data with a least-squares or pattern-matching algorithm before subtraction (Guitton and Verschuur, 2004). Multiple models of the M154-1 2D MCS data were created by shifting the original primary traces to the TWT of the multiples in a shot gather. The adaptive subtraction method then fitted this input model to the actual multiple amplitude and reflection pattern and subtracted the optimized model from the original data (Figure 2.6). Figure 2.7 shows the multiple attenuation result in a stacked section next to the same stacked profile but without multiple attenuation.

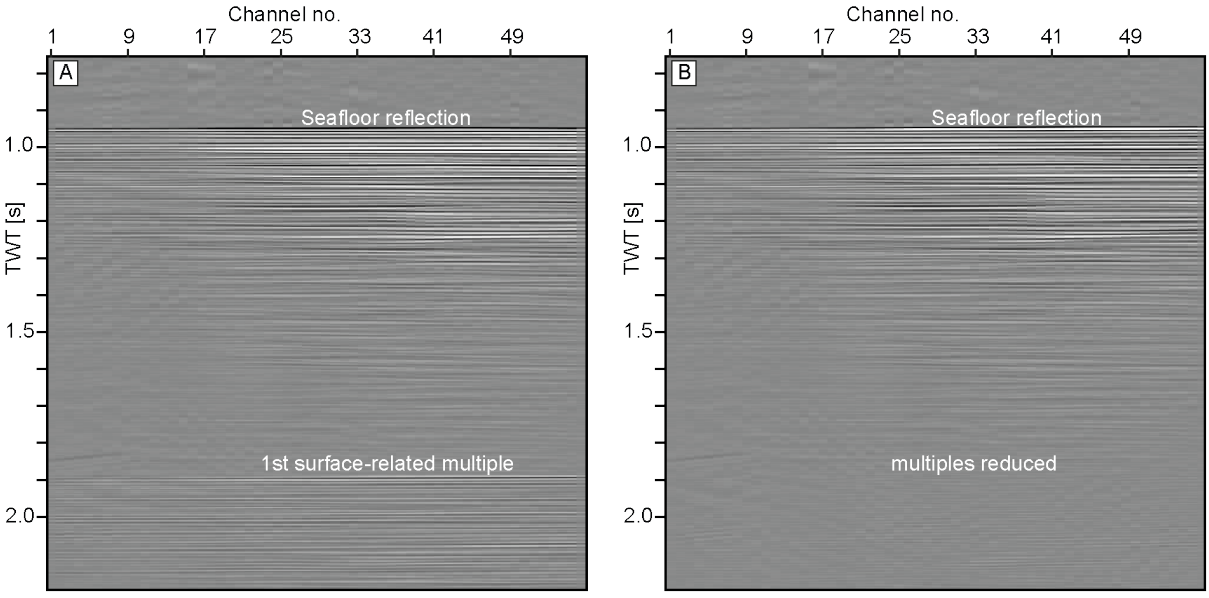

Figure 2.6: *A: Denoised shot gather before multiple attenuation. B: Denoised shot gather after multiple attenuation.*

After multiple attenuation and resorting of the traces to common-midpoint gathers, a hyperbolic normal-moveout correction compensated incorrect arrival times that resulted from the non-zero-offset acquisition geometry (Yilmaz, 2001). A seismic pressure-wave velocity (V_p) of 1511 m/s (from Conductivity-Temperature-Depth (CTD) measurements, see Berndt et al., 2019) was used as input velocity for this correction and led to a good result (Fig. 3.7).

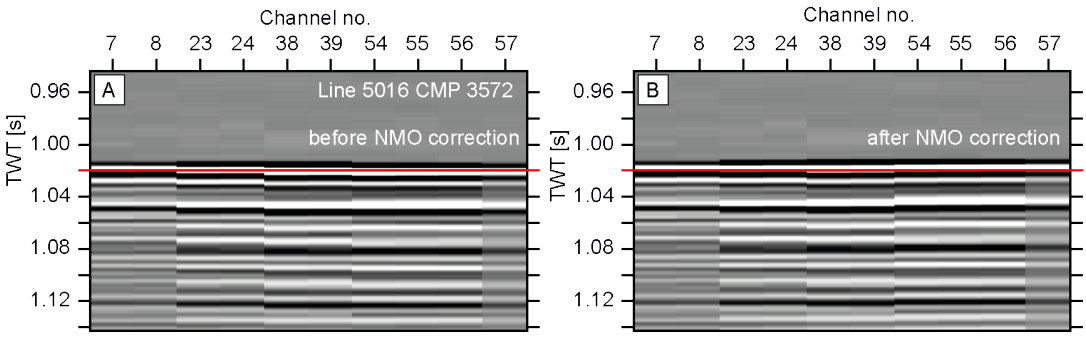

Figure 2.7: *A: CMP gather before NMO correction. B: CMP gather after NMO correction.*

Stacking – the process of summing up and normalizing adjacent traces with a common location into a single sample – of the NMO-corrected common-midpoint (CMP) gathers created seismic sections with an increased signal-to-noise ratio due to constructive and destructive interference of the stacked traces (Yilmaz, 2001). Figure 2.8 illustrates the stacking result before and after multiple attenuation.

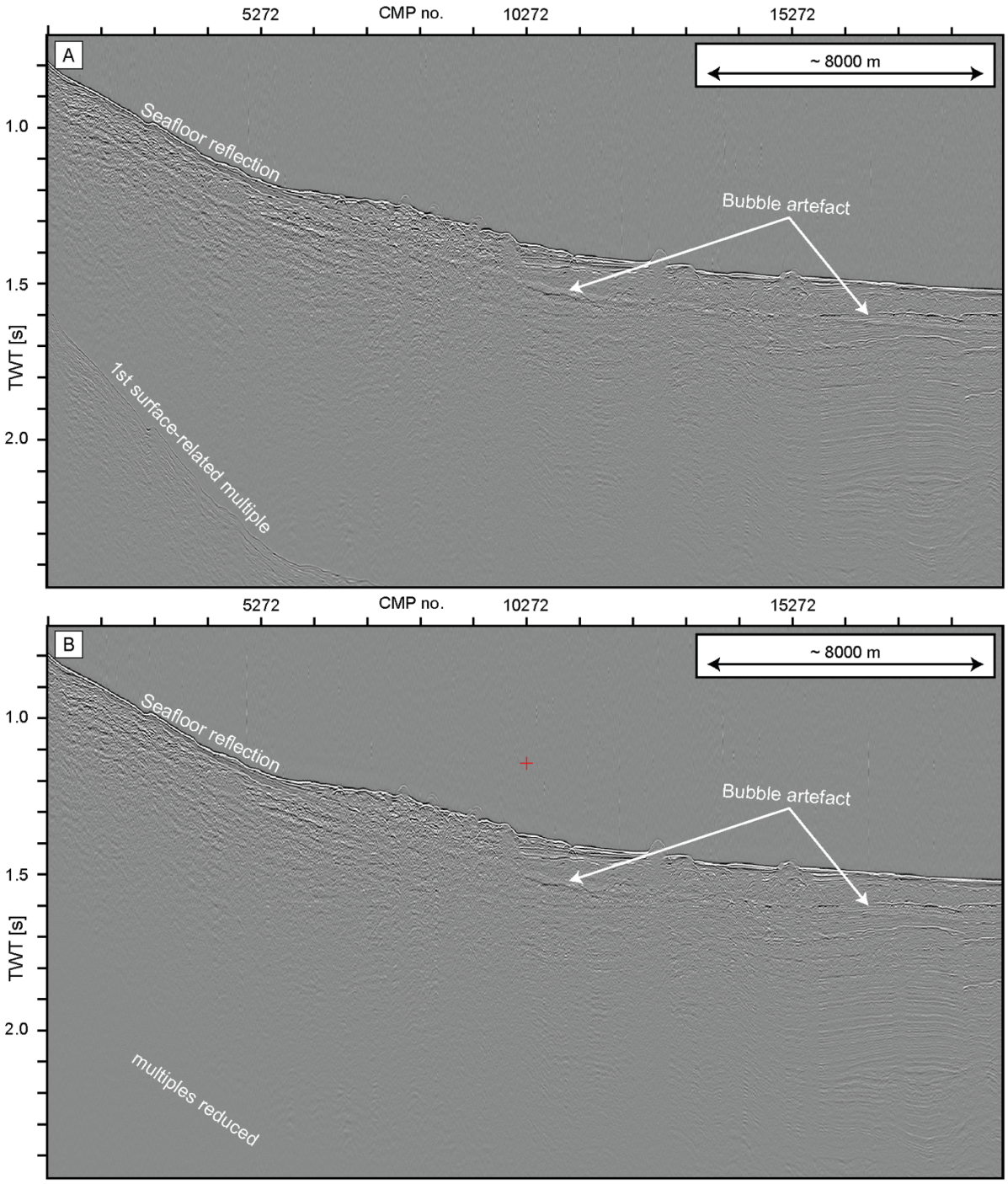

Figure 2.8: *A: stacked section of profile 5016 before multiple attenuation. B: stacked section of profile 5016 after multiple attenuation. A bubble artefact that follows the shape of the seafloor reflection with a time difference of 0.08 s TWT is visible in both sections.*

Figure 2.8 shows a bubble artefact that resembles the seafloor reflection with a delay of 0.08 s two-way-travel-time (TWT) and that can be reduced with a predictive deconvolution (Peacock and Treitel, 1969; Sheriff, 1982). Input for the deconvolution was the autocorrelation of the

stacked section and the prediction operator was designed with 0.08 s prediction length. Figure 2.9 illustrates that the predictive deconvolution slightly reduced the bubble artefact. However, the artefact is still clearly visible, although less coherent and with reduced amplitude. A post-stack zero-phase high-pass filter with 25 Hz cut and 55 Hz slope frequencies filtered noise remnants and increased the signal-to-noise ratio further.

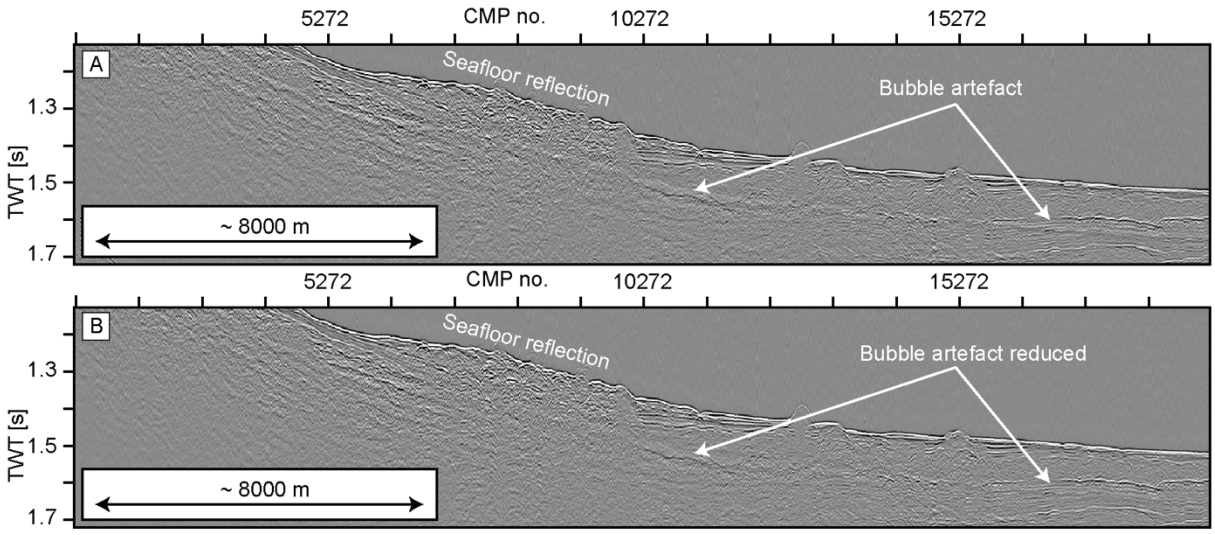

Figure 2.9*: A: Stacked seismic section from line 5016 before predictive deconvolution with a strong and coherent bubble artefact. B: Stacked seismic section from line 5016 after predictive deconvolution and with the bubble artefact reduced and less continuous.*

In seismic processing, migration describes the process of correcting dipping events in seismic data to their supposedly real positions and collapsing diffraction hyperbolae to their apices (Yilmaz, 2001). The stacked sections of the M154-1 2D MCS data were migrated with a Finite-Difference Migration algorithm that uses the Finite-Difference method to numerically approximate the scalar wave equation in order to backward propagate the seismic wavefield until points of scattering or reflections are reached in the time domain (Claerbout and Doherty, 1972; Sheriff and Geldart, 1995). The input velocity model for the migration was an interval V_p model based on OBS measurements during M154-1 (Berndt et al., 2019) that found velocities between 1600 and 1800 m/s for the upper ~100 m of sediment (Kunde, 2020). The model starts with a velocity of 1600 m/s at the seafloor and increases with a gradient to 1800 m/s at end of the traces (Figure 2.10C). With this migration velocity the diffraction hyperbola in the stacked sections (Figure 2.10A) sufficiently collapsed towards their apices (Figure 2.10B). An exponential gain with an exponent of 1.5 was applied on the data before they were exported into SEG-Y files. The processed dataset consists of 28 MCS profiles.

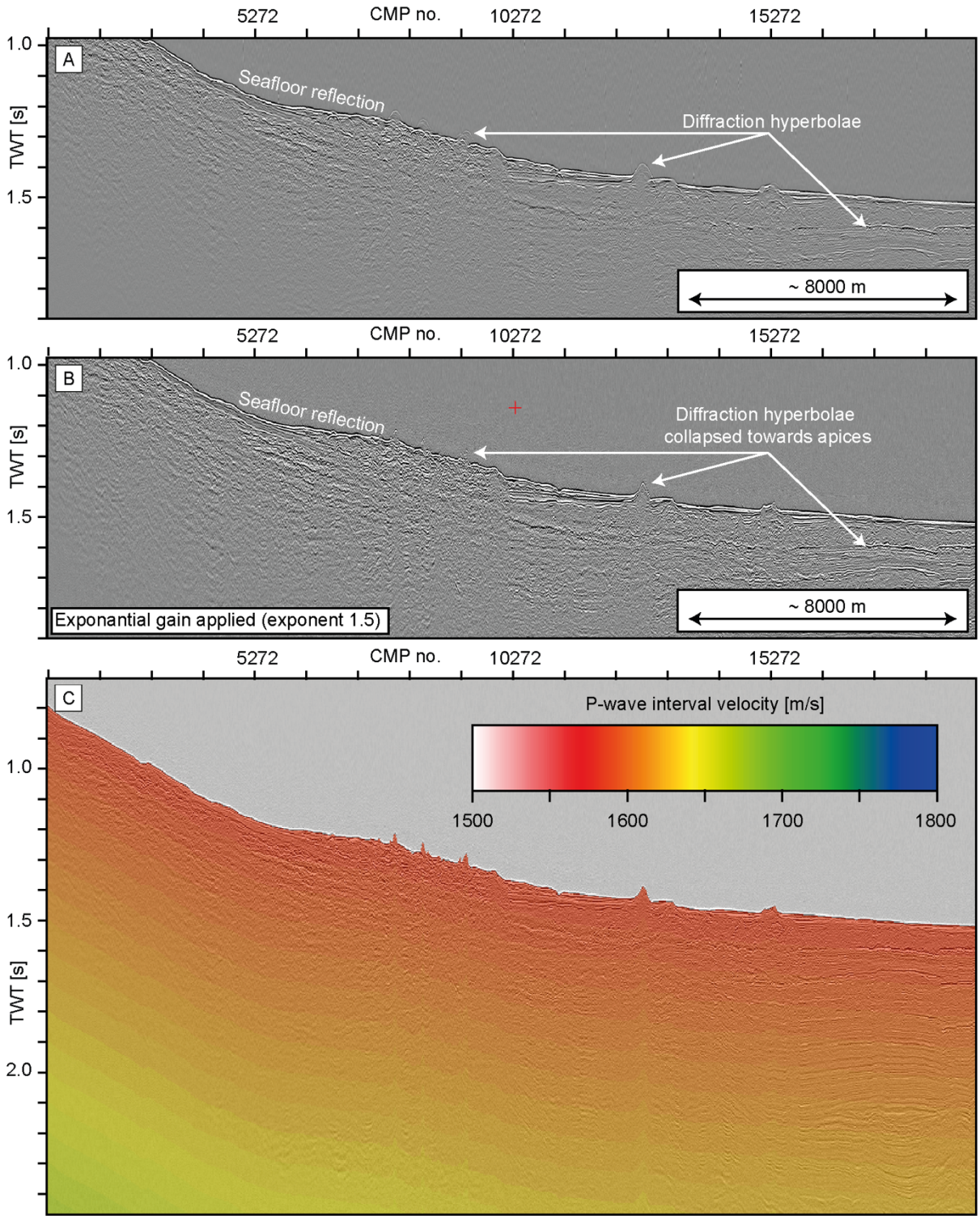

Figure 2.10: *A: Stacked section of Line 5016 with visible diffraction hyperbola. B: After the Finite-Difference Migration the diffraction hyperbolae are collapsed. C: Velocity model used for the migration based on OBS velocities from Kunde, 2020.*

Figure 2.11. shows the processing flow for the 3D MCS data that includes geometry repositioning, noise attenuation, static time correction, NMO correction, stacking, trace

interpolation, post-stack denoising, bubble artefact attenuation, multiple-attenuation, and a pseudo-3D finite-difference migration. Processing steps that also have been performed on the 2D MCS data, e.g., NMO correction, stacking, bubble attenuation etc., were performed analogously during the 3D MCS processing are not elaborated in detail in the following to avoid redundancies.

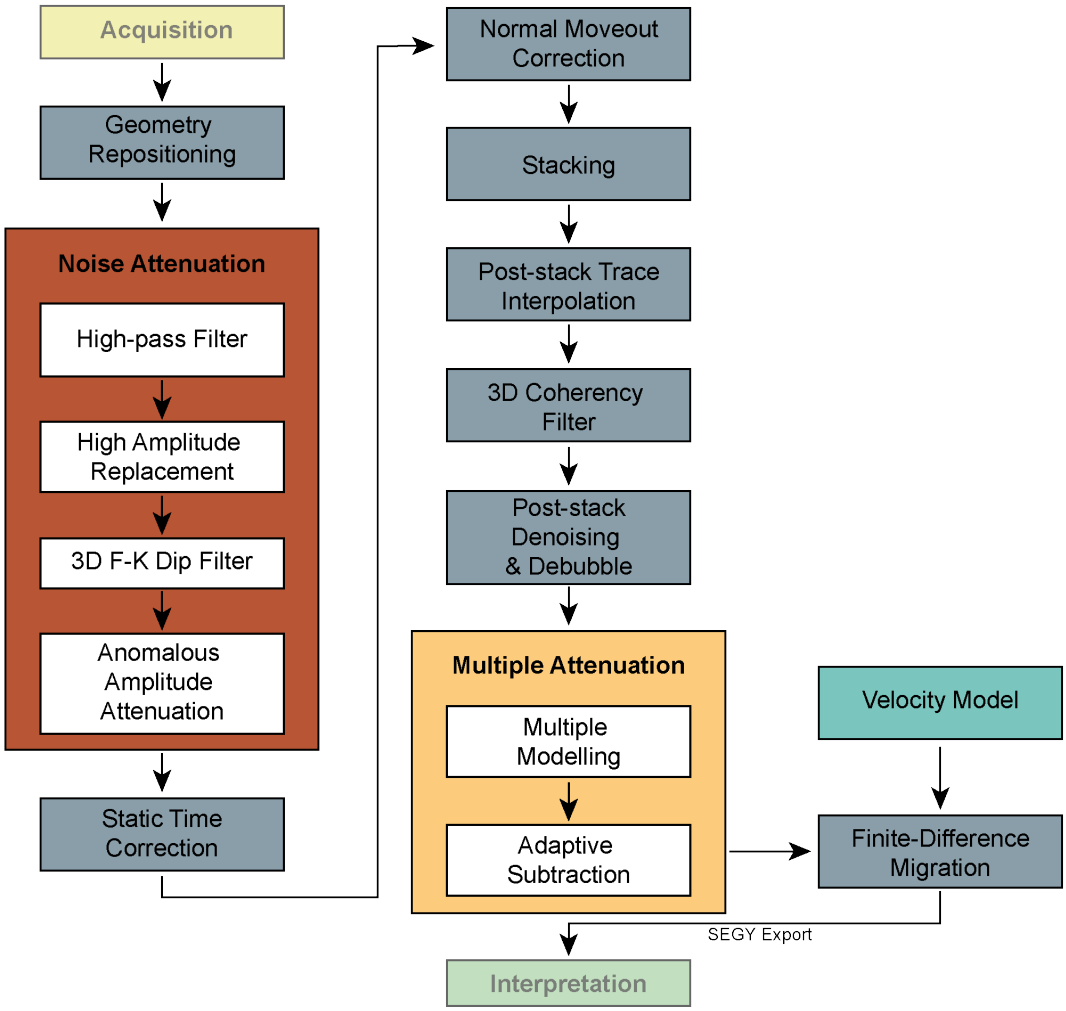

Figure 2.11: *The seismic processing flow used for the M154-1 3D MCS dataset.*

Initial nominal source and receiver geometries were calculated with a catenary-function between the known GPS positions of the paravanes (see Figure 2.3) following the approach of Petersen et al. (2010) and Crutchley et al. (2011). The geometry repositioning consisted of corrections of the source position and subsequent corrections of the receiver channels in each streamer segment based on first arrivals of the direct wave. The source position was corrected based on the direct wave first arrivals at the first channels of the first streamer segment (streamer

number 1, Figure 2.3) and the last streamer segment (streamer number 16, Figure 2.3). These channel positions were considered to be accurate, due to their close position to the paravane GPS antennas (see Figure 2.3). The receiver channels were then repositioned based on first arrivals in respect to the corrected gun position by automatically picking the direct wave first arrival at the first channel, recalculation of the channel position and linear projection of the following 7 channels of the streamer section behind this position (Figure 2.12). Traces were then binned with a grid cell size of 3.125 m.

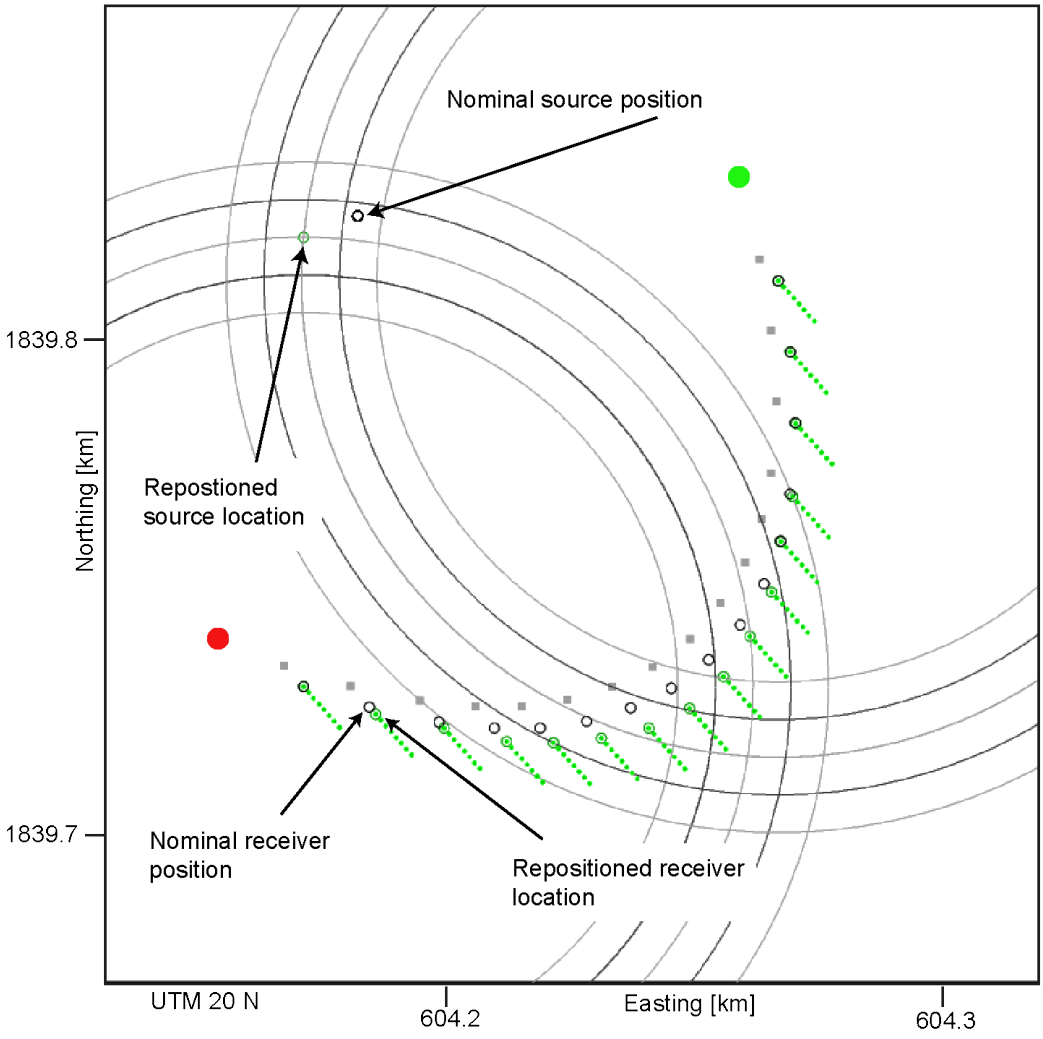

Figure 2.12: *3D Repositioning. Black dots mark nominal locations of source and receivers for one exemplary shot. Large red and large green dot are GPS antenna locations on the portside and starboard paravane, respectively. Grey rectangles mark the locations on the cross cable where streamers are connected via lead-in cables. The green circle marks the repositioned source. Small green dots mark the repositioned receiver channels.*

Figure 2.13A shows a shot gather from the 3D MCS survey where the primary data is overlain by different types of noise. Four different processing techniques improved the signal-to-noise ratio in a shot gather domain: (1) a zero-phase high-pass filter (Yilmaz, 2001) removed frequencies below 15 Hz and gradually attenuated frequencies below 60 Hz (Figure 2.13B). (2) A high-amplitude replacement filter removed horizontal high-spectral amplitude noise by scaling the traces of one streamer segment to the average spectral amplitude of the traces at adjacent streamer segments similar to AAA (see above). (3) A 3D-frequency-wavenumber-dip filter (Stewart and Schieck, 1989) suppressed coherent dipping high-amplitude noise (Figure 2.13B/C). (2) and (3) required a zero-offset extrapolation of the data with a parabolic Radon transformation (Hampson, 1986). (4) AAA suppressed high-amplitude noise remnants in the frequency domain (Figure 2.13C). Extrapolated traces were removed after noise attenuation.

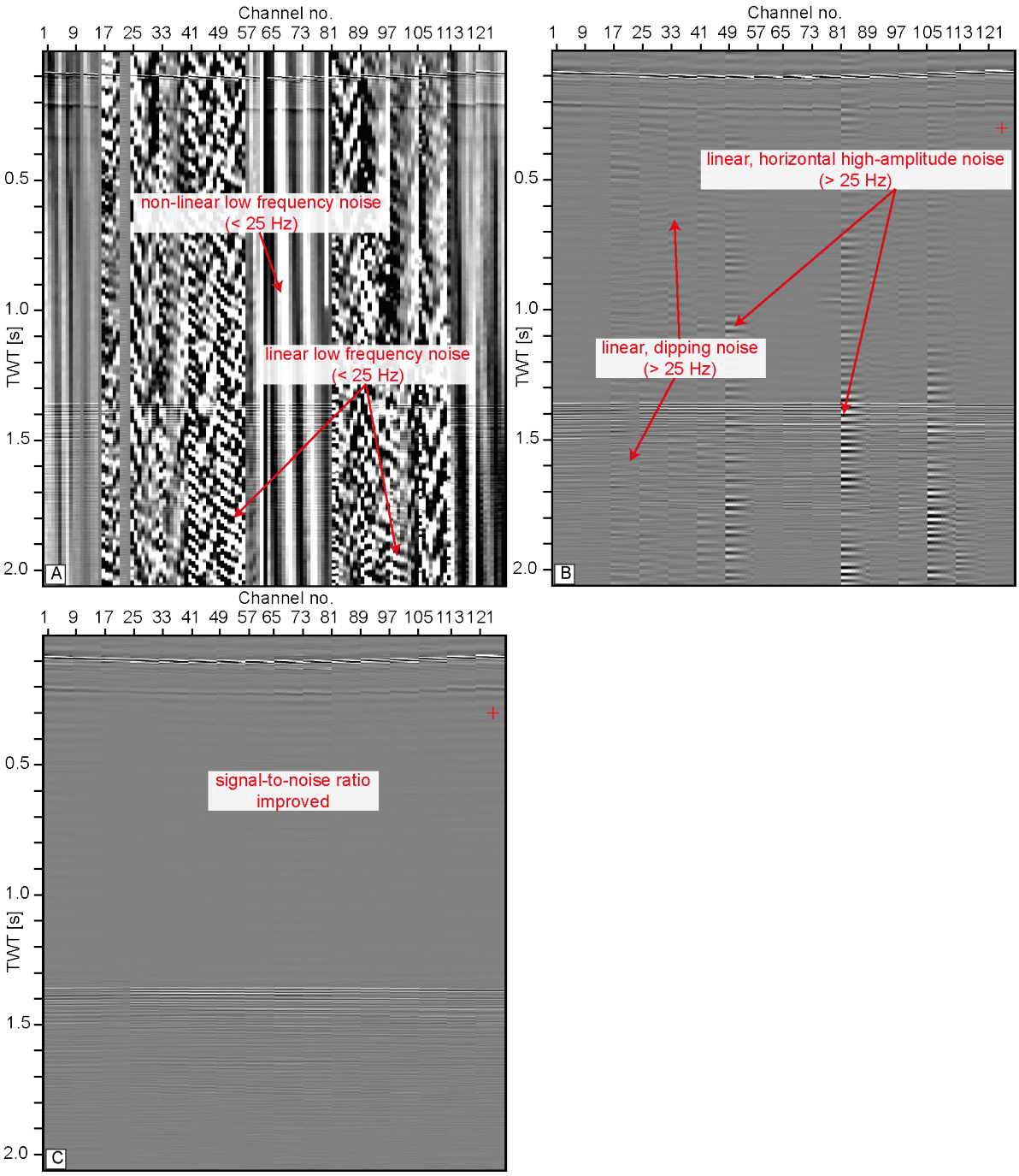

Figure 2.13: *Shot gather of 4403 of the 3D MCS data at different stages of noise attenuation. A: Raw data. B: High-pass filtered data. Noise below 25 Hz is filtered and frequencies to 60 Hz are gradually attenuated. Noise remnants include linear coherent horizontal high-amplitude noise and linearly dipping noise. C: Filtered shot gather after steps (1) to (4) with improved signal-to-noise ratio.*

Figure 2.14A shows a horizontal time slice from the 3D MCS volume after static time shift, NMO-correction, and stacking with gaps of various sizes between traces resulting from

technical problems during acquisition or fishery gear in the survey area. A post-stack trace interpolation iteratively filled these gaps with increasing interpolation gap distances (Figure 2.14B-E). The interpolation module summarized and time shifted adjacent traces until the maximum coherency was reached along associated dip directions. Each iteration included interpolation in inline direction first and crossline direction second. The increasing maximum interpolation distances of 15.625 (Figure 2.14B), 31.25 (Figure 2.14C), 62.5 (Figure 2.14D), 312.5 m (Figure 2.14E) successfully closed the gaps in the volume. A 3D-coherency filter then normalized the amplitudes of the interpolated traces to the amplitudes of the original traces in the frequency-wavenumber-domain (Figure 2.14F). Figure 2.15 shows an inline from the 3D MCS volume before and after the interpolation.

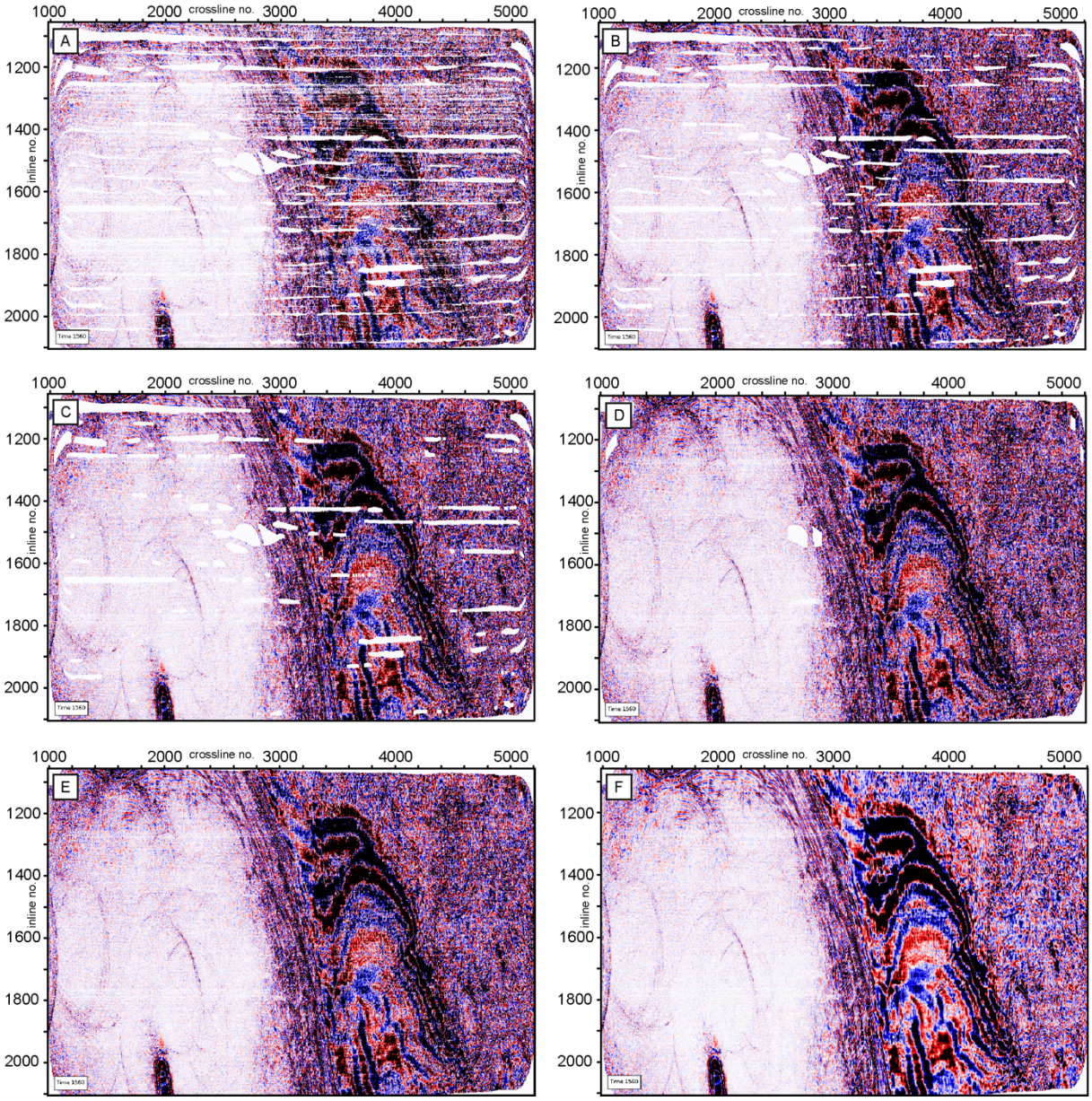

Figure 2.14: *Post-stack trace interpolation results shown in a horizontal time slice at 1.56s TWT. A: Before interpolation. Gaps vary between ~3 m and ~300 m. B: First interpolation result with a maximum interpolation distance of 15.626 m. C: Second interpolation result with a maximum interpolation distance of 31.25 m. D: Third interpolation result with a maximum interpolation distance of 62.5 m. E: Fourth interpolation result with a maximum interpolation distance of 312.5 m. F: Interpolated time slice after coherency filtering. Compared to A-E amplitudes are more balanced.*

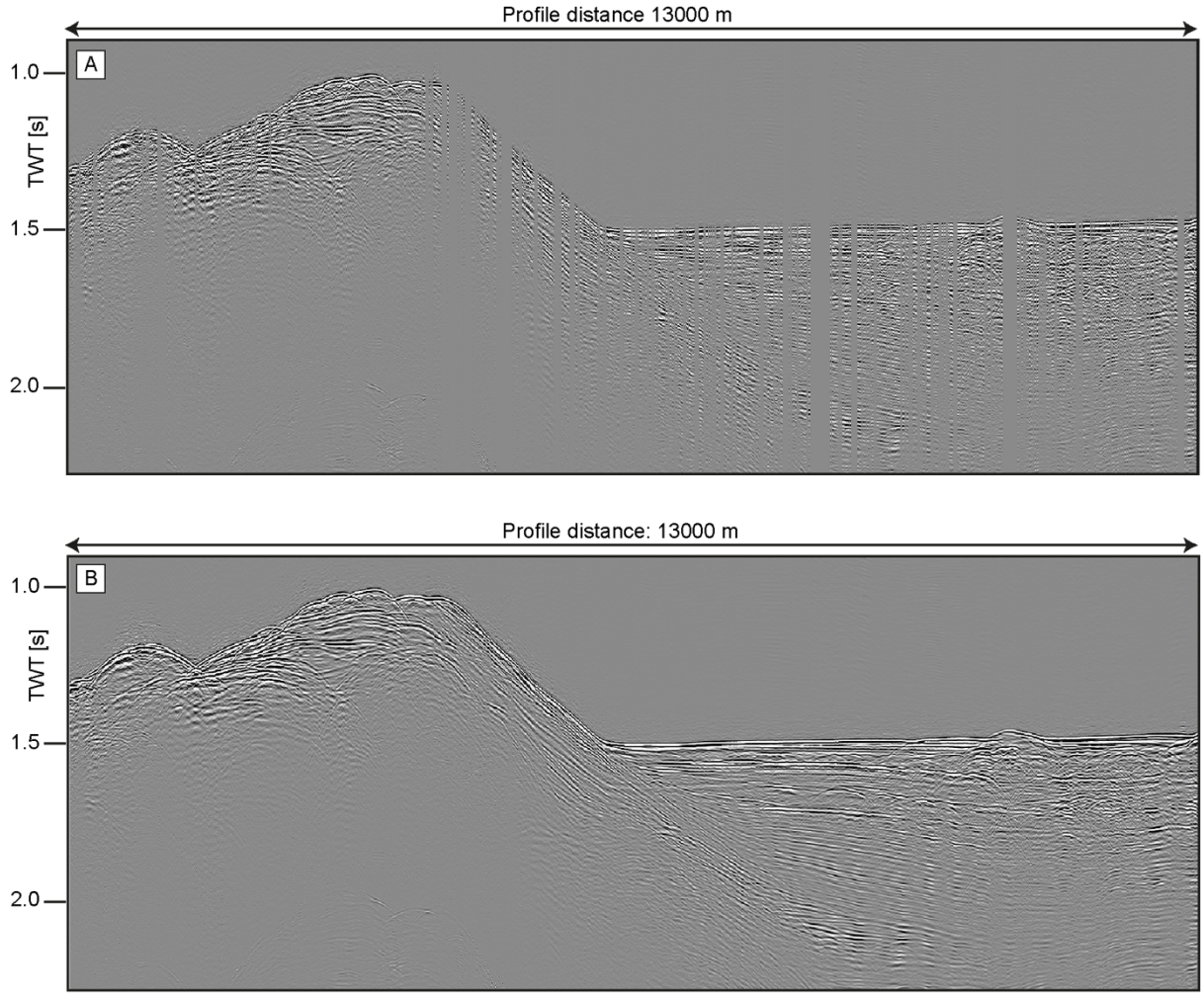

Figure 2.15: *Inline 1385 of the 3D MCS volume. A: Stacked inline before interpolation. Gaps are visible as empty CMPs along the profile. B: Stacked inline after interpolation. Gaps are filled and reflections appear generally coherent and balanced.*

A multiple attenuation approach similar to that applied on the 2D MCS data was used on 3D seismic data, but after stacking. A multiple model was created by migration of the data with a 3D-phase-shift migration algorithm (Gazdag, 1978) to reduce diffraction hyperbola and to correct steep slopes at the multiple to the slope angle of the seafloor. This migrated 3D volume was then time-shifted in a way, that the seafloor reflection was located at the TWT of the first seafloor multiple and input to the adaptive subtraction described above. This approach successfully attenuated the multiples within the 3D MCS volume (Figure 2.16A). After multiple attenuation the dataset was de-migrated with the same 3D-phase-shift algorithm. Figure 2.16A shows a migrated inline of the 3D MCS data. For that, a Finite-Difference migration algorithm (see description above) was applied in crossline direction first and subsequently in inline direction. The velocity model used for that was an interval velocity model based on OBS

experiment velocities from Kunde (2020). The final 3D cube consists of 1047 inlines and 4203 crosslines with a bin-spacing of 3.125 m and was exported as a SEG-Y file. The M154-1 2D and 3D MCS datasets will be accessible via PANGAEA after a moratorium (Kühn et al., 2023b, 2023a).

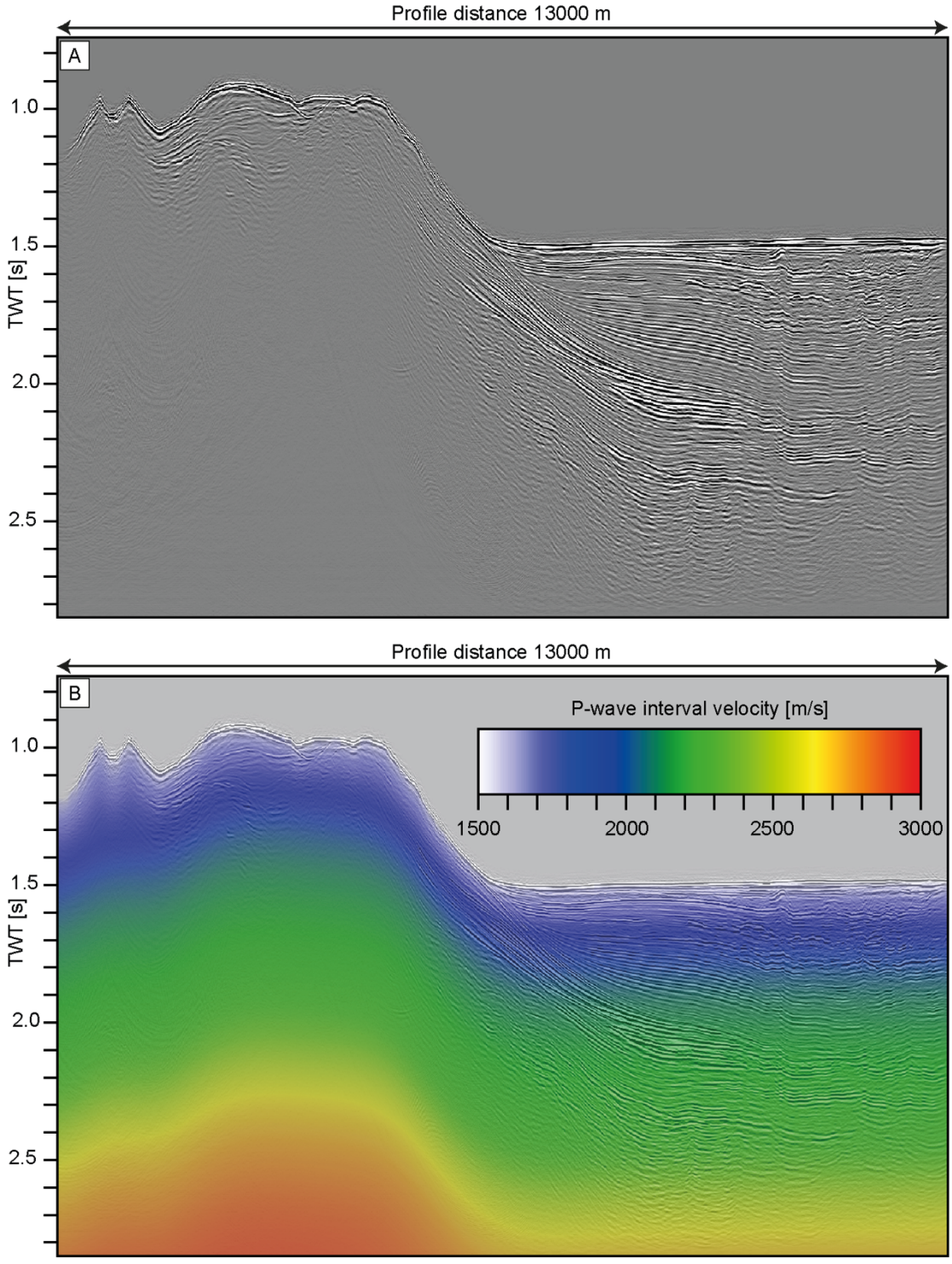

Figure 2.16: *A: Stacked and migrated inline number 1558 of the 3D MCS volume. Diffraction hyperbolae are generally collapsed. B: Interval velocity model used for the migration overlain on the seismic section. Velocities were derived from OBS experiments (Kunde, 2020).*

2.2 Bathymetry and sediment echosounder data

A shipboard Kongsberg EM122 multibeam echosounder with an operating frequency of 12 kHz collected bathymetric data on both cruises SO252 and M154-1/2 (Berndt et al., 2019, 2017; Huhn et al., 2019). Multibeam echosounders are a common tool for the acquisition of high-resolution bathymetry (Glenn, 1970; Hughes Clarke, 2018). The onboard processing of the data included tidal corrections and velocity corrections based on sound velocity profiles (Berndt et al., 2019), automatic filtering of erroneous soundings and manual removal of residual incorrect beams (Berndt et al., 2019, 2017; Huhn et al., 2019). Chapter 3 of this thesis analyses the gridded SO252 bathymetry data, which has a grid cell size of 25 m and is publicly available on the PANGAEA data publishing platform (Berndt et al., 2021b). The Chapters 4 to 6 of this thesis analyze the gridded M154-1/2 bathymetry data with a grid cell size of 10 m (Huhn et al., 2019). The bathymetry raw data from M154-1 is publicly accessible via PANGAEA (Berndt et al., 2021a). Figure 2.17 gives an overview of the bathymetry acquired offshore Montserrat.

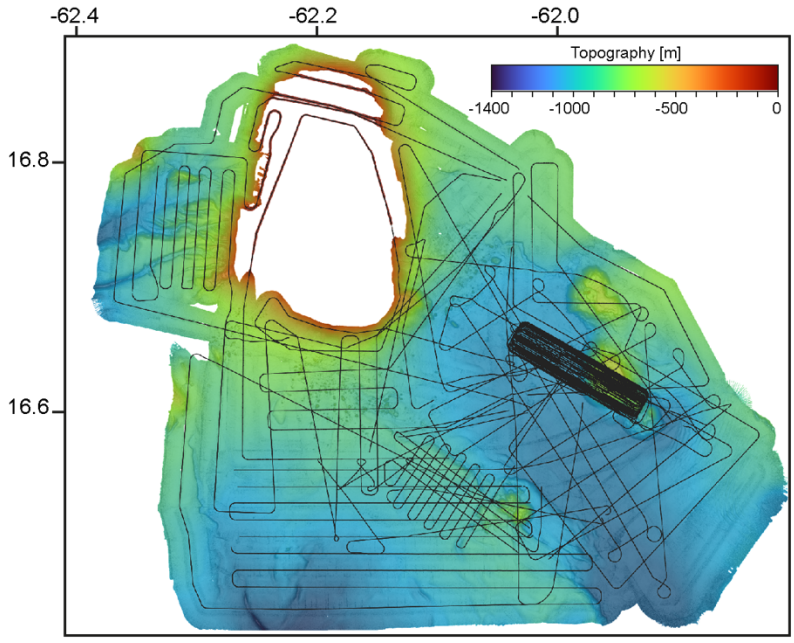

Figure 2.17: *Overview map showing the bathymetry acquired during M154-1 and M154-2. Black lines mark Parasound echosounder profiles.*

The shipboard Parasound P70 echosounder system onboard R/V METEOR acquired sediment echosounder data of the first > 100 m of sediments during M154-1/2 (Berndt et al., 2019; Huhn et al., 2019). The Chapters 4, 5, and 6 interpret this echosounder data. The Parasound P70 system generates primary frequencies between 18 and 25 kHz and secondary frequencies

between 0.5 and 6 kHz as a consequence of the parametric effect. The latter are used for the sub bottom imaging of sediments below the seafloor (Wentzell and Ziese, 1988). Berndt et al. (2019) and Huhn et al. (2019) provide the following information on data acquisition: A secondary frequency of 4 kHz was used for sub bottom profiling. Processing of the acquired data included bandpass frequency filtering (2 kHz and 4 kHz corner frequencies), calculation of the envelope and automatic gain control with a time window of 0.01 s. The data was exported and stored in the SEG-Y format. Figure 2.17 shows the profile locations.

2.3 Heat flow assessment

The rate at which heat energy is transferred trough Earth's surface - heat flow – can be assessed in the marine environment with different measurement techniques, e.g., thermistors deployed in a borehole during or after drilling operations (Heesemann et al., 2008; Riedel et al., 2018), outrigged temperature sensors on shallow coring devices (Pfender and Villinger, 2002), or Lister-type (or violin-type) probes (Hyndman et al., 1979; Lister, 1979; Riedel et al., 2021). Chapter 5 of this thesis analyses temperature measurements offshore Montserrat that were realised with two different tools: (1) A Hybrid Lister Outrigger (HyLO) probe (Hornbach et al., 2021) and (2) borehole temperature-depth measurements acquired with the seafloor drill rig MeBo70 (Freudenthal and Wefer, 2013) with a thermistor attached to the acoustic logging tool of the drill rig (Freudenthal et al., 2022). The HyLO probe (Figure 2.18A) can be used in two configurations: as a stand-alone probe for deployments in shallow water and as an outrigger attached to a gravity coring device for temperature measurements in greater water depths. For the measurements presented in Chapter 5, we attached the HyLO probe to a 3 m core length gravity corer at 5 coring sites (Huhn et al., 2019). At 5 other locations during the M154-2 operations temperature was measured with a temperature sensor implemented into the acoustic logging tool of MeBo70 during a logging-while-tripping experiment at the end of the drilling operation at each drill site (Huhn et al., 2019, Hornbach et al., (in revision)). Figure 2.18B shows a sketch of the logging tool. Chapter 5 of this thesis provides detailed experiment parameters, processing steps, and modelling concepts for both probe types.

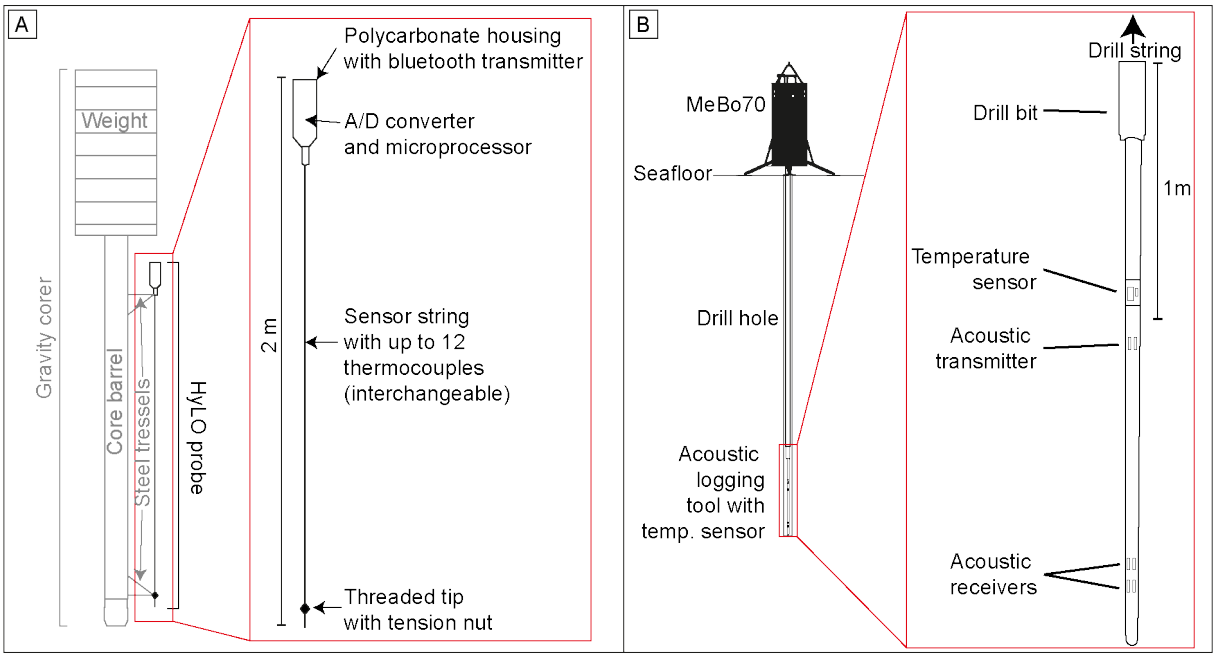

Figure 2.18: *A: The Hybrid-Lister-Outrigger (HyLO) probe adapted from Hornbach et al. (2021). B: The MeBo acoustic logging tool with temperature sensor adapted from Freudenthal et al. (2022). Figure not to scale.*

2.4 Numerical pore pressure modelling

Pore pressure – the pressure of fluids in the pore space of a sediment or rock – can be measured or estimated with various techniques or approaches. In situ pore pressure can be measured during drilling operations using downhole penetrometers (e.g., Flemings et al., 2008; Stegmann et al., 2007) or by downhole monitoring (e.g., Davis et al., 1991; Screaton et al., 1997). In shallow sediments, pore pressure can be measured directly with piezometer probes (e.g., Çağatay et al., 2015; Sultan et al., 2007). Where in situ measurements are not available, pore pressure can be estimated by combining logging-while-drilling logs with consolidation tests (e.g., Moran et al., 1993; Schneider et al., 2009) or using velocity-porosity-pressure relationships integrated with regional seismic velocity models (e.g., Bahmaei and Hosseini, 2020; Bowers, 1995; Kitajima and Saffer, 2012). Chapter 6 of this thesis presents a pore pressure modelling study that aims to assess excess pore pressure due to rapid loading by the deposition of Deposit 2b on top of Deposit 2a offshore Montserrat and its effect on the stability of the sediments on and around the volcanic slope (including buried and surficial mass transport deposits (MTD's), as well as background sediments).

Subsurface pore pressure changes are calculated in both space and time using the non-steady two-dimensional pore pressure diffusion equation for porous media with spatially variable hydraulic conductivity:

$$(1)\ \frac{dP}{dt} = \frac{1}{S}\nabla * (k\ \nabla P)$$

where P is the fluid pressure (in space and time) above hydrostatic pressure (Pa), k is the hydraulic conductivity (m/s) variable in space, and S the specific storage coefficient (1/m), is treated as constant. $\frac{dP}{dt}$ is the change in pressure at a particular location with respect to time, ∇ is the gradient operator, and ∇P is the change in pressure with respect to space. Here, hydraulic conductivity - the ease at which a fluid can moved through pore space - is defined in space for different sedimentary units by direct measurement of drilling samples collected from offshore of the Lesser Antilles (e.g., Hornbach et al., 2015; Koehn et al., 2022). The highest permeability sediment (sand-rich volcaniclastic turbidites) is assigned a permeability of 1.11e-11 m^2 (averaged from Koehn et al., 2022), and the lower-permeability hemipelagic sediments are assigned end member values of 9.92e-17 m^2 minimum (hemipelagic clay, Hornbach et al., 2015), a mid-range 9.14e-15 m^2 (minimum hemipelagic sand from Koehn et al., 2022), and 3.81e-13 m^2 (hemipelagic silt/silty sand, averaged from Koehn et al., 2022) maximum. For the pressure calculations these permeabilities were converted to hydraulic conductivity (Table 1). The specific storage coefficient, S - the amount of water per unit volume an aquifer releases from storage for a given drop in pressure (due to aquifer compressibility) - is assigned end member values of 0.001 m^{-1} minimum for a turbidite (Urgeles et al., 2010) and 0.027 m^{-1} maximum for hemipelagic sediments (Mencaroni et al., 2020) broadly consistent with measurements for unconsolidated sediments (e.g., Domenico and Mifflin, 1965). It is assumed that the landslide associated with Deposit 2b is deposited initially at time t=0, and that all sediments not buried by the landslide exhibit hydrostatic pressure conditions (i.e., no overpressure) at this time. For sediments located directly below the landslide, we assume at t=0 an instantaneous increase in pore fluid pressure equal to the weight per unit area of the submerged landslide deposit:

$$(2)\ P_i = (\rho_b - \rho_w)gh$$

where P_i is the initial fluid pressure (Pa) at t=0 above hydrostatic for all sediments located directly below the landslide that feel the initial weight of the deposited landslide, ρ_b is the bulk sediment density (assumed to be, on average, 1750 kg/m^3 based on IODP measurements

(Expedition 340 Scientists, 2013), ρ_w is seawater density (1025 kg/m^3), g is gravitational acceleration, and h is the vertical thickness of the landslide deposit at a particular location (m). The change in pressure is modelled in space and time using an explicit (forward in time, center in space), 4th order 2D finite difference method consistent with previously published pressure and groundwater flow models (e.g., Fetter, 2018; McDonald and Harbaugh, 1988). Figure 2.19 shows seismic line 5016 offshore Montserrat with label lithological units (interpretation elaborated in Chapter 4 of this thesis), which is used to set up the model dimensions and parameters, overlain with the two endmember hydraulic conductivity models. We assume isotropy of the hydraulic conductivity within the interpreted lithological units. Model dimensions are 8500 m x 425 m with cell dimensions of 30 m^2 (10 m horizontal and 3 m vertical resolution). We assume open (Neuman) side and bottom boundary conditions that allow for pressure to flow out of the model domain, and a constant (Dirichlet) boundary condition at the seabed of zero (hydrostatic) fluid pressure. Based on the structural seismic interpretations in Chapter 4 of this thesis we then assigned different hydraulic conductivities to the interpreted MTD's and background sediments (Figure 2.19).

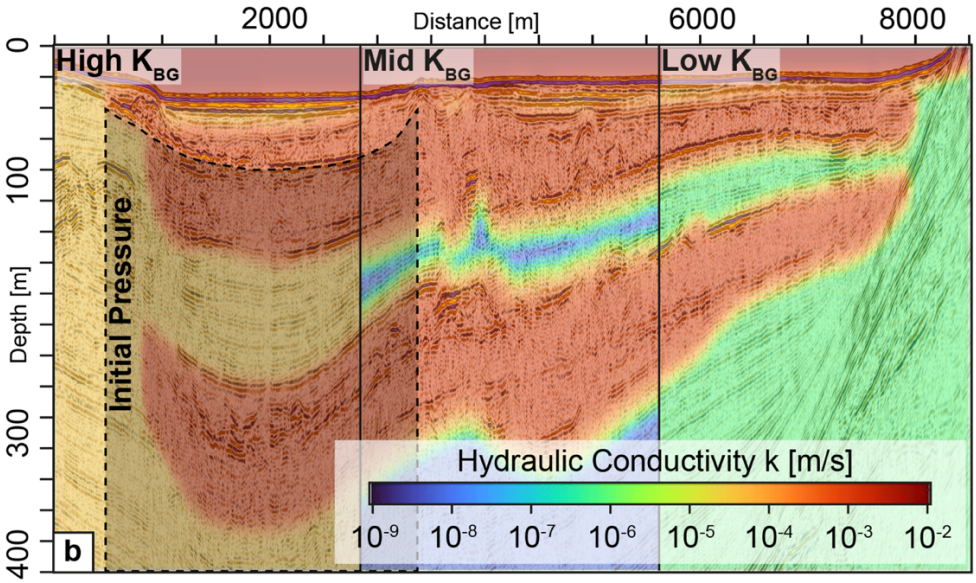

Figure 2.19: *Hydraulic conductivity models and initial pressure setup. The dark-shaded polygon marks the location where the initial pressure builds at t=0. The left side shows the hydraulic conductivity model with maximum endmember of background sediment hydraulic conductivity (hemipelagic silt/silty sand, 'Low K_{BG}'). The middle panel shows the medium hydraulic conductivity model (hemipelagic mud, 'Mid K_{BG}'). The right side shows the hydraulic conductivity model with the minimum endmember of background sediment hydraulic conductivity (hemipelagic clay, 'Low K_{BG}').*

References

Bahmaei, Z., Hosseini, E., 2020. Pore pressure prediction using seismic velocity modeling: case study, Sefid-Zakhor gas field in Southern Iran. J Pet Explor Prod Technol 10, 1051–1062. https://doi.org/10.1007/s13202-019-00818-y

Berndt, C., Böttner, C., Elger, J., Kontradowitz, S., Kühn, M., Müller, S., Schramm, B., Stelzner, M., 2019. Sector collapse kinematics and tsunami implications - SEKT, Cruise No. M154/1, April 3 - April 25, 2019, Mindelo (Cape Verde) - Point-á-Pitre (Guadeloupe). METEOR-Berichte, M154/1. Gutachterpanel Forschungsschiffe, Bonn, 47 pp.

Berndt, C., Böttner, C., Wölfl, A.-C., 2021a. Multibeam bathymetry raw data (Kongsberg EM 122 entire dataset) of RV METEOR during cruise M154/1. https://doi.org/10.1594/PANGAEA.935598

Berndt, C., Klaucke, I., Kühn, M., 2021b. Multibeam bathymetry gridded data from SONNE cruise SO252. https://doi.org/https://doi.org/10.1594/PANGAEA.929026

Berndt, C., Kühn, M., Karstens, J., 2021c. 2D multi-channel seismic data from SONNE cruise SO252 offshore Ritter Island, 2016, Bismarck Sea, Papua New Guinea. https://doi.org/10.1594/PANGAEA.929022

Berndt, C., Muff, S., Klaucke, I., Watt, S., Böttner, C., Schramm, B., Völsch, A., Bennecke, S., Elger, J., Chi, W.-C., 2017. RV SONNE 252 Cruise Report/Fahrtbericht, Yokohama: 05.11. 2016-Nouméa: 18.12. 2016. SO252: RITTER ISLAND Tsunami potential of volcanic flank collapses.

Bowers, G.L., 1995. Pore pressure estimation from velocity data: Accounting for overpressure mechanisms besides undercompaction. SPE Drilling & Completion 10, 89–95.

Çağatay, M.N., Géli, L., Gasperini, L., Henry, P., Gürbüz, C., Görür, N., 2015. Seafloor observations and observatory activities in the sea of marmara, in: Seafloor Observatories: A New Vision of the Earth from the Abyss. Springer Berlin Heidelberg, pp. 59–79. https://doi.org/10.1007/978-3-642-11374-1_4

Canales, L.L., 1984. Random noise reduction, in: SEG Technical Program Expanded Abstracts 1984. Society of Exploration Geophysicists, pp. 525–527.

Claerbout, J.F., Doherty, S.M., 1972. Downward continuation of moveout-corrected seismograms. Geophysics 37, 741–768.

Crutchley, G.J., Berndt, C., Klaeschen, D., Masson, D.G., 2011. Insights into active deformation in the Gulf of Cadiz from new 3-D seismic and high-resolution bathymetry data. Geochemistry, Geophysics, Geosystems 12. https://doi.org/10.1029/2011GC003576

Davis, E.E., Becker, K., Pettigrew, T., Carson, B., MacDonald, R., 1991. 3. CORK: A HYDROLOGIC SEAL AND DOWNHOLE OBSERVATORY FOR DEEP-OCEAN BOREHOLES. Proceedings of the Ocean Drilling Program: Initial report. Part A 139, 43.

Domenico, P.A., Mifflin, dan M.D., 1965. Water from low-permeability sediments and land subsidence. Water Resour Res 1, 563–576.

Expedition 340 Scientists, 2013. Expedition 340 summary, in: Le Friant, A., Ishizuka, O., Stroncik, N.A., and the Expedition 340 Scientists, Proc. IODP, 340: Tokyo (Integrated Ocean Drilling Program Management International, Inc.). https://doi.org/10.2204/iodp.proc.340.101.2013

Fetter, C.W., 2018. Applied hydrogeology. Waveland Press.

Flemings, P.B., Long, H., Dugan, B., Germaine, J., John, C., Behrmann, J.H., Sawyer, D., 2008. Pore pressure penetrometers document high overpressure near the seafloor where multiple submarine landslides have occurred on the continental slope, offshore Louisiana, Gulf of Mexico. Earth Planet Sci Lett 269, 309–325. https://doi.org/10.1016/j.epsl.2007.12.005

Freudenthal, T., Villinger, H., Riedel, M., Pape, T., 2022. Heat flux estimation from borehole temperatures acquired during logging while tripping: a case study with the sea floor drill rig MARUM-MeBo. Marine Geophysical Research 43. https://doi.org/10.1007/s11001-022-09500-1

Freudenthal, T., Wefer, G., 2013. Drilling cores on the sea floor with the remote-controlled sea floor drilling rig MeBo. Geoscientific Instrumentation, Methods and Data Systems 2, 329–337. https://doi.org/10.5194/gi-2-329-2013

Gazdag, J., 1978. Wave equation migration with the phase-shift method. Geophysics 43, 1342–1351.

Glenn, M.F., 1970. Introducing an operational multi-beam array sonar. The International Hydrographic Review.

Guitton, A., Verschuur, D.J., 2004. Adaptive subtraction of multiples using the L1-norm. Geophys Prospect 52, 27–38. https://doi.org/10.1046/j.1365-2478.2004.00401.x

Hampson, D., 1986. Inverse velocity stacking for multiple elimination, in: SEG Technical Program Expanded Abstracts 1986. Society of Exploration Geophysicists, pp. 422–424.

Heesemann, M., Villinger, H., Fisher, A.T., Tréhu, A.M., White, S., 2008. Data report: testing and deployment of the new APCT-3 tool to determine in situ temperatures while piston coring. Advances in the acquisition and processing of subseafloor temperature and pressure data and their interpretation in the context of convergent margin processes 21.

Hornbach, M.J., Sylvester, J., Hayward, C., Kühn, M., Huhn-Frehers, K., Freudenthal, T., Watt, S.F.L., Berndt, C., Kutterolf, S., Kuhlmann, J., Sievers, C., Rapp, S., Pallapies, K., Gatter, R., Hoenekopp, L., 2021. A Hybrid Lister-Outrigger Probe for Rapid Marine Geothermal Gradient Measurement. Earth and Space Science 8. https://doi.org/10.1029/2020EA001327

Hughes Clarke, J.E., 2018. Multibeam Echosounders, in: Springer Geology. Springer, pp. 25–41. https://doi.org/10.1007/978-3-319-57852-1_3

Huhn, K., Freudenthal, T., Dehning, K., Gatter, R., Hilgenfeldt, C., Hönekopp, L., Hornbach, M., Kühn, M., Kuhlmann, J., Kutterolf, S., Meyer-Schack, B., Pallapies, K., Rapp, S.K., Sievers, C., Watt, S.,

Stelzner, M., 2019. Sector collapse kinematics and tsunami implications - SEKT, Cruise No. M154-2, April 29 - Mai 23, 2019, Pointe-à-Pitre (Guadeloupe) - Pointe-à-Pitre (Guadeloupe).

Hyndman, R.D., Davis, E.E., Wright, J.A., 1979. The measurement of marine geothermal heat flow by a multipenetration probe with digital acoustic telemetry and insitu thermal conductivity. Mar Geophys Res (Dordr) 4, 181–205.

Kitajima, H., Saffer, D.M., 2012. Elevated pore pressure and anomalously low stress in regions of low frequency earthquakes along the Nankai Trough subduction megathrust. Geophys Res Lett 39. https://doi.org/10.1029/2012GL053793

Kühn, M., Berndt, C., Krastel, S., 2023a. 2D multichannel seismic reflection processed data (GI Gun entire dataset) of RV METEOR during cruise M154/1. https://doi.org/10.1594/PANGAEA.957490

Kühn, M., Berndt, C., Krastel, S., 2023b. 3D multichannel seismic reflection processed data (P-Cable system with GI Gun) of RV METEOR during cruise M154/1, Montserrat, Lesser Antilles. https://doi.org/10.1594/PANGAEA.963076

Kühn, M., Karstens, J., Berndt, C., Watt, S.F.L., 2021. Seismic reconstruction of seafloor sediment deformation during volcanic debris avalanche emplacement offshore Sakar, Papua New Guinea. Mar Geol 439. https://doi.org/10.1016/j.margeo.2021.106563

Kunde, D., 2020. Seismic velocity of sector collapse deposits off Montserrat (Master's thesis). Christian-Albrechts-Universität zu Kiel, Kiel.

Lister, C.R.B., 1979. The pulse-probe method of conductivity measurement, Geophys. J. R. astr. Soc.

McDonald, M.G., Harbaugh, A.W., 1988. A modular three-dimensional finite-difference ground-water flow model. US Geological Survey.

Mencaroni, D., Llopart, J., Urgeles, R., Lafuerza, S., Gràcia, E., Friant, A. Le, Urlaub, M., 2020. From gravity cores to overpressure history: The importance of measured sediment physical properties in hydrogeological models, in: Geological Society Special Publication. Geological Society of London, pp. 289–300. https://doi.org/10.1144/SP500-2019-176

Moore, I., Ferber, R., Vauthrin, B., 2008. Quality control and bandwidth optimization of compact Fourier interpolation operators, in: SEG International Exposition and Annual Meeting. SEG, p. SEG-2008.

Moran, K., Brückmann, W., Feeser, V., Campanella, R.G., 1993. Over-pressure stress conditions at Nankai Trough, Site 808, in: Proceedings of the Ocean Drilling Program: Scientific Results. pp. 283–291.

Peacock, K.L., Treitel, S., 1969. Predictive deconvolution: Theory and practice. Geophysics 34, 155–169.

Petersen, C.J., Bünz, S., Hustoft, S., Mienert, J., Klaeschen, D., 2010. High-resolution P-Cable 3D seismic imaging of gas chimney structures in gas hydrated sediments of an Arctic sediment drift. Mar Pet Geol 27, 1981–1994. https://doi.org/10.1016/j.marpetgeo.2010.06.006

Pfender, M., Villinger, H., 2002. Miniaturized data loggers for deep sea sediment temperature gradient measurements. Mar Geol 186, 557–570.

Riedel, M., Bialas, J., Villinger, H., Pape, T., Haeckel, M., Bohrmann, G., 2021. Heat flow measurements at the Danube deep-sea fan, western black sea. Geosciences (Switzerland) 11. https://doi.org/10.3390/geosciences11060240

Riedel, M., Wallmann, K., Berndt, C., Pape, T., Freudenthal, T., Bergenthal, M., Bünz, S., Bohrmann, G., 2018. In situ temperature measurements at the svalbard continental margin: Implications for gas hydrate dynamics. Geochemistry, Geophysics, Geosystems 19, 1165–1177. https://doi.org/10.1002/2017GC007288

Schneider, J., Flemings, P.B., Dugan, B., Long, H., Germaine, J.T., 2009. Overpressure and consolidation near the seafloor of Brazos-Trinity Basin IV, northwest deepwater Gulf of Mexico. J Geophys Res Solid Earth 114. https://doi.org/10.1029/2008JB005922

Screaton, E.J., Fisher, A.T., Carson, B., Becker, K., 1997. Barbados Ridge hydrogeologic tests: Implications for fluid migration along an active decollement. Geology 25, 239–242.

Sheriff, R.E., 1982. History, theory, and data acquisition. Exploration seismology Volume 1 154.

Sheriff, R.E., Geldart, L.P., 1995. Exploration seismology. Cambridge university press.

Stegmann, S., Strasser, M., Anselmetti, F., Kopf, A., 2007. Geotechnical in situ characterization of subaquatic slopes: The role of pore pressure transients versus frictional strength in landslide initiation. Geophys Res Lett 34. https://doi.org/10.1029/2006GL029122

Stewart, R.R., Schieck, D.G., 1989. 3-D fk filtering. Internat. Mtg. Soc. of Expl. Geophys 1123.

Stockwell Jr, J.W., 1999. The CWP/SU: seismic Un∗ x package. Comput Geosci 25, 415–419.

Sultan, N., Voisset, M., Marsset, B., Marsset, T., Cauquil, E., Colliat, J.L., 2007. Potential role of compressional structures in generating submarine slope failures in the Niger Delta. Mar Geol 237, 169–190. https://doi.org/10.1016/j.margeo.2006.11.002

Tian, X., Lu, W., Li, Y., 2022. Improved Anomalous Amplitude Attenuation Method Based on Deep Neural Networks. IEEE Transactions on Geoscience and Remote Sensing 60. https://doi.org/10.1109/TGRS.2021.3052898

Urgeles, R., Locat, J., Sawyer, D.E., Flemings, P.B., Dugan, B., Binh, N.T.T., 2010. History of pore pressure build up and slope instability in mud-dominated sediments of Ursa Basin, Gulf of Mexico continental slope. Submarine mass movements and their consequences 179–190.

Weglein, A.B., Hsu, S.-Y., Terenghi, P., Li, X., Stolt, R.H., 2011. Multiple attenuation: Recent advances and the road ahead (2011). The Leading Edge 30, 864–875.

Wentzell, H.F., Ziese, R., 1988. New echosounding methods for shallow water and deep sea surveying, in: SUT Oceanology: Proceedings of an International Conference. SUT, p. SUT-AUTOE.

Wessel, P., Smith, W.H.F., Scharroo, R., Luis, J., Wobbe, F., 2013. Generic mapping tools: Improved

version released. Eos (Washington DC) 94, 409–410. https://doi.org/10.1002/2013EO450001

Xia, Y., Geersen, J., Klaeschen, D., Ma, B., Lange, D., Riedel, M., Schnabel, M., Kopp, H., 2021. Marine forearc structure of eastern Java and its role in the 1994 Java tsunami earthquake. Solid Earth 12, 2467–2477. https://doi.org/10.5194/se-12-2467-2021

Yen, J.L., 1956. On nonuniform sampling of band-limited signals. IRE Trans. Circuit Theory 3, 4.

Yilmaz, Ö., 2001. Seismic data analysis: Processing, inversion, and interpretation of seismic data. Society of exploration geophysicists.

3. Seismic reconstruction of seafloor sediment deformation during volcanic debris avalanche emplacement offshore Sakar, Papua New Guinea

Michel Kühn[1,2], Jens Karstens[1], Christian Berndt[1], and Sebastian F. L. Watt[3]

[1]GEOMAR Helmholtz Centre for Ocean Research Kiel, Wischhofstraße 1-3, 24148 Kiel, Germany
[2]Institute of Geosciences, Christian-Albrechts-Universität zu Kiel, Otto-Hahn-Platz 1, 24118 Kiel, Germany
[3]School of Geography, Earth and Environmental Sciences, University of Birmingham, Edgebaston, Birmingham, B15 2TT, United Kingdom

Abstract

Volcanic island sector-collapses have produced some of the most voluminous mass movements on Earth and have the potential to trigger devastating tsunamis. In the marine environment, landslide deposits offshore the flanks of volcanic islands often consist of a mixture of volcanic material and incorporated seafloor sediments. The interaction of the initial volcanic failure and the substrate can be highly complex and have an impact on both the total landslide deposit volume and its emplacement velocity, which are important parameters during tsunami generation and need to be correctly assessed in numerical landslide-tsunami simulations. Here, we present a 2D seismic analysis of two previously unknown, overlapping volcanic landslide deposits north-west of the island of Sakar (Papua New Guinea) in the Bismarck Sea. The deposits are separated by a package of well-stratified sediment. Despite both originating from the same source, with the same broad movement direction, and having similar deposit volumes (~15.5-26 km^3), the interaction of these landslides with the seafloor is markedly different. High-resolution seismic reflection data show that the lower, older deposit comprises a proximal, chaotic, volcanic debris avalanche component and a distal, frontally confined component of deformed pre-existing well-bedded seafloor-sediment. We infer that deformation of the seafloor-sediment unit was caused by interaction of the initial volcanic debris avalanche with the substrate. The deformed sediment unit shows various compressional structures, including thrusting and folding, over a downslope distance of more than 20 km, generating >27 % of shortening over a 5 km distance at the deposit's toe. The volume of the deformed sediments is almost the same as the driving debris avalanche deposit. In contrast, the upper, younger landslide deposit does not show evidence for substrate incorporation or deformation. Instead, the landslide is a structurally simpler deposit, formed by a debris avalanche that spread freely

along the contemporaneous seafloor (i.e., the top boundary of the intervening sediment unit that now separates this younger landslide from the older deposit). Our observations show that the physical characteristics of the substrate on which a landslide is emplaced control the amount of seafloor incorporation, the potential for secondary seafloor failure, and the total landslide runout far more than the nature of the original slide material or other characteristics of the source region. Our results indicate the importance of accounting for substrate interaction when evaluating submarine landslide deposits, which is often only evident from internal imaging rather than surface morphological features. If substrate incorporation or deformation is extensive, then treating landslide deposits as a single entity substantially overestimates the volume of the initial failure, which is much more important for tsunami generation than secondary sediment failure.

Keywords: flank collapse, Bismarck Sea, landslide, volcano, tsunami, sediment failure

3.1 Introduction

In December 2018, a lateral collapse of the Indonesian volcano Anak Krakatau triggered a devastating tsunami, killing more than 400 people around the Sunda Strait. The initial collapse volume calculated at 0.2-0.3 km³, is relatively small in the context of volcano sector collapse (Siebert, 1984; Siebert and Roverato, 2021), but was still capable of generating a highly destructive tsunami (Gouhier and Paris, 2019; Grilli et al., 2019; Walter et al., 2019). In historic times, volcanic sector collapses have produced several devastating tsunamis, causing thousands of casualties around island-arc volcanoes (Auker et al., 2013; Day et al., 2015; Karstens et al., 2019; Watt et al., 2021). The global frequency of historically documented tsunami-generating events is approximately 50-100 years (Day et al., 2015), including collapses at Oshima-Oshima, Japan, in 1741, Mt. Unzen, Japan, in 1792, Ritter Island, Papua New Guinea, in 1888, and Anak Krakatau in 2018 (Walter et al., 2019). This shows that volcanic flank failure and resultant tsunami genesis poses a serious natural hazard for coastal regions in volcanic settings worldwide.

The Bismarck Archipelago hosts several island-arc volcanoes, of which more than eleven have recognized offshore debris avalanche deposits (Silver et al., 2009), the product of past lateral collapses. The most recent and best studied of these is the 1888 Ritter Island collapse (Johnson et al., 1987; Silver et al., 2009; Ward and Day, 2003; Watt et al., 2019), which is also the largest volcanic sector collapse globally that has been recorded in historic times (Day et al., 2015). Recent studies show that the volume of the submarine landslide-derived deposit west of Ritter

is 13 km^3, but the initial tsunamigenic flank collapse that produced these deposits was only ~2.4 km^3 (Karstens et al., 2019; Watt et al., 2019). This substantial difference in volume between the offshore deposits and the primary failure illustrates the potential complexity of landslide processes in volcanic-island settings, where the initial mass movement can lead to extensive substrate incorporation and secondary failure. Such complexities are not restricted to volcanic islands, but have also been recognized in submarine landslides in non-volcanic settings (e.g., Lenz et al., 2019; Morita et al., 2011; Ogata et al., 2019; Sobiesiak et al., 2018), and constitute an important general process in the emplacement of subaqueous landslide deposits. Past work at Ritter, as well as a survey of landslide deposits offshore Montserrat, Lesser Antilles (Crutchley et al., 2013; Watt et al., 2012a, 2012b), has also shown that both bathymetric and internal geophysical data (with further insights provided by direct sampling) are required to accurately reconstruct the complex sequence of transport and dynamics involved in landslide emplacement offshore volcanic islands. In particular, the internal architecture of deposits is key to revealing evidence of substrate incorporation, and for the estimation of the initial volume of volcanic debris. The process of substrate incorporation as well as the decoupling of submarine landslides from the substrate, has also been extensively studied on exhumed ancient mass transport deposits onshore (Ogata et al., 2019; Sobiesiak et al., 2018). These studies show that substrate decoupling occurs where a lubricating layer between the landslide and the substrate prevents the transmission of shear stress from the flow into the substrate (Ogata et al., 2014b; Sobiesiak et al., 2018) and that substrate incorporation occurs where either the basal drag of the flow is great enough to plough the slide mass into the substrate, or where a dragged tool (e.g., a coherent slide block) is pressed into the substrate's surface at the base of the flow, ripping off substrate material (Sobiesiak et al., 2018).

During a marine geophysical survey on board RV SONNE (SO252), we surveyed the seafloor around Ritter and the neighboring islands of Sakar and Umboi (Fig. 3.3.1). Beside the deposits of the 1888 Ritter Island sector collapse, we identified two additional, buried landslide deposits west of Sakar that vary in extent and morphology. These differences relate to distinct patterns of seafloor interaction and internal structures. Understanding the transport and emplacement processes that lead to such deposits, and how and why the morphology and extent of deposits vary, is key to constraining tsunami magnitudes and providing hazard assessments for coastal regions potentially subject to volcanic-tsunami hazards (Løvholt et al., 2015).

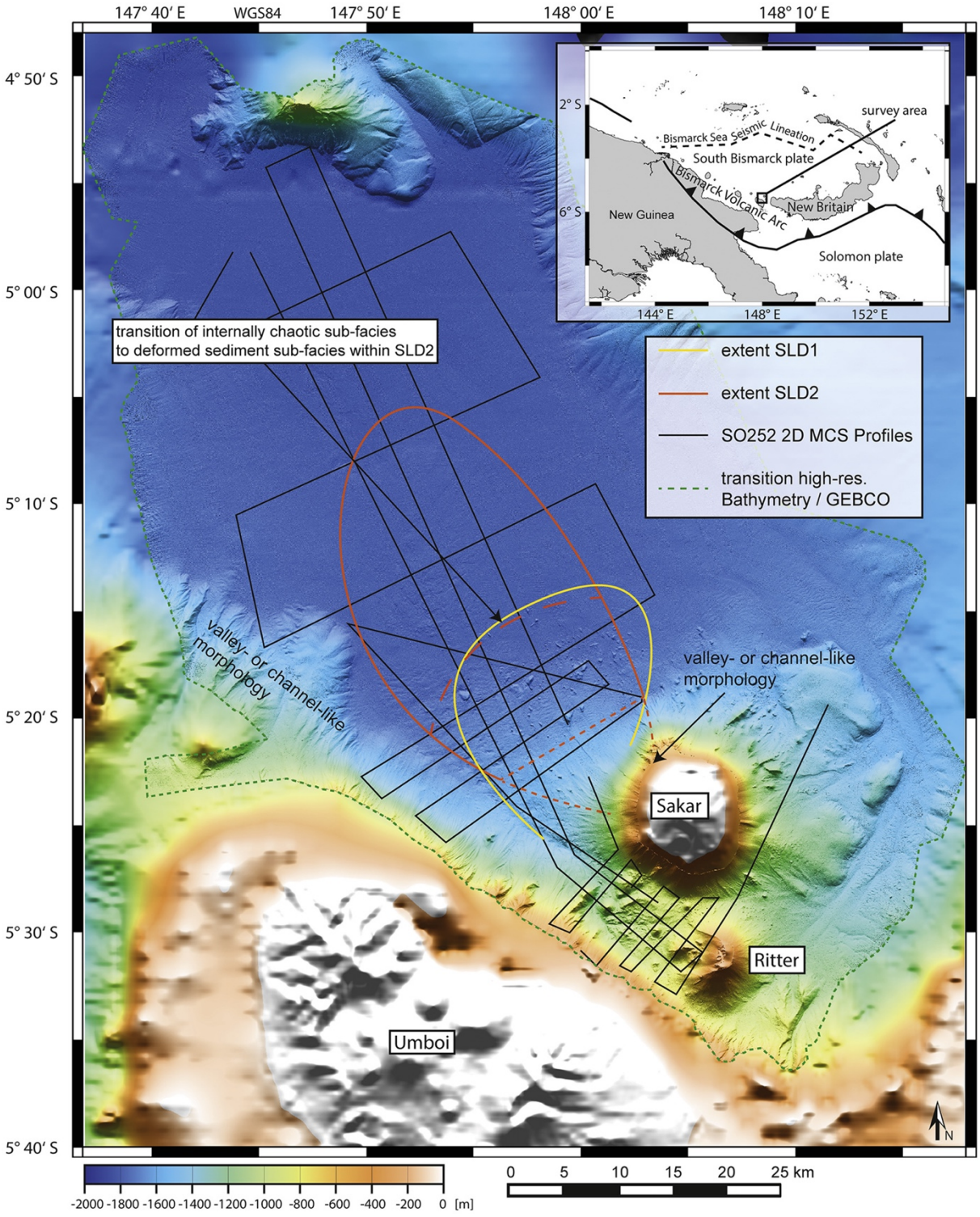

Figure 3.1: *Map of the study region, showing the extents of SLD1 and SLD2 (dashed line indicates the limits of clear deposit imaging). The solid black lines mark acquired 2D multichannel seismic profiles (Karstens et al., 2019; Watt et al., 2019). Background: High-resolution bathymetry acquired during SO252 merged with low-resolution GEBCO grid (transition at dotted green line). Right corner: Overview map showing the general tectonic setting of the area.*

The main aim of this paper is to identify the processes that resulted in the two different types of volcanic landslide deposit observed offshore Sakar, by targeting two objectives. The first objective is to determine the origin of the seismically imaged deposits. We use high-resolution 2D seismic data to reconstruct the geometry (extent and thickness) of the deposits to test whether they originated from Umboi, Sakar or Ritter. The second objective is to constrain the emplacement dynamics of the landslides with a focus on their interaction with the underlying substrate. We use seismic characteristics such as internal reflection patterns, amplitude variations, and the configuration of the top and bottom bounding reflectors to interpret the origin of different sub-facies within the landslide deposits and their relationship to each other, thereby evaluating the extent of the primary failure mass and evidence of substrate incorporation and deformation.

3.2 Geological Background

3.2.1 Regional tectonics

Sakar is a volcanic island located on the southern margin of the Bismarck microplate, forming a part of the Western Bismarck volcanic arc (Fig. 3.1). This 1000 km-long volcanic arc extends onto the larger island of New Britain to the east, and arc volcanism in this setting is associated with the northward subduction of the Solomon microplate and of a relict slab further west, where the arc has collided with the New Guinea continental margin (Baldwin et al., 2012; Honza et al., 1989; Johnson et al., 1987; Taylor, 1979). This tectonically complex zone of microplates lies in a region of oblique convergence between the Pacific and Australian plates (Baldwin et al., 2012; Holm and Richards, 2013; Woodhead et al., 2010). The eastern and western ends of the Bismarck arc are cut by the Bismarck Sea Seismic Lineation, a seismically active series of left-lateral transform faults and spreading segments separating the South Bismarck plate and the North Bismarck plate (Baldwin et al., 2012; Taylor, 1979; Fig. 3.1).

3.2.2 Geology and topography

Sakar is the northernmost of a group of three islands approximately 25 km west of New Britain, (Fig. 3.1). The larger volcanic island of Umboi is 15 km south of Sakar, and the much smaller island of Ritter – the subaerial remnant of the 1888 lateral collapse – lies in between. Rock samples show that the volcanism of the western Bismarck arc, including that on Ritter, Umboi and Sakar, is dominated by basaltic magmas (Johnson, 1977; Woodhead et al., 2010).

Sakar has a broadly symmetrical conical form, with gullied slopes that rise steeply to the island summit. The island diameter at sea level is approximately 8 km, but the entire structure rises from a base ~1500 m below the sea surface, with a diameter of ~25 km, to a maximum height of ~900 m above sea level. The summit crater is approximately 1.5 km wide and contains a crater lake (Johnson et al., 1972). The island is formed by this single main volcanic edifice, which is dominated by porphyritic basaltic lavas, with subsidiary andesites. Around the island shoreline are volcaniclastic alluvial deposits, and there are parasitic volcanic cones in the northern part of the island (Johnson et al., 1972). No historical eruptions are known from Sakar, but several hot springs on the southwestern shore (Johnson et al., 1972), as well as its youthful morphology, suggest that it is potentially active. Offshore, the island is fringed by coral reefs.

The seafloor offshore Sakar was surveyed in 2004 by the RV Kilo Moana, on a research expedition that mapped 12 landslide deposits in the Bismarck volcanic arc (Silver et al., 2009). This expedition investigated in detail the submarine deposits from the lateral collapse of Ritter in 1888 (Day et al., 2015; Johnson et al., 1987; Karstens et al., 2019; Silver et al., 2009; Ward and Day, 2003), which travelled between Sakar and Umboi and into the basin northwest of the islands. It also identified a field of hummocks north of Sakar – a different area from that described in this paper – and interpreted this to be the blocky facies of a debris avalanche deposit originating from Sakar. This deposit covers an area of 30 km² to a distance of more than 10 km from the island's coast (Fig. 3.2). The lack of a collapse scar was explained by later volcanic growth and the formation of coral reefs within the avalanche's source area. However, several irregular valleys at the flanks around Sakar indicate potential source areas of landslides (Fig. 3.2; Silver et al. 2009).

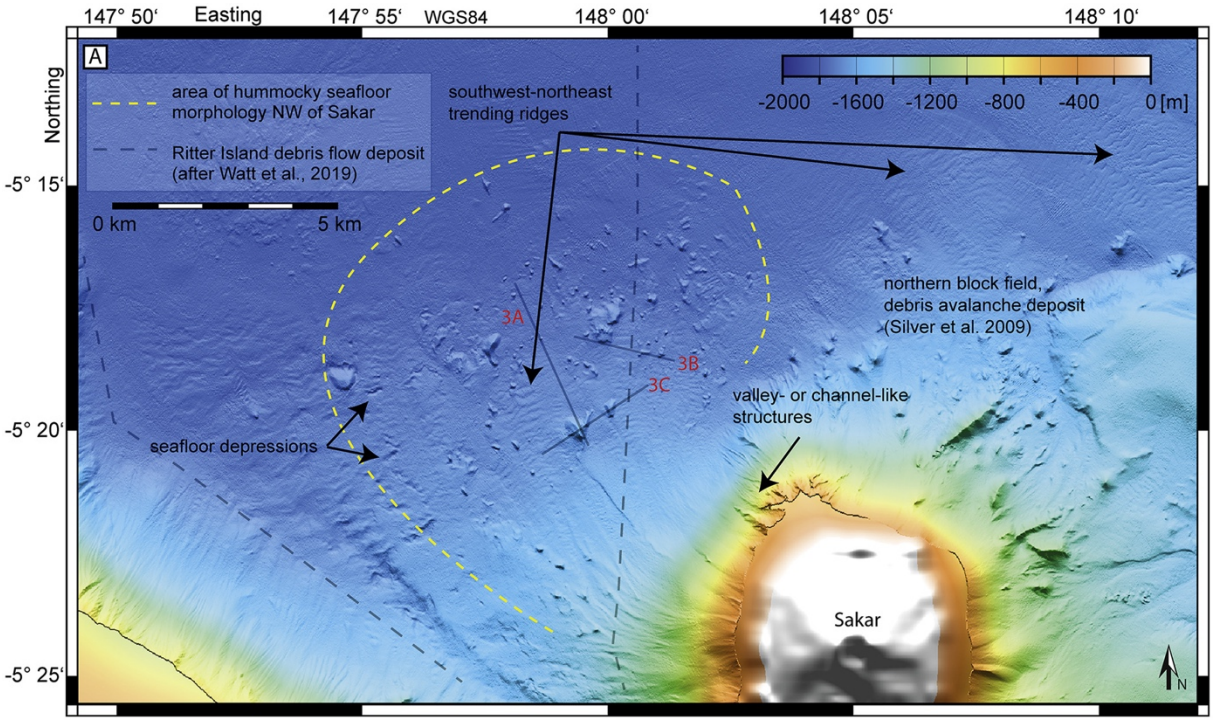

Figure 3.2: *A: Bathymetry of the hummock field northwest of Sakar. The dashed yellow line marks the extent of the hummock field, broadly coinciding with the margin of SLD1 in seismic reflection profiles. The dashed grey lines mark the margins of the 1888 Ritter Island collapse deposit, after Watt et al. (2019). Grey lines mark the locations of the seismic sections shown in Fig. 3.3.3A, B and C.*

3.3 Data and Methods

During scientific cruise SO252 on R/V SONNE in November/December 2016, we collected 2D multichannel seismic data using a 250 m-long (160 channels) streamer system with a group spacing of 1.56 m [dataset](Berndt et al., 2021b). As the seismic source, we used two GI airguns, shot in harmonic mode (105/105 cubic inch). In total, we collected 680 km of seismic reflection profiles (Fig. 3.1). The data were processed with a 10, 45, 250, 400 Hz bandpass filter, a normal moveout correction (constant velocity: 1495 m/s, derived from CTD measurements), and a post-stack 2D-stolt-migration using a constant velocity of 1500 m/s. The bathymetry of the survey area was mapped using two multibeam systems (Kongsberg EM710 and EM122) with a horizontal resolution of 25 m [dataset](Berndt et al., 2021a). For the maps shown in this study, we merged the acquired high-resolution bathymetry grid with a low-resolution global GEBCO grid. Detailed acquisition and processing descriptions can be found in the SO252 cruise report (Berndt et al., 2016).

The range of data collected on cruise SO252 also includes a 3D seismic dataset (Karstens et al., 2019), high-resolution sub-bottom echosounder profiles (Parasound P70 system) and high-resolution video sledge derived photography (Watt et al., 2019), as well as grab samples. To derive a 2D velocity model by forward modeling, six three-component ocean bottom seismometers (OBS) were deployed along a profile within the 3D seismic cube.

Depth, thickness, and volume calculations of sedimentary units mapped using the 2D seismic data were carried out with a seismic velocity of 1760 m/s, derived from OBS experiments (Karstens et al., 2019). Areas and volumes were determined by picking the top and base reflections of sedimentary units on cross-cutting seismic profiles. Relative shortening in units with resolvable compressional structures along the profiles was graphically estimated, using the ratio between the observed extent of the compressional zone and the length of mappable reflections within the seismic data along the deformed reflectors at zero vertical exaggeration. As parts of the compressional structures cannot be resolved properly in the seismic data, shortening values have to be considered minimum estimates. Absolute displacement values of thrust faults were calculated by dividing the picked horizontal distance of a thrusted horizon overlying its undeformed counterpart by the cosine of the fault dip angle.

3.4 Results

3.4.1 Seismic facies

The stratigraphy northwest of Sakar and Ritter, and north of Umboi, was extensively imaged within the seismic data collected during cruise SO252, with examples shown in Figs. 3.3 and 3.4. The data reveal two generally different seismic facies: one defined by continuous and parallel reflections and a second one characterized by chaotic and rather transparent (i.e., lower amplitude) seismic reflections.

The dominant sub-seafloor facies consists of continuous and parallel reflections. This facies is typified by laterally coherent reflections with generally consistent amplitudes. The reflections appear relatively homogenous and are sub-horizontal, lacking any hummocky or steeply dipping morphological features, and representing the seismic image of well-bedded sediments. Subsequently we will refer to this facies as the well-bedded sediment facies.

The second facies, characterized by chaotic and relatively transparent reflections, occurs in two discrete and broadly horizontal packages, that interrupt the well-bedded sediment facies

northwest of Sakar. We divide this chaotic facies into two types. The first type contains irregular surfaces with dipping, sometimes irregular or wavy top boundary reflections. This sub-facies has top and bottom boundaries with high seismic amplitudes, while it is internally chaotic, with most parts being significantly more transparent than the well-bedded sediment facies. This internally chaotic sub-facies is present in two distinct packages of reflections on and near the western flank of Sakar. We consider these packages to represent landslide deposits: a shallow deposit subsequently referred to as Sakar Landslide Deposit 1 (SLD1) and a deeper deposit referred to as Sakar Landslide Deposit 2 (SLD2), which we describe in detail within the following subsections. The second chaotic sub-facies is relatively transparent, too, but contains internal reflections that are parallel-bedded and mostly continuous. This sub-facies occurs as a distal continuation of the internally chaotic sub-facies in SLD2. We interpret its characteristics as corresponding to deformed bedded sediments, forming the outer part of SLD2, and will subsequently refer to this as the deformed sediment sub-facies.

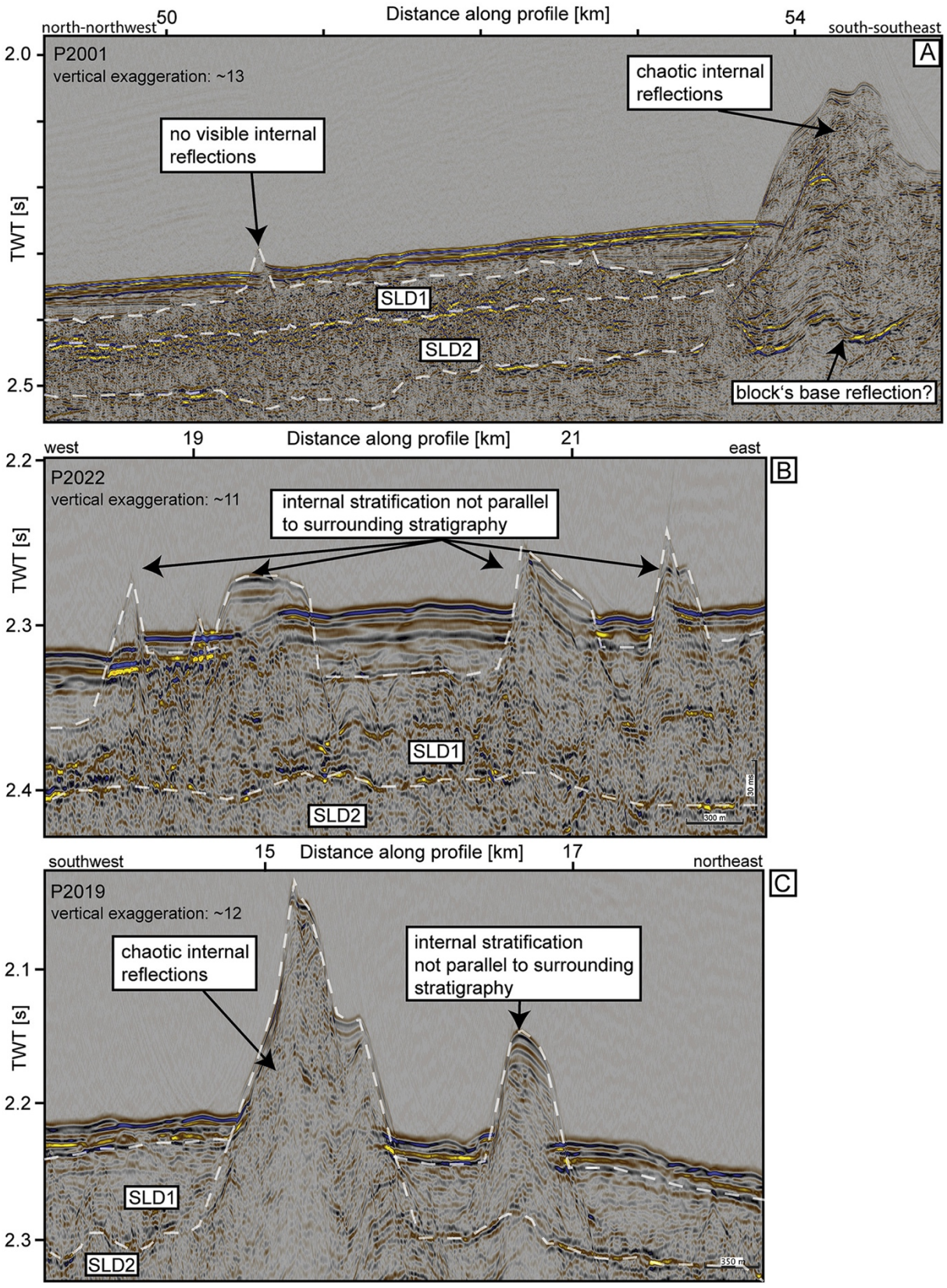

Figure 3.3: *Selected seismic-reflection profiles through SLD1 and SLD2 (locations on Fig. 3.2). A: Profile across a ~ 900 m wide hummock with chaotic internal stratification (right) and a hummock with no visible internal reflections (left). The large hummock appears to be rooted*

within SLD2. B: Profile showing four hummocks apparently rooted within SLD1, which are either seismically transparent (low amplitude) or have stratigraphically chaotic internal structures or stratification that is not parallel to the surrounding stratigraphy. C: Profile showing the 900-m-wide hummock from A in an orthogonal direction and another, smaller hummock with stratification not parallel to the surroundings. In all panels, dashed lines indicate the top and bottom boundaries of SLD1 and SLD2.

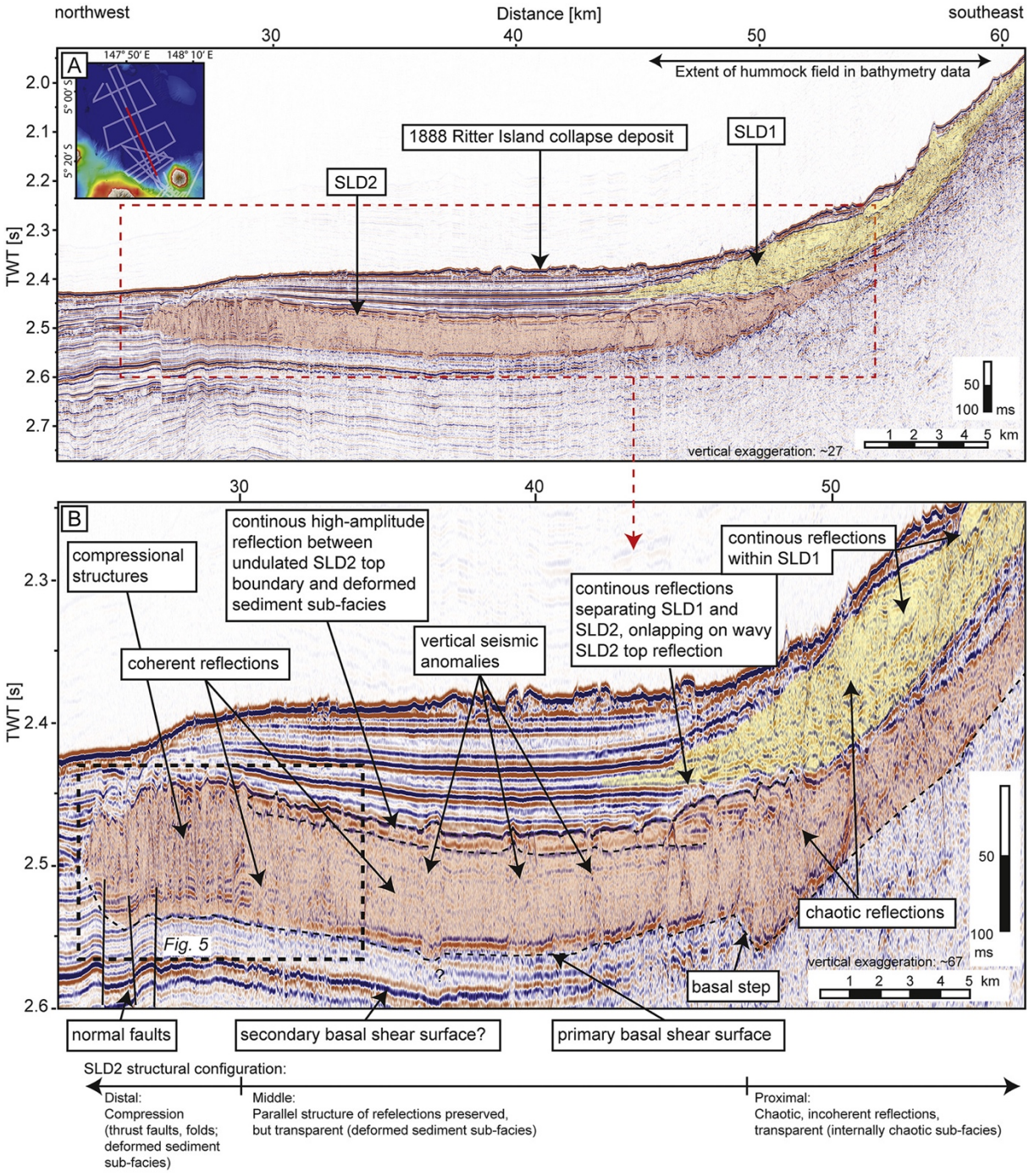

Figure 3.4: *Northwest-southeast oriented seismic section showing SLD1 and SLD2 with annotated interpretations. A: Extent of SLD1, SLD2 and the 1888 Ritter Island collapse deposit (see inset map). B: Detail of the internal architecture of SLD1 and SLD2.*

3.4.2 Seafloor morphology

The submarine morphology northwest of Sakar is dominated by a sub-circular field of 107 randomly distributed hummocks (i.e., positive, relatively steep-sided bathymetric features encircled by a clear break in slope), covering an area of 240 km² with long-axis diameters >100 m (Fig. 3.2). This hummock field is separated from that previously identified north of Sakar by Silver et al. (2009), and partially overlaps with the distal part of the transport path of the 1888 Ritter Island landslide deposits (Fig. 3.2; Day et al., 2015; Watt et al., 2019). Within the hummock field northwest of Sakar, 92 hummocks have maximum diameters between 100 and 500 m (at the basal break in slope), 23 between 500 and 1,000 m and two between 1,000 and 1,100 m, covering individual surface areas between ~0.05 km² and ~1.21 km². The second largest hummock was transected by two seismic profiles (Fig. 3.3A, C), and covers a surface area of ~1 km² with a height > 80 m above the surrounding seafloor. The flanks of this hummock continue down to 120 m below the seafloor and are resolvable to the center of SLD2 (internally chaotic sub-facies) (Fig. 3.3). In contrast, the basal reflection of SLD1 continues below most of the other, smaller hummocks that are transected by seismic profiles, but is bent upwards, which we attribute to seismic velocity pull-up. Most of the hummocks observable at the present-day seafloor therefore appear to be rooted within SLD1 (Fig. 3.3B), and are partially buried by overlying sediment. Some hummocks show an internal seismic stratification that is not parallel to the surrounding stratigraphy (Figs. 3.3B, C), while some show chaotic internal reflections (Fig. 3.3C) and others show no visible internal reflections (Fig. 3.3B), which is most likely a problem of seismic imaging. None of these hummocks has a conical shape, comparable to the conic landforms northwest of Ritter and south of Sakar (Karstens et al., 2019); instead, they appear elongated and sub-angular, but without a preferred orientation. Their broad form is similar to volcanic landslide blocks in other offshore settings, such as those offshore Montserrat (Watt et al., 2012b) or El Hierro, Canary Islands (Masson et al., 2002), or in many subaerial volcanic settings (e.g., Yoshida et al., 2012). The average slope between the hummocks dips 2.5 ° seaward close to Sakar and < 0.5 ° at the north-western limits of the hummock field. Outside of the hummocky field the seafloor is generally smooth and flat (Fig. 3.2) with an overall slope gradient below 0.5 °. However, there are areas within the field containing parallel

ridges trending southeast-northwest (Fig. 3.2) with wavelengths of ~200 m and amplitudes of ~ 5 m; and a relatively small field of elongated seafloor depressions with diameters between 200 and 500 m and 5 to 15 m depth. Northwest of the hummock field the seafloor morphology is dominated by several smooth-surfaced lobes, interpreted as the distal deposits of the 1888 Ritter Island collapse (Watt et al., 2019).

Our bathymetric data show that the field of hummocks north of Sakar (cf. Silver et al., 2009) has block sizes and distribution similar to those in the north-western field mapped here. As there are no seismic data imaging the subsurface of the second hummock field to the north, and because it is separated from the one mapped here by several kilometers, we do not further investigate the area north of Sakar within this paper.

3.4.3 Landslide deposit stratigraphy

3.4.3.1 Sakar Landslide Deposit 1 stratigraphy

Directly below the seafloor reflection west of Sakar, a ~10 m-thick unit with chaotic internal reflections is located (Fig. 3.3A, 4). Watt et al. (2019) interpreted it to be the deposit of the 1888 Ritter Island sector collapse. The Ritter deposit overlies a ~50 m-thick package of well-stratified reflections (Fig. 3.4), but to the east, closer towards the slope of Sakar, it overlies SLD1. In 2D profiles, the latter forms a tapering, wedge-shaped deposit, seismically characterized by the internally chaotic sub-facies, with an average thickness of 67 m (Figs. 3.3, 3.4). SLD1 can be correlated across multiple profiles, defining a laterally fan-shaped deposit (Fig. 3.1) extending over an area of ~250 km² with a volume of ~15.5 km³. Close to the flank of Sakar, the boundary between SLD1 and the underlying bedded stratigraphy, which has an increasingly chaotic general appearance in seismic reflection profiles, becomes obscure (Fig. 3.4A). Although the general seismic appearance of SLD1 corresponds to the internally chaotic sub-facies, at least two continuous internal reflections can be traced over a distance of 1 km, with a seismic waveform that consists of one peak overlying one trough.

SLD1 is thickest on the slope of Sakar (slope gradient 2.5 °), tapering to the west. In this area, its top boundary reflection is indistinguishable from the seafloor reflection, which has a hummocky seismic appearance. The lateral margins of SLD1 as well as the area where its upper surface is indistinguishable from the seafloor (on the outer flank of Sakar), correlate with the margins of the hummock field northwest of Sakar observed in the bathymetry (Fig. 3.2). The volume stated above includes the hummocks intersected by the seismic data that appear to be rooted within SLD1; hummocks between and off the seismic profiles, as well as the large block

shown in Fig. 3.3A, which appears to be rooted within SLD2, are not included. Due to the limited coverage of the 2D seismic lines, the extent of SLD1 could not be mapped entirely. Extent and volume thus have to be considered minimum values.

3.4.3.2 Sakar Landslide Deposit 2 stratigraphy

At a depth of 60 – 70 m below the seafloor, the top boundary of SLD2 extends over an area of 590 km² (Fig. 3.1) and has an elongated shape. The average thickness of the deposit is 71 m, which remains relatively consistent over the entire extent. Deposit thickness tapers to less than 60 m at the north-eastern and south-western margins. We divide the deposit into three parts: A proximal part close to Sakar, seismically characterized by the internally chaotic sub-facies (similar to SLD1); a middle part, characterized by the deformed sediment sub-facies; and a distal toe consisting of the deformed sediment sub-facies as well, but with more coherent reflections that show extensively folded and thrust-faulted reflections (Fig. 3.4B). All three parts are included in the volume and extent values stated here.

In the southeasternmost part of the seismic profile in Fig. 3.4, the proximal part of SLD2 is separated from SLD1 by a continuous reflection package of ~15 m maximum thickness over a downslope distance of ~3 km. Close to the outer flank of Sakar, seismic reflections are generally chaotic, and amplitudes decrease with time in respect to depth more strongly than in the basin west of the island. Because of this, it is very difficult to distinguish the bottom boundary of the internally chaotic sub-facies in SLD2. For this study, we chose the first continuous high-amplitude reflection to define the base of SLD2 in this area, but the true boundary may be located even deeper. Therefore, we consider the volume of this part of SLD2, of 12.5 km³, as a minimum volume. The depth of the continuous basal reflection varies within +/- 10 m, resulting in a proximal deposit thickness of 47 m to 61 m (Fig. 3.4). Within the seismic data the surface of the proximal SLD2 has an apparent downslope angle between 0.5 and 2.0 °, following the general slope trend close to Sakar.

The downslope limit of the proximal part of SLD2 coincides with the appearance of more continuous internal reflections (the transition from the internally chaotic to the deformed sediment sub-facies), a basal upward step of the deposit's bottom boundary reflection, and a break in the slope gradient. This defines the start of the middle part of SLD2. Internally, the reflections in this part of SLD2 have lower amplitudes than the bounding stratigraphy but show visible continuity over ~ 17 km distance. This continuity is only disrupted by vertical seismic anomalies of upward bent reflections (Fig. 3.4B). Across the transition from the proximal to the middle part of SLD2, the top reflections are undulated, over a distance of more than 5 km

(Fig. 3.4B). This upper surface morphology consists of seven undulations with wavelengths between 500 m and 1300 m and amplitudes between 3 m and > 8 m. These transition, to the northwest into reflections concordant to the well-bedded sediment facies above (Fig. 3.4B). Directly below the top reflection, a ~10 m thick package of continuous reflections with higher coherency than the internal reflections below is resolvable, until it is cut by the deformation marking the start of the distal toe of the deposit (Fig. 3.4B). The upper surface of SLD2 transitions from a (apparent) north-western dip of 0.16° to an (apparent) south-eastern dip of 0.17° towards the deposit's toe. The bottom boundary reflection steps upwards from the proximal part of SLD2, becoming shallower by ~ 23 m over a downslope distance of ~ 1000 m. This marks the bottom boundary-limit between the internally chaotic sub-facies in the proximal part and the deformed sediment sub-facies in the middle part of SLD2. Beyond this step, the basal reflection is generally continuous and concordant with the underlying stratigraphy, and its amplitude decreases towards the distal part of SLD2.

The distal part of SLD2 is dominated by thrusting and folding. The boundary between the middle and distal part is characterized by the appearance of higher-amplitude internal reflections, in which compressional structures become clearly visible. At least five thrust faults can be identified over a downslope distance of more than 5 km, with fault dip angles between 12° and 17° and an apparent southeast dip direction, parallel to the profile direction (Fig. 3.5C). Between the thrusts and folds, the seismic reflections are irregularly deformed, with a chaotic appearance and without resolvable faulting or folding. Due to this chaotic nature, absolute displacement calculations were only possible for two of the thrust faults, giving individual displacement values of 73 m and 82 m (± 20 m picking uncertainty due to the chaotic seismic character). From relative graphical estimations (see 3. Data and Methods) a horizontal shortening of 27% caused by thrusting and folding is estimated over the most distal 5 km of the toe region (in the direction of the seismic profile; Fig. 3.5C).

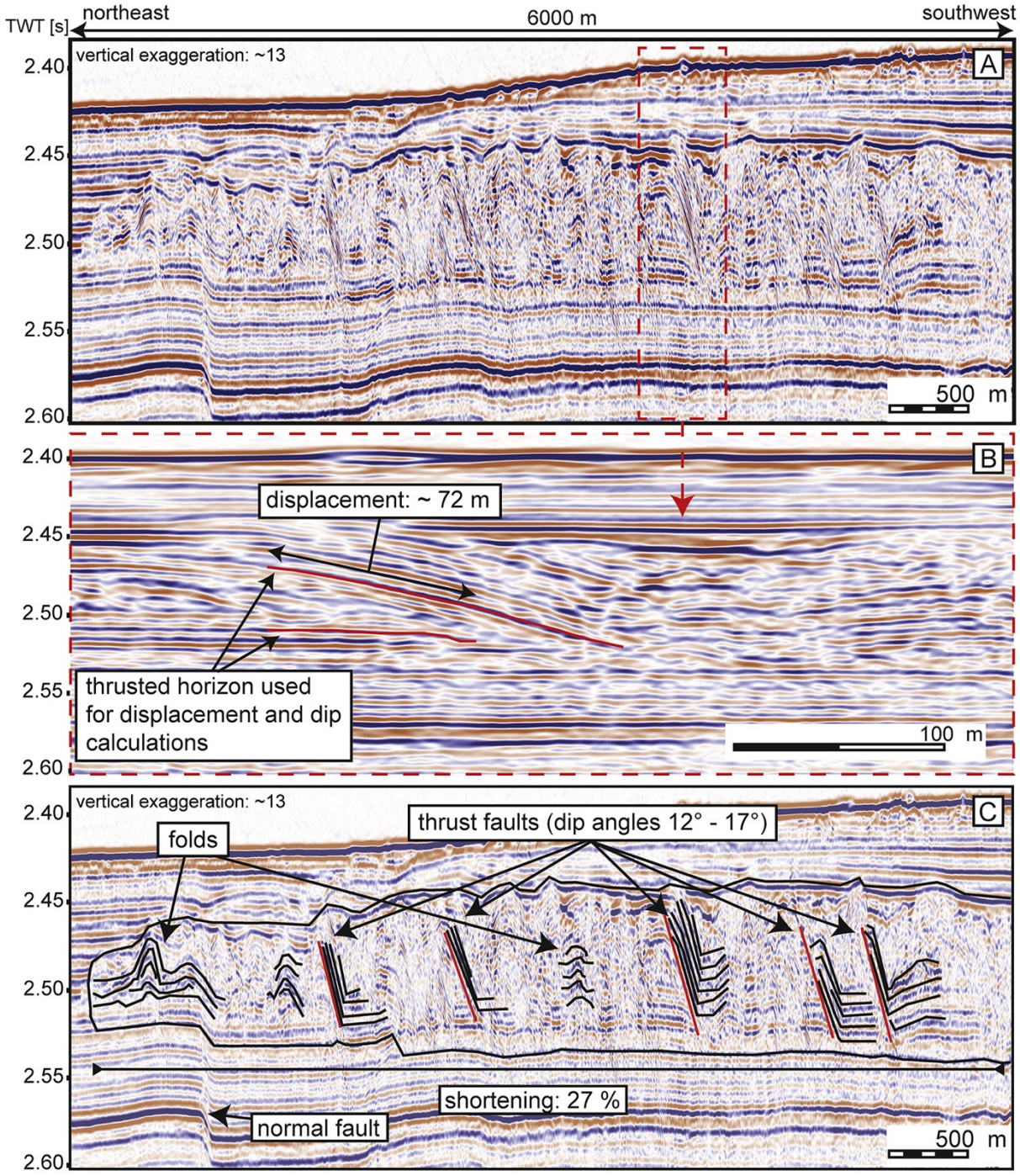

Figure 3.5: *A: Profile through the distal section of SLD2, revealing compressional structures including thrust faults and folds, over ~5 km. B: Detail of a thrust fault without vertical exaggeration. C: Interpreted version of Panel A, showing horizons used to constrain the minimum magnitude of shortening.*

The deformation of both the middle and distal part of SLD2 occurs on the same basal reflection and suggests that this represents the primary shear surface. The reflections directly below this basal shear surface are coherent, but within the first 25 ms-interval they are more transparent

than deeper reflections, with evidence for some disturbance (Fig. 3.4B), suggesting a narrow zone of additional shear, decreasing downwards, and terminating at the base of this 25 ms interval. Below the distal toe region, reflections are truncated by a series of apparently northeast and southeast dipping normal faults (Fig. 3.4B). The middle and distal part of SLD2, all comprising the deformed sediment sub-facies, have a volume of ~ 13.5 km³.

3.5 Discussion

3.5.1 Origin and emplacement of SLD1

SLD1 is characterized by a fan-shaped hummocky topography and its seismic character corresponds to the internally chaotic sub-facies. Hummocky topographies around many volcanoes globally are representative of the blocky facies of debris avalanche deposits (e.g. Mount St Helens, Glicken 1996), although broadly comparable topographies may also be formed by scattered volcanic vents and cones (e.g. Azores, Weiß et al. 2015), or by erosional processes (e.g. Ritter Island, Karstens et al. 2019). Internal reflections indicate stratification within the hummocks of SLD1, and these can be used as an indicator of their origin. Reflections parallel to the underlying stratigraphy would be expected if the hummocks are the result of erosion, while conical forms, with reflections parallel to the flanks of the hummock or with broken, upward-bended reflections at the base of the hummock, would be typical for volcanic cones (both examples can be found west of Ritter; Karstens et al., 2019). However, most of the hummocks off Sakar lack internal stratification or have internal reflections with a dip that is discordant with that of the surrounding stratigraphy. They also have irregular, sub-angular shapes, steep sides and in some cases relatively flat tops. Together, these observations suggest that the hummocks represent transported blocks. Due to the fan-shaped distribution of these blocks at the foot of Sakar we interpret them as being from a common source and emplaced in a single mass movement, and that they thus represent the blocky facies of a debris avalanche deposit. The random distribution of these blocks within the fan is indicative of a freely spreading avalanche (Yoshida et al., 2012). This implies that the flow velocity in the emplacement direction was not significantly higher than the flow-perpendicular spreading velocity (Crutchley et al., 2013).

The areal extent of the northwestern block field in the bathymetric data matches the seismic extent of SLD1, except in the northwesternmost part of the profiles, where the burial depth of SLD1 is too deep for blocks to protrude at the seafloor. This indicates that the bathymetric expression can be used to constrain the minimum extent of the blocky part of the debris

avalanche but does not resolve the margins of the shallowly buried deposit. The high seismic amplitude of the boundary reflections is indicative of a significant change in seismic impedance, implying a different nature of the deposited material within and around SLD1. Seismic reflections within SLD1 are generally discontinuous, chaotic, and transparent. However, there are some coherent reflections extending laterally up to 1000 m. These suggest that the deposit was not emplaced as a simple, fully disaggregated one-directional flow or avalanche. The reflections may either indicate deposition in separate stages or phases of one major event, representing the interface between different flow lobes or pulses (e.g., Deposit 1, Montserrat, Crutchley et al., 2013; Lebas et al., 2011), or they may correspond to a thin (i.e., sub-seismic) unit of hemi-pelagic sediments indicating a period of normal sedimentation between unrelated flank collapse events. As these reflections are not visible on all seismic lines that image the deposit and are laterally restricted, we consider the first scenario more likely.

Due to the geometry and location of SLD1, the debris avalanche most likely originated from Sakar. There are multiple morphological structures that may reflect the scars of past sector collapses onshore Sakar Island (Silver et al., 2009). However, none of them correlates spatially with the deposit, and it is ambiguous if they have large enough dimensions to be the source of a >10 km^3 landslide deposit, suggesting that younger volcanic activity has entirely overprinted the onshore part of the SLD1 collapse scarp.

The hummocky proximal morphology of SLD1, in combination with its fan-shaped extent and chaotic internal structure, unequivocally shows that it is a submarine landslide deposit (Frey-Martínez et al., 2006). Similar deposits with volcanic origin have been identified in many locations (Watt et al., 2021) including Montserrat (Deposit 1; Watt et al. 2012b, a; Crutchley et al. 2013; Karstens et al. 2013) and Fogo, Cape Verde (Day et al., 1999; Le Bas et al., 2007; Masson et al., 2008). The fan shape of the deposit suggests a cohesionless flow dominated by energy dissipation through granular particle interactions, which is typical for freely-spreading heterogenous and generally coarse-grained volcanic debris avalanches (Mulder and Cochonat, 1996; Watt et al., 2012a, Watt et al., 2021).

Within SLD1, there is no seismic or bathymetric evidence for the secondary incorporation of underlying material (including that of SLD2). According to Sobiesiak et al. (2018), a decoupling of the sliding mass from the substrate, “free-slip flow”, occurs where shear stress transmission from the flow into the substrate is prevented by a lubricating layer. The study suggests the formation of this lubricating layer by one (or a combination) of the following mechanisms: hydroplaning, shear wetting, and/or liquefaction. During hydroplaning the

hydrodynamic water pressure at the flow front increases and is transferred into the underlying bed, forming a water-rich sediment layer between flow and substrate (Mohrig et al., 1998). Shear wetting describes the generation of a soft, diluted, lubricating layer due to high shear rates between the water and the sediment boundary during flow (De Blasio et al., 2005). Ogata et al. (2014a) describe liquefaction of poorly consolidated sands where the induced shear of the flow causes a loss of grain contacts within the sand layers. As the flow stops, these liquified sands inject upwards into the basal flow deposit. Our seismic data do not provide the resolution to allow us to distinguish between these different processes (such as the observation of basal injections of sand (e.g. vertical fluid escape structures), which would be indicative for liquefaction (Ogata et al., 2014a, 2012), and while we cannot provide further constraints, we consider it likely that one or a combination of these processes led to a decoupling of the SLD1 debris avalanche and the contemporaneous seafloor.

Southwest-northeast trending ridges within the hummock field and north of Sakar (Fig. 3.2) are most likely related to later sedimentary processes, e.g., sediment waves (Pope et al., 2018). They also could be related to the deposition of the 1888 Ritter Island collapse debris flow (Watt et al. 2019), but in either case, we do not interpret them as being directly associated with SLD1. As the Ritter Island 1888 deposits partially overlap with the SLD1 hummock field (Fig. 3.2), we cannot exclude some erosion of SLD1 by the Ritter Island debris flow, although the burial depth of SLD1 in most places is deeper than the bottom boundary of the Ritter Island, and any erosion is thus not likely to have had a major impact on the morphology or our estimated volume of SLD1.

3.5.2 Origin and emplacement of SLD2

SLD2 extends from the outer flank of Sakar 30 km into the neighboring basin northwest of Sakar and Umboi (Fig. 3.1). Based on its location and its shape, an origin from Umboi, Sakar or Ritter may be possible. However, an origin from the relatively small edifice of Ritter is unlikely due to the large volume of the proximal component (12.5 km^3) and because the deposit lies partly on the flanks of Sakar, which would require an element of upslope, northward bending transport and deposition. The shape and thinning pattern are most consistent with a landslide originating from the western slope of Sakar. This agrees with the direction of deformation patterns in the outer parts of SLD2, indicating northwestward compressional deformation in the toe domain (Fig. 3.5).

The proximal part of SLD2 is seismically characterized by the internally chaotic sub-facies (Fig. 3.4). This is similar to the overall seismic image of SLD1, suggesting that this part of the

deposit originated as a volcanic debris avalanche, similar to SLD1. The apparent rooting of a large, transported block that protrudes from SLD2 to the seafloor (Fig. 3.3A, C) supports this interpretation, and it is likely that the surface of SLD2 contained many such blocks or hummocks, the majority of which are now buried and no longer evident at the seafloor. The outer margin of the internally chaotic sub-facies shows a direct lateral transition into the deformed sediment sub-facies (Fig. 3.4B). Hence, SLD2 shows characteristics typical for volcanic debris avalanches off volcanic islands, but at the same time its middle and distal part comprise large volume of deformed pre-existing sediments, and SLD2 thus represents a composite deposit of volcanic material and seafloor sediments.

As described above, the middle part of SLD2 contains a discrete unit in its uppermost part (Fig. 3.4B), which may indicate the deposit of an overrunning flow. This unit has an undulated upper surface, and although this morphology could be a result of later sedimentary processes, its seismic image is markedly different from bedforms typically associated with sediment waves, (Pope et al., 2018), and we interpret this undulating form to be a primary characteristic of the upper surface of SLD2.

The transition from a proximal debris avalanche deposit to deformed seafloor sediments (marked by basal step, Fig. 3.4B) suggests that SLD2 originated as a debris avalanche from Sakar that incised into the substrate, as shown by the lateral transition between the internally chaotic sub-facies and the deformed sediment beyond. This transition indicates that some seafloor sediment must be incorporated within the proximal, internally chaotic part of SLD2, unless this pre-existing sediment was entirely evacuated from this area. Beyond the proximal part of SLD2, some evacuated sediment, or a more mobile part of the driving debris avalanche, may have overran the pre-existing seafloor, giving rise to the discrete uppermost unit in the middle part of SLD2. This overrunning flow may have facilitated the downslope-propagating deformation of the underlying seafloor sediment (i.e., the deformed sediment sub-facies of SLD2), which formed beyond the front of the driving debris avalanche (e.g., see processes discussed in Watt et al., 2012b) (Fig. 3.6). This seafloor sediment package shows strong evidence of *in situ* compressional deformation, particularly at its toe, but was not evacuated, defining a frontally confined mass transport deposit (Frey-Martínez et al., 2006). Beyond the limits of the frontally confined margin (Fig. 3.4B), we cannot find seismic indications for further mass transport, although it is possible that the thin, distal parts of an overrunning flow are not resolvable within our seismic data.

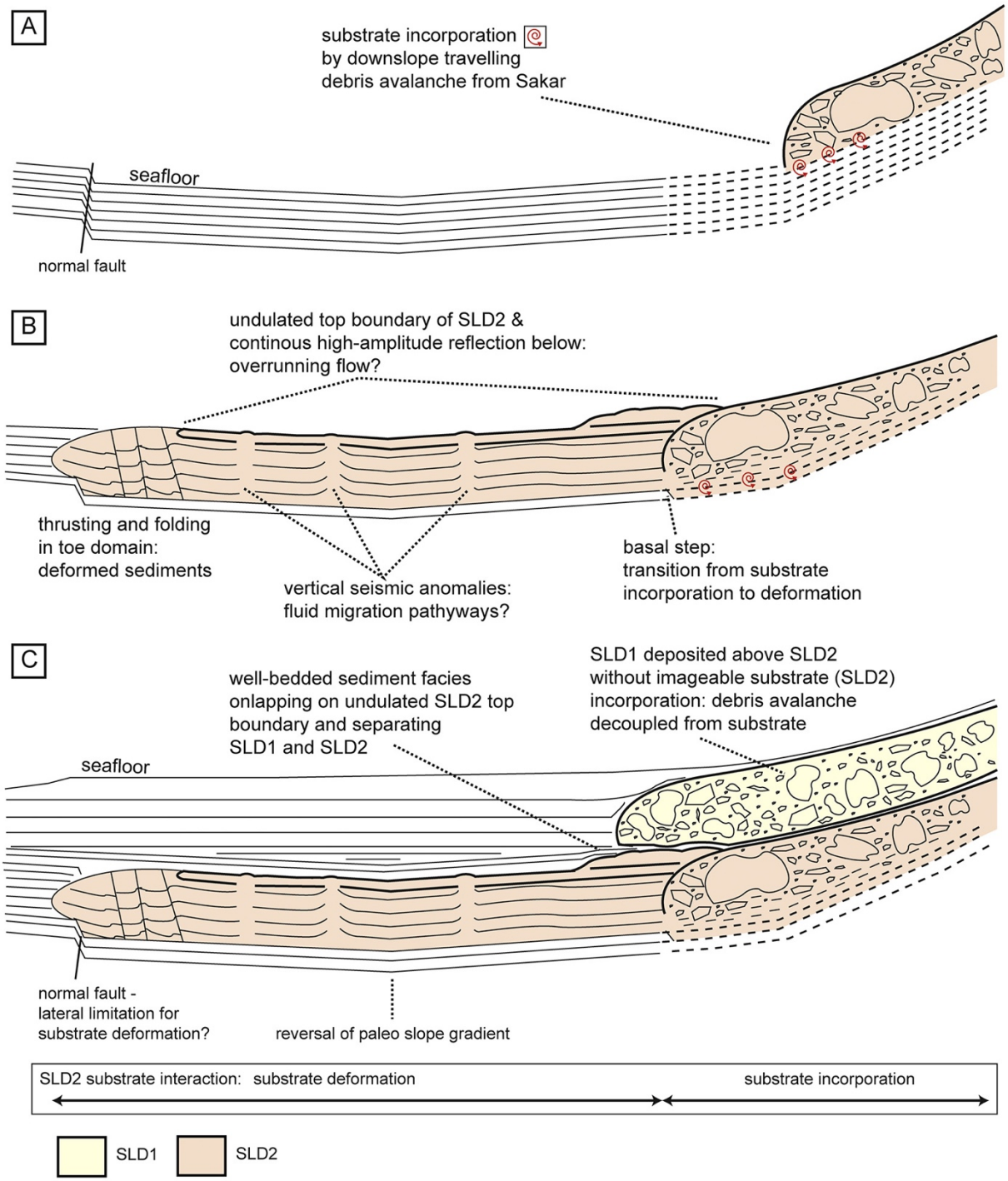

***Figure 3.6**: Model for the emplacement of SLD1 and SLD2. A: A blocky debris avalanche associated with SLD2 flowing downslope, starting to incorporate and incise into the substrate. Different specific incorporation mechanisms are discussed in the text. B: The situation after the emplacement of SLD2, showing substrate incorporation (right) and frontal, downslope deformation, driven by impact and augmented by an overrunning flow, derived from the initial debris avalanche. The distal deformation limit is associated with a pre-existing fault, disrupting the stratigraphy, and a reversal in the paleo-basin slope gradient. C: The situation before the*

Ritter Island 1888 landslide deposit, showing the blocky debris avalanche of SLD1, emplaced above SLD2 without incorporating the substrate (SLD2 and the relatively thin intervening sediment package), indicating a decoupling of the slide mass from the substrate. Both landslides have been subsequently buried by younger basin infill.

The seismic analyses of debris avalanche deposits offshore Montserrat revealed composite deposits consisting of a volcanic subunit and a subunit of deformed and mobilized seafloor sediments (Deposits 2 and 8, Watt et al. 2012b, a; Crutchley et al. 2013), similar to SLD2. These composite deposits formed as the result of the collision of a volcanic debris avalanche with seafloor sediments, resulting in their mobilization and deformation. This interpretation was confirmed by IODP expedition 340 (Le Friant et al. 2015), which revealed the absence of volcanic debris avalanche deposits within the seismically transparent, distal subunit of Montserrat Deposit 2 and of comparable deposits offshore Martinique. The processes involved in the interaction between volcanic debris avalanches and underlying seafloor sediments are complex and there are various potential mobilization mechanisms (Watt et al. 2012b; Le Friant et al. 2015).

Studies on exhumed ancient mass transport deposits onshore confirm the potential composite nature of landslide deposits. “Megabreccia” deposits in the Paleogene Friuli Basin (Italy/Slovenia) were interpreted as the result of bipartite slide masses with a lower cohesive blocky flow and an upper turbulent flow, deeply eroding into and deforming the substrate (Ogata et al., 2014b). Sobiesiak et al. (2018) discuss substrate incorporation mechanisms such as that driven by a basal drag of the flow mass great enough for it to erode into the substrate, ripping off the latter and incorporating it into the flow. Alternatively, similar effects may occur by the dragging of a tool (e.g., a transported block) pressed against the substrate and ripping it off, or by peel-back, where the substrate is pushed along a basal weak layer laterally bounded by sub-vertical shear zones. Ogata et al. (2019) suggest similar substrate incorporation processes such as the erosion of positive paleobathymetric highs, and the transfer of inertial stress of a moving flow into the substrate due to an abrupt change of the slope angle, where the momentum of well-lithified blocks is transferred into the substrate as the slide comes to rest.

Large blocks such as that imaged in Fig. 3.3A could potentially have functioned as tools, eroding the slide mass into the substrate where the gradient of Sakar’s slope decreases. However, due to the limited resolution of our seismic data we cannot identify if one of the

specific mechanisms outlined above represented the dominant mode of substrate erosion by the SLD2 debris avalanche.

The deformation pattern in the outer region of SLD2 is typical for the deposits of frontally confined landslides (Frey-Martínez et al., 2006) and has been observed in non-volcanic submarine mass-movements (e.g., Oregon, USA, Lenz et al., 2019; Shimokita peninsula, northeast Japan, Morita et al., 2011) as well as volcanic settings (e.g., Deposit 8 offshore Montserrat, Watt et al., 2012b). Substrate deformation as the result of the emplacement of volcanic debris avalanches has been seismically documented offshore Montserrat (Crutchley et al., 2013; Watt et al., 2012b, 2012a) and at Ritter Island (Karstens et al., 2019; Watt et al., 2019), where deformed and incorporated sediments contribute 80% of the total slide volume. Potential factors that define the absolute limit of deformation at the toe of SLD2 could be the reversal of the slope direction, adding gravitational forces to the shear resistance of the sediments against progressive shear failure of the deforming sediments as well as a topographic effect caused by several normal faults cutting through the strata below (Fig. 3.4B).

For the deformation of the well-bedded sediment sub-facies of SLD2, we favor a combined substrate deformation model, as follow (Fig. 3.6): Substrate incorporation (i.e., physical mixing of the volcanic debris avalanche with seafloor sediments) did not reach beyond the basal step that marks the foot of the internally chaotic sub-facies of SLD2. This coincides with a break in the slope gradient, (Fig. 3.4). The initial loading that triggered frontal deformation beyond this point could have been the result of a transfer of the blocky debris avalanche's momentum as it decelerated into the substrate, progressively increasing the shear stress on the sediment, causing disaggregation, deformation, and compression. Added to this, an overrunning flow may have facilitated propagation of deformation in the underlying sediment, but the potential mechanisms of this process remain ambiguous. An overrunning flow could potentially liquify underlying sediments by increasing the pore pressure due to grain reorganization during shearing (Hornbach et al., 2015; Ogata et al., 2014a) similar to the shear failure of sensitive clay deposits onshore (Bjerrum, 1955; Quinn et al., 2012). With the vertical seismic anomalies in the middle SLD2 (Fig. 3.4B), we find indications for fluid migration pathways (Gee et al., 2007) which could represent liquefaction. However, we cannot rule out that these structures represent seismic imaging artifacts. A mechanism of shear coupling, as proposed for paleo-landslide deposits in the Karoo Basin, South Africa (Van Der Merwe et al., 2011) and discussed for Deposit 8 off Montserrat (Watt et al., 2012b), where the motion of an overrunning flow exerts forces on the underlying strata leading to deformation, appears less plausible for SLD2. Seismic

evidence for an overrunning flow is only visible in the middle part of SLD2, whereas if this flow was the main agent of deformation via shear coupling, we would expect it to be present over the entire deposit, an alternative model that could explain the seafloor sediment beyond the margin of SLD2 could be that the younger emplacement of SLD1 loaded the older deposits, and triggered failure downslope of these via the shear failure mechanisms described above. Similar secondary seafloor mobilization and deformation of deeper sediment packages, including thrust faulting and folding, has been observed for non-volcanic landslides, e.g. offshore Oregon, where a series of slide blocks have caused deformation and horizontal compaction of underlying sediments within a 10 km area (Lenz et al., 2019). However, because the sediment failure in SLD2 is confined to a package that coincides with both the upper and lower boundaries of its proximal part, and does not affect younger sediment, a role for SLD1 in this process would only make sense if there was no time gap between SLD1 and SLD2. This is not the case, because we observe a package of sediment, partly onlapping on the top boundary of SLD2, that separates the two landslides (Fig. 3.4B).

A further possible model is that both SLD1 and SLD2 are part of one multistage sector collapse, whereby the deeper unit slowly creeped downslope (forming SLD2), until the slope stability reached a critical point and the shallower flank failed, resulting in a collapse that emplaced SLD1. This type of process was postulated by Karstens *et al.* 2019 for the 1888 sector collapse of Ritter Island. Such slow, deep-seated deformations are known from other volcanoes, e.g. Mt. Etna, Sicily (Urlaub et al., 2018). Again, the similar proximal characteristics of SLD1 and SLD2, and the observation of reflections separating the two deposits, indicates a time gap between them that implies they are entirely separate lateral collapses. This does not preclude that the emplacement of both debris avalanches could have been preceded by prolonged gradual deformation at the base of Sakar's flanks that promoted instability, comparable to processes at Ritter Island (Karstens et al., 2019) and around other volcanoes.

The base of SLD2 is defined by a mostly continuous, high-amplitude reflection representing a basal shear surface for the deformation of the sediment package above. However, below this reflection, the well-stratified sediments appear more transparent than further below (Fig. 3.4). A second strong reflection about 25 ms TWT below may represent another, secondary basal shear surface. This second reflection correlates vertically with the depth of the proximal chaotic part of the unit. As the reflections between both surfaces are weak and transparent, but not deformed, this may represent a zone of deeper, distributed deformation, less extensive than that within SLD2 above. The development of a basal shear zone, with different layers of shearing,

rather than one single basal shear surface has been described on onshore exhumed mass transport deposits (Ogata et al., 2014a; Sobiesiak et al., 2018). The seismic data are inconclusive in indicating if this basal shear zone involved shear of the sedimentary strata, or just mobilization of pore fluids.

3.5.3 Dissimilarity of two landslide deposits from Sakar

The results described here show that Sakar has produced at least two voluminous debris avalanches, deposited on the western submerged island slope and the basin floor to the northwest. Because both debris avalanches are the result of sector collapse (i.e., they have mobilized large parts of the flank of the same island) it may be expected that they have a similar composition and that their dynamic evolution was similar. However, while SLD1 appears to consist completely of volcanic debris avalanche material, only the proximal part of SLD2 hosts a debris avalanche component. The middle and distal parts of the deposit consist of deformed seafloor sediments. The volumes of SLD1 and the proximal, internally chaotic sub-facies of SLD2 are nearly equal. However, the entire SLD2, when including the deformed-sediment facies, has twice the volume of SLD1. The fan-shape of SLD1, indicating free-spreading of a cohesionless flow, contrasts with the elongated shape of SLD2, indicating a concentration of forces in one primary direction, equivalent to the direction of mass movement during the initial stage of a debris avalanche. The proximal part of SLD2 most likely eroded into and partly overran the substrate (coupling of flow and substrate), causing deformation in the frontal direction, while the seismically imageable part of SLD1 spread along and above the pre-existing seafloor (decoupling of flow and substrate).

Seismic interpretations of marine landslide deposits off volcanic islands in the Lesser Antilles have shown that debris avalanches can incorporate large volumes of substrate during transport (Deplus et al., 2001; Le Friant et al., 2003; Watt et al., 2012b, 2012a). In a most basic sense, the process of substrate incorporation into moving debris is an energy exchange between the flowing debris mass and the initially static seafloor sediments, where kinetic energy of the flowing mass is consumed to put the static mass in motion. The required amount of energy depends on the stability of the seafloor sediments, which is controlled by the slope gradient and the thickness of the sediment layer (Mangeney et al., 2010), but also by the type of the substrate material and its shear strength. The two deposits examined in this study differ in the nature of their substrate: the continuation of the sedimentary well-bedded seismic facies underneath the proximal part of SLD2 (albeit poorly imaged) suggests that it was deposited on relatively fine-

grained and water-saturated seafloor sediment (i.e., typical basin-infilling sediment), that typically has a low shear resistance. This would have promoted incorporation and a proximal incision of the debris avalanche mass into the substrata. In contrast, the base of SLD1 coincides with a package of chaotic reflections on the flanks of Sakar, separating it from the proximal part of SLD2, and in some profiles corresponds directly with the upper part of SLD2. We interpret this substrate as likely comprising coarse-grained, heterogenous volcanic material derived from the flanks of Sakar, which would be much harder to mobilize than the hemipelagic seafloor sediments of the basin floor (Karstens et al., 2013) – the sediment type on which SLD2 was emplaced. Because of this, SLD1 slid decoupled from it base. Landslide deposits are considered to generally have a higher resistance to being eroded and incorporated into overflowing landslide masses (Alves and Lourenço, 2010). Outcrop-oriented studies on sedimentary mélanges link different mechanisms of substrate incorporation not only to the physiographic setting, but also to different lithological characteristics of the associated mass transport deposits (Ogata et al., 2019). Combined with our interpretations of SLD1 and SLD2, this suggests that the substrate is a major control on the incorporation of seafloor sediment by a debris avalanche. The difference in the nature of the substrate from water-saturated, homogenous seafloor sediments below SLD2 and a denser and more heterogenous volcaniclastic substrate below SLD1, minimized the substrate incorporation and kinetic energy loss in SLD1. This led not only to a smaller total volume of SLD1 but also to a longer runout compared to the debris avalanche component of SLD2.

3.5.4 Tsunami hazard

Landslides are the second most common trigger for tsunamis (Harbitz et al 2014) and have received increased attention with the 2018 Anak Krakatau flank collapse (Grilli et al., 2019). Numerical tsunami simulations of this event were conducted assuming a volume of initially 0.22 – 0.3 km^3 of volcanic material, which was inferred from pre- and post-collapse aerial and satellite imagery and produced results that were consistent with the observed wave characteristics and run-up heights (Grilli et al., 2019). However, numerical landslide tsunami simulations rely heavily on the applied input parameters. In case of submarine landslides, the most important tsunami source parameters are the slide volume and its emplacement velocity (Løvholt et al., 2005), which are only poorly constrained for most historic events (with Ritter Island being a rare exception). Instead, volume estimations are often based on acoustic imaging data of flank collapse deposits, such as bathymetric and seismic data. Our results on SLD2 as well as those from Montserrat and Ritter (Karstens et al., 2019; Watt et al., 2012a) show that

estimating the volume of the initial volcanic debris avalanche only from the surface area of a landslide deposit and the thickness of a stratigraphic unit can be misleading. Without high-resolution seismic data, SLD2 could be easily misinterpreted as one unit of chaotic reflections that resulted from a single-event debris avalanche. The actual volume of the debris avalanche component in SLD2 is less than half that of the complete stratigraphic unit, while the remainder consists of deformed or mobilized seafloor sediments. This underlines the necessity of high-resolution seismic data for accurate volume estimations and tsunami modelling constraints.

The second important constraint in tsunami modelling is the emplacement velocity, which is likely heavily influenced by interaction of the slide mass and the substrate causing a transfer of kinetic energy. A more rapid deceleration of the sliding mass (if occurring in water depths relevant for tsunami genesis) would reduce the magnitude of the resulting tsunami, while the effect of substrate incorporation (increasing the water column) has little impact compared to the initial volcanic flank component. Numerical tsunami simulations of the 1888 Ritter Island sector collapse suggest that tsunami generation was primarily controlled by the collapse of the volcano, i.e. the initial failure volume and acceleration, and that deeper seated deformation and seafloor sediment incorporation had no significant effect on the tsunami amplitude (Karstens et al., 2020). This is in agreement with tsunami potential calculations for landslide deposits off Montserrat, which have shown that tsunami amplitudes for submarine sediment failures with an associated low height drop are an order of magnitude smaller than flank collapse-related tsunami amplitudes of the same volume (Watt et al., 2012a). Hence, it is unlikely that the seafloor sediment failure and deformation imaged in the middle and distal parts of SLD2 affected the tsunami amplitude significantly, although they may result in longer wavelengths, as shown by a tsunami model for Deposit 2 off Montserrat (Watt et al., 2012a). Our analysis reveals once again that the complexity of volcanic sector collapse and debris avalanche emplacement in island settings, and highlights that tsunami hazard assessment for this comparably common process is still lacking reliable constraints for the most important source parameters.

3.6 Conclusions

The slope west of Sakar hosts two previously unknown landslide deposits. The younger deposit, SLD1, comprises volcanic debris avalanche material from Sakar, whereas the deeper SLD2 is a combination of a primary debris avalanche deposit and deformed and incorporated substrate. The toe domain of SLD2, which hosts folded and thrust-faulted sediments was shortened by at

least 27 %. We suggest that the debris avalanche component of SLD2 partly eroded into and overran the substrate and triggered a progressive, lateral increase of the sediment pore pressure, resulting in a decrease of shear strength in the direction of the initial mass movement and mobilization and deformation of the pre-slide subsurface stratigraphy. We propose that the nature of the slide plane substrate is the most important control on sediment mobilization and secondary failures, and that this determined the different sizes and evolution of the two landslide deposits west of Sakar, which originated from the same source and were deposited on the same slope.

The main controlling parameters of landslide-generated tsunami amplitudes are the initial volume of the sliding mass that interacts with the ocean and its further acceleration. Estimating the initial volume of a flank or sector collapse by calculating the volume of the associated landslide deposits involves a significant uncertainty. For SLD2 there is evidence that less than half of the landslide deposit's volume can be assigned to the initial debris avalanche.

Acknowledgements

We thank the master and the crew of the RV SONNE for their support during research cruise SO252. We also thank Dr. Ingo Klaucke and Dr. Christoph Böttner for the onboard-processing of the bathymetry data. We acknowledge Kei Ogata, Fabiano Gamberi and Derek Sawyer for improving the quality of the manuscript with their reviews. We would like to thank the GEBCO initiative for providing access to global digital elevation data and Schlumberger and IHS for granting educational software licenses for the interpretation of the seismic data. The German Ministry of Science and Education (BMBF) funded this study through the "Ritter Island project" grant [03G0252A].

Data Availability

The datasets analyzed in this study will be publicly available at the PANGAEA data repository (multibeam echosounder data: https://doi.org/10.1594/PANGAEA.929026, seismic data: https://doi.org/10.1594/PANGAEA.929022), once this article is published.

References

Alves, T.M., Lourenço, S.D.N., 2010. Geomorphologic features related to gravitational collapse: Submarine landsliding to lateral spreading on a Late Miocene-Quaternary slope (SE Crete, eastern Mediterranean). Geomorphology 123, 13–33. https://doi.org/10.1016/j.geomorph.2010.04.030

Baldwin, S.L., Fitzgerald, P.G., Webb, L.E., 2012. Tectonics of the New Guinea Region. Annu. Rev. Earth Planet. Sci. 40, 495–520. https://doi.org/10.1146/annurev-earth-040809-152540

Berndt, C., Klaucke, I., Kühn, M., 2021a. Multibeam bathymetry gridded data from SONNE cruise SO252. https://doi.org/https://doi.org/10.1594/PANGAEA.929026

Berndt, C., Kühn, M., Karstens, J., 2021b. 2D multi-channel seismic data from SONNE cruise SO252 offshore Ritter Island, 2016, Bismarck Sea, Papua New Guinea. https://doi.org/10.1594/PANGAEA.929022

Berndt, C., Muff, S., Klaucke, I., Watt, S., Böttner, C., Schramm, B., Völsch, A.-M., Bennecke, S., Elger, J., Chi, W.-C., Van Haren, J., Micallef, A., Roth, T., 2016. RV SONNE 252 Cruise Report / Fahrtbericht Tsunami potential of volcanic flank collapses Table of content. https://doi.org/http://dx.doi.org/10.3289/CR_SO252

Bjerrum, L., 1955. Stability of natural slopes in quick clay. Géotechnique 5, 101–119. https://doi.org/https://doi.org/10.1680/geot.1955.5.1.101

Crutchley, G.J., Karstens, J., Berndt, C., Talling, P.J., Watt, S.F.L., Vardy, M.E., Hühnerbach, V., Urlaub, M., Sarkar, S., Klaeschen, D., Paulatto, M., Le Friant, A., Lebas, E., Maeno, F., 2013. Insights into the emplacement dynamics of volcanic landslides from high-resolution 3D seismic data acquired offshore Montserrat, Lesser Antilles. Mar. Geol. 335, 1–15. https://doi.org/10.1016/j.margeo.2012.10.004

Day, S., Llanes, P., Silver, E., Hoffmann, G., Ward, S., Driscoll, N., 2015. Submarine landslide deposits of the historical lateral collapse of Ritter Island, Papua New Guinea. Mar. Pet. Geol. 67, 419–438. https://doi.org/10.1016/j.marpetgeo.2015.05.017

Day, S.J., Heleno Da Silva, S.I.N., Fonseca, J.F.B.D., 1999. A past giant lateral collapse and present-day flank instability of Fogo, Cape Verde Islands. J. Volcanol. Geotherm. Res. 94, 191–218. https://doi.org/10.1016/S0377-0273(99)00103-1

De Blasio, F.V., Elverhøi, A., Issler, D., Harbitz, C.B., Bryn, P., Lien, R., 2005. On the dynamics of subaqueous clay rich gravity mass flows - The giant Storegga slide, Norway. Mar. Pet. Geol. 22, 179–186. https://doi.org/10.1016/j.marpetgeo.2004.10.014

Deplus, C., Le Friant, A., Boudon, G., Komorowski, J.C., Villemant, B., Harford, C., Ségoufin, J., Cheminée, J.L., 2001. Submarine evidence for large-scale debris avalanches in the Lesser Antilles Arc. Earth Planet. Sci. Lett. 192, 145–157. https://doi.org/10.1016/S0012-821X(01)00444-7

Frey-Martínez, J., Cartwright, J., James, D., 2006. Frontally confined versus frontally emergent submarine landslides: A 3D seismic characterisation. Mar. Pet. Geol. 23, 585–604. https://doi.org/10.1016/j.marpetgeo.2006.04.002

Gee, M.J.R., Uy, H.S., Warren, J., Morley, C.K., Lambiase, J.J., 2007. The Brunei slide: A giant submarine landslide on the North West Borneo Margin revealed by 3D seismic data. Mar. Geol. 246, 9–23. https://doi.org/10.1016/j.margeo.2007.07.009

Glicken, H., 1996. Rockslide-debris avalanche of may 18, 1980, Mount St. Helens volcano, Washington. Open-file Rep. 96-677 1–5.

Gouhier, M., Paris, R., 2019. SO2 and tephra emissions during the December 22, 2018 Anak Krakatau flank-collapse eruption. Volcanica 2, 91–103. https://doi.org/10.30909/vol.02.02.91103

Grilli, S.T., Tappin, D.R., Carey, S., Watt, S.F.L., Ward, S.N., Grilli, A.R., Engwell, S.L., Zhang, C., Kirby, J.T., Schambach, L., Muin, M., 2019. Modelling of the tsunami from the December 22, 2018 lateral collapse of Anak Krakatau volcano in the Sunda Straits, Indonesia. Sci. Rep. 9, 1–13. https://doi.org/10.1038/s41598-019-48327-6

Holm, R.J., Richards, S.W., 2013. A re-evaluation of arc-continent collision and along-arc variation in the Bismarck Sea region, Papua New Guinea. Aust. J. Earth Sci. 60, 605–619. https://doi.org/10.1080/08120099.2013.824505

Honza, E., Miyazaki, T., Lock, J., 1989. Subduction erosion and accretion in the Solomon Sea region. Tectonophysics 160, 49–62. https://doi.org/10.1016/0040-1951(89)90383-1

Hornbach, M.J., Manga, M., Genecov, M., Valdez, R., Miller, P., Saffer, D., Adelstein, E., Lafuerza, S., Adachi, T., Breitkreuz, C., Jutzeler, M., LeFriant, A., Ishizuka, O., Morgan, S., Slagle, A., Talling, P.J., Fraass, A., Watt, S.F.L., Stroncik, N.A., Aljahdali, M., Boudon, G., Fujinawa, A., Hatfield, R., Kataoka, K., Maeno, F., Martinez-Colon, M., McCanta, M., Palmer, M., Stinton, A., Subramanyam, K.S. V., Tamura, Y., Villemant, B., Wall-Palmer, D., Wang, and F., 2015. Permeability and pressure measurements in Lesser Antilles submarine slides: Evidence for pressure-driven slow-slip failure. J. Geophys. Res. Solid Earth 120, 7986–8011. https://doi.org/10.1002/2015JB012061

Johnson, R., Kitts, S., Indies, W., Roobol, M.J., I, A.L.S., Wright, J. V, 1987. Large-scale volcanic cone collapse: the 1888 slope failure of Ritter volcano, and other examples from Papua New Guinea. Bull. Volcanol. 49, 669–679.

Johnson, R.W., 1977. Distribution and major-element chemistry of late Cainozoic vol-canoes at the southern margin of the Bismarck Sea, PNG. Aust. Bur. Miner. Resour. Geol. Geophys. Rep.188. 162 pp.

Karstens, J., Berndt, C., Urlaub, M., Watt, S.F.L., Micallef, A., Ray, M., Klaucke, I., Muff, S., Klaeschen, D., Kühn, M., Roth, T., Böttner, C., Schramm, B., Elger, J., Brune, S., 2019. From gradual

spreading to catastrophic collapse – Reconstruction of the 1888 Ritter Island volcanic sector collapse from high-resolution 3D seismic data. Earth Planet. Sci. Lett. 517, 1–13. https://doi.org/10.1016/j.epsl.2019.04.009

Karstens, J., Crutchley, G.J., Berndt, C., Talling, P.J., Watt, S.F.L., Hühnerbach, V., Friant, A. Le, Lebas, E., Trofimovs, J., 2013. Emplacement of pyroclastic deposits offshore Montserrat: Insights from 3D seismic data. J. Volcanol. Geotherm. Res. 257, 1–11. https://doi.org/10.1016/j.jvolgeores.2013.03.004

Karstens, J., Kelfoun, K., Watt, S.F.L., Berndt, C., 2020. Combining 3D seismics, eyewitness accounts and numerical simulations to reconstruct the 1888 Ritter Island sector collapse and tsunami. Int. J. Earth Sci. https://doi.org/10.1007/s00531-020-01854-4

Le Bas, T.P., Masson, D.G., Holtom, R.T., Grevemeyer, I., 2007. Slope failures of the flanks of the southern Cape Verde Islands. Submar. Mass Movements Their Consequences, 3rd Int. Symp. 337–345. https://doi.org/10.1007/978-1-4020-6512-5_35

Le Friant, A., Ishizuka, O., Boudon, G., Palmer, M.R., Talling, P.J., Villemant, B., Adachi, T., Aljahdali, M., Breitkreuz, C., Brunet, M., Caron, B., Coussens, M., Deplus, C., Endo, D., Feuillet, N., Fraas, A.J., Fujinawa, A., Hart, M.B., Hatfield, R.G., Hornbach, M., Jutzeler, M., Kataoka, K.S., Komorowski, J.C., Lebas, E., Lafuerza, S., Maeno, F., Manga, M., Martínez-Colõn, M., McCanta, M., Morgan, S., Saito, T., Slagle, A., Sparks, S., Stinton, A., Stroncik, N., Subramanyam, K.S.V., Tamura, Y., Trofimovs, J., Voight, B., Wall-Palmer, D., Wang, F., Watt, S.F.L., 2015. Submarine record of volcanic island construction and collapse in the Lesser Antilles arc: First scientific drilling of submarine volcanic island landslides by IODP Expedition 340. Geochemistry, Geophysics, Geosystems 16, 420–442. https://doi.org/10.1002/2014GC005652

Le Friant, A., Boudon, G., Deplus, C., Villemant, B., 2003. Large-scale flank collapse events during the activity of Montagne Pelée, Martinique, Lesser Antilles. J. Geophys. Res. Solid Earth 108, 1–15. https://doi.org/10.1029/2001jb001624

Lenz, B.L., Sawyer, D.E., Phrampus, B., Davenport, K., Long, A., 2019. Seismic imaging of seafloor deformation induced by impact from large submarine landslide blocks, offshore oregon. Geosci. 9. https://doi.org/10.3390/geosciences9010010

Løvholt, F., Harbitz, C.B., Haugen, K.B., 2005. A parametric study of tsunamis generated by submarine slides in the Ormen Lange/Storegga area off western Norway. Mar. Pet. Geol. 22, 219–231. https://doi.org/10.1016/j.marpetgeo.2004.10.017

Løvholt, F., Pedersen, G., Harbitz, C.B., Glimsdal, S., Kim, J., 2015. On the characteristics of landslide tsunamis. Philos. Trans. R. Soc. A Math. Phys. Eng. Sci. 373. https://doi.org/10.1098/rsta.2014.0376

Mangeney, A., Roche, O., Hungr, O., Mangold, N., Faccanoni, G., Lucas, A., 2010. Erosion and mobility in granular collapse over sloping beds. J. Geophys. Res. Earth Surf. 115, 1–21.

https://doi.org/10.1029/2009JF001462

Masson, D.G., Le Bas, T.P., Grevemeyer, I., Weinrebe, W., 2008. Flank collapse and large-scale landsliding in the Cape Verde Islands, off West Africa. Geochemistry, Geophys. Geosystems 9, 1–16. https://doi.org/10.1029/2008GC001983

Masson, D.G., Watts, A.B., Gee, M.J.R., Urgeles, R., Mitchell, N.C., Le Bas, T.P., Canals, M., 2002. Slope failures on the flanks of the western Canary Islands. Earth-Science Rev. 57, 1–35. https://doi.org/10.1016/S0012-8252(01)00069-1

Mohrig, D., Whipple, K.X., Hondzo, M., Ellis, C., Parker, G., 1998. Hydroplaning of subaqueous debris flows. Bull. Geol. Soc. Am. 110, 387–394. https://doi.org/10.1130/0016-7606(1998)110<0387:HOSDF>2.3.CO;2

Morita, S., Nakajima, T., Hanamura, Y., 2011. Submarine slump sediments and related dewatering structures: Observations of 3D seismic data obtained for the continental slope off Shimokita Peninsula, NE Japan. J. Geol. Soc. Japan 117, 95–98. https://doi.org/10.5575/geosoc.117.95

Mulder, T., Cochonat, P., 1996. Classification of offshore mass movements. J. Sediment. Res. 66, 43–57.

Ogata, K., Festa, A., Pini, G.A., Pogačnik, Lucente, C.C., 2019. Substrate deformation and incorporation in sedimentary mélanges (olistostromes): Examples from the northern Apennines (Italy) and northwestern Dinarides (Slovenia). Gondwana Res. 74, 101–125. https://doi.org/10.1016/j.gr.2019.03.001

Ogata, K., Mountjoy, J.J., Pini, G.A., Festa, A., Tinterri, R., 2014a. Shear zone liquefaction in mass transport deposit emplacement: A multi-scale integration of seismic reflection and outcrop data. Mar. Geol. 356, 50–64. https://doi.org/10.1016/j.margeo.2014.05.001

Ogata, K., Mutti, E., Pini, G.A., Tinterri, R., 2012. Mass transport-related stratal disruption within sedimentary mélanges: Examples from the northern Apennines (Italy) and south-central Pyrenees (Spain). Tectonophysics 568–569, 185–199. https://doi.org/10.1016/j.tecto.2011.08.021

Ogata, K., Pogačnik, Z., Pini, G.A., Tunis, G., Festa, A., Camerlenghi, A., Rebesco, M., 2014b. The carbonate mass transport deposits of the Paleogene Friuli Basin (Italy/Slovenia): Internal anatomy and inferred genetic processes. Mar. Geol. 356, 88–110. https://doi.org/10.1016/j.margeo.2014.06.014

Pope, E.L., Jutzeler, M., Cartigny, M.J.B., Shreeve, J., Talling, P.J., Wright, I.C., Wysoczanski, R.J., 2018. Origin of spectacular fields of submarine sediment waves around volcanic islands. Earth Planet. Sci. Lett. 493, 12–24. https://doi.org/10.1016/j.epsl.2018.04.020

Quinn, P.E., Diederichs, M.S., Rowe, R.K., Hutchinson, D.J., 2012. Development of progressive failure in sensitive clay slopes. Can. Geotech. J. 49, 782–795. https://doi.org/10.1139/T2012-034

Siebert, L., 1984. Large volcanic debris avalanches: Characteristics of source areas, deposits, and

associated eruptions. J. Volcanol. Geotherm. Res. 22, 163–197. https://doi.org/10.1016/0377-0273(84)90002-7

Siebert, L., Roverato, M., 2021. A Historical Perspective on Lateral Collapse and Volcanic Debris Avalanches, in: Roverato, M., Dufresne, A., Procter, J. (Eds.), Volcanic Debris Avalanches: From Collapse to Hazard. Springer International Publishing, Cham, pp. 11–50. https://doi.org/10.1007/978-3-030-57411-6_2

Silver, E., Day, S., Ward, S., Hoffmann, G., Llanes, P., Driscoll, N., Appelgate, B., Saunders, S., 2009. Volcano collapse and tsunami generation in the Bismarck Volcanic Arc, Papua New Guinea. J. Volcanol. Geotherm. Res. 186, 210–222. https://doi.org/10.1016/j.jvolgeores.2009.06.013

Sobiesiak, M.S., Kneller, B., Alsop, G.I., Milana, J.P., 2018. Styles of basal interaction beneath mass transport deposits. Mar. Pet. Geol. 98, 629–639. https://doi.org/10.1016/j.marpetgeo.2018.08.028

Taylor, B., 1979. Bismarck Sea: Evolution of a back-arc basin. Geology 7, 171–174. https://doi.org/10.1130/0091-7613(1979)7<171:BSEOAB>2.0.CO;2

Urlaub, M., Petersen, F., Gross, F., Bonforte, A., Puglisi, G., Guglielmino, F., Krastel, S., Lange, D., Kopp, H., 2018. Gravitational collapse of Mount Etna's southeastern flank. Sci. Adv. 4, 1–8. https://doi.org/10.1126/sciadv.aat9700

Van Der Merwe, W.C., Hodgson, D.M., Flint, S.S., 2011. Origin and terminal architecture of a submarine slide: A case study from the Permian Vischkuil Formation, Karoo Basin, South Africa. Sedimentology 58, 2012–2038. https://doi.org/10.1111/j.1365-3091.2011.01249.x

Walter, T.R., Haghshenas Haghighi, M., Schneider, F.M., Coppola, D., Motagh, M., Saul, J., Babeyko, A., Dahm, T., Troll, V.R., Tilmann, F., Heimann, S., Valade, S., Triyono, R., Khomarudin, R., Kartadinata, N., Laiolo, M., Massimetti, F., Gaebler, P., 2019. Complex hazard cascade culminating in the Anak Krakatau sector collapse. Nat. Commun. 10. https://doi.org/10.1038/s41467-019-12284-5

Ward, S.N., Day, S., 2003. Ritter Island Volcano - Lateral collapse and the tsunami of 1888. Geophys. J. Int. 154, 891–902. https://doi.org/10.1046/j.1365-246X.2003.02016.x

Watt, S.F.L., Karstens, J., Berndt, C., 2021. Volcanic-Island Lateral Collapses and Their Submarine Deposits, Advances in Volcanology. Springer International Publishing. https://doi.org/10.1007/978-3-030-57411-6_10

Watt, S.F.L., Karstens, J., Micallef, A., Berndt, C., Urlaub, M., Ray, M., Desai, A., Sammartini, M., Klaucke, I., Böttner, C., Day, S., Downes, H., Kühn, M., Elger, J., 2019. From catastrophic collapse to multi-phase deposition: Flow transformation, seafloor interaction and triggered eruption following a volcanic-island landslide. Earth Planet. Sci. Lett. 517, 135–147. https://doi.org/10.1016/j.epsl.2019.04.024

Watt, S.F.L., Talling, P.J., Vardy, M.E., Heller, V., Hühnerbach, V., Urlaub, M., Sarkar, S., Masson, D.G.,

Henstock, T.J., Minshull, T.A., Paulatto, M., Le Friant, A., Lebas, E., Berndt, C., Crutchley, G.J., Karstens, J., Stinton, A.J., Maeno, F., 2012a. Combinations of volcanic-flank and seafloor-sediment failure offshore Montserrat, and their implications for tsunami generation. Earth Planet. Sci. Lett. 319–320, 228–240. https://doi.org/10.1016/j.epsl.2011.11.032

Watt, S.F.L., Talling, P.J., Vardy, M.E., Masson, D.G., Henstock, T.J., H??hnerbach, V., Minshull, T.A., Urlaub, M., Lebas, E., Le Friant, A., Berndt, C., Crutchley, G.J., Karstens, J., 2012b. Widespread and progressive seafloor-sediment failure following volcanic debris avalanche emplacement: Landslide dynamics and timing offshore Montserrat, Lesser Antilles. Mar. Geol. 323–325, 69–94. https://doi.org/10.1016/j.margeo.2012.08.002

Weiß, B.J., Hübscher, C., Wolf, D., Lüdmann, T., 2015. Submarine explosive volcanism in the southeastern Terceira Rift/São Miguel region (Azores). J. Volcanol. Geotherm. Res. 303, 79–91. https://doi.org/10.1016/j.jvolgeores.2015.07.028

Woodhead, J., Hergt, J., Sandiford, M., Johnson, W., 2010. The big crunch: Physical and chemical expressions of arc/continent collision in the Western Bismarck arc. J. Volcanol. Geotherm. Res. 190, 11–24. https://doi.org/10.1016/j.jvolgeores.2009.03.003

Yoshida, H., Sugai, T., Ohmori, H., 2012. Geomorphology Size – distance relationships for hummocks on volcanic rockslide-debris avalanche deposits in Japan. Geomorphology 136, 76–87. https://doi.org/10.1016/j.geomorph.2011.04.044

4. Volcanic flank collapse, secondary sediment failure and flow-transition: multi-stage landslide emplacement offshore Montserrat, Lesser Antilles

Michel Kühn[1,2], Christian Berndt[1], Sebastian F. L. Watt[3], Matthew J. Hornbach[4,5], Sebastian Krastel[2], Kristina Sass[6], Steffen Kutterolf[1], Tim Freudenthal[6], Katrin Huhn[6], Jens Karstens[1], Bettina Schramm[7], Judith Elger[1], Christoph Böttner[8], and Dirk Klaeschen[1]

[1]GEOMAR Helmholtz Centre for Ocean Research Kiel, Kiel, Germany
[2]Institute of Geosciences, Kiel University, Kiel, Germany
[3]School of Geography, Earth and Environmental Sciences, University of Birmingham, Birmingham, United Kingdom
[4]Huffington Department of Earth Sciences, Southern Methodist University, Dallas, TX, USA
[5]United States Naval Research Laboratory, Stennis Space Center, MS, USA
[6]MARUM, University of Bremen, Bremen, Germany
[7]Federal Institute for Geosciences and Natural Resources, Hannover, Germany
[8]Institute for Geoscience, Aarhus University, Aarhus, Denmark

Key points

- Landslide emplacement offshore Montserrat included volcanic flank collapses, sediment incorporation, and a late-stage erosive flow
- Highly erosive flows are likely to be common processes during volcanic flank collapse deposition
- Pre-existing topography plays a major role in shaping flank collapse-associated mass transport deposits

Abstract

Volcanic flank collapses, especially those in island settings, have generated some of the most voluminous mass transport deposits on Earth and can trigger devastating tsunamis. Reliable tsunami hazard assessments for flank collapse-driven tsunamis require an understanding of the complex emplacement processes involved. The seafloor sequence southeast of Montserrat (Lesser Antilles) is a key site for the study of volcanic flank collapse emplacement processes that span subaerial to submarine environments. Here, we present new 2D and 3D seismic data as well as MeBo drill core data from one of the most extensive mass transport deposits offshore Montserrat, which exemplifies multi-phase landslide deposition from volcanic islands. The deposits reveal emplacement in multiple stages including two blocky volcanic debris

avalanches, secondary seafloor failure and a late-stage erosive density current, that carved channel-like incisions into the hummocky surface of the deposit about 15 km from the source region. The highly erosive density current potentially originated from downslope-acceleration of fine-grained material that is suspended in the water column earlier during the slide. Late-stage erosive turbidity currents may be a more common process following volcanic sector collapse than has been previously recognized, exerting a potentially important control on the observed deposit morphology, as well as on the runout and the overall shape of the deposit.

Plain language summary

Disintegration of volcanic islands can cause very large landslides and destructive tsunamis. To assess the tsunami hazard of such events, it is crucial to understand the processes that are involved in their formation. We present new insights from seismic data and drill cores from a landslide deposit offshore Montserrat, a volcanic island in the Lesser Antilles Arc in the Caribbean. Our analysis reveals the emplacement of landslide material in several stages, including multiple volcanic flank collapses, incorporation of seafloor sediments and an erosive flow that carved channels into the top of the deposit right after its emplacement. We suggest that highly erosive flows are a common process during volcanic flank collapse deposition and that they play a significant role in the shaping of the deposit's appearance.

4.1 Introduction

The devastating tsunamigenic collapse of Anak Krakatau, Indonesia, in December 2018 emphasized the potential of volcanic sector collapses to threaten coastal communities and infrastructure around volcanic islands. In the last 200 years, volcanic sector collapses have produced several destructive tsunamis and caused thousands of casualties around the world (Auker et al., 2013; Watt et al., 2021). The Anak Krakatau collapse in 2018 led to a tsunami with runup heights of up to 13 m at the coast of the Sunda Strait (Walter et al., 2019), even though the slide volume of 0.2 to 0.3 km^3 (Grilli et al., 2019) was relatively small in the context of many of the pre-historical sector collapse deposits mapped offshore volcanic islands globally (e.g., Moore and Normark, 1994). The largest historical tsunamigenic sector collapse was that at Ritter Island, Papua New Guinea, in 1888 (Ward and Day, 2003), which had an initial collapse volume of 2.4 km^3 (Karstens et al., 2019), while the geological record from offshore other volcanic islands revealed deposits involving tens or even hundreds of cubic kilometers of material (Krastel et al., 2001; Masson et al., 2006, 2002). However, the tsunami potential of a

volcanic landslide is not solely controlled by the volume of the sliding mass, but is influenced by both emplacement dynamics and bathymetric controls.

The emplacement of volcanic island flank collapse deposits on the adjacent seafloor involves a complex interplay of different geological processes, influenced by the dimensions, lithologies, geometry and position of this initial failure of the flank (in some instances subaerially), the extent of disintegration of the flank material, the interaction of the failed mass with the substrate, including the entrainment of pre-existing seafloor materials, and the runout, deceleration and compression of the distal collapse-derived deposits (Karstens et al., 2019; Masson et al., 2006; Watt et al., 2019). Given this complexity, collapse deposit morphology and volume cannot be related to tsunamigenic potential in a simple way. The most important controls on the magnitude of a collapse-generated tsunami are parameters such as the initial volume of the collapsing flank and its initial slide velocity during failure and emplacement, relative to water depth (Karstens et al., 2020; Løvholt et al., 2015; Ward, 2001). For adequate tsunami hazard assessments, we therefore need to understand how a submarine landslide changes size and velocity in both space and time during failure. In particular for ancient flank collapse deposits, without independent tsunami observations, a full understanding of tsunamigenic potential is reliant on being able to connect depositional characteristics and processes to tsunami generation. However, the characteristics (e.g., the origin from a single collapse versus the origin from multiple collapse events) of those deposits may obscure original landslide parameters (e.g., final or total deposit volume versus the initial volcanic flank collapse volume). Potential complexities in mass transport deposit emplacement include determining whether a collapse was a single- or multiphase event (Karstens et al. 2019, 2020; Watt et al. 2019), if secondary seafloor failure occurred (Barrett et al., 2020; Brunet et al., 2016; Crutchley et al., 2013; Le Friant et al., 2015), how much seafloor sediment was incorporated into the slide mass (Kühn et al., 2021; Ogata et al., 2019), and if more than one collapse event led to the final mass transport deposit.

Here we present an extensive new data set for one of the best studied submarine mass transport deposits resulting from volcanic flank collapse: Deposit 2 offshore Montserrat, Lesser Antilles (Lebas et al., 2011; Watt et al., 2012a). Deposit 2 is an elongated deposit showing indications for a volcanic flank collapse (Watt et al., 2015), secondary failure of preexisting seafloor sediments (Crutchley et al., 2013), and has also been separated into two subunits (2a/2b) by interpretation of an internal package of continuous reflections, suggesting that the deposit originated via at least two separate landslide events (Lebas et al., 2011; Watt et al., 2012b,

2012a). To advance our understanding of Deposit 2, as an exemplar of a complex mass transport deposit offshore a volcanic island, we combine high-resolution 2D and 3D seismic reflection data, sediment echosounder data and bathymetry with MeBo70 drill cores. The objectives are to re-evaluate the delimitation of individual events represented within Deposit 2 and to constrain the geological processes that produced these. Particular emphasis is put on the relative timing and interplay of these processes.

4.2 Geological Background

The island of Montserrat is located in the northern part of the Lesser Antilles volcanic arc, NW of Guadeloupe and SW of Antigua (Fig. 4.1, inset). The northern Lesser Antilles arc is formed by the subduction of the North American plate beneath the Caribbean plate with a present-day subduction rate of 2-4 cm/a (Bouysse and Westercamp, 1990; Grindlay et al., 2005). Volcanism on Montserrat migrated southward over time, from Silver Hills volcano in the north (2.6 Ma), via Centre Hills in the center of the island (0.95 to 0.55 Ma) to Soufrière Hills (alongside the South Soufrière Hills cone) < 0.17 Ma (Davis, 1924; Harford et al., 2002). The mainly andesitic Soufrière Hills most recently erupted between 1995 and 2010 (Wadge et al., 2014). This eruption produced a long-lived lava-dome that underwent several partial collapses, devastating large parts of the island and burying the capital, Plymouth under extensive pyroclastic deposits (Young et al., 1998). The eruption and collapse history of Soufrière Hills from 1995 onwards has been intensively documented (Herd et al., 2005; Le Friant et al., 2009; Sparks et al., 2002; Young et al., 1998).

The offshore topography SE of Montserrat is formed by the NNW-SSE striking Montserrat-Bouillante-Graben (Fig. 4.1; in the following, *M-B-Graben*), which is bordered to the SW by the Montserrat-Bouillante-Les Saints Fault System, to the NE by the Kahouanne Seamounts (Feuillet et al., 2010), and to the north by a broadly west-east striking headwall scarp (Crutchley et al., 2013).

Several surficial and buried mass transport deposits (Le Friant et al., 2004; Lebas et al., 2011), as well as pyroclastic flow deposits and turbidites have been mapped out around Montserrat in seismic, bathymetry and core data (Karstens et al., 2013; Le Friant et al., 2009; Trofimovs et al., 2008). One of the most intensively studied mass transport deposits is Deposit 2 (Coussens et al., 2016; Crutchley et al., 2013; Hornbach et al., 2015; Le Friant et al., 2004; Lebas et al., 2011; Watt et al., 2012b, 2012a). Deposit 2 is an elongated deposit located east and SE of Montserrat broadly following the slope of the M-B-Graben over an extent of roughly 30 km

(Lebas et al., 2011; Le Friant et al., 2004; Watt et al., 2012b) covering an area of ~200 km² (Watt et al., 2012a). The deposit extends from east of Soufrière Hills onshore to a broad chute in the submerged island flank. Volume estimates for Deposit 2 in previous studies vary between 8.4 km^3 (Lebas et al., 2011) and 9.5 km^3 (Watt et al., 2012b). Deposit 2 is divided into two subunits, Deposit 2a and Deposit 2b, by a package of continuous reflections in seismic data that can be traced over a distance of more than 15 km (Lebas et al., 2011). The central part of the deposit has a hummocky morphology, while the more distal part is rather smooth surfaced (Watt et al., 2012b). Crutchley et al. (2013) demonstrated (using 3D seismic data) that the headwall scarp, that limits the northern extent of Deposit 2 (Fig. 4.1), was formed by a seafloor sediment failure that was caused by the emplacement of Deposit 2 and incorporated into the main slide mass associated with the deposit. Le Friant et al. (2004) suggested a collapse of Soufrière Hills volcano as the potential origin of Deposit 2. Remotely Operated Vehicle (ROV) sampling and imagery confirmed that some of the steep-sided polygonal hummocks in the proximal part of Deposit 2, visible in bathymetry and seismic profiles, represent intact fragments of volcanic edifice material (Watt et al., 2015). Deposit 2 and the surficial, sub-circular Deposit 1 were targets of an International Ocean Discovery Program (IODP) drilling campaign in 2012 (Expedition 340 Scientists, 2013). During this campaign only a few meters of volcaniclastic material from Deposit 1 were recovered (Site U1393; Le Friant et al., 2015). Deposit 2 core material included a horizontally stratified and visually undisturbed sedimentary sequence within Deposit 2 (Site U1394; Le Friant et al., 2015), implying that the deposit contains incorporated units of intact seafloor material, alongside turbidite deposits that have been correlated with Deposit 2 based on thickness and stratigraphic relationships, beyond the southern limit of the deposit (Site U1395, Coussens et al., 2016).

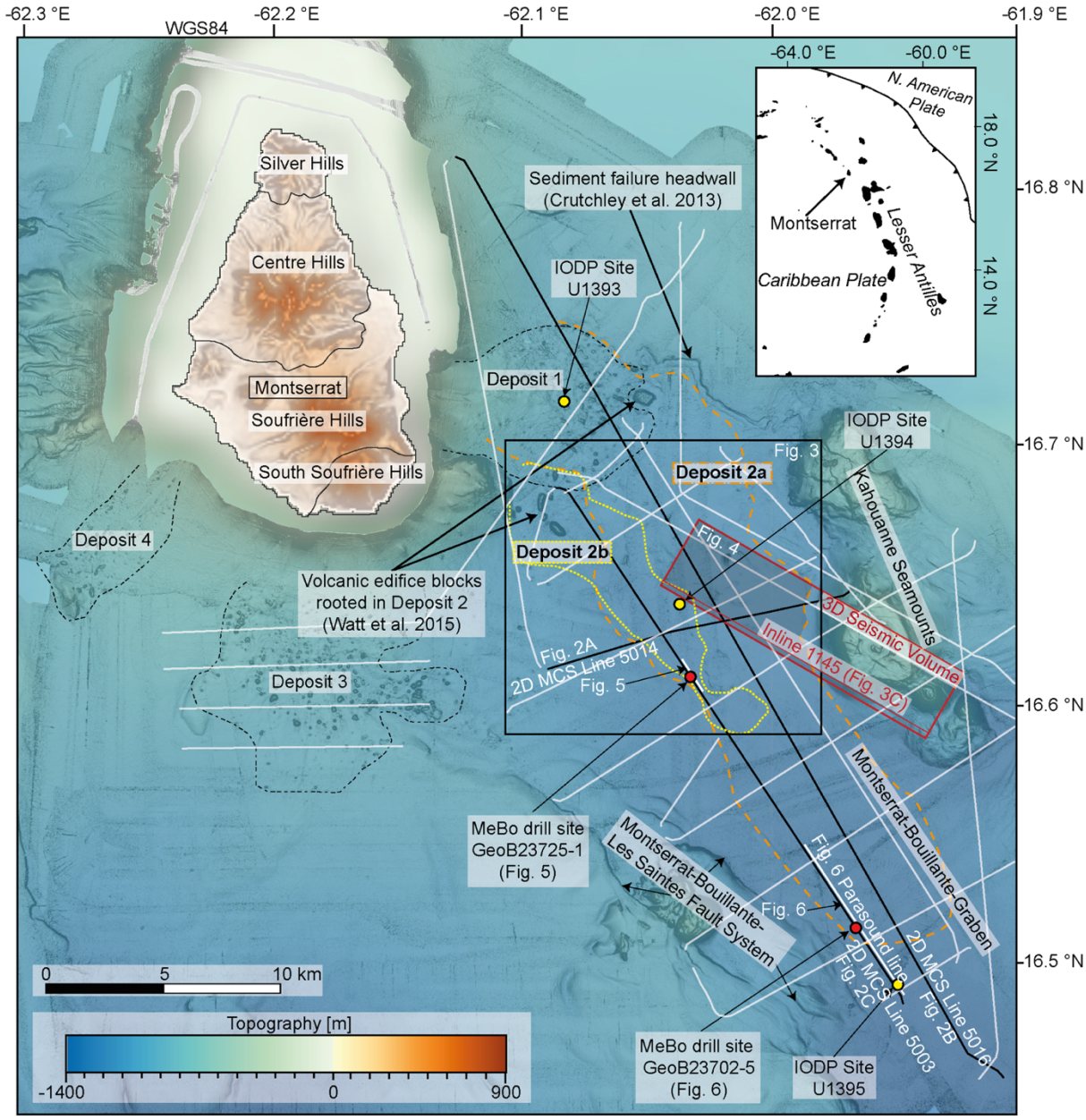

Figure 4.1: *Overview map of the survey area offshore Montserrat. The inset shows the location of Montserrat on the Lesser Antilles Arc. The main map shows Montserrat (SRTM topography) and the newly acquired high-resolution bathymetry data merged with a global GMRT grid (Ryan et al., 2009). The outlines of Deposit 2a and 2b are derived from our new seismic interpretation. White lines mark the newly acquired 2D seismic data, black lines mark the 2D seismic lines shown in Figure 4.2. The red rectangle outlines the newly acquired 3D seismic volume.*

4.3 Methods and Data

During cruise M154-1 aboard R/V METEOR in April 2019 we acquired 2D multichannel seismic data (Berndt et al., 2019; Kühn et al., 2023a), a 3D seismic volume (Berndt et al., 2019; Kühn et al., 2023b), Parasound echosounder data, and multibeam bathymetry (Berndt et al., 2019; Berndt et al., 2021). We collected additional Parasound echosounder data and multibeam bathymetry during M154-2 in April/May 2019, and conducted a drilling campaign with MARUM's MeBo70 seafloor drilling device (Huhn et al., 2019).

We collected 2D multichannel seismic data (Fig. 4.2) mainly with an 87.5 m-long (65 channels) active streamer system with a group spacing of 1.56 m and a 3.3 x 13 km 3D seismic data volume (Fig. 4.3, Fig. 4.4) with a P-Cable system. The acquisition geometry of the 3D seismic survey consisted of 14 to 16 12.5 m-long active sections with a group spacing of 1.54 m attached to a cross cable dragged perpendicular to the sail line direction with a streamer spacing of ~9 m (Berndt et al., 2019). These nominal streamer configurations changed repeatedly (Berndt et al., 2019). Two GI air guns (105/105 cubic inch) fired every five seconds as a seismic source. Before the seismic processing, we applied geometry corrections to the 3D seismic data based on direct wave first arrivals. A malfunction of the seismic source is visible over an extent of > 10 km on one profile in Figure 4.3C. Seismic data processing included binning (bin sizes: 1.54 m (2D) and 3.125 (3D)), trace editing, high-pass filtering (25 Hz cut and 55 Hz slope corner frequencies), denoising (anomalous amplitude attenuation, random noise attenuation, multiple attenuation by adaptively subtracting a multiple model obtained by time-shifting the original traces to the multiple arrival time), predictive deconvolution (to remove bubble noise), normal moveout correction (with 1511 m/s constant velocity model), stacking, post-stack trace interpolation to infill empty bins (3D only), and finite-difference migration. The velocity model for the migration was built with a velocity of 1511 m/s in the water column and a gradually increasing velocity of 1580 m/s at the seafloor reflection to 1725 m/s at the end of the traces). These velocities are adapted from an Ocean Bottom Seismometer (OBS) experiment during M154-1 (Kunde, 2020) by reducing the OBS velocities until diffraction hyperbola were successfully collapsed to their apices during migration. The vertical resolution of data is ~4 m (one quarter of the dominant wavelength, with a dominant frequency of ~100 Hz and a seismic velocity of 1580 m/s at the seafloor). Given the binning at 3.125 m (3D) and 1.54 m (2D) the horizontal resolution varies from 1.5 to 5 m from the seafloor to the lower boundary of imaging assuming an increase of migration velocity uncertainty with depth.

Multibeam bathymetry was acquired with a shipboard EM122 multibeam echosounder and gridded with a cell size of 10 m (Huhn et al., 2019). Parasound data were acquired parallel to the acquisition of 2D seismic lines with a dominant secondary frequency of 4 kHz and vertical resolution between 15 cm and 2% of the water depth (range provided by manufacturer). More detailed information on Parasound and multibeam bathymetry acquisition can be found in Berndt et al. (2019) and Huhn et al. (2019). See supporting information for uninterpreted data.

Volumes, vertical separations, and thicknesses of mass transport deposits and sediments in their vicinity were calculated with a seismic velocity of 1700 m/s derived from the OBS experiment (Kunde, 2020) consistent with seismic velocities measured during IODP Expedition 340 of 1650 to 1800 m/s obtained from volcanic layers and 1550 to 1650 obtained from background sediments (Le Friant et al., 2015). These velocity ranges indicate a numerical error of +/- 9% of our calculated volumes, separations, thicknesses. We used the same velocity for the integration of core observations and acoustic data. The most proximal portion of the deposits is not imaged with geophysical data. This implies that the stated volumes are minimum volumes. Based on the overall configuration of the slope stratigraphy with the deposits pinching out towards Montserrat and being more constricted on the upper slope, we assess that the missing volumes are small, i.e., less than 0.5 km^3. However, the proximal part of Deposit 2 suffers from lower imaging quality as seismic imaging is affected by the overlying Deposit 1. The similarity map shown in Fig. 4.4B was calculated using the Kingdom software with a temporal window length of 0.005 s. The similarity attribute analyses how similar a seismic trace looks compared to its neighboring traces and is widely used in seismic interpretation for the analysis of discontinuities in seismic reflections (Chopra and Marfurt, 2008). Here, similarity was calculated for the whole 3D seismic volume and similarity values were then extracted along the top boundary horizon of Deposit 2a. Volumes and extents outside of the 3D seismic volume result from interpolation of the picked horizons between 2D seismic profiles.

We used the seafloor drill rig MARUM-MeBo70 to retrieve sediment core samples of the stratigraphy offshore Montserrat, especially the mass transport deposit referred to as Deposit 2. Freudenthal and Wefer (2013) provide a detailed description of the MeBo70 system. This system recovered 55 mm diameter core samples with a wire-line coring technique and a stroke length per core barrel of 2.5 m. We drilled two holes into Deposit 2 at two different locations: GeoB23725-1 in central part and GeoB23702-5 in the distal part of the slide deposit (Fig. 4.1). As expected from Expedition 340 (Le Friant et al., 2015), coarse grained sandy sediments were hard to drill and intruded into the borehole frequently. For this reason, large parts of the drill

length were washed and 17 m of core were retrieved in total (Huhn et al., 2019). Drilling depth is given in meters below the seafloor (mbsf). Core parameters and recoveries are given in Table 1.

Table 4.1: *MeBo70 drill sites included in this study.*

Drill site	Latitude	Longitude	Drill Depth (mbsf)	Coring Length (mbsf)	Recovery (m)	Recovery (%)
GeoB23702-5	16°30.883‘ N	-61°58.038‘ W	30.30	25.71	14.62	57
GeoB23725-1	16°36.728‘ N	-62°02.032‘ W	41.00	4.00	1.92	48

4.4 Results

4.4.1 Seismic and hydroacoustic data

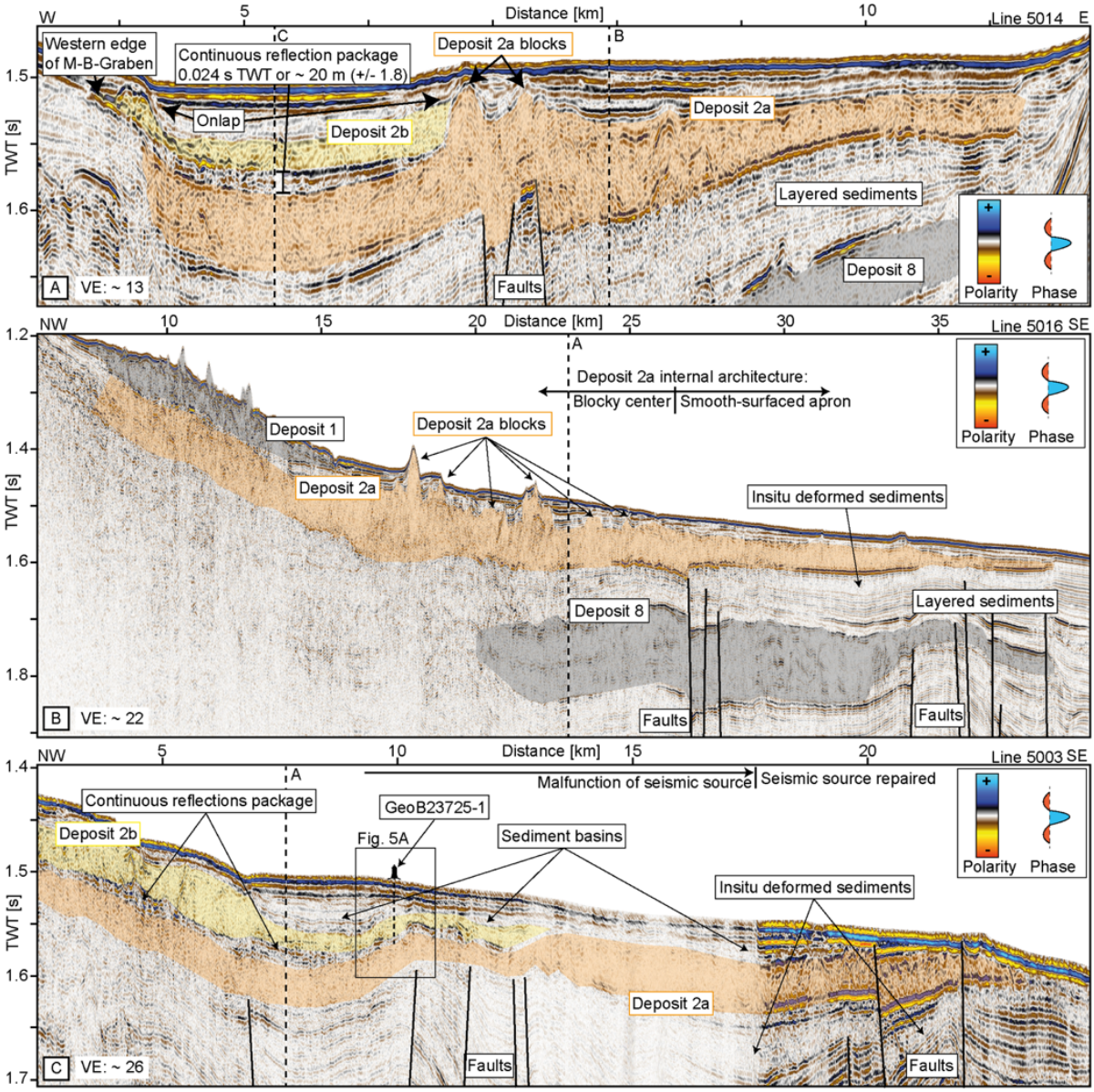

Figure 4.2: *Newly acquired 2D multichannel seismic profiles. A: Seismic profile 5014 crossing the M-B-Graben and Deposit 2. Deposit 2a (orange) has a blocky center but smoother-surfaced apron west and east of the central blocks. The bottom boundary of the central part is affected by a series of extensional faults. A package of continuous reflections separates 2a and 2b (yellow). The blocks in Deposit 2a and the western edge of the M-B graben form a topographic depression where Deposit 2b is located. B: Seismic profile along the M-B-Graben. In the proximal domain, Deposit 2a is overlain and overprinted (and likely partly eroded) by Deposit*

1. In the center, Deposit 2 blocks breach the seafloor. Downslope of the blocks the surface of Deposit 2 is smooth, while the amplitude of the base reflection is generally increasing with distance. C: Seismic profile cutting Deposit 2b and the western edge of Deposit 2a. The continuous reflections between both deposits extend more than 12 km. The morphology is strongly controlled by normal faults within the graben that offset and cut Deposit 2. Topographic depressions above both slide deposits show continuous seismic reflections consistent with the stratified seismic facies.

4.4.1.1 Seismic configuration

In the seismic dataset from offshore Montserrat, we interpret two distinct seismic facies consistent with the seismic facies definitions and descriptions in Lebas et al. (2011) and Watt et al. (2012b). The main seismic facies consists of lateral continuous and coherent, mostly (sub-) parallel seismic reflections with generally consistent amplitudes along the reflection's spatial extent. This seismic facies likely represents stratified and layered sediments. In the following we refer to this seismic facies as stratified sediment facies. The second seismic facies comprises partly chaotic, discontinuous, and relatively transparent (i.e., low amplitude) reflections. The top and bottom reflections of this seismic facies are generally of higher amplitude and coherency than the chaotic internal reflections. This seismic facies represents mass transport/landslide deposits and in the following we refer to it as landslide facies. The internal structures of Deposit 2 and the outlines of Deposit 2a and 2b have been refined here, with the differences from prior interpretations explained in Section 5.1.

The seismic data presented here provide insight into the shallow (upper ~500 m) stratigraphy of the M-B-Graben with the stratified sediment facies repeatedly interrupted by and interbedded with the landslide facies in discrete horizontal packages of variable extent and thickness (Fig. 4.2A-C,4.3C, 4.4C-D, 4.5A). The surfaces of the landslide facies units are partly hummocky in their centers (e.g., Fig. 4.2A-B) and partly flat and coherent around these centers (Fig. 4.2A-C, 4.3C, 4.4C-D). Correlation of the landslide facies units with interpretations from earlier studies that used different datasets (Lebas et al., 2011; Le Friant et al., 2004; Watt et al., 2012b) allows an attribution to the Deposits 1, 2a, 2b and 8. Lebas et al. (2011) provide overview maps of legacy seismic data collected offshore Montserrat, defining these various deposits. In the following we address specific landslide facies units within these previously established deposits. Our analysis is focused on Deposit 2a and Deposit 2b.

Extensional faults cut through the stratigraphy and offset entire sediments bodies (e.g., Deposit 8, Fig. 4.2B) and appear to influence the basal surface topography of more recent events (e.g., Deposit 2a, Fig. 4.2B). Topographic depressions formed by faulting or between hummocks are infilled with the stratified sediment facies with onlapping reflections (e.g., Fig. 4.2A).

Table 4.2: *Deposit 2 characteristics in literature and in this study.*

Reference	Area (km^2)	Runout (km)	Thickness (m)	Volume (km^3)	Age (ka)
Le Friant et al., 2004	200 (total)	30 (total)	40–50 (total)	-	112-130
Lebas et al., 2011	190 (total)	30 (total)	58–64 (total)	8.4–9.2 (total)	~233
Watt et al., 2012b	212 (total) 84 (Deposit 2a) 181 (Deposit 2b)	23 (Deposit 2a) 34 (Deposit 2b)	45 (total) 39 (Deposit 2a) 35 (Deposit 2b)	9.5–10.3 (total) 3.2–3.5 (Deposit 2a) 6.3–6.8 (Deposit 2b)	~140
Le Friant et al., 2015	-	-	-	-	138 (Deposit 2; Deposit 2b in this study)
This study	183 km^2 (Deposit 2a) 37 km^2 (Deposit 2b)	32 (Deposit 2a) 15 (Deposit 2b)	~43 (Deposit 2a) ~30 (Deposit 2b)	9.9 (total) 8.9 (Deposit 2a) 1.1 (Deposit 2b)	~318 (Deposit 2a)*

*based on the age dating of Deposit 2b in Le Friant et al (2015).

4.4.1.2 Deposit 2a

The internal seismic character of Deposit 2a is generally defined by the landslide facies. The deposit has an elongated shape and covers an area of 183 km^2 with a volume 8.9 km^3 (+/- 0.4). The thickness of the deposit is variable, with the greatest thickness of more than 180 m (+/- 16), at the deposit's center, a median thickness of 43 m (+/- 2), thinning out in the most distal part and at the deposit's sides. The northern limit of Deposit 2a is defined by a sediment failure headwall (Fig. 4.1), where the truncation of seafloor strata has been previously interpreted to reflect sediment failure that occurred concurrent with volcanic flank collapse emplacement (Crutchley et al., 2013; Watt et al., 2012a, 2012b).

The chaotic internal seismic character of Deposit 2a is broadly consistent over its extent. However, the morphology of the surface can be used to gain insight into its internal architecture. Based on the morphology we divide it into two structural domains: A V-shaped blocky center that is characterized by up to 180 m (+/- 9) high blocks protruding through the seafloor (Fig. 4.2B,4.4D), with an irregular, rough surface that is elevated from its surroundings by several tens of meters, with sharp lateral margins defining a shape that narrows towards the SE (Fig. 4.3A). This blocky center (outlined in Fig. 4.3A) has a volume of 5.2 km^3 (+/- 0.3). The surface of this blocky deposit, examined in detail using the new 3D seismic volume, reveals features not previously resolvable in the mass transport deposits offshore Montserrat. The images reveal a complex system of 100- to 1000-m wide channels incised into the top of the blocky surface, with a NW to SE direction in the 3D seismic volume, and with a consistent gradient to the SE (Fig. 4.4). A main channel opens up into three radially distributed sub-channels widening towards the marginal part of the system, coinciding with the limits of the blocky deposit. The observable length of the individual sub-channels combined with the main channel is 2.5 to 3 km (Fig. 4.4A). Since the extent of the imaging of the main channel is limited in the NW by the extent of the 3D seismic volume, the channel system may be sourced from more proximal parts of the blocky deposit, but this area is only covered by sparsely spaced 2D seismic profiles, where the extent of the channel system cannot be tracked due to the more limited spatial coverage. Beyond the blocky central part of Deposit 2a, the channels appear to have an outflow to the SE (Fig. 4.4B), into a portion of the deposit with a smoother surface: the second structural domain of Deposit 2a. We observe reflections characterized by the stratified sediment facies within the channels (Fig. 4.4B, 4C, 4D). This infill is limited to the channels without any indications of a drape over the channel margins, with a maximum thickness of up to 30 m (+/- 1.5) in the northwesternmost part of the main channel.

The smooth surfaced domain of Deposit 2a, which extends as an apron around the southern limits of the blocky central domain (Fig. 4.3, 4), has a volume of 3.7 km^3 (+/- 0.2). In the 2D seismic data this domain is generally defined by the landslide facies. In the Parasound echosounder data, most of Deposit 2a is transparent and no internal reflections are visible (Fig. 4.6A). However, the 3D seismic data shows a transition of the landslide facies to a more transparent (i.e., low amplitude) sub-facies of the stratified sediment facies towards SE (Fig. 4.3C).

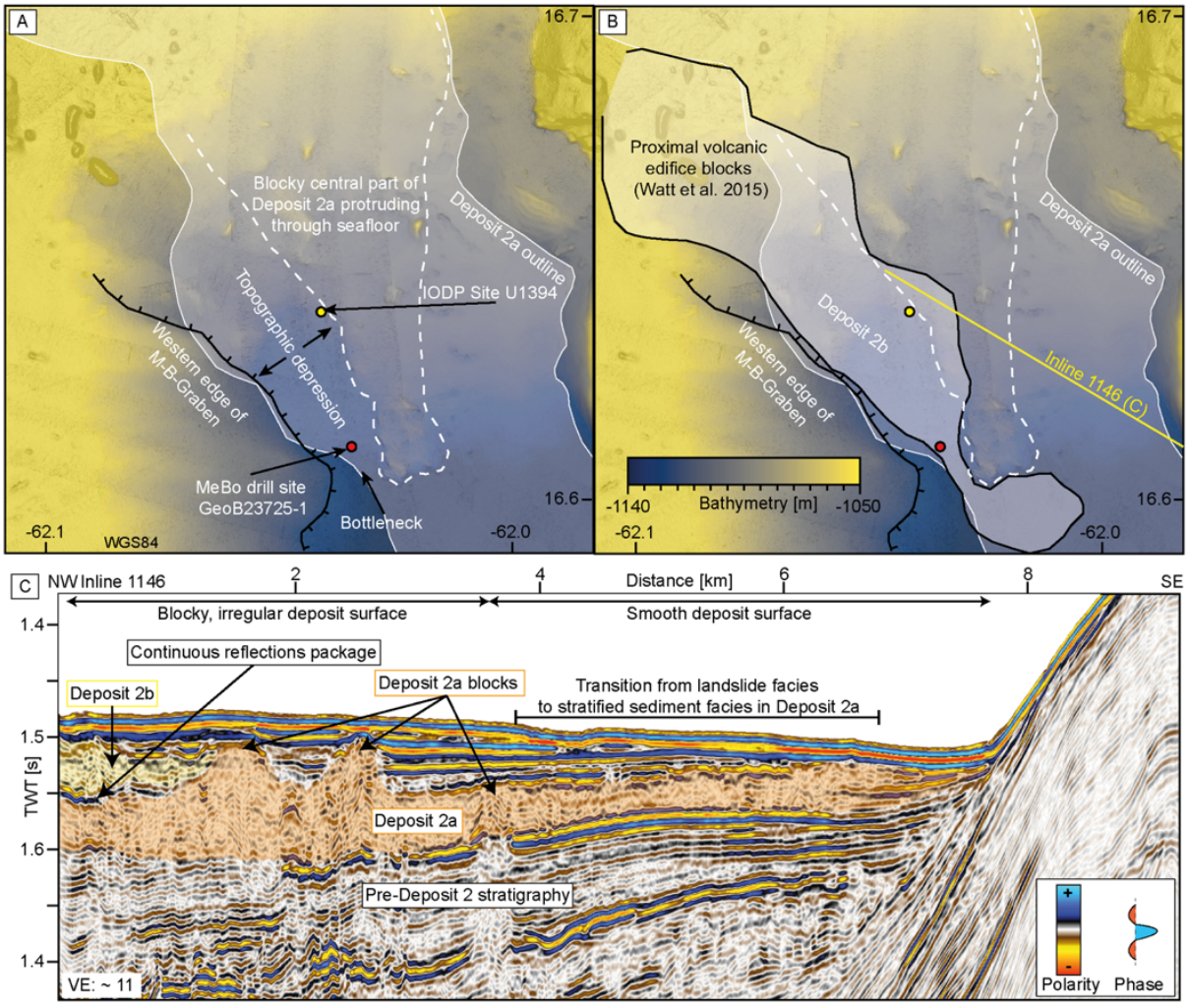

Figure 4.3: *Morphology of the central Deposit 2. A: The blocky center of the Deposit 2a is clearly elevated from the adjacent sediments and forms an elongated chute with the western edge of the M-B-graben. B: The outline of Deposit 2b shows that it was deposited in the chute described in A. Once the associated slide passed the bottleneck at the most distal block accumulation it was emplaced in a sub-circular shape. C: Inline 1146 from the 3D seismic volume revealing the internal seismic architecture of Deposit 2.*

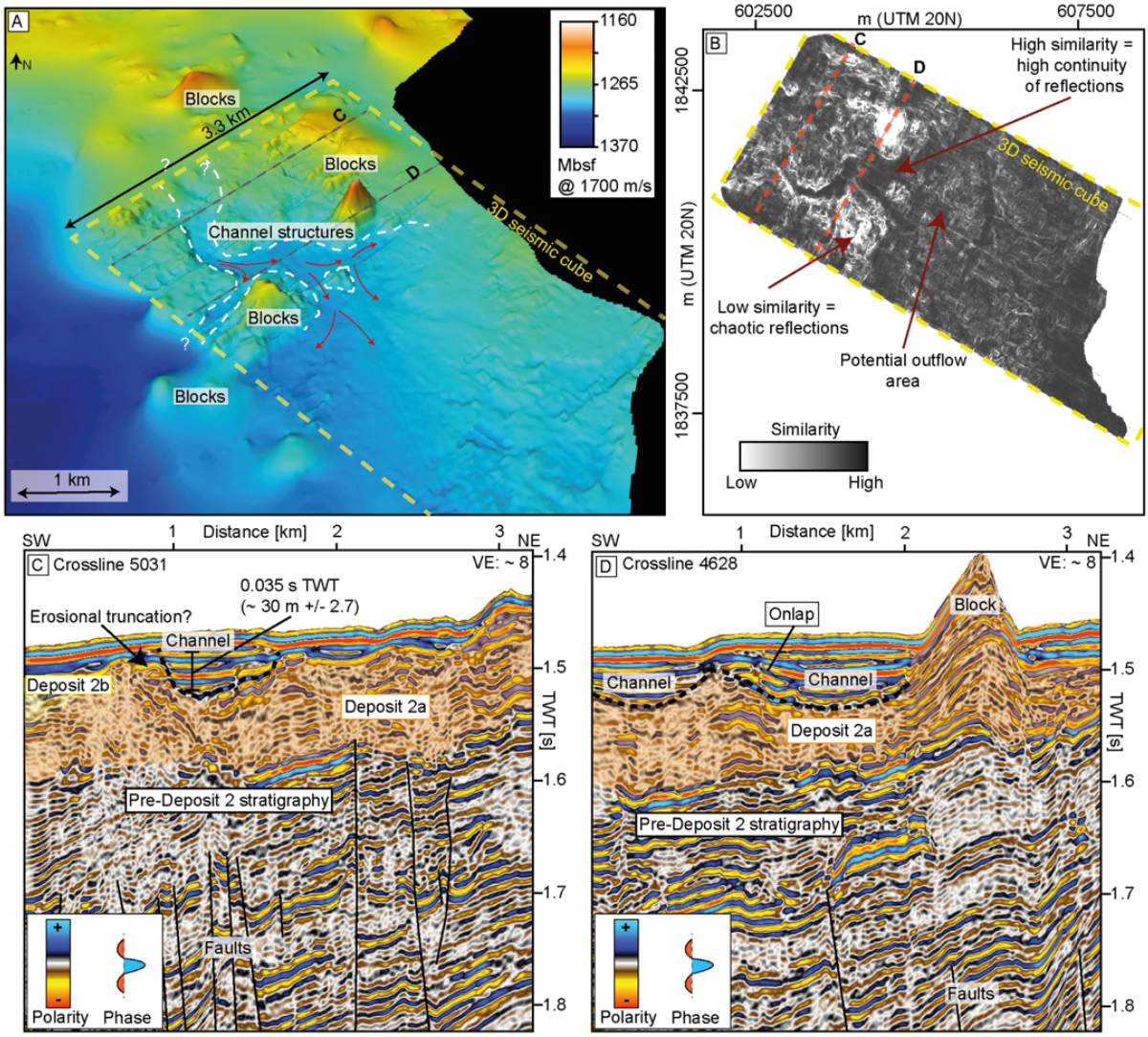

Figure 4.4: *3D seismic analysis of the top surface of Deposit 2a. A: 3D surface of Deposit 2a reveals channel structures incised on top of the deposit (black lines). Depths were calculated with a constant velocity of 1700 m/s. B: Similarity map of Deposit 2a's surface extracted from the 3D seismic volume. C: Crossline 5031 from 3D seismic volume showing Deposit 2a (orange), the eastern edge of Deposit 2b (yellow) and the 30 m deep channel incised into the blocky center of Deposit 2a. D: Crossline 4628 from 3D seismic volume showing Deposit 2a (orange) and two shallower channels incised into it.*

4.4.1.2 Deposit 2b

The relief of the blocky center of Deposit 2a and the western edge of the M-B-Graben form an approximately 3 km-wide elongated topographic depression (Fig. 4.2A, 4.3), which was infilled

by Deposit 2b. The internal seismic character of Deposit 2b is represented by the landslide facies. Deposit 2b covers an area of ~37 km^2 (Fig. 4.3B) with a volume of 1.0 km^3 (+/- 0.05). The deposit's shape is generally elongated (Fig. 4.3B), up to 4.5 km wide closer to Montserrat and gradually narrowing towards its distal margin. Where the most distal blocks of Deposit 2a and the western edge of the M-B-Graben form a bottleneck (Fig. 4.3B), Deposit 2b is only 0.4 km wide, but the deposit radiates south of this bottleneck in a 2.4 km wide, sub-circular shape (Fig. 4.3B). The thickness of Deposit 2b gradually decreases from a 30 m (+/- 1.5) median in its proximal parts to a 20 m (+/- 1) median at the deposit's toe. The morphology of the proximal Deposit 2b is shaped by a field of up to 800 m wide and up to 180 m (+/- 16.2) high blocks protruding through the present seafloor. Beyond the proximal blocks, the deposit has a slightly hummocky surface that contrasts with the smooth surface of the Deposit 2a apron (Fig. 4.3A, B). Some seismic reflectivity in Deposit 2a (Fig. 4.2B) may be interpreted as the boundary between Deposit 2a and a younger deposit. However, this is not consistent with that boundary being part of Deposit 2b, because the overall shape of Deposit 2b indicates a transport pathway farther west, and we propose that the associated slide bypassed this area.

4.4.1.3 Continuous reflections package

The continuous reflections package that defines the separation of Deposit 2a and 2b in the western parts of Deposit 2 (Watt et al., 2012a) has a seismic character defined by the stratified sediment facies. This unit is up to 20 m (+/- 1) thick. We picked the seismic reflections from a distance of 6 km away from the southeastern shore of Montserrat up to a distance of 13 km in southeastern direction (Fig. 4.2A, C). The shape of the reflections package broadly corresponds with the elongated shape of Deposit 2b. This unit is limited to the topographic depression formed by the edge of the M-B-Graben to the SE and by the blocks of the central Deposit 2a to the east.

4.4.2 MeBo drill core results

In order to constrain the lithologies within and around Deposit 2 we draw on MeBo drilling at a proximal site, where Deposit 2b, the continuous reflections package and Deposit 2a overlap (GeoB23725-1), ~3 km south of Site U1394, and at a site in the distal part of Deposit 2a (GeoB23702-5), ~3km NW of Site U1395. The retrieved cores provide insight into the lithological composition of the Deposit 2 subunits and add to the interpretation of processes that led to the seismic characteristics described in the previous subsection.

4.4.2.1 GeoB23725-1 drill core results

GeoB23725-1 (Fig. 4.5) was drilled in a water depth of 1127 m in a topographic depression between the blocky center of Deposit 2a and the western edge of the M-B-Graben ~15 km SE of Montserrat. Drilling was conducted to a depth of 41 mbsf (Table 1). With the overarching aim to sample different sections of Deposit 2, large parts were flushed down without intentional coring to avoid the drill tool getting stuck in the coarse and heterogeneous sediment at this site. A seafloor section from 0 to 1.07 mbsf was located above (seismically defined) Deposit 2b and we do not further analyze it in this study. The other recovered material was from two short sections, which provide insights into the internal composition of Deposit 2b, from 25.30 to 25.85 mbsf (including core catcher) (Fig. 4.5C), and the continuous reflections package from 40.30 to 40.58 mbsf (including core catcher) (Fig. 4.5D). Core recovery was 48% in these sections. The core interval from 25.30 to 25.85 mbsf was located within Deposit 2b (Fig. 4.5A) and comprises mixed-component volcanic gravels with cm-sized silt and sand intraclasts, and pumice intraclasts in the lowermost 2 cm (Fig. 4.5C). Although core recovery from Deposit 2b within the prior IODP cores at Site U1394 was extremely low, isolated sections recovered in the core catcher retrieved volcanic clasts, sand and hemipelagic mud (Coussens et al., 2016). Based on our observation of mixed marine sediment intraclasts within volcaniclastic gravels, the recovered material from Site U1394 is consistent with our new observations of Deposit 2b. The bottommost core interval from 40.30 to 40.58 mbsf was located at the base of the continuous reflections package separating the seismic units of Deposit 2b and Deposit 2a (Fig. 4.5D). This interval comprises fine to medium sand, mixed sand and clay clasts, silty clay and laminated silts. The lowermost 2 cm of the core catcher material comprise fine sandy silt with volcanic gravel and pumice. Coring of the continuous reflections package was not previously successful during IODP drilling of the equivalent section at Site U1394, although the underlying Deposit 2a had good recovery, comprising hemipelagic muds interbedded with compositionally varied turbidites (Le Friant et al., 2015; Coussens et al., 2016), indicating that Deposit 2a at this location was comprised of the local marine stratigraphy.

4.4.2.2 GeoB23702-5 drill core results

GeoB23702-5 (Fig. 4.6) was drilled ~27 km SE of Montserrat in a water depth of 1170 m to a depth of 30.30 mbsf (Table 1). Sections retrieved from a depth of 0 to 3.24 mbsf comprise flat-lying hemipelagic mud with frequent thin, horizontal volcaniclastic medium to fine sands, interbedded with mixed volcaniclastic and bioclastic sands, silty clay layers, and discontinuous

sand and mud patches (Fig. 4.6B). This is consistent with the lithologies found in the shallowest sections at the previously drilled IODP Site U1395 (Coussens et al., 2016). From 5.30 to 9.40 mbsf, GeoB23702-5 comprises flat-lying hemipelagic mud overlying mixed volcaniclastic and bioclastic sands and silty clay layers, with patchy sands and rounded mud clasts. Although this is generally consistent with the hemipelagic mud-dominated lithology found at Hole U1395B, core recovery with MeBo was very low within the upper 10 mbsf (Fig. 4.6C, inset) and we do not observe several of the shallow turbidites described in Coussens et al. (2016) and Le Friant et al. (2015) due to this poor recovery. The correlation between the Parasound line 5003 and GeoB23702-5 (Fig. 4.6) allows us to identify the position of Deposit 2a within 9.4 to 21 mbsf, where we observe a sharp transition from horizontal beds to deformed beds (Fig. 4.6D), within a similar set of lithologies to the overlying beds. The deformation is evident as distorted beds and structureless sections (with similar color, grain-size and compositional characteristics to the upper stratigraphy), and as tilted beds in the central part of this section (Fig. 4.6E). Comparable deformation in the distal part of a mass transport deposit was observed at Sites U1399 and U1400 offshore Martinique where tilted beds broadly correspond to thrust and fold structures in seismic data (Brunet et al., 2016), within the outer parts of a large mass transport deposit comparable in overall form to Deposit 2. The lower part of Deposit 2a in GeoB23702-5 contains distorted and folded beds with pods of volcaniclastic gravel and sand. In its lowermost interval, this contains a ~50 cm thick layer of volcaniclastic coarse sand grading up into an upper layer of volcaniclastic gravel, at a depth of 20.30 to 20.89 m (Fig. 4.6F). The pre-Deposit 2a stratigraphy contains mostly hemipelagic background mud with a variety of thin, flat lying beds similar in character to those of the sediment above Deposit 2: volcaniclastic sands, and beds of fine sand with a mixture of volcaniclastics and bioclasts. The pre-Deposit 2a unit at ~24 m (Fig. 4.6B) is distinctive in being coarse grained and pumice rich, contrasting with the dark volcaniclastic sands and gravels that are dominant offshore Montserrat (cf. Trofimovs et al., 2013). This unit is consistent with the stratigraphic sequence in the previously drilled IODP Hole U1395B (Coussens et al., 2016), supporting a correlation between the two sites (Fig. 4.6). In Hole U1395B, the next volcaniclastic horizon above the pumice is a dark volcaniclastic coarse sand to gravel, which we correlate with the coarse sand at the base of Deposit 2a at site GeoB23703-5 (as defined in Fig. 4.6). In Hole U1395B, this is separated by ~25 cm of hemipelagite from an overlying very thick turbidite, containing volcaniclastic sands and gravels, with deformed hemipelagite and multiple graded units (best recovered in Hole U1395A), and spanning ~8 m. This very thick turbidite is clearly imaged in our Parasound data (Fig. 4.6A) with a thickness and stratigraphic position consistent with the core stratigraphy at

Site U1395. Taken together, these observations suggest that the coarse volcaniclastic sand to gravel that defines the base of Deposit 2 at GeoB23703-5 represents a discrete high-energy event that preceded Deposit 2 emplacement.

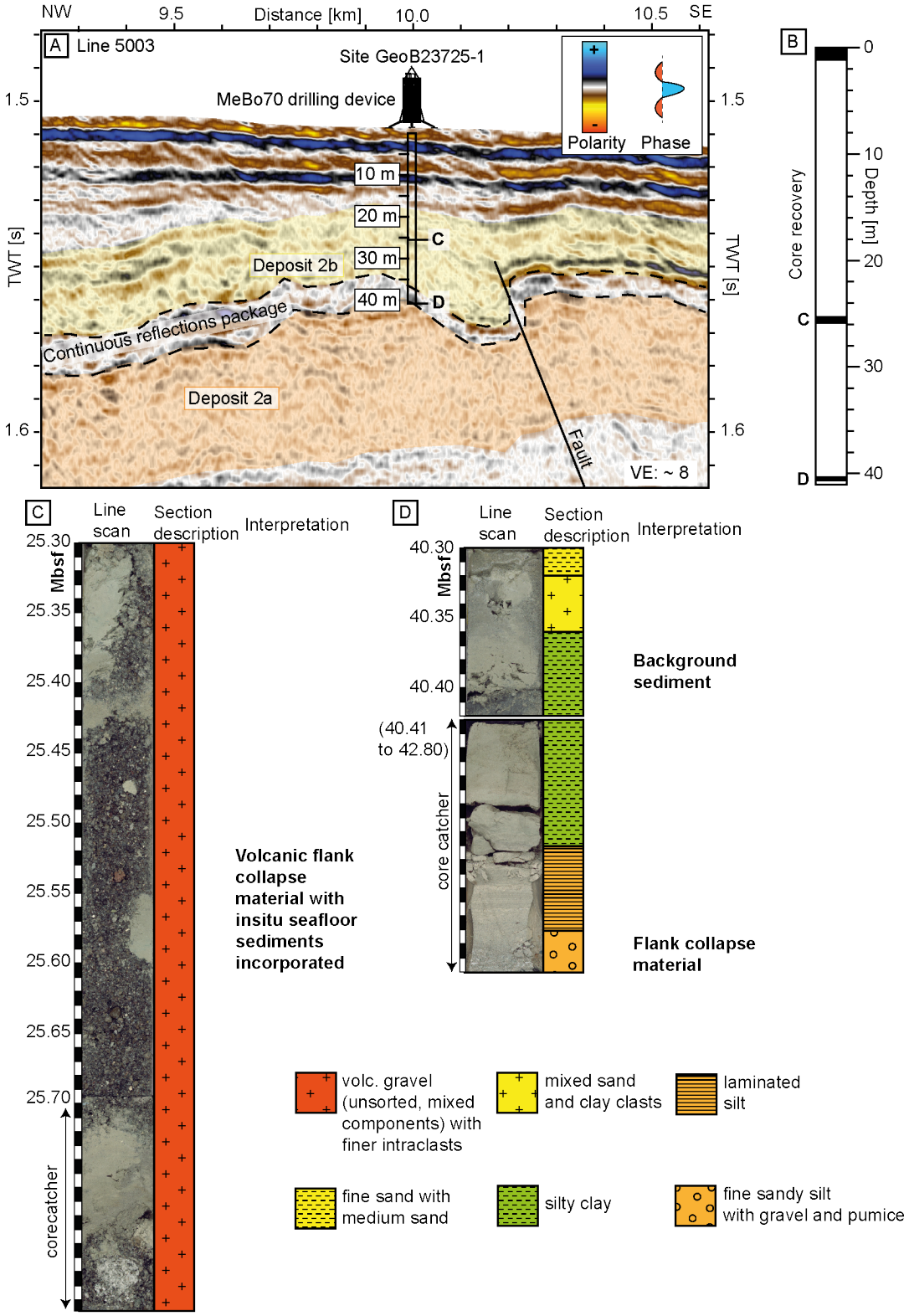

Figure 4.5: *A: Seismic line 5003 cutting the Deposit 2a-/2b sequence from NW to SE with the location of MeBo drill site GeoB23725-1. B: Core recovery at the drill site. White intervals indicate no core recovery. The topmost coring interval is not presented in this study. C: Core photography alongside stratigraphic logs and facies interpretation. Deposit 2b comprises*

volcanic flank collapse material with insitu incorporated seafloor sediments, the continuous reflections unit comprises background sediments. Deposit 2a could not be penetrated at this drill site.

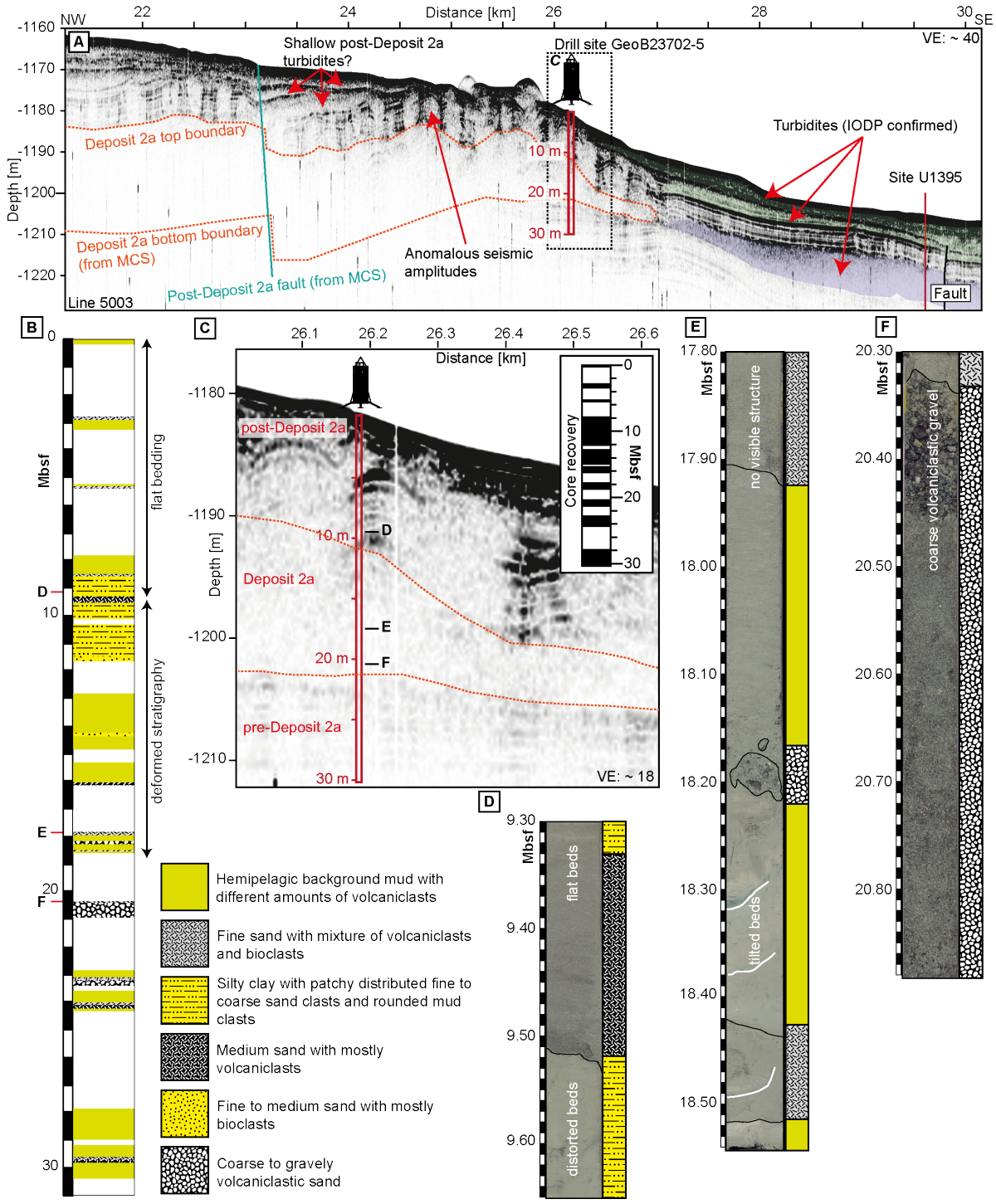

Figure 4.6: *A: Parasound echosounder profile parallel to 2D MCS line 5003 with MeBo drill site GeoB23702-5 location. Most parts of Deposit 2a are acoustically transparent in the echosounder, except the southeasternmost km showing deformed stratigraphy with flat lying*

stratigraphy below the deposit's bottom boundary. B: Stratigraphic log for drill site GeoB23702-5. C: Zoomed snippet of A. Internal stratification within Deposit 2a is visible. Inset: Core recovery. White intervals indicate no core recovery. D-F: Core photographies alongside corresponding stratigraphic logs.

4.5 Discussion

4.5.1 Volume and shape differences in respect to previous studies

Volume, vertical distance, and thickness calculations require the conversion of seismic TWT to depth involving specific seismic velocities. For this study, we used a constant seismic velocity of 1700 m/s (Kunde, 2020) which was derived from an OBS experiment that targeted Deposit 2. The value is within the range of velocities measured during Expedition 340 between 1550 m/s minimum for hemipelagic background sediments and 1800 m/s maximum for volcanic deposits (Le Friant et al., 2015). The uncertainty in this conversion velocity implies an uncertainty of the calculated vertical distances of +/- 9%. Given the fact that the MeBo cores presented here (e.g., Fig. 4.4C) and also the cores from IODP Expedition 340 (e.g., Le Friant et al., 2015) and the new OBS data provide a consistent velocity range, and because of the interlayering of background sediments with volcaniclastic turbidites and mobilized clasts of background sediments within volcaniclastic units, it is prudent to use this average value for all depth conversions. The new volumes presented in this study are therefore more robust than previous estimations for which no independent seismic velocity information was available. This has to be taken into account when comparing the new volumes to previously published results. In addition to the uncertainty from the seismic velocity, there are some uncertainties and error sources that are less quantifiable: (1) Large parts of the volumes and thicknesses were calculated with seismic horizons that were interpolated between 2D seismic lines, sometimes over several kilometers. (2) The derived volumes neglect erosional processes and do not include turbidites beyond the data resolution or data limits creating a bias towards smaller volumes. (3) There will be subjective choices of the seismic interpreter regarding the identification of horizons (Clare et al., 2019), but the new denser data reduce these uncertainties. In spite of these limitations our calculated Deposit 2 volume of 9.9 km^3 (+/- 0.9) is broadly consistent with previous studies (Lebas et al. 2011: 8.4 km^3, Watt et al. 2012b: 9.5 km^3; Table 2). However, the volumes for the sub-units Deposit 2a (8.9 km^3 +/- 0.8) and 2b (1.0 km^3 +/- 0.09) are markedly different: Watt et al. (2012a) attribute a volume of 3.2 km^3 to Deposit 2a and 6.3 km^3 to Deposit 2b (Table 2). This discrepancy with our new results is mostly caused by the increased spatial

resolution of the new, closely spaced 2D seismic data as well as the 3D seismic volume from M154-1. These data allow us to trace the continuous reflections package and hence Deposit 2b in greater detail compared to earlier studies. For completeness, we tied the new interpretations to the previous interpretations based on previously available (expedition JC45) seismic data (Lebas et al., 2011; Watt et al., 2012;). The 3D seismic volume allows precise reconstruction of the central blocky region of the deposit into the zone of 2D seismic coverage. This leads to a more precise and narrower outline of Deposit 2b, and to the assignment of the eastern and southernmost part of Deposit 2 to Deposit 2a rather than 2b. This assignment has profound implications for the interpretation of the emplacement mechanisms and the sequence of events represented by Deposit 2.

4.5.2 Multi-stage emplacement of Deposits 2a and 2b

Deposit 2b is separated from Deposit 2a by an up to 20 m thick package of broadly continuous, parallel reflections. Understanding the nature of this unit is key in reconstructing the emplacement sequence amalgamating in Deposit 2. The MeBo drill core that targeted the continuous reflections package separating Deposits 2a and 2b, at Site GeoB23725-1, recovered fine sands and silts within this depth range (Fig. 4.5). We interpret this fine-grained material as background hemipelagic sediments, and it is typical of the sediment types recovered in offshore stratified sequences elsewhere in the region (e.g., Trofimovs et al., 2013; Le Friant et al., 2015; Coussens et al., 2016). The sediments observed at Site GeoB23725-1 are horizontally layered, well-stratified, undeformed, and broadly undisturbed. Thus, they do not represent failed and remobilized sediments comparable to those that would be expected to derive from the seafloor failure headwall at the northern end of Deposit 2 (Crutchley et al., 2013). This supports the hypothesis that Deposit 2a and 2b were not deposited during one event, and instead, indicates a time gap between them great enough for several meters of background sediment to accumulate. Le Friant et al. (2015) correlate mafic deposits overlying Deposit 2 at Site U1394 to the South Soufriere Hills activity on Montserrat, thus obtaining a minimum age of 138 ka for Deposit 2b. The 15 m of sediment that overlie Deposit 2b at Site U1394 allows us to speculate on the age represented by the ~20 m sediment package that separates Deposits 2a and 2b, assuming a similar rate of accumulation of ~ 0.08 m/k.y.. This rate is within the range of sedimentation rates at Site U1395 of 0.02 – 0.17 m/k.y. based on oxygen isotope stratigraphy (Coussens et al., 2016) and consistent with the mean sedimentation rate of the shallowest sediments at Site U1395 of ~0.09 m/k.y. based on magnetostratigraphy (Le Friant et al., 2015). This implies a time span of ~180 k.y. for the intervening package, and a minimum age estimate

for Deposit 2a of 318 ka. This is a minimum, because Deposit 2b likely eroded and incorporated underlying substrate during its emplacement. We also note that any age estimate not derived from absolute age dating methods are associated with large uncertainties mainly caused by the fact that they cannot accurately account for erosional processes and that sedimentation rates derived from sequences rich in turbidite deposits are likely highly variable. The age of 318 ka is older than any dated subaerial rocks from Soufriere Hills and lies within a time gap between this volcano and the youngest known rocks from Centre Hills (0.55 Ma) (Watt et al., 2012b). The event may therefore represent a part of the Soufriere Hills stratigraphy that is no longer represented in subaerial exposures.

4.5.2.1 Volcanic flank collapse

Our data combined with previous studies (Lebas et al., 2011; Le Friant et al., 2004; Watt et al., 2012a, 2012b; Watt et al., 2015) indicate that the formation of Deposits 2a and 2b was initiated by a volcanic flank collapse that originated from Soufrière Hills volcano on Montserrat (Fig.7A). We observe an accumulation of blocks in the proximal domain of Deposit 2a. Such proximal block accumulations are often observed at volcanic flank collapse deposits, e.g., at the Cape Verde islands (Barrett et al., 2020; Day et al., 1999), the Canary Islands (Krastel et al., 2001), or Ritter Island (Karstens et al., 2019; Silver et al., 2009), as well as at the Deposits 1, 3 and 4 offshore Montserrat (Fig. 4.4.1; Lebas et al. 2011, Watt et al., 2012a, 2012b). Often such block fields have a fan-like or sub-circular shape that indicates a freely spreading flow of the associated debris avalanche along the seafloor during emplacement (Yoshida et al., 2012) and a common source of the material, as well as a deposition by one single event (Kühn et al., 2021). Deposit 2a is different: it is elongate and the V-shaped proximal block field extends with a main axis parallel to the graben axis of the M-B-Graben from NW to SE. This indicates a focused transport of the blocks first downslope of the flank of Montserrat in an initially eastward direction followed by a turn of the transport direction by ~45° along the graben axis following the steepest downslope trend into the graben center. Lebas et al. (2011) suggest a link between the formation of the mass transport deposits offshore Montserrat to the fault systems that form the M-B-Graben. Compared to Deposit 1, that has a fan-shaped distribution of proximal blocks (Crutchley et al., 2013; Lebas et al., 2011; Le Friant et al., 2004; Watt et al., 2012a), the blocks of Deposit 2a travelled much further. The mechanism behind this increased travel distance remains unclear, although a focus of the kinetic energy of the slide by a narrowing of the slide plane due to the graben morphology might have led to an increased slide velocity and thus a longer runout of the blocks. The channelization of debris flows can also lead to an increased

water-saturation at the base of the flow that ultimately results in increased mobility and longer runouts (Tost et al., 2014). Several numerical models of onshore landslides support that channeling of a slide mass can increase the overall runout distance (Fannin and Wise, 2001; Shen et al., 2022). Watt et al. (2015) showed that some of the most proximal Deposit 2a blocks are indeed transported volcanic edifice blocks originated from Soufrière Hills. Therefore, it is likely that the blocky center part of Deposit 2a mainly consists of volcanic flank collapse material, but the secondary seafloor failure at the northern headwall (Crutchley et al., 2013) also contributed to the total volume of this part of the deposit (Fig. 4.7B). The sparse data in the proximal deposition area does not allow a distinction between volcanic material or secondary failed and incorporated seafloor sediments within the blocky center.

The drill cores from site GeoB23725-1, where Deposit 2b overlies Deposit 2a, despite their very limited recovery, suggest that the landslide facies comprises mixed volcaniclastic gravel with hemipelagic background sediment intraclasts. This lithology is consistent with volcanic flank collapse processes forming a debris avalanche that incorporated preexisting seafloor sediment (intraclasts) during emplacement (Fig. 4.7E). The geometry of the deposit and the proximal accumulation of blocks indicates an origin from Soufrière Hills on Montserrat (cf. Watt et al., 2015; Fig. 4.1). Similar to the formation of Deposit 2a, the blocky, proximal part of Deposit 2b was confined between the prior accumulation of Deposit 2a and the western edge of the M-B-Graben (Fig. 4.3), focusing the flow and producing an elongated geometry rather than a freely spreading deposit. Once the associated slide mass passed the distal bottleneck of this transport pathway (Fig. 4.3B) it was deposited in a sub-circular shape, consistent with unconfined spreading (cf. De Haas et al., 2015). We conclude that the topographic complexity of this volcanic setting, including topography generated by stacked debris avalanche deposits, exerts a strong control on the transport distance and morphology of debris avalanche deposits. Due to the unusual seafloor morphology in volcanic island areas (partly caused by emplaced volcanic landslide deposits) it seems likely that this effect might be widely seen around other volcanic islands.

4.5.2.2 Sediment erosion, incorporation, and deformation

Beyond the blocky central part of Deposit 2a, the morphology of the bounding surfaces of the deposit is defined by a laterally confined, smooth surfaced apron. The drill cores from the distal site GeoB23702-5 show that this deposit comprises a mixture of deformed, tilted and structureless sediment, lithologically consistent with the hemipelagic basin infill, and with an

intermixed volcaniclastic component. The visually deformed and disrupted nature of the sediment comprising Deposit 2a at this site is consistent with the mostly acoustically transparent nature of the deposit in Parasound profiles. Although even small amounts of deformation may have large consequences for the seismic character of a sedimentary unit (Ford et al., 2023; Karstens et al., 2023), the seismic character suggests that the deformation observed in the cores is laterally extensive and may imply disaggregation and loss of structures within the materials mobilized in this part of Deposit 2a (Fig. 4.6). NW/SE oriented seismic profiles show that emplacement of the blocky center and of the smooth-surfaced apron occurred broadly on the same bottom surface, although seismic amplitudes are much higher and more continuous in the apron (Fig. 4.2B, C). We suggest the blocky slide mass that constitutes the center of Deposit 2a incised into the M-B-Graben substrate during emplacement, incorporated pre-existing seafloor sediments and deformed the frontal and adjacent seafloor sediments (Fig. 4.7C). This is broadly consistent with findings from IODP Expedition 340 that recovered hemipelagic mud and turbidites at Site U1394 (Le Friant et al., 2015). Although undeformed, Le Friant et al. (2015) interpret these layers as an intact sediment block within Deposit 2a (Le Friant et al., 2015). Similar deformation of adjacent sediments has been observed in deeper mass transport deposits offshore Montserrat (Deposit 8; Watt et al. 2012b), Martinique (e.g., Brunet et al., 2016; Le Friant et al., 2015), Israel (Frey-Martínez et al., 2006), Japan (Morita et al., 2011) and Oregon, USA (Lenz et al., 2019). We observe substrate incorporation in the Deposit 2b core sections (background sediment intraclasts) and this process has also been observed elsewhere (Karstens et al., 2019; Kühn et al., 2021; Ogata et al., 2019, 2014; Watt et al., 2019). The volcaniclastic gravel at the base of the distal Deposit 2a apron (Fig. 4.6F) marks the transition of the (seismic) Deposit 2a into the pre-Deposit 2a stratigraphy and was likely deposited in an earlier (pre-Deposit 2a) volcanic flank collapse event. Site U1395 shows a similar volcaniclastic sand-gravel deposit at an equivalent horizon (also stratigraphically constrained by an underlying pumiceous deposit) (between 18 and 20 mbsf; Coussens et al., 2016) causing strong peaks in natural gamma radiation and magnetic susceptibility logging (Expedition 340 Scientists, 2012). We suggest that this volcaniclastic gravel unit potentially acted as a basal shear surface for the deformation of the Deposit 2a apron sediment package (Frey-Martínez et al., 2006; Sobiesak et al. 2018; Watt et al., 2012b), which would have enhanced total runout distance and potentially controlled the thickness of the deformed sediment package and incision driven by the Deposit 2a event. However, the data available does not provide clear evidence for this and the nature and age of the older event, depositing the basal volcaniclastic unit in Deposit 2a, is unconstrained. Given its lithology and its coarseness, it would be expected to correlate with a

proximal volcaniclastic debris avalanche deposit, but this cannot be clearly distinguished in seismic reflection profiles across the proximal sequence offshore Montserrat. Regardless, the sequence points to the occurrence of at least two major mass transport events over several tens of kiloyears, which collectively contributed to the seismically defined Deposit 2.

4.5.2.3 Suspension of fine-grained flow material and channel formation

Submarine canyons and channels are common morphological features around volcanic islands and an expression of downslope sediment transport by bottom currents usually parallel to the topographic gradient (Casalbore et al., 2021; Hansen et al., 2015; Normark and Carlson, 2003; Shepard, 1981). The channels incised into the top of Deposit 2a bend around obstacles while broadly being oriented downslope along the axis of the M-B-Graben from NW to SE. The channel system bypasses GeoB23725-1 and Site U1394 and so does not allow any correlation of specific cored lithologies to a channel forming event. The fact that these channels are incised directly on top of Deposit 2a indicates that they were formed after the main slide event. The lack of meandering and their sharp edges indicate their origin from high energetic, high velocity, erosive flow (Davies and Tinker, 1984).

These observations mimic what has been observed at the top of the Ritter Island sector collapse deposits, where sets of similar channels exist (Karstens et al. 2019, Watt et al. 2019). At Ritter Island, a set of channels formed in the proximal deposit are the result of erosive evacuation of the main collapse material, that then transported most of the sector collapse material into the more distal area of the deposit (Karstens et al., 2019; Watt et al., 2019). This erosion intensified when the flow was focused between two adjacent islands, resulting in an increasing channel depth (Karstens et al., 2019). A second set of channels developed in the distal Ritter Island sector collapse deposits, where a late-stage turbidity current linked to a post-collapse eruption eroded into the distal parts of the initial debris flow deposits (Watt et al., 2019). Due to lack of drill cores from Deposit 2a we cannot draw further insights into how directly the channelization observed at Montserrat replicates the processes inferred at Ritter Island, but the fact that the channels are situated topographically higher than Deposit 2b indicates that their formation is not associated with the emplacement of Deposit 2b and that they were rather formed at the end of deposition of Deposit 2a or shortly after.

Trofimovs et al. (2008) report the transition of pyroclastic flows associated to the 2003 dome collapse of Soufrière Hills into turbidity currents that transported fine grained material from the near-shore down the slopes of Montserrat and eroded and incorporated substrate material. The

2022 eruption of Hunga volcano demonstrated that the resulting turbidity currents can travel with velocities up to 33 m/s, run out for long distances (>100 km) and erode substantial amounts of the seafloor (Clare et al., 2023). Water tank experiments on subaqueous landslides also showed that fine grained sediments can be suspended in the water column during sliding (Elverhoi et al., 2010; Mohrig et al., 1998) and there are multiple studies providing evidence for elevated sediment suspension in the water column after earthquake-related turbidity currents (McHugh et al., 2011; Noguchi et al., 2012; Thunell et al., 1999). After the deposition of turbidity currents related to Tohoku Earthquake in 2011, Noguchi et al. 2012 report an elevation of suspended sediments in the water column from ~0.6 mg/L to up to 5 mg/L maximum. For the Deposit 2a slide our data suggests two stages: the primary volcanic flank collapse and the secondary seafloor failure; both could potentially have suspended large amounts of sediment in the water column resulting in a density flow after the main slide mass had already come to rest, and this may be the origin of the post-depositional channelization. Although it is possible that a separate event, undetected within our data, may have incised the channels atop of Deposit 2a, the fact that there are no similar incised channels observed elsewhere in our stratigraphic succession leads us to conclude that the channel and turbidite formation are causally related to Deposit 2a emplacement.

4.5.2.4 Turbidite deposition

IODP Expedition 340 reports several (partly) volcaniclastic turbidites at Site U1395 in the M-B-Graben beyond the distal limit of Deposit 2a (Le Friant et al., 2013, 2015). This is consistent with our observation of several near-surface, frontally non-confined, and transparent units in the Parasound echosounder data south of the Deposit 2a toe (Fig. 4.6A) that likely represent turbidite deposits or *in situ* deformed sediments. Two of these transparent units are located in a depth interval of 0 to 8 mbsf and are stratigraphically within the corresponding depth interval to Deposit 2a (green-colored units in Fig. 4.6A). Site U1395 cores comprise several cm to m thick turbidites in this depth (Coussens et al., 2016) but due to the limited vertical resolution of the Parasound data we cannot link single turbidites from the IODP cores to certain transparent units. However, the turbidites are likely related to the formation of the channels on top of the Deposit 2a blocky center as well as potentially to the later deposition of Deposit 2b. A very thick turbidite at Site U1395 (~12 to 20 mbsf; Coussens et al., 2016) has a stratigraphic depth that corresponds closely with the position of Deposit 2a in our seismic and Parasound profiles (purple-colored units in Fig. 4.6A), and with the deformed sediment of Deposit 2a observed at Site GeoB23702-5. While the stratigraphic position of a distinctive pumiceous horizon at both

core sites supports a correlation of this turbidite with Deposit 2a, the lithology found in our MeBo drill cores (mainly background sediment) and the seismic mapping results described in this study rather suggest an earlier (i.e., pre-Deposit 2a) emplacement of this turbidite. Although we favor the latter hypothesis here, more data and analysis are required to infer a correlation of these distal turbidites with Deposit 2a or other mass transport deposits. Shallow transparent units on top of Deposit 2a (Fig. 4.6A) show similar seismic characteristics as the distal turbidites and therefore we interpret them as post-Deposit 2a turbidites. This is consistent with the occurrence of shallow, several meter thick turbidites above Deposit 2b at Site U1394 (Le Friant et al., 2015). The relationship between Deposit 2a and the downslope turbidite stratigraphy also depends on whether the distal part of Deposit 2a was frontally confined or unconfined. Parasound profiles suggest a confined mass, but this interpretation remains equivocal based on the available profiles. A complete resolution of turbidite stratigraphic relationships and their correlation with individual landslide events would require geochemical and sedimentological correlations, alongside further geophysical data.

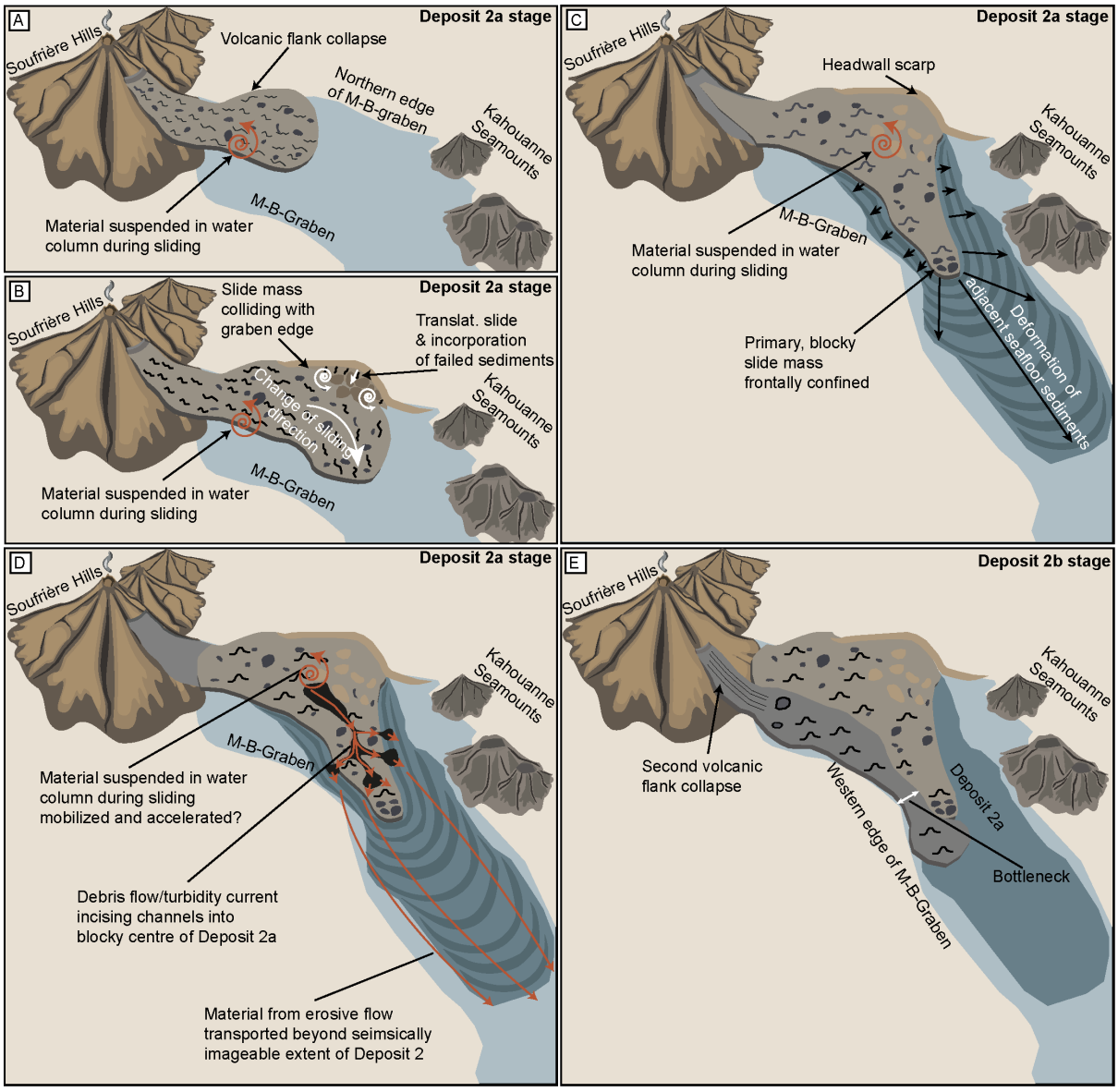

Figure 4.7: *Geological processes involved in the emplacement of Deposit 2 and their assumed timing within the deposition sequence. A: Initial volcanic debris avalanche from Montserrat. B: The volcaniclastic slide mass collides with northern edge of the M-B-Graben and triggers secondary failure of seafloor sediments. C: The slide mass incises into the substrate and deforms adjacent sediments. Fine grained material is suspended in the water column. D: Fine grained material suspended in the water column accelerates downslope and forms an erosive flow that incises channel structures into the top surface of Deposit 2a. E: A second volcanic debris avalanche is emplaced in a topographic chute formed by the Deposit 2a blocks and the western edge of the M-B-Graben.*

4.6 Conclusions

Deposit 2 consists of two separate volcanic flank collapse deposits with a significant time gap (~180 k.y.) in between, great enough for the deposition of ~20 m of background sediments. In consequence, the bulk volume of Deposit 2 cannot be used for tsunami modelling as it (1) does not account for the origin of material as it neglects any erosional bulking and as it (2) does not account for the individual timing of the at least two discrete volcaniclastic landslides. If these stratigraphic complexities are not resolved, simplified interpretations of debris avalanche deposits offshore volcanic islands overestimate tsunami magnitude. Conversely, the same interpretations may underestimate flank collapse frequency, given that what may initially appear to be a single deposit within bathymetric or low-resolution seismic reflection datasets may actually comprise a series of stacked deposits from discrete events. We suggest that the possibility of multiple stages in the formation of deposits offshore volcanic islands must be considered to produce robust assessments of the tsunamigenic potential of ancient deposits. However, we acknowledge that such assessments remain highly challenging; even with the rare combination of 3D seismic-reflection datasets alongside core sampling and other geophysical datasets, there remain a number of uncertainties in the relative timing and nature of the events that formed Deposit 2 offshore Montserrat.

Our new observations provide a clear illustration of how topography exerts a crucial influence on the transport evolution of blocky debris avalanches. Graben structures or earlier deposits can focus an elongated transport following the slope instead of a free spreading of blocks along contour lines and earlier deposits may control the transport and evolution of subsequent events. Accurate landslide modelling therefore needs to consider topographic influences on slide dynamics. It is unlikely that these complexities have a significant influence on tsunami generation at Montserrat because of the depth of the Montserrat-Bouillante Graben (>1000 m), but have likely more important implications for shallower water settings such as at Anak Krakatau or Ritter Island.

Based on the available high-resolution 3D seismic datasets from volcanic flank collapses at Montserrat and Ritter Island, we suggest that erosive late-stage density currents are a common process during volcanic flank collapse emplacement. This process requires huge amounts of sediment suspended in the water column. The complexity of the subsequent deposits and their emplacement challenges simplified flow models as they are unlikely to reproduce an accurate picture of the depositional sequence. However, simplified models are still useful for assessing

tsunami potential as long as they are based upon an estimation of the initial landslide failure volume, rather than the final deposit volume, as the initial stage of landslide failure is likely to be the most significant in tsunami genesis.

Open Research

The geophysical datasets used in this study can be found in the PANGAEA data repository. The 2D seismic data can be accessed via https://doi.org/10.1594/PANGAEA.957490 (Kühn et al., 2023A) and the 3D seismic data via https://doi.org/10.1594/PANGAEA.963076 (Kühn et al., 2023B) and will be downloadable after a moratorium in 04/2025 and 09/2025 respectively. Hydroacoustic data can be accessed via https://doi.org/10.1594/PANGAEA.935598 (Berndt et al., 2021). Supplementary information can be accessed online via *https://doi.org/10.1029/2024GC011564.*

Acknowledgements

We thank the master and the crew of RV METEOR for their support during the research cruises M154-1 and M154-2. We also thank the scientific crews of both expeditions for their work. We would also like to thank dGB Earth Sciences (OpendTect) and S&P Global (Kingdom Suite) for granting educational software licenses for the interpretation of the seismic data. This study was funded by the Deutsche Forschungsgemeinschaft (DFG, German Research Foundation) through the “SEKT”-project (grant no. *453685300*). Research cruise M154 was financed through the DFG grant *MerMet 14-104* and the *Program-Oriented Funding IV* (PoF IV) of the Helmholtz Association.

Supporting information to this article can be accessed online via **https://doi.org/10.1029/2024GC011564**.

References

Auker, M.R., Sparks, R.S.J., Siebert, L., Crosweller, H.S., Ewert, J., 2013. A statistical analysis of the global historical volcanic fatalities record. Journal of Applied Volcanology 2, 1–24. https://doi.org/10.1186/2191-5040-2-2

Barrett, R., Lebas, E., Ramalho, R., Klaucke, I., Kutterolf, S., Klügel, A., Lindhorst, K., Gross, F., Krastel, S., 2020. Revisiting the tsunamigenic volcanic flank collapse of fogo island in the cape verdes, offshore West Africa, in: Geological Society Special Publication. Geological Society of London, pp. 13–26. https://doi.org/10.1144/SP500-2019-187

Berndt, C., Böttner, C., Elger, J., Kontradowitz, S., Kühn, M., Müller, S., Schramm, B., Stelzner, M., 2019. Sector collapse kinematics and tsunami implications - SEKT, Cruise No. M154/1, April 3 - April 25, 2019, Mindelo (Cape Verde) - Point-á-Pitre (Guadeloupe). METEOR-Berichte, M154/1. Gutachterpanel Forschungsschiffe, Bonn, 47 pp.

Berndt, C., Böttner, C., Wölfl, A.-C., 2021. Multibeam bathymetry raw data (Kongsberg EM 122 entire dataset) of RV METEOR during cruise M154/1. https://doi.org/10.1594/PANGAEA.935598

Bouysse, P., Westercamp, D., 1990. Subduction of Atlantic aseismic ridges and Late Cenozoic evolution of the Lesser Antilles island arc. Tectonophysics, 175(4), 349-380.

Brunet, M., Le Friant, A., Boudon, G., Lafuerza, S., Talling, P., Hornbach, M., ... & IODP Expedition 340 Science Party. (2016). Composition, geometry, and emplacement dynamics of a large volcanic island landslide offshore M artinique: From volcano flank-collapse to seafloor sediment failure?. *Geochemistry, Geophysics, Geosystems*, *17*(3), 699-724.

Canals, M., Puig, P., de Madron, X.D., Heussner, S., Palanques, A., Fabres, J., 2006. Flushing submarine canyons. Nature 444, 354–357. https://doi.org/10.1038/nature05271

Casalbore, D., Clare, M.A., Pope, E.L., Quartau, R., Bosman, A., Chiocci, F.L., Romagnoli, C., Santos, R., 2021. Bedforms on the submarine flanks of insular volcanoes: New insights gained from high resolution seafloor surveys. Sedimentology 68, 1400–1438. https://doi.org/10.1111/sed.12725

Chopra, S., Marfurt, K.J., 2008. Emerging and future trends in seismic attributes. The Leading Edge 27, 298–318. https://doi.org/10.1190/1.2896620

Clare, M.A., Yeo, I.A., Watson, S., Wysoczanski, R., Seabrook, S., Mackay, K., Hunt, J.E., Lane, E., Talling, P.J., Pope, E., Cronin, S., Ribó, M., Kula, T., Tappin, D., Henrys, S., de Ronde, C., Urlaub, M., Kutterolf, S., Fonua, S., Panuve, S., Veverka, D., Rapp, R., Kamalov, V., Williams, M., 2023. Fast and destructive density currents created by ocean-entering volcanic eruptions. Science (1979) 381, 1085–1092. https://doi.org/10.1126/science.adi3038

Clare, M., Chaytor, J., Dabson, O., Gamboa, D., Georgiopoulou, A., Eady, H., Hunt, J., Jackson, C., Katz, O., Krastel, S., León, R., Micallef, A., Moernaut, J., Moriconi, R., Moscardelli, L., Mueller, C., Normandeau, A., Patacci, M., Steventon, M., Urlaub, M., Völker, D., Wood, L., Jobe, Z., 2019.

A consistent global approach for the morphometric characterization of subaqueous landslides. Geological Society, London, Special Publications 477, 455–477. https://doi.org/10.1144/SP477.15

Coussens, M.F., Wall-Palmer, D., Talling, P.J., Watt, S.F.L., Hatter, S.J., Cassidy, M., Clare, M., Jutzeler, M., Hatfield, R., McCanta, M., Kataoka, K.S., Endo, D., Palmer, M.R., Stinton, A., Fujinawa, A., Boudon, G., Le Friant, A., Ishizuka, O., Gernon, T., Adachi, T., Aljahdali, M., Breitkreuz, C., Frass, A.J., Hornbach, M.J., Lebas, E., Lafuerza, S., Maeno, F., Manga, M., Martinez-Colon, M., McManus, J., Morgan, S., Saito, T., Slagle, A., Subramanyam, K.S.V., Tamura, Y., Trofimovs, J., Villemant, B., Wang, F., 2016. Synthesis: stratigraphy and age control for IODP Sites U1394, U1395, and U1396 offshore Montserrat in the Lesser Antilles. https://doi.org/10.2204/iodp.proc.340.204.2016

Crutchley, G.J., Karstens, J., Berndt, C., Talling, P.J., Watt, S.F.L., Vardy, M.E., Hühnerbach, V., Urlaub, M., Sarkar, S., Klaeschen, D., Paulatto, M., Le Friant, A., Lebas, E., Maeno, F., 2013. Insights into the emplacement dynamics of volcanic landslides from high-resolution 3D seismic data acquired offshore Montserrat, Lesser Antilles. Mar Geol 335, 1–15. https://doi.org/10.1016/j.margeo.2012.10.004

Davies, T.R.H., Tinker, C.C., 1984. Fundamental characteristics of stream meanders. GSA Bulletin 95, 505–512. https://doi.org/10.1130/0016-7606(1984)95<505:FCOSM>2.0.CO;2

Davis, W.M., 1924. The formation of the Lesser Antilles. Proceedings of the National Academy of Sciences 10, 205–211.

Day, S.J., Heleno Da Silva, S.I.N., Fonseca, J.F.B.D., 1999. A past giant lateral collapse and present-day flank instability of Fogo, Cape Verde Islands. Journal of Volcanology and Geothermal Research 94, 191–218. https://doi.org/10.1016/S0377-0273(99)00103-1

De Haas, T., Braat, L., Leuven, J.R.F.W., Lokhorst, I.R., Kleinhans, M.G., 2015. Effects of debris flow composition on runout, depositional mechanisms, and deposit morphology in laboratory experiments. J Geophys Res Earth Surf 120, 1949–1972. https://doi.org/10.1002/2015JF003525

Elverhoi, A., Breien, H., De Blasio, F. V., Harbitz, C.B., Pagliardi, M., 2010. Submarine landslides and the importance of the initial sediment composition for run-out length and final deposit. Ocean Dyn 60, 1027–1046. https://doi.org/10.1007/s10236-010-0317-z

Expedition 340 Scientists, 2012. Integrated Ocean Drilling Program Expedition 340 Preliminary Report Lesser Antilles Volcanism and Landslides Implications for hazard assessment and long-term magmatic evolution of the arc. IODP Prel. Rept. 340. https://doi.org/10.2204/iodp.pr.340.2012

Expedition 340 Scientists, 2013. Expedition 340 summary. *In* Le Friant, A., Ishizuka, O., Stroncik, N.A., and the Expedition 340 Scientists, *Proc. IODP,* 340: Tokyo (Integrated Ocean Drilling Program Management International, Inc.). doi:10.2204/iodp.proc.340.101.2013

Fannin, R.J., Wise, M.P., 2001. An empirical-statistical model for debris flow travel distance. Canadian

Geotechnical Journal 38, 982–994. https://doi.org/10.1139/cgj-38-5-982

Feuillet, N., Leclerc, F., Tapponnier, P., Beauducel, F., Boudon, G., Le Friant, A., Deplus, C., Lebrun, J.F., Nercessian, A., Saurel, J.M., Clément, V., 2010. Active faulting induced by slip partitioning in montserrat and link with volcanic activity: New insights from the 2009 GWADASEIS marine cruise data. Geophys Res Lett 37, 1–6. https://doi.org/10.1029/2010GL042556

Ford, J., Camerlenghi, A., Zolezzi, F., Calarco, M., 2023. Seismic amplitude response to internal heterogeneity of mass-transport deposits. Solid Earth 14, 137–151. https://doi.org/10.5194/se-14-137-2023

Freudenthal, T., Wefer, G., 2013. Drilling cores on the sea floor with the remote-controlled sea floor drilling rig MeBo. Geoscientific Instrumentation, Methods and Data Systems 2, 329–337. https://doi.org/10.5194/gi-2-329-2013

Frey-Martínez, J., Cartwright, J., James, D., 2006. Frontally confined versus frontally emergent submarine landslides: A 3D seismic characterisation. Mar Pet Geol 23, 585–604. https://doi.org/10.1016/j.marpetgeo.2006.04.002

Grilli, S.T., Tappin, D.R., Carey, S., Watt, S.F.L., Ward, S.N., Grilli, A.R., Engwell, S.L., Zhang, C., Kirby, J.T., Schambach, L., Muin, M., 2019. Modelling of the tsunami from the December 22, 2018 lateral collapse of Anak Krakatau volcano in the Sunda Straits, Indonesia. Sci Rep 9, 1–13. https://doi.org/10.1038/s41598-019-48327-6

Grindlay, N.R., Hearne, M., Mann, P., 2005. High risk of tsunami in the Northern Caribbean. Eos (Washington DC). https://doi.org/10.1029/2005EO120001

Hansen, L.A.S., Callow, R.H.T., Kane, I.A., Gamberi, F., Rovere, M., Cronin, B.T., Kneller, B.C., 2015. Genesis and character of thin-bedded turbidites associated with submarine channels. Mar Pet Geol. https://doi.org/10.1016/j.marpetgeo.2015.06.007

Harford, C.L., Pringle, M.S., Sparks, R.S.J., Young, S.R., 2002. The volcanic evolution of Montserrat using $^{40}Ar/^{39}Ar$ geochronology. Geological Society, London, Memoirs 21, 93–113. https://doi.org/10.1144/GSL.MEM.2002.021.01.05

Herd, R.A., Edmonds, M., Bass, V.A., 2005. Catastrophic lava dome failure at Soufrière Hills Volcano, Montserrat, 12-13 July 2003. Journal of Volcanology and Geothermal Research 148, 234–252. https://doi.org/10.1016/j.jvolgeores.2005.05.003

Hornbach, M.J., Manga, M., Genecov, M., Valdez, R., Miller, P., Saffer, D., Adelstein, E., Lafuerza, S., Adachi, T., Breitkreuz, C., Jutzeler, M., LeFriant, A., Ishizuka, O., Morgan, S., Slagle, A., Talling, P.J., Fraass, A., Watt, S.F.L., Stroncik, N.A., Aljahdali, M., Boudon, G., Fujinawa, A., Hatfield, R., Kataoka, K., Maeno, F., Martinez-Colon, M., McCanta, M., Palmer, M., Stinton, A., Subramanyam, K.S. V., Tamura, Y., Villemant, B., Wall-Palmer, D., Wang, and F., 2015. Permeability and pressure measurements in Lesser Antilles submarine slides: Evidence for

pressure-driven slow-slip failure. J Geophys Res Solid Earth 120, 7986–8011. https://doi.org/10.1002/2015JB012061

Huhn, K., Freudenthal, T., Dehning, K., Gatter, R., Hilgenfeldt, C., Hönekopp, L., Hornbach, M., Kühn, M., Kuhlmann, J., Kutterolf, S., Meyer-Schack, B., Pallapies, K., Rapp, S.K., Sievers, C., Watt, S., Stelzner, M., 2019. Sector collapse kinematics and tsunami implications - SEKT, Cruise No. M154-2, April 29 - Mai 23, 2019, Pointe-à-Pitre (Guadeloupe) - Pointe-à-Pitre (Guadeloupe).

Karstens, J., Berndt, C., Urlaub, M., Watt, S.F.L., Micallef, A., Ray, M., Klaucke, I., Muff, S., Klaeschen, D., Kühn, M., Roth, T., Böttner, C., Schramm, B., Elger, J., Brune, S., 2019. From gradual spreading to catastrophic collapse – Reconstruction of the 1888 Ritter Island volcanic sector collapse from high-resolution 3D seismic data. Earth Planet Sci Lett 517. https://doi.org/10.1016/j.epsl.2019.04.009

Karstens, J., Crutchley, G.J., Berndt, C., Talling, P.J., Watt, S.F.L., Hühnerbach, V., Friant, A. Le, Lebas, E., Trofimovs, J., 2013. Emplacement of pyroclastic deposits offshore Montserrat: Insights from 3D seismic data. Journal of Volcanology and Geothermal Research 257, 1–11. https://doi.org/10.1016/j.jvolgeores.2013.03.004

Karstens, J., Kelfoun, K., Watt, S.F.L., Berndt, C., 2020. Combining 3D seismics, eyewitness accounts and numerical simulations to reconstruct the 1888 Ritter Island sector collapse and tsunami. International Journal of Earth Sciences. https://doi.org/10.1007/s00531-020-01854-4

Karstens, J., Haflidason, H., Berndt, C., & Crutchley, G. J. (2023). Revised Storegga Slide reconstruction reveals two major submarine landslides 12,000 years apart. *Communications Earth & Environment*, *4*(1), 55.

Krastel, S., Schmincke, H.U., Jacobs, C.L., Rihm, R., Le Bas, T.P., Alibés, B., 2001. Submarine landslides around the Canary Islands. J Geophys Res Solid Earth 106, 3977–3997. https://doi.org/10.1029/2000jb900413

Kühn, M., Berndt, C., Krastel, S., 2023a. 2D multichannel seismic reflection processed data (GI Gun entire dataset) of RV METEOR during cruise M154/1. https://doi.org/10.1594/PANGAEA.957490

Kühn, M., Berndt, C., Krastel, S., 2023b. 3D multichannel seismic reflection processed data (P-Cable system with GI Gun) of RV METEOR during cruise M154/1, Montserrat, Lesser Antilles. https://doi.org/10.1594/PANGAEA.963076

Kühn, M., Karstens, J., Berndt, C., Watt, S.F.L., 2021. Seismic reconstruction of seafloor sediment deformation during volcanic debris avalanche emplacement offshore Sakar, Papua New Guinea. Mar Geol 439. https://doi.org/10.1016/j.margeo.2021.106563

Kunde, D., 2020. Seismic velocity of sector collapse deposits off Montserrat (Master's thesis). Christian-Albrechts-Universität zu Kiel, Kiel.

Le Friant, A., Deplus, C., Boudon, G., Sparks, R.S.J., Trofimovs, J., Talling, P., 2009. Submarine

deposition of volcaniclastic material from the 1995-2005 eruptions of Soufrière Hills volcano, Montserrat. J Geol Soc London 166, 171–182. https://doi.org/10.1144/0016-76492008-047

Le Friant, A., Harford, C.L., Deplus, C., Boudon, G., Sparks, R.S.J., Herd, R.A., Komorowski, J.C., 2004. Geomorphological evolution of Montserrat (West Indies): importance of flank collapse and erosional processes. J Geol Soc London 161, 147–160. https://doi.org/10.1144/0016-764903-017

Le Friant, A., Ishizuka, O., Boudon, G., Palmer, M.R., Talling, P.J., Villemant, B., Adachi, T., Aljahdali, M., Breitkreuz, C., Brunet, M., Caron, B., Coussens, M., Deplus, C., Endo, D., Feuillet, N., Fraas, A.J., Fujinawa, A., Hart, M.B., Hatfield, R.G., Hornbach, M., Jutzeler, M., Kataoka, K.S., Komorowski, J.C., Lebas, E., Lafuerza, S., Maeno, F., Manga, M., Martínez-Colõn, M., McCanta, M., Morgan, S., Saito, T., Slagle, A., Sparks, S., Stinton, A., Stroncik, N., Subramanyam, K.S.V., Tamura, Y., Trofimovs, J., Voight, B., Wall-Palmer, D., Wang, F., Watt, S.F.L., 2015. Submarine record of volcanic island construction and collapse in the Lesser Antilles arc: First scientific drilling of submarine volcanic island landslides by IODP Expedition 340. Geochemistry, Geophysics, Geosystems 16, 420–442. https://doi.org/10.1002/2014GC005652

Le Friant, A., Ishizuka, O., Stroncik, N.A.,, and the Expedition 340 Scientists, 2013. Site U1395, in: Proceedings of the Integrated Ocean Drilling Program. https://doi.org/10.2204/iodp.proc.340.105.2013

Lebas, E., Le Friant, A., Boudon, G., Watt, S.F.L., Talling, P.J., Feuillet, N., Deplus, C., Berndt, C., Vardy, M.E., 2011. Multiple widespread landslides during the long-term evolution of a volcanic island: Insights from high-resolution seismic data, Montserrat, Lesser Antilles. Geochemistry, Geophysics, Geosystems 12. https://doi.org/10.1029/2010GC003451

Lenz, B.L., Sawyer, D.E., Phrampus, B., Davenport, K., Long, A., 2019. Seismic imaging of seafloor deformation induced by impact from large submarine landslide blocks, offshore oregon. Geosciences (Switzerland) 9. https://doi.org/10.3390/geosciences9010010

Løvholt, F., Pedersen, G., Harbitz, C.B., Glimsdal, S., Kim, J., 2015. On the characteristics of landslide tsunamis. Philosophical Transactions of the Royal Society A: Mathematical, Physical and Engineering Sciences 373. https://doi.org/10.1098/rsta.2014.0376

Masson, D.G., Harbitz, C.B., Wynn, R.B., Pedersen, G., Løvholt, F., 2006. Submarine landslides: processes, triggers and hazard prediction. Philos Trans A Math Phys Eng Sci 364, 2009–2039. https://doi.org/10.1098/rsta.2006.1810

Masson, D.G., Watts, A.B., Gee, M.J.R., Urgeles, R., Mitchell, N.C., Le Bas, T.P., Canals, M., 2002. Slope failures on the flanks of the western Canary Islands. Earth Sci Rev 57, 1–35. https://doi.org/10.1016/S0012-8252(01)00069-1

McHugh, C.M., Seeber, L., Braudy, N., Cormier, M.H., Davis, M.B., Diebold, J.B., Dieudonne, N., Douilly, R., Gulick, S.P.S., Hornbach, M.J., Johnson, H.E., Mishkin, K.R., Sorlien, C.C., Steckler, M.S., Symithe, S.J., Templeton, J., 2011. Offshore sedimentary effects of the 12 January 2010

Haiti earthquake. Geology 39, 723–726. https://doi.org/10.1130/G31815.1

Mohrig, D., Ellis, C., Parker, G., Whipple, K.X., Hondzo, M., 1998. Hydroplaning of subaqueous debris flows. GSA Bulletin 110, 387–394. https://doi.org/10.1130/0016-7606(1998)110<0387:HOSDF>2.3.CO;2

Moore, J.G., Normark, W.R., 1994. Giant Hawaiian Landslides. Annu Rev Earth Planet Sci 22, 119–144.

Morita, S., Nakajima, T., Hanamura, Y., 2011. Submarine slump sediments and related dewatering structures: Observations of 3D seismic data obtained for the continental slope off Shimokita Peninsula, NE Japan. The Journal of the Geological Society of Japan 117, 95–98. https://doi.org/10.5575/geosoc.117.95

Noguchi, T., Tanikawa, W., Hirose, T., Lin, W., Kawagucci, S., Yoshida-Takashima, Y., Honda, M.C., Takai, K., Kitazato, H., Okamura, K., 2012. Dynamic process of turbidity generation triggered by the 2011 Tohoku-Oki earthquake. Geochemistry, Geophysics, Geosystems 13. https://doi.org/10.1029/2012GC004360

Normark, W.R., Carlson, P.R., 2003. Giant submarine canyons: Is size any clue to their importance in the rock record? GSA Special Papers 370, 175–190.

Ogata, K., Festa, A., Pini, G.A., Pogačnik, Lucente, C.C., 2019. Substrate deformation and incorporation in sedimentary mélanges (olistostromes): Examples from the northern Apennines (Italy) and northwestern Dinarides (Slovenia). Gondwana Research 74, 101–125. https://doi.org/10.1016/j.gr.2019.03.001

Ogata, K., Pogačnik, Z., Pini, G.A., Tunis, G., Festa, A., Camerlenghi, A., Rebesco, M., 2014. The carbonate mass transport deposits of the Paleogene Friuli Basin (Italy/Slovenia): Internal anatomy and inferred genetic processes. Mar Geol 356, 88–110. https://doi.org/10.1016/j.margeo.2014.06.014

Ryan, W.B.F., Carbotte, S.M., Coplan, J.O., O'Hara, S., Melkonian, A., Arko, R., Weissel, R.A., Ferrini, V., Goodwillie, A., Nitsche, F., Bonczkowski, J., Zemsky, R., 2009. Global multi-resolution topography synthesis. Geochemistry, Geophysics, Geosystems 10. https://doi.org/10.1029/2008GC002332

Shen, W., Berti, M., Li, T., Benini, A., Qiao, Z., 2022. The influence of slope gradient and gully channel on the run-out behavior of rockslide-debris flow: an analysis on the Verghereto landslide in Italy. Landslides 19, 885–900. https://doi.org/10.1007/s10346-022-01848-0

Shepard, F.P., 1981. Submarine Canyons: Multiple Causes and Long-Time Persistence. Am Assoc Pet Geol Bull 65, 1062–1077. https://doi.org/10.1306/03B59459-16D1-11D7-8645000102C1865D

Silver, E., Day, S., Ward, S., Hoffmann, G., Llanes, P., Driscoll, N., Appelgate, B., Saunders, S., 2009. Volcano collapse and tsunami generation in the Bismarck Volcanic Arc, Papua New Guinea.

Journal of Volcanology and Geothermal Research 186, 210–222. https://doi.org/10.1016/j.jvolgeores.2009.06.013

Sobiesiak, M.S., Kneller, B., Alsop, G.I., Milana, J.P., 2018. Styles of basal interaction beneath mass transport deposits. Mar Pet Geol 98, 629–639. https://doi.org/10.1016/j.marpetgeo.2018.08.028

Sparks, R.S.J., Barclay, J., Calder, E.S., Herd, R.A., Komorowski, J.-C., Luckett, R., Norton, G.E., Ritchie, L.J., Voight, B., Woods, A.W., 2002. Generation of a debris avalanche and violent pyroclastic density current on 26 December (Boxing Day) 1997 at Soufrière Hills Volcano, Montserrat. Geological Society, London, Memoirs 21, 409–434. https://doi.org/10.1144/GSL.MEM.2002.021.01.18

Thunell, R., Tappa, E., Varela, R., Llano, M., Astor, Y., Muller-Karger, F., Bohrer, R., 1999. Increased marine sediment suspension and fluxes following an earthquake. Nature 398, 233–236. https://doi.org/10.1038/18430

Tost, M., Cronin, S.J., Procter, J.N., 2014. Transport and emplacement mechanisms of channelised long-runout debris avalanches, Ruapehu volcano, New Zealand. Bull Volcanol 76, 1–14. https://doi.org/10.1007/s00445-014-0881-z

Trofimovs, J., Sparks, R.S.J., Talling, P.J., 2008. Anatomy of a submarine pyroclastic flow and associated turbidity current: July 2003 dome collapse, Soufri??re Hills volcano, Montserrat, West Indies. Sedimentology 55, 617–634. https://doi.org/10.1111/j.1365-3091.2007.00914.x

Trofimovs, J., Talling, P. J., Fisher, J. K., Sparks, R. S. J., Watt, S. F. L., Hart, M. B., ... & Leng, M. J. (2013). Timing, origin and emplacement dynamics of mass flows offshore of SE Montserrat in the last 110 ka: Implications for landslide and tsunami hazards, eruption history, and volcanic island evolution. *Geochemistry, Geophysics, Geosystems*, *14*(2), 385-406.

Wadge, G., Voight, B., Sparks, R.S.J., Cole, P.D., Loughlin, S.C., Robertson, R.E.A., 2014. An overview of the eruption of Soufrière Hills Volcano, Montserrat from 2000 to 2010. Geological Society Memoir 39, 1–39. https://doi.org/10.1144/M39.1

Walter, T.R., Haghshenas Haghighi, M., Schneider, F.M., Coppola, D., Motagh, M., Saul, J., Babeyko, A., Dahm, T., Troll, V.R., Tilmann, F., Heimann, S., Valade, S., Triyono, R., Khomarudin, R., Kartadinata, N., Laiolo, M., Massimetti, F., Gaebler, P., 2019. Complex hazard cascade culminating in the Anak Krakatau sector collapse. Nat Commun 10. https://doi.org/10.1038/s41467-019-12284-5

Ward, S.N., 2001. Landslide tsunami. J Geophys Res Solid Earth 106, 11201–11215. https://doi.org/10.1029/2000jb900450

Ward, S.N., Day, S., 2003. Ritter Island Volcano - Lateral collapse and the tsunami of 1888. Geophys J Int 154, 891–902. https://doi.org/10.1046/j.1365-246X.2003.02016.x

Watt, S.F.L., Jutzeler, M., Talling, P.J., Carey, S.N., Sparks, R.S.J., Tucker, M., Stinton, A.J., Fisher, J.K.,

Wall-Palmer, D., Hühnerbach, V., Moreton, S.G., 2015. New insights into landslide processes around volcanic islands from Remotely Operated Vehicle (ROV) observations offshore Montserrat. Geochemistry, Geophysics, Geosystems 16, 2240–2261. https://doi.org/10.1002/2015GC005781

Watt, S.F.L., Karstens, J., Berndt, C., 2021. Volcanic-Island Lateral Collapses and Their Submarine Deposits, Advances in Volcanology. Springer International Publishing. https://doi.org/10.1007/978-3-030-57411-6_10

Watt, S.F.L., Karstens, J., Micallef, A., Berndt, C., Urlaub, M., Ray, M., Desai, A., Sammartini, M., Klaucke, I., Böttner, C., Day, S., Downes, H., Kühn, M., Elger, J., 2019. From catastrophic collapse to multi-phase deposition: Flow transformation, seafloor interaction and triggered eruption following a volcanic-island landslide. Earth Planet Sci Lett 517. https://doi.org/10.1016/j.epsl.2019.04.024

Watt, S.F.L., Talling, P.J., Vardy, M.E., Heller, V., Hühnerbach, V., Urlaub, M., Sarkar, S., Masson, D.G., Henstock, T.J., Minshull, T.A., Paulatto, M., Le Friant, A., Lebas, E., Berndt, C., Crutchley, G.J., Karstens, J., Stinton, A.J., Maeno, F., 2012a. Combinations of volcanic-flank and seafloor-sediment failure offshore Montserrat, and their implications for tsunami generation. Earth Planet Sci Lett 319–320, 228–240. https://doi.org/10.1016/j.epsl.2011.11.032

Watt, S.F.L., Talling, P.J., Vardy, M.E., Masson, D.G., Henstock, T.J., H??hnerbach, V., Minshull, T.A., Urlaub, M., Lebas, E., Le Friant, A., Berndt, C., Crutchley, G.J., Karstens, J., 2012b. Widespread and progressive seafloor-sediment failure following volcanic debris avalanche emplacement: Landslide dynamics and timing offshore Montserrat, Lesser Antilles. Mar Geol 323–325, 69–94. https://doi.org/10.1016/j.margeo.2012.08.002

Yoshida, H., Sugai, T., Ohmori, H., 2012. Geomorphology Size – distance relationships for hummocks on volcanic rockslide-debris avalanche deposits in Japan. Geomorphology 136, 76–87. https://doi.org/10.1016/j.geomorph.2011.04.044

Young, S.R., Sparks, R.S.J., Aspinall, W.P., Lynch, L.L., Miller, A.D., Robertson, R.E.A., Shepherd, J.B., 1998. Overview of the eruption of Soufriere Hills Volcano, Montserrat, 18 July 1995 to December 1997. Geophys Res Lett 25, 3389–3392. https://doi.org/10.1029/98GL01405

5. New Heat Flow Measurements Offshore Montserrat: Advective Heat Flow Detected via MeBo Borehole Temperature Logging

Submitted to *The Journal of Geophysical Research-Solid Earth*

Matthew J. Hornbach[1,2], Michel Kühn[3,4], Tim Freudenthal[5], Jordan Graw[2], Christian Berndt[3], Katrin Huhn-Frehers[5], S.F.L. Watt[6], Benjamin J. Phrampus[2], Warren T. Wood[2]

[1]Huffington Department of Earth Sciences, Southern Methodist University, Dallas, TX, USA
[2]United States Naval Research Laboratory, 1005 Balch Boulevard, Stennis Space Center, MS 39529
[3]GEOMAR Helmholtz Centre for Ocean Research Kiel, Kiel, Germany
[4]Institute of Geosciences, Christian-Albrechts-Universität zu Kiel, Kiel, Germany
[5]MARUM, University of Bremen, Bremen, Germany
[6]School of Geography, Earth, and Environmental Sciences, University of Birmingham, Birmingham, UK

Key Points

- New heat flow measurements at the Lesser Antilles arc show evidence for advection within mass transport deposits.
- Advective heat flow in mass transport deposits at convergent margins may represent an important, under-reported source of heat flow.
- The MeBo acoustic logging thermistor provides a unique tool for identifying isothermal zones at unprecedented vertical resolution.

Abstract

New heat flow measurements collected at the Lesser Antilles Arc using a Hybrid Lister-Outrigger (HyLO) probe and a new logging-while-tripping MeBo70 drilling approach provide the first high-resolution (cm-scale) temperature-depth measurements across the Lesser Antilles volcanic arc and offer new insight into heat and fluid transfer at convergent oceanic margins. At multiple sites where logging-while-tripping MeBo temperature measurements were made, temperature increases linearly with depth in shallowly buried hemipelagic sediment but is isothermal or significantly hotter in deeper, coarser-grained sediments associated with mass flows. We interpret these isothermal zones as regions where advective heat flow dominates. The implication is that apparently conductive heat flow regimes observed in the shallowest upper 5-10 m of hemipelagic sediment across the Lesser Antilles Arc measured using standard lister-type probes may often unknowingly be influenced by deeper, advective flow along buried mass transport deposits. We suggest previous IODP-based heat flow measurements at this site, and perhaps other similar sites, are unable to identify advective flow due to the sparse

temperature measurements with depth. Since mass transport deposits are ubiquitous on convergent margins, these deposits may play a fundamental, widespread, and previously unrecognized role in fluid and heat transport at convergent zones.

Plain language summary

How do large colliding oceanic plates “cool off”, and what tools best measure this cooling process? While some studies suggest that heat is exchanged primarily through conduction, and therefore may depend on physical properties of the two interacting plates, other studies suggest advection—or direct movement of heat via fluid flow—is the primary driver of heat exchange. One reason this question remains unresolved is that the high-resolution temperature measurements required to assess whether conductive versus advective heat flow dominants at a particular site often do not exist. To address this issue, we provide the first cm-scale temperature-depth measurements from drilling at the Lesser Antilles-North American plate boundary. From these measurements, we show that advective heat flow appears to be facilitated by the presence of highly permeable landslide deposits. Since such deposits are typical for volcanic islands, advective heat flow may be far more common in these settings than previously thought because previous studies typically did not have the cm-resolution provided by MeBo drilling to detect this type of heat flow. The results support the idea that when two oceanic plates collide, they may transport and release much of their heat via fluid flow, not just conduction.

5.1 Introduction

Heat flow - the rate at which heat energy passes through the surface of the earth - is a fundamental geophysical measurement that provides insight into the subsurface structure, composition, dynamics, and history of the Earth (e.g., Beardsmore & Cull, 2001; Sclater et al., 1980). Traditionally, heat flow measurements in the marine environment are made using either thermistors intermittently deployed down boreholes during scientific ocean drilling (e.g., Heesemann et al., 2008), Lister probes (Lister, 1979), or using outrigged temperature sensors on core-barrels (Pfender & Villinger, 2002). In all cases the depth resolution of these temperature measurements is at best one measurement every few tens of centimeters in the upper 1-6 meters of sediment. Greater than 6 meters depth, where scientific drilling is required to make these temperature measurements, the temperature-depth resolution is even lower, with 1 measurement often made only every ~10 meters or more (e.g., Manga et al., 2012). Obtaining accurate, high quality, high-resolution heat flow measurements in the ocean is difficult due to several factors, including the complexity and cost of drilling, the time required to collect

temperature data, and the associated spatial aliasing caused by limited point measurements. Seafloor heat flux is therefore often inferred broadly over large areas (e.g., 1x1 degree grids) using indirect geophysical proxies such as shear wave velocities that often have both low precision and resolution, resulting in high uncertainty (e.g., Shapiro & Ritzwoller, 2004). Here, we assess heat flow across a transect of the Lesser Antilles arc by integrating new measurements made using a Hybrid Lister Outrigger (HyLO) Probe and a new approach that has the potential to provide higher temperature-depth resolution at the expense of lower temperature accuracy: borehole temperature-depth measurements acquired with a thermistor attached to the acoustic-logging tool on the sea floor drill rig MARUM-MeBo70 (Freudenthal et al., 2022; Freudenthal & Wefer, 2013). As we demonstrate here, this new and potentially insightful temperature-depth measurement approach provides cm-scale temperature resolution that enables us to better identify potential isothermal zones associated with changes in sediment permeability and advection. Our analysis indicates that the heat flow profile measured across the Lesser Antilles averages 56 mW/m^2, consistent with previously published machine learning model predictions (Graw et al., 2023), but that heat flow is highly variable with depth, and likely controlled by subsurface advection along both faults and higher permeability deposits associated with mass transport events. Specifically, we suggest that heat flow values derived at the Lesser Antilles Arc and Forearc may in part be the result of deeper-seated advection that is difficult to detect or constrain using traditional IODP or Lister-type heat flow measurements, as evidenced by high-resolution MeBo70 temperature measurements at several sites. This observation might explain why discrepancies sometimes exist between arc thermal models and arc thermal measurements: Lister and IODP-based heat flow measurements - the standard tools used to estimate heat flow - are often unable to differentiate advection and diffusion-dominated heat flow at these sites due to limited vertical resolution with depth - heat flow information that MeBo may better resolve.

5.2 Study Area: The Lesser Antilles Arc

Located at the eastern boundary of the Caribbean plate, The Lesser Antilles arc consists of more than 13 volcanic islands formed as a result of westward subduction of the North American plate below the Caribbean plate (Figure 5.1, inset). We focused collecting new heat flow measurements on the central Lesser Antilles Arc between the islands of Montserrat and Guadeloupe (Figure 5.1, inset), where several previously collected IODP cores and one IODP heat flow measurement (Site U1395) exists (e.g., Manga et al., 2012). The arc in this area initially formed east of Montserrat in the early Eocene (~55 Mya) and tectonic adjustment in

the mid-Miocene caused arc volcanism to migrate westward to its present location (Bouysse & Westercamp, 1990).

Both Montserrat and Guadeloupe are well-studied active volcanic islands in the Lesser Antilles (e.g., Wadge et al., 2014). On Montserrat, a long-lasting eruption, characterized by episodic lava-dome growth with intermittent intense explosive activity, began in 1995 at the Soufrière Hills Volcano, located in the southeast third of the island. Dome-collapse driven pyroclastic density currents and subsequent lahars devastated the southern part of the island, burying its capital, Plymouth (Kokelaar, 2002; Young et al., 1998). The former city, as well the southern half of the island, remains in a ~40 km^2 exclusion zone, uninhabitable today due to the risk of lahars, pyroclastic flows, and other eruption-related hazards (Miller & Calder, 2020). Although eruptions since 1995 are the only historically documented eruptive events on Montserrat, onshore surveying, marine sediment coring, IODP ocean drilling, and offshore active source seismic studies provide constraints on the nature, size and frequency of prehistoric events that have shaped the island. Soufriere Hills has been shaped by multiple andesitic effusive eruptions, with evidence for large-magnitude explosive activity in earlier stages of its history (Coussens et al., 2017). Offshore studies demonstrate that development of the island has been accompanied by several large (> 0.5 km^3) lateral collapses of the subaerial volcano and/or the submerged island flanks. These may be temporally connected with eruptive episodes, and at least 5 major events have been documented since ~250 ka from their offshore deposits, with additional smaller events – based on the identification of offshore turbidite deposits - occurring more frequently (e.g., Cassidy et al., 2013; Le Friant et al., 2008; Wall-Palmer et al., 2014).

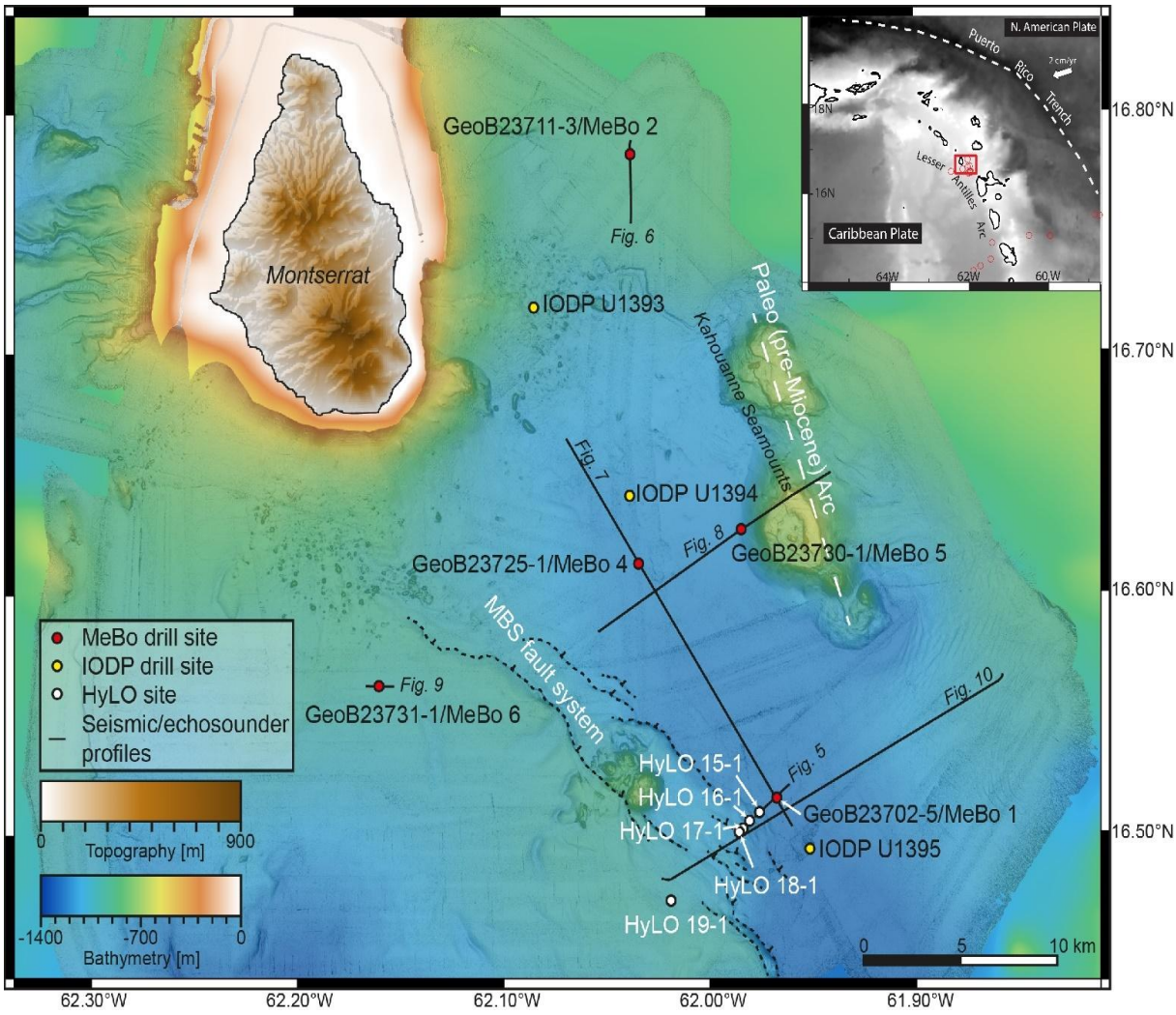

Figure 5.1: *Study Area: the central Lesser Antilles Arc (inset) between the islands of Montserrat and Guadeloupe with open red circles showing the location of quality heat flow values collected across the arc from previous drilling and heat flow studies (Fisher & Hounslow, 1990; Manga et al., 2012; Vacquier & Von Herzen, 1964). The main figure shows multibeam bathymetry collected in the region on the R/V Meteor in 2019* (Berndt et al., 2021) *merged with regional GMRT satellite data* (Ryan et al., 2009)*. The dashed black lines show the approximate location of a series of normal faults known as the Montserrat-Bouillante-Les Saintes (MBS) fault system that extends from Montserrat towards Guadeloupe and Les Saintes (based on* Feuillet et al., 2010 and Watt et al., 2012*). Solid Red dots, white dots, and yellow dots indicate heat flow measurements obtained using the HyLO probe, MeBo drilling, or previous Expedition 340 IODP drilling respectively. The solid black line shows the location of active source seismic profile collected across the arc in 2019.*

Marine coring and drilling studies indicate that the largest submarine mass transport deposits off the southern and eastern flank of Montserrat (e.g., Cassidy et al., 2013; Watt, Talling, Vardy, Heller, et al., 2012; Watt, Talling, Vardy, Masson, et al., 2012) involve large volumes of remobilized seafloor sediment, likely driven by the initial volcanic failure, that produced deposits that extend for many tens of kilometers from the island, reaching thicknesses of tens of meters. Comparable deposits, at an even larger scale, have been documented offshore other islands of the Lesser Antilles to the south (Deplus et al., 2001). Though the timing and location of these deposits are constrained, understanding both how and why marine sediments are remobilized by these events remains unclear and a topic of on-going research with multiple competing hypotheses (e.g., Le Friant et al., 2019; Watt, Talling, Vardy, Masson, et al., 2012). The two mass transport deposits above which we measured heat flow are defined from previous studies as “Deposit 2” and “Deposit 3” (e.g., Le Friant et al., 2015; Watt, Talling, Vardy, Heller, et al., 2012; Watt, Talling, Vardy, Masson, et al., 2012). Deposit 2 is an elongated, buried landslide deposit, covering an area of ~200 km² with a volume of ~ 10 km³ southeast of Montserrat (Lebas et al., 2011; Watt, Talling, Vardy, Masson, et al., 2012). According to previous interpretations of seismic and core data from IODP Expedition 340 and ROV-recovered rock samples, Deposit 2 consists of collapsed volcanic edifice material as well as remobilized and deformed hemipelagic sediments (Le Friant et al., 2015; Watt et al., 2015; Watt, Talling, Vardy, Heller, et al., 2012; Watt, Talling, Vardy, Masson, et al., 2012). Deposit 3 has a sub-circular shape and covers an area of ~ 59 km² with a volume of ~ 1.3 km³ (Lebas et al. 2011). Its hummocky surface partly protrudes the seafloor south of Montserrat and suggests a volcanic origin of the associated flank collapse (Lebas et al. 2011).

In situ physical properties of mass transport deposits offshore Montserrat vary significantly spatially, and likely play an important - though currently ill-defined - role in subsurface fluid flow, heat flux, pore pressure diffusion, and slope stability. Near the volcanic island shelf break of Montserrat, mass transport deposits typically consist of high permeability, sand-rich volcanoclastic debris avalanches bounded above and below by lower permeability hemipelagic mud (e.g., Hornbach et al., 2015; Koehn et al., 2022; Watt, Talling, Vardy, Heller, et al., 2012; Watt, Talling, Vardy, Masson, et al., 2012). Measured sediment permeability offshore Montserrat range from 10^{-11} to 10^{-15} m^2, however, it is likely that this range is even greater than 4 orders of magnitude as few measurements exist, especially in the most coarse and likely highest permeability sediment where drilling recovery is typically poorest. These debris avalanche deposits appear significantly more efficient (1-4 orders of magnitude higher

permeability) at transporting fluids than hemipelagic sediment (e.g., Hornbach et al., 2015, Koehn et al., 2022), although vertical faults also likely act as important conduits for fluid flow. At greater distances (>5 km) from the island , mass transport deposits offshore Montserrat generally become finer grained, and although their permeability is reduced, it remains higher than their bounding hemipelagic sediments (e.g., Koehn et al., 2022). Analysis of IODP cores and well logs of submarine slope failure deposits along this arc indicate that the mass-transport deposits are potentially overpressured (e.g., Hornbach et al., 2015; Lafuerza et al., 2014). One hypothesis explaining potential overpressure and slope failure associated with distal hemipelagic sediments adjacent to volcanic arcs is that more permeable volcaniclastic debris bounded by lower permeability hemipelagic sediment acts as a fluid flow path and a decollement along which sediment fails as pressures elevate with time (e.g., Lafuerza et al., 2014; Le Friant et al., 2015; Hornbach et al., 2015; Le Friant et al., 2019). Testing this hypothesis, however, requires a detailed understanding of fluid transport and fluid pressure in the subsurface that can confirm where differential pressures and variability in hydraulic head exists. Temperature measurements with depth provide a valuable additional tool for assessing not only heat flow, but also subsurface fluid flow caused by pressure differential, since advection may be caused by subsurface pressure differences.

Here, using a combination of *in situ* high resolution (cm-scale vertical resolution) temperature measurements from both a hybrid Lister probe and MeBo thermometer attached to a logging tool, we provide the first detailed assessment of heat - and, from this, fluid - transport in the subsurface at the Lesser Antilles Arc. Our analysis demonstrates that anomalously high temperatures exist with depth away from the volcanic arc, and that warm isothermal zones exist in more deeply buried, higher permeability, volcaniclastic slope failure deposits, consistent with focused lateral fluid flow within these zones.

5.3. Background heat flow theory

Heat flow - the amount of heat energy transferred through an area of the earth per unit time - represents a fundamental measurement used to identify the location of active tectonics, volcanism, heat transport, and subsurface fluid flow. Heat flow in the Earth is typically dominated by either conductive or advective processes, and the mechanism (conduction versus advection) provides important insight into the subsurface environment. Heat flow in oceanic crust is a function of plate age, with advection dominated heat flow in young crust and diffusion dominated heat flow in old crust. Specifically, in old (>30 Ma) tectonically quiescent regions,

heat flow in oceanic crust is usually low (<50 mW/m^2) (e.g., Sclater et al., 1980) and characterized by Fourier's Law of steady conductive heat transfer:

$$q = -k\nabla T \qquad \text{(equation 1)}$$

Where q is the heat flux per unit area (W/m^2), k is thermal conductivity (W/m*^{o}C)—a constant for a given homogenous material--and ∇T is the temperature gradient (^{o}C/m) in the x-, y-, and z-directions.

In tectonically quiescent regions where diffusive heat flow dominates, Earth's heat flow in the shallow (<1 km) crust is perpendicular to the surface and often assumed approximately constant in space and time with usually minor physical or temporal corrections (such as bathymetry, bottom water changes, sedimentation/erosion) applied. Where shallow marine sediments are homogenous and flat lying (as is routinely the case in marine basin settings), thermal conductivity generally varies between 0.9-1.5 W/m*K, and we typically observe a nearly linear increasing temperature-depth profile in these tectonically passive settings (e.g., Beardsmore et al., 2001).

In contrast, heat flow in geologically active areas is often high (>100 mW/m^2), dynamic in space and time, and frequently advection-dominated, with temperature sometimes increasing non-linearly with depth. In these geologically dynamic settings where subsurface fluid flow occurs, heat flow and subsurface temperature is often characterized by the time-dependent advection-diffusion equation:

$$\frac{dT}{dt} = \nabla(D\nabla T) - \nabla(vT) + S \qquad \text{Equation 2}$$

Where $\frac{dT}{dt}$ is the change in temperature T (^{o}C) with respect to time t (s) for a given location, $\nabla(D\nabla T)$ is the diffusive heat flow term where D is the thermal diffusivity (m^2/s), $\nabla(vT)$ is the advective term where v is the fluid flow velocity in a particular direction (m/s), and S represents any net temperature source or sink (^{o}C). Where sub-horizontal bedding exists, advective flow can be lateral, with fluids preferentially flowing along higher permeability sediments that may act as aquifers (e.g., Fetter, 2018). In settings where vertical fluid flow in the upper kilometer exceeds as little as ~0.03 m per year, the advective term in Equation 2 can dominate the heat flow process, resulting in temperature-depth profiles that often appear non-linear with depth (e.g., Bredehoeft & Papaopulos, 1965). In extreme cases where lateral fluid flow from a heat source is significantly greater than diffusive heat transfer, temperatures-depth profiles will also

sometimes appear nearly isothermal, or in instances where fluid flux changes at short time scale, even have a negative thermal gradient through some depth intervals (Figure 5.2C).

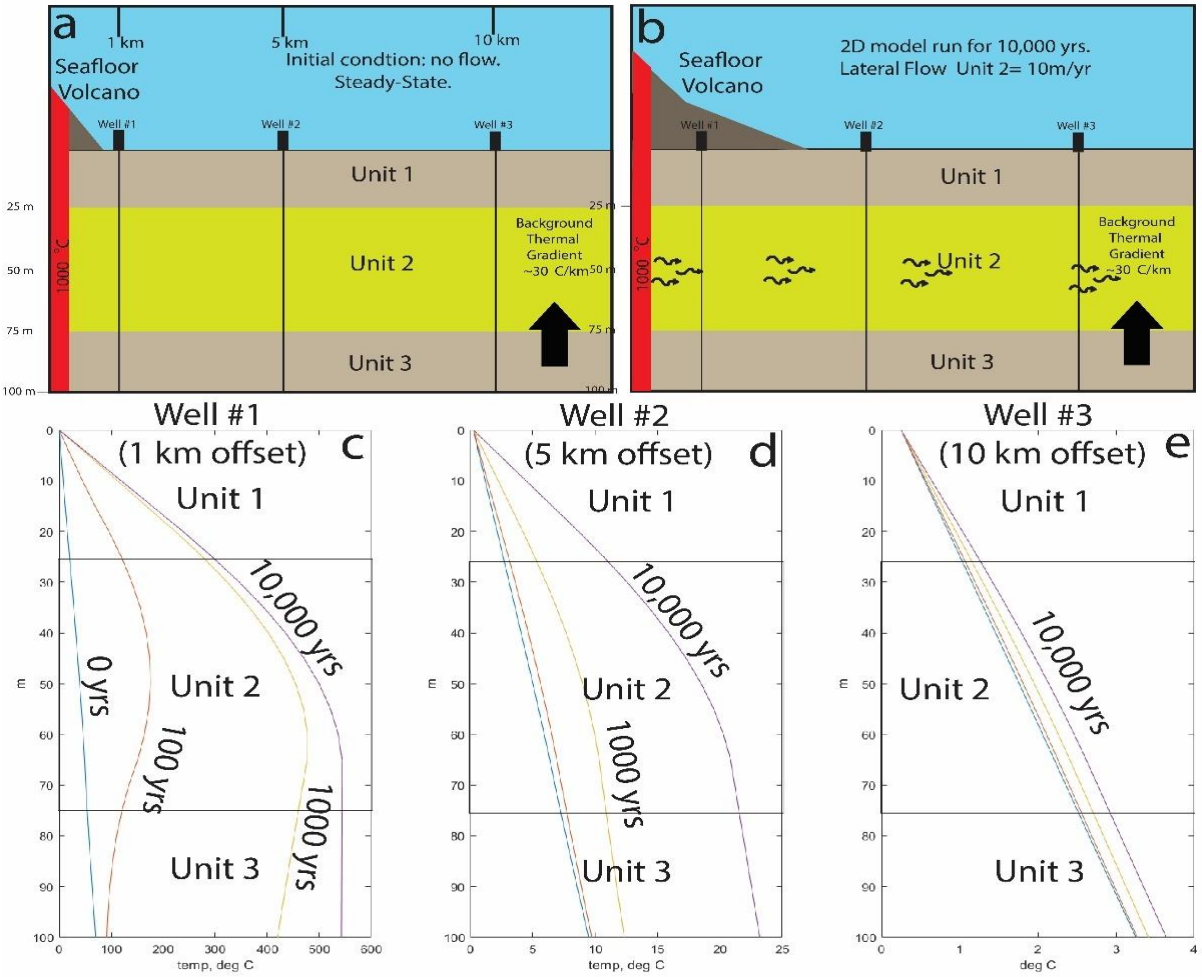

Figure 5.2: *Results from a simplified 2D advection-diffusion finite difference heat flow model showing the effect of lateral fluid flow on the temperature depth regime at three hypothetical wells located adjacent to a volcanic island over time. Here, advection occurs laterally only in Unit 2 from left to right at a rate of 10 m/yr (no flow occurs in units 1 and 3—heat only conducts in these units). At time t= 0 years, there is initially no lateral flow, and heat flow is diffusive, vertical, and steady state, with a background thermal gradient of 30 °C/km. The left edge of the boundary has a constant temperature of 1000 °C associated with a magmatic intrusion. The right boundary of the model is open; the upper boundary at the water-seabed interface is held constant, and the bottom boundary has a constant temperature. The model ignores possible influences of convection and buoyancy driven flow and provides a first-order picture of how temperature versus depth might vary at a site where advection preferentially occurs along a stratigraphic layer. A shows a schematic of the initial steady-state model with no fluid flow and locations of the wells; B shows the location of a higher permeability zone (Unit 2) along which*

flow occurs after t=0. Figures 5.2C, D, and E, show how the temperature-depth profile changes with time for t=0 (i.e., no flow and at steady state), 100 years, 1000 years, and 10,000 years for fluid flow laterally from left to right.

Pure diffusive heat flow versus pure advective heat flow represent endmembers of heat transport in the Earth, with nearly linear (due to limited variability in thermal conductivity) temperature-depth profiles often interpreted as steady, diffusion-dominated heat transport in homogenous sediment, and non-linear, isothermal or even negative temperature-depth profiles indicating advection-dominated and potentially non-steady heat transport (Figure 5.2). The shape and character of subsurface temperature-depth profiles therefore provide insight into subsurface heat and fluid transport in marine sediments: if fluid flow is dynamic and changing over short (< 1000 year) time periods, we may observe non-linear or even negative temperature-depth profiles (e.g., Figure 5.2C). In all instances, the apparent influence of fluid flow on temperature diminishes with distance from the heat source due to heat lost into the surrounding sediments as fluids flow laterally away, and as a result, it can be difficult to assess whether the linear temperature-depth profile measured in the upper few meters of the sea floor is a result of diffusion or broader-scale, longer-lived, deeper advective processes (Figure 5.2C vs 5.2E). For this study, we use new temperature-depth profiles collected along the lesser Antilles arc to gain insight into both shallow (HyLO) and deeper (MeBo70) heat flow character.

5.4 Methods

We acquired new temperature-depth measurements at the Lesser Antilles Arc in May 2019 during the SEKT cruise M154-2 on the R/V *Meteor*. Temperature-depth measurements were acquired with two tools: a 1.5 m long Hybrid-Lister Outrigger (HyLO) probe that was outrigged to the bottom of a 3 m gravity core barrel (Hornbach et al., 2021), and a thermistor attached to a MeBo acoustic logging tool that made downhole temperature measurements during acoustic logging while tripping of the drill string (Freudenthal et al., 2022). A preliminary study comparing the HyLO probe thermal gradients with the MeBo acoustic log thermal gradients in the upper 3 meters of sediment shows consistent thermal gradient results (Hornbach et al., 2021), implying the thermistor on the MeBo acoustic logging tool may represent a useful, yet currently untapped tool for measuring temperature with depth at drill sites. In total, these instruments provide thermal gradient and heat flow measurements across the volcanic arc at 10 new sites that extend from the upper 3-5 meters of sediment (HyLO probe measurements) to a maximum depth of ~50 mbsf (MeBo measurements).

5.4.1 HyLO temperature-depth measurements

The HyLO probes used for this study consisted of eight thermocouples spaced ~0.2 m apart inside a high-conductivity resin-filled stainless-steel rod (Hornbach et al., 2021). In all cases, the bottom thermocouple was mounted 41 cm above the bottom of the 3 m core barrel, so that the probe head was approximately ~1.1 m below the top of the 3 m core barrel. Two steel outrigger brackets - one attached to the probe head, the other attached to the tip of the probe lance - outrigged the probe approximately 14 cm from the core barrel. The probe head, where the probe is powered and data are stored/transmitted also contains a thermistor, internal pressure sensors and a three-component accelerometer to measure orientation of the probe and gravity corer.

For each HyLO probe deployment on the 3-m gravity core barrel, we held the probe approximately 100 m above the sea floor for a minute to calibrate thermistors. Probes were inserted into the seafloor for approximately 5-7 minutes at each deployment site to allow subsurface temperatures to decay towards steady-state equilibrium after initial frictional heating. Once back on deck, we downloaded data and calculated steady state temperature and associated uncertainty at each thermistor following the approach of Villinger & Davis (1987). With initial temperatures constrained, we then generated preliminary temperature-depth plots and removed any temperature outliers associated with either anomalously sandy zones where temperatures often fail to converge to steady state via the Villinger & Davis (1987) approach - likely due to localized advection in sand-rich bodies - or in the upper meter below the seafloor where temperature may be influenced by bottom water temperature changes (Vogt & Sundvor, 1996). We also corrected for penetration depth profiles using insertion angle reported in accelerometer data. With steady state temperature and uncertainty for each sub-seafloor thermistor constrained, we then applied a least-squares fit to the temperature-depth profile to calculate the thermal gradient at each site (Figure 5.3). We estimate uncertainty in the thermal gradient by applying a Monte Carlo approach where we randomly vary each steady state temperature uncertainty by two-sigma. Finally, we account for bathymetric thermal refraction effects by using the method described in Manga et al. (2012) that integrates regional bathymetry data with ocean temperature-depth profiles.

5.4.2 MeBo temperature-depth measurements

We measure temperature using a thermistor that is attached to the MeBo acoustic logging tool (Freudenthal et al., 2022). This thermistor extends away from the outer wall of the logging tool

and collects data during acoustic logging. For these measurements, the drill string is first pulled up approximately 1 pipe section (~2.5 m), and the acoustic tool is then dropped through the drill casing such that the top of the tool catches the bottom of the drilling string, and the bottom of the tool is located in the open borehole below the drill string, measuring the borehole fluid temperature in direct contact with the formation. As each 2.5 m of the casing is recovered at the seabed, the tool is pulled upward with the drill string, recording formation acoustic velocities and borehole temperature - an approach known as "logging-while-tripping".

5.4.2.1 The MeBo Logging-While-Tripping processes

The process of tripping the logging tool from the bottom of the drill hole to the sea floor using MeBo takes significant time (typically several hours depending on hole depth) because the acoustic tool rests at the base of the drill pipe. This requires slowly unthreading, tripping, and racking each individual section of 2.5 m long pipe. During pipe racking, the thermistor will be stationary for several minutes. Also, when pipe motion occurs during recovery, the trip-out speed is low (~0.01 m/s) (Freudenthal et al., 2022). The thermistor (an integrated platinum resistance sensor - PT1000) outrigged on the acoustic logging tool has a small (<2 mm) diameter, and, therefore, a rapid thermal-relaxation time (Carslaw et al., 1962): tests we conducted with the sonde where we lowered it into a cold bath indicate the thermistor and tool approaches to within 0.001 ^{o}C of equilibrium in less than 2 seconds. With a sample rate of 0.5 Hz, the thermistor is capable of logging instantaneous temperatures during tripping every ~2 cm. Alternatively, we can also estimate an average temperature every 2.5 m by averaging the temperature data collected during the several minutes the tool is stationary for pipe racking (Freudenthal et al., 2022). In general, during the pipe racking processes when the thermistor is stationary, we observe a slow but steady increase in temperature with time. This rate of temperature warming, defined as the Temperature Adaption rate, or "T_{adapt}", is usually positive due to the fact that the formation is warming up after initially being cooled down by the flushing of bottom water during drilling. T_{adapt} is typically highest at the greatest depths since the difference between bottom water and formation temperature is greatest at the deepest depths (Freudenthal et al., 2022), and the time between flushing and logging is shortest at the bottom of the hole during the logging-while-tripping process. As the tool measures temperature at shallower depth, we would anticipate the T_{adapt} rate to remain positive, but decrease in magnitude since there has been both more time for upper part of the formation to re-equilibrate and less of a difference between formation and bottom water temperature at shallower depths.

Following the method of Freudenthal et al. (2022), we focus our analysis on temperature time series data collected when the tool is stationary during pipe racking, and from this, quantify (1) average temperature during the stationary phase, (2) temperature adaption rate (T_{adapt}) and (3) temperature variability via the coefficient of determination value (R^2) (Freudenthal et al., 2022). The magnitude of both T_{adapt} and R^2 provide important insight into mechanisms controlling heat flow at each location: when temperatures at a particular depth converge slowly and smoothly towards a steady state value with time such that the T_{adapt} rate is low and R^2 value is high, diffusive heat flow likely dominates. In contrast, time series temperature data where erratic or highly variable absolute T_{adapt} values and/or low R^2 values exist indicate more complex - potentially advective - heat flow. In the very few instances where an anomalous (negative T_{adapt} value) occurred in past studies, the sediments encountered were either associated with gas hydrate destabilization (an endothermic process), or a sand-rich turbidite zone (Freudenthal et al., 2022). We therefore use T_{adapt} and the R^2 values to estimate not only temperature, but also to distinguish more clearly whether diffusive versus more dynamic and potentially non-diffusive heat flow dominates at a particular depth. The trip out of the drill string may cause some turbulence within the borehole. The duration of the stationary phases between the trip-out phases vary typically between 5 and 20 minutes depending on the ease of drill pipe thread disconnection. In order to account for this, we start the analysis of the temperatures 50 s after stop of tripping and calculate T_{adapt} and R^2 by linear regression of temperature versus time. The average stationary stage temperature (T_{av}) is calculated as mean temperature within the time period 50 to 250 s after stop of tripping.

Previous analysis of MeBo acoustic tool thermistor data collected using this approach (i.e., assessing temperature during the pipe threading and racking process) indicates subsurface temperature approaches steady-state values with average thermal gradients (measured by fitting a line through all of the measured MeBo temperature-depth data) similar to those observed using standard heat flow measurement (Freudenthal et al., 2022). However, raw MeBo temperature measurements will typically result in an underestimation of the formation temperature, since the drilling process generally cools the formation, with the most significant differences expected at the greatest depth (Freudenthal et al., 2022). This cooling effect is caused by colder seawater being circulated downward into the hotter sediments during the drilling processes. Specifically, as the drill string is lengthened and drilling continues downward, seawater is circulated intermittently at rates typically of 20-50 liters/minute for a few minutes to help facilitate drilling. Intermittently circulating colder fluids from the seafloor

into the warmer formation will cause the formation to cool, and as a result, can cause an anomalously low thermal gradient using the Freudenthal et al. (2022) approach. As more time passes between fluid circulation and temperature measurement, the more the temperature equilibrates towards steady state, and the closer the subsurface temperatures will be to their true thermal equilibrium. Additionally, the less fluid circulation that occurs during temperature logging, the more accurate the subsurface temperatures will be, since the subsurface will be less disturbed by the injection of colder fluids into the subsurface. In unfortunate instances where the logging tool is stuck and fluid circulation must occur to free the temperature logging tool, we would expect to observe a sharp reduction in temperature at the depth where fluid injection occurs, followed by a positive increase in temperature with time at that particular depth as the system slowly starts to warm back up towards equilibrium after circulation stops. Importantly, at 4 of the 5 MeBo drill sites, no significant fluid circulation occurred once temperature logging and tool tripping commenced. At MeBo site 4, however, we were forced to circulate fluid during tool removal at multiple depths due to the tool getting stuck in the formation. Because of this, we expect temperature measurements at this site to be systematically low and have higher uncertainty. We also very briefly circulated fluid at MeBo site 5, but this occurred near the very end of logging, and, as we later show, appears to have had minimal impact on thermal gradient measurements.

5.4.2.2 Estimating MeBo Thermal Gradients with Numerical Modeling

To remove the effects of drilling fluid circulation and estimate *in situ* steady-state thermal gradient at each MeBo site, we follow a method similar to Freudenthal et al. (2022) where we model in 4D (3D in space and time) the drilling process using a finite difference cylindrical heat conduction model. The cylindrical model, consisting of 20,000-40,000 cells (depending on drill depth) with a radial cell length of 1-3 mm, assumes the top boundary condition maintains a constant seabed temperature, the bottom boundary condition maintains constant heat flow, the left boundary - representing the central axis of the borehole - and the right boundary located at least 0.5 m away from the borehole maintain open (Neumann) thermal boundary conditions. The model assumes a drill pipe with a thermal diffusivity of 3.81×10^{-5} m^2/s that has an inner and outer diameter 85 and 95 mm, respectively; a borehole diameter of 103 mm filled with fluid with a thermal diffusivity of 1.46×10^{-7} m^2/s, and a constant thermal diffusivity for all sediment of 3.33×10^{-7} m^2/s - a value consistent with average measurements for the region (e.g., Manga et al., 2012). The model mimics the drilling process by forward modeling drilling for each time step based on the drilling logs, where we change the thermal

diffusivity of the formation with time depending on the reported drill pipe depth, consistent with the Freudenthal et al. (2022) method. Additionally, when borehole flushing occurs during the drilling process (flush timing is noted in associated Figures for each MeBo site), we set all borehole temperatures to bottom water temperatures. We assume all sediments adjacent to the borehole experience diffusive heat flow and that at time t=0 (immediately prior to drilling) the temperature of the sediment is in thermal equilibrium and a linear thermal gradient exists with depth (since sediment diffusivity is held constant). Once drilling is completed, we continue running the model during the logging-while-tripping process to assess both temperature and T_{adapt} in the borehole with time. We assume no advection or fluid circulation occurs during the logging while tripping process, again, similar to the approach of Freudenthal et al., (2022).

We estimate in situ thermal gradients with this model by running the model multiple times with multiple different thermal gradient starting conditions, and from this, determine which modeled borehole temperatures best replicate observed MeBo temperature measurements during the logging-while tripping process. Specifically, in instances where we use *too low* an initial thermal gradient, the model will significantly *under-predict* both observed MeBo average temperatures and positive T_{adapt} rates since the formation temperature values used in the model will be too low. Conversely, in instances where our numerical starting model uses *too high* a background thermal gradient, the model will *over-predict* both average MeBo temperature values and positive T_{adapt} rates. As noted in Freudenthal et al. (2022), we require the model-predicted thermal gradient to never produce a temperature that exceeds measured MeBo temperatures, as this would require a negative T_{adapt} rate for the temperature to converge—a non-physical result if heat flow is diffusion dominated. An example of the MeBo modeling script (written in MATLAB) applied to MeBo site 6 is provided in the supplementary material.

It is important to recognize, as highlighted by Freudenthal et al. (2022), that this numerical model only applies to sites where diffusive heat flow dominates (both in situ and during the drilling process). Freudenthal et al. (2022) notes that diffusion dominated systems should only generate positive T_{adapt} rates and that anomalous negative T_{adapt} rates are likely evidence of dynamic, non-diffusive heat flow associated with sediment/fluid mobilization, gas hydrate dissociation, or other convection/advection related processes (Freudenthal et al., 2022). Where we observe negative T_{adapt} rates during the logging-while-tripping process, we cannot apply the model, since advective processes likely dominate. Nonetheless, in the discussion section of the text, we do provide potential explanations for why we observe these negative T_{adapt} rates at some locations during the logging-while-tripping process.

5.4.3 Calculating heat flow

Estimating conductive heat flow at the seafloor requires knowing both thermal gradient and thermal conductivity of the sediment. Both the HyLO and MeBo temperature-depth measurements provide thermal gradient values. IODP Expedition 340 previously collected hundreds of thermal conductivity measurements at depths ranging from 0 to 220 m below the seafloor across this region. These measurements, made using a thermal conductivity needle probe, provide accurate thermal conductivity measurements on fine grained, low permeability, undrained sediment only. Results from Expedition 340 indicate that shallowly buried fine-grained sediments offshore Montserrat have a nearly uniform thermal conductivity, averaging 1.04 +/- 0.1 W/mK, with no clear dependence on depth in the upper 50 m at this site (Manga et al., 2012). We therefore use this value to estimate heat flow at depths where temperature measurements exist and the HyLO and MeBo tools encountered fine grained sediments.

5.4.4 Additional geophysical data collection to constrain heat flow

For all heat flow measurements, temperature-depth data were integrated with regional active source seismic, bathymetric, and sediment physical properties data derived from previous seismic surveys, Expedition 340 drilling, or associated/adjacent core interpretations - where available (Hornbach et al., 2015; Koehn et al., 2022; Watt, Talling, Vardy, Heller, et al., 2012; Watt, Talling, Vardy, Masson, et al., 2012) - to place thermal gradients and heat flow measurements into stratigraphic and structural context. The stratigraphy west and south of Montserrat has been extensively imaged in the past by several active source seismic survey campaigns (Lebas et al., 2011; Watt, Talling, Vardy, Heller, et al., 2012; Watt, Talling, Vardy, Masson, et al., 2012). During the *R/V Meteor* Cruise M154-1 in April and M154-2 in May 2019 we collected additional high-resolution multi-channel seismic data and Parasound echosounder data (e.g., Figures 5.4-5.10) (Kühn et al., 2023, 2024). Multichannel seismic data were acquired with a 25 to 87.5 m long (16 to 56 channels) streamer with a channel spacing of 1.56 m. The seismic source consisted of two 105/105 cubic inch GI-Guns fired at a shot interval of 5 seconds. Seismic data processing included trace editing, highpass filtering (25 Hz cut and 55 Hz slope corner frequencies), denoising, deconvolution, stacking and finite-difference migration with a gradient velocity model (1580 m/s to 1725 m/s) based on OBS measurements (Kunde, 2020). Detailed information on the acquisition and processing of the Parasound sediment echosounder data can be obtained from Berndt et al. (2019) and Huhn et al. (2019). Parasound data have an automatic gain-control with a window length of 10 ms applied to the

data and depth conversions were performed with a constant acoustic velocity of 1500 m/s. The bathymetric data that were used for the map in Figure 5.1 can be found in Berndt et al. (2021).

5.5 Results

New seismic data reveal two generally distinct seismic facies that we use to characterize temperature depth measurements. The prevalent sub-seafloor facies consist of lateral continuous, coherent, parallel seismic reflections with generally consistent amplitudes. Expedition 340 Drilling results (e.g., LeFriant et al. 2015; 2019) confirm that these homogeneous, sub-horizontal reflections consist of well-stratified, layered hemipelagic sediments. The second set of facies occurs in discrete, broadly horizontal packages and is typified by partly chaotic, discontinuous and relatively transparent (i.e., low amplitude) reflections that represent mass transport deposits (Crutchley et al., 2013; Lebas et al., 2011; Watt, Talling, Vardy, Heller, et al., 2012; Watt, Talling, Vardy, Masson, et al., 2012) (e.g., Figures 5.4, 5.5, 5.6, 5.7). IODP Expedition 340 cores showed that these mass transport deposits can consist of both deformed or remobilized hemipelagic sediments and volcanic debris (Le Friant et al. 2015).

Using seismic, echosounder, and multibeam data as a guide for targeting heat flow measurement sites, we successfully obtained 5 closely spaced heat flow measurements across the arc using the HyLO system and 5 additional regional heat flow measurements adjacent to the arc axis both to the south and east of Montserrat via MeBo drilling (Figure 5.1). Merging these 10 measurements with other heat flow measurement in this area (e.g., Fisher & Hounslow, 1990; Manga et al., 2012; Vacquier & Von Herzen, 1964) (Table 1), we generate a new and more complete analysis of the heat flow regime across the northern Lesser Antilles arc. Analyzing the character of temperature-depth measurements at MeBo sites, we observe evidence for advective fluid flow at multiple drill sites where significant negative T_{adapt} values are reported. We use this information to note where the strongest evidence for advective versus diffusive heat flow exists across the region.

5.5.1 HyLO results

We deployed the HyLO probe successfully five times along a profile perpendicular to the arc (Figure 5.1). For all five insertions, at least 4 of the 8 thermistors penetrated the seafloor with the probe orientated within ~2 degrees of vertical, indicating no significant dip angle corrections were necessary. Temperature at all five HyLO sites linearly increases with depth

(Figure 5.3). We observe the highest heat flow values (~420 mW/m^2) at Site 16-1 in a heavily faulted zone known as the Montserrat-Bouillante-Les Saintes (MBS) fault system located near the arc between the active volcanic centers of Montserrat and Guadeloupe (Figure 5.1). We observe the lowest HyLO heat flow value (~57 mW/m^2) at site 19-1, the most distant HyLO site from the arc, located approximately 5 km west of the MBS fault system. Heat flow increases systematically as we approach the MBS fault system, where seismic data reveal several faults breaching the seafloor.

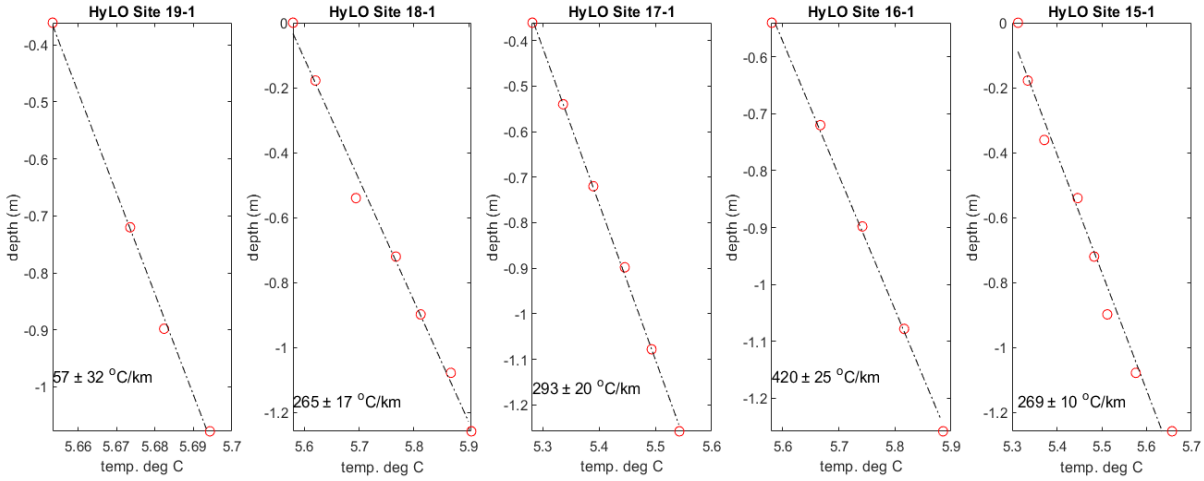

Figure 5.3: *Temperature depth profiles for each of the 5 HyLO sites with a linear best-fit line through each. Sensor depth was estimated based on the known location of the HyLO probe on the gravity corer and the mudline measured on the core barrel. Thermal gradient uncertainty is estimated by randomly applying up to 2-sigma uncertainties for each of the temperature measurements for 10,000 iterations, and assigning a best fit for each. Raw temperature-time data for each HyLO probe deployment are included in HyLO Supplemental Datasets 1 through 5 and correspond to HyLO Site 15-1 to 19-1 as labeled in each of the dataset headers.*

5.5.2 MeBo results and initial interpretations

We collected temperature-depth profiles at five MeBo sites at distances ranging from ~1-15 km from the MBS fault system at maximum depths below the seafloor ranging from ~23-60 m. At the one MeBo Site (MeBo Site 1) located near (within 1 km) of a HyLO HF measurement (HyLO Site 15-1), we observe similar (consistent to within uncertainty) heat flow estimates. Nonetheless, the MeBo measurements provide deeper temperature-depth measurements compared to HyLO, and suggest more dynamic heat flow conditions exist at greater depths. At each of the MeBo drill sites, temperature-depth profiles increase approximately linearly in

shallow (upper 5-10 mbsf) zones where hemipelagic mud was recovered or inferred, however, wherever recovery was poorer due to higher sand content (as evidence by poor core recovery, chaotic seismic reflections or direct observations confirmed by prior IODP drilling/coring (e.g., Le Friant et al., 2019), we repeatedly observe anomalously warm isothermal zones and negative T_{adapt} rate values, resulting in greater heat flow estimate uncertainty in these sand-rich zones. Below we provide more detailed results for heat flow at each MeBo site.

5.5.2.1 GeoB23731-1/MeBo Site 6 heat flow results

GeoB23731-1/MeBo Site 6 was drilled in a water depth of 1189 m along the flank of a broad, generally featureless bathymetric plateau approximately 7 km west of the MBS graben (Figure 5.1). Temperature was measured from 23-0 mbsf at this site during the upward progression of logging-while tripping. This site arguably provided the simplest results as no flushing was required during logging-while-tripping, and besides a small negative temperature anomaly during tool insertion (due perhaps to advection associated with tool insertion into the borehole), T_{adapt} is consistently small and positive (Figure 5.4), as anticipated at a MeBo drill site where diffusive heat flow dominates (Freudenthal et al., 2022). The temperature-depth profile at the site appears nearly linear (Figure 5.4), and applying an initial, raw best-fit to the T_{av} values measured at each pipe-wracking stage yields a low average thermal gradient with low uncertainty of 27 +/-4 °C/km. As noted in the Methods section, this observed gradient represents a minimum as it neglects the impact of fluid circulation during drilling.

Since we observe both a nearly linear thermal gradient in the MeBo raw temperature-depth data and positive T_{adapt} values (as predicted by numerical models), MeBo site 6 represents an ideal candidate for determining the true *in situ* steady-state thermal gradient using the numerical model approach of Freudenthal et al. (2022). We therefore estimate the *in situ* thermal gradient at this site by running a suite of 3D heat flow models where we varied the thermal gradient in 5 ˚C/km increments from 30 ˚C/km-100 ˚C/km, and from this, assess which thermal gradient best fits MeBo 6 observations (Figure 5.4C-E).

Modeling results indicate that the true *in situ* thermal gradient at MeBo 6 is approximately 75 +/- 10 ˚C/km, with the moderately high uncertainty due multiple thermal gradient values (ranging from 65-85 ˚C/km) resulting in nearly identical least squares fit. This value is consistent with the nearest HyLO measurement (Site 19-1, 57 +/-32 ˚C/km) that is also located west of the MBS fault system on the same oceanic plateau, implying this region maintains a modest heat flow compared to values measured closer to the active fault system.

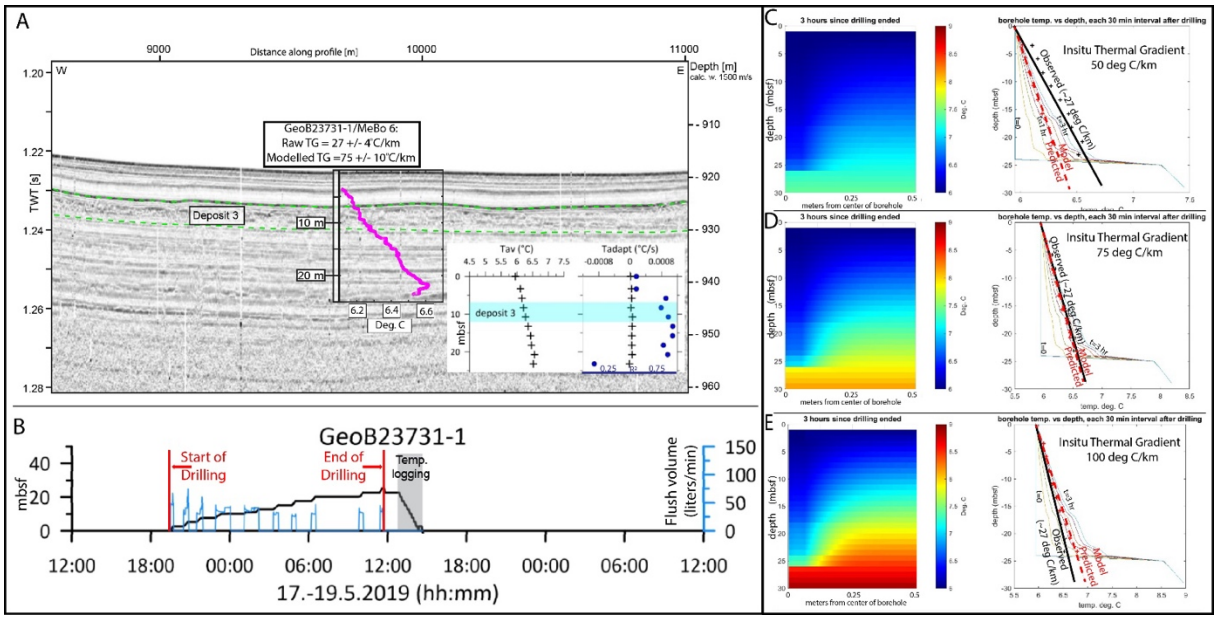

Figure 5.4: *(A) Raw heat flow temperature depth profile at GeoB23731-1/MeBo Site 6 (pink points) overlain on Parasound sediment echosounder line M154-1-P7019, with inset showing both average stationary stage temperature (T_{av}) and T_{adapt} values (blue dots are R^2 values) versus depth. (B) Time versus drill depth and borehole fluid circulation at MeBo Site 6. (C-E) Radial heat flow modeling results for three different background heat flow scenarios: 50 ˚C/km (C), 75 °C/km (D), 100 °C/km. The left side of C-E) shows the model-predicted temperature-depth profile at the end of logging-while-tripping for the three different thermal gradient scenarios. The right side (C-E) shows the model-predicted (red) temperature-depth-time values versus the MeBo observed value of temperature-depth-time during logging-while-tripping. We obtain a best fit with a thermal gradient of ~75 ˚C/km.*

5.5.2.2 GeoB23702-3/MeBo Site 1 heat flow results

GeoB23702-3/MeBo Site 1 was drilled to a depth of ~40 m below the sea floor in a geologically more dynamic site compared to MeBo 6, approximately 1 km east of the main MBS fault system and a kilometer east of HyLO Site 15-1 (Figure 5.5). The logging profile at this site was disturbed by significant flushing during drilling, and after drilling initially to a depth of 10 m, the tool had to be recovered, then redeployed resulting in significant shallow water flushing. Additionally significant flushing occurred at the very base of the well during trip out, and as a result, bottom temperatures in the well at depths greater than 25 mbsf are ignored and we only model temperatures for times after the final flushing occurs (i.e., the last three hours of logging-while-tripping) (Figure 5.5).The temperature recorded between 10-20 mbsf appears remarkably isothermal but with positive T_{adapt} (Figure 5.5). The isothermal zone is coincident with a zone

of sand-rich sediments and low core recovery. Surprisingly, temperature adaption rates turn clearly negative from 5-10 mbsf at the boundary between the sand-rich sediment (below) and more clay-rich sediment (above)—an indication of possible advection driven processes at these shallow depths perhaps associated with fluids flowing from the sand rich zones up the borehole, as we will discuss later (Figure 5.5).

Results indicate the temperature-depth profile in the upper 9 m of sediment is approximately linear with depth, averaging ~214 ˚C/km (+/- 130 ˚C/km) - a high value as this represents perhaps a minimum thermal gradient measurement - however, it is comparable to values measured approximately 1 km away at the adjacent HyLO site 15-1 of 269 ˚C/km (Figure 5.3). In general, however, it is difficult to fit a robust thermal gradient to these data with confidence due to (1) significant curvature observed in the temperature depth profile below ~10 meters, and (2) negative T_{adapt} values in the upper 10 mbsf that imply possible advection. Sediments in the upper ~10 m of the drill site consist predominantly of fine-grained, low permeability hemipelagic muds and silts (Huhn et al., 2019) that are typically associated with conductive, linear temperature depth profiles, and it is therefore surprising that we observe negative T_{adapt} values that imply advection at these depths. From 10 to ~25 m depth below the seafloor, where temperatures appear approximately constant at 6.6 to 6.8 ˚C, MeBo core recovery was poor, however, sediments from Expedition 340 drilling in this interval are known to contain higher permeability sand-rich material interpreted as mass transport Deposit 2 (e.g., Koehn et al., 2022).

Model results for this site are ambiguous due to the erratic nature of temperature with depth at this site, particularly for depths greater than ~12 meters. Applying a best fit to model results with observations. We estimate a high thermal gradient of ~800 °C/km. If we analyze only measurements shallower than 10 m, the best fit thermal gradient is closer to ~400 °C/km. The observations that (1) the diffusive model can only best explain our observations with a remarkably high thermal gradient and (2) clear zones where negative T_{adapt} values exist, supports the hypothesis that advective flow likely occurs at this site.

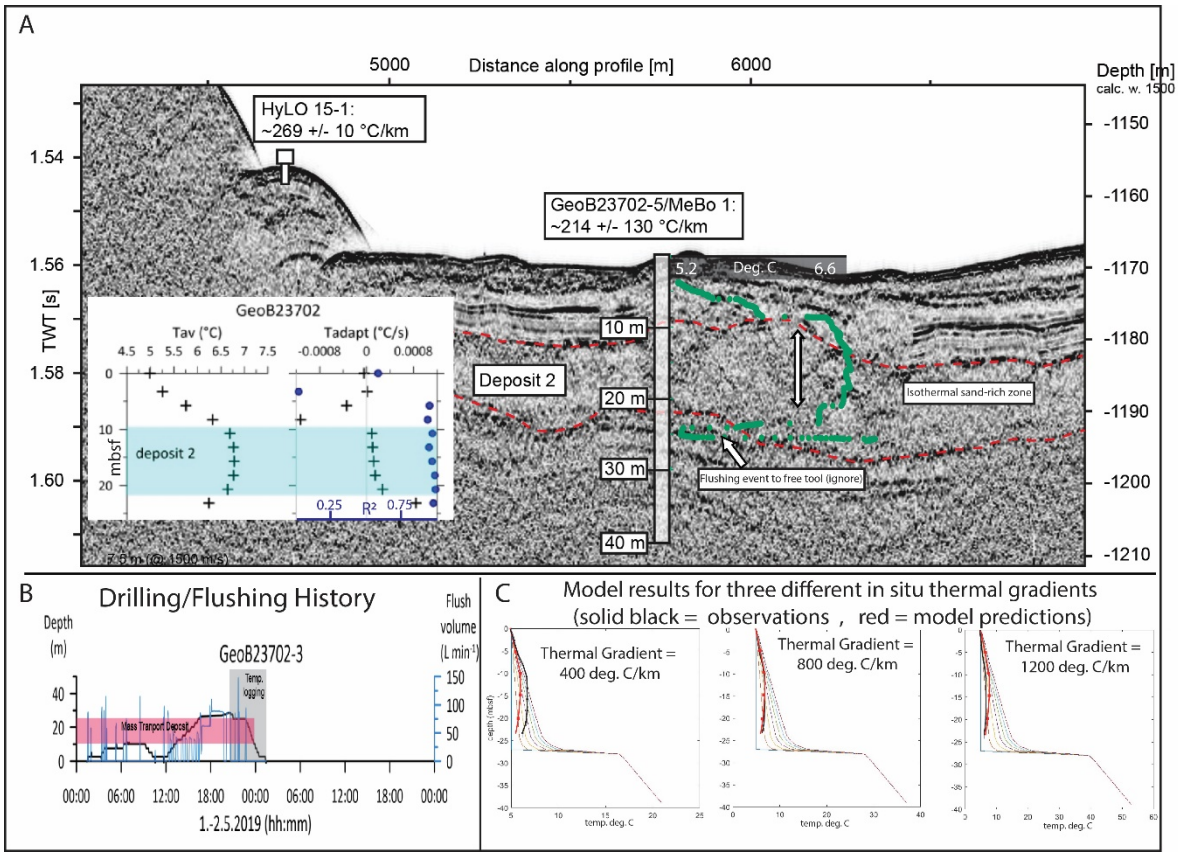

Figure 5.5: *(A) Raw temperature depth measurements at GeoB23702-5/MeBo Site 1 (green dots) overlaying Parasound sediment echosounder line M154-2-P1000. The area between the red dashes with poor seismic reflectivity represents the interpreted location of Deposit 2. The left inset shows average temperature values with depth for borehole stationary stages (left), and, on the right, the T_{adapt} (+) values and R^2 values (blue dots) versus depth. A clear correlation exists between the location of Deposit 2 and the isothermal zone observed in the temperature-depth profile at the MeBo drill site. An unusually strong negative T_{adapt} occurs at the boundary between low-permeability clay-rich sediments above 10 m and sand-rich sediments below, implying temperature is cooling just above the isothermal zone with time as that it recently warmed, despite significant fluid circulation of seawater at this depth during drilling. (B) the fluid circulation history during drilling and logging at this site. At a depth of 10 m, the drilling tool had to be recovered and redeployed. We account for this circulation and drill timing in thermal modeling. (C) model results for logging-while-tripping for the time period after the last fluid circulation occurs, with results shown for assumed in situ thermal gradients of 400, 800, and 1200 °C/km (left to right).*

5.5.2.3 GeoB23711-3/MeBo Site 2 heat flow results

GeoB23711-3/MeBo Site 2 was drilled to a depth of ~65 mbsf at a location approximately 14 km east of the volcanic arc and ~4 km north of the Deposit 2 headwall (Figure 5.1). Temperature was measured to a depth of ~64 mbsf at this site and no flushing was necessary during logging-while-tripping. The temperature-depth profile increases step-wise with depth with small near isothermal zones occurring at a depth of 25-35 mbsf, where large negative absolute changes in T_{adapt} were measured, and a known gravel layer exists in the sediment (Figure 5.6). We observe anomalous negative T_{adapt} values from 5 to 35 mbsf, implying non-diffusive thermal processes in this region. rates. The thermal gradient for the well averages ~84 $^{\circ}$C/km (Figure 5.6). Deeper than 35 mbsf, the temperature depth profile is more variable. Several minor isothermal zones appear to exist in the 35-63 mbsf depth zone, including 40-43 m depth, 49-55 m depth, and 59-64 m depth. Although it remains unclear if these isothermal zones are associated with changes in sediment character due to limited core recovery, what is clear is that the change in the slope of the temperature-depth profile at ~25 m depth correlates with a strong seismic reflection that has been interpreted to represent a sand/gravel-rich layer associated with the Deposit 2 failure further downslope of the drill site (e.g., Watt et al., 2012a). T_{adapt} becomes weakly positive again just below the gravel layer, at a depth of ~35 m, implying diffusive heat flow dominates below this depth. Applying the 3D radial diffusive heat flow model to this site where we again account for fluid circulation during drilling, we estimate a true *in situ* thermal gradient of 205 +/-20 $^{\circ}$C/km, or approximately 2.4x the raw measurement - a offset value consistent with previous modeling studies (Freudenthal et al., 2022). We speculate that the high thermal gradient value at this site may be associated with deeper advective flow away from the volcanic arc or along basement faults (Figure 5.6).

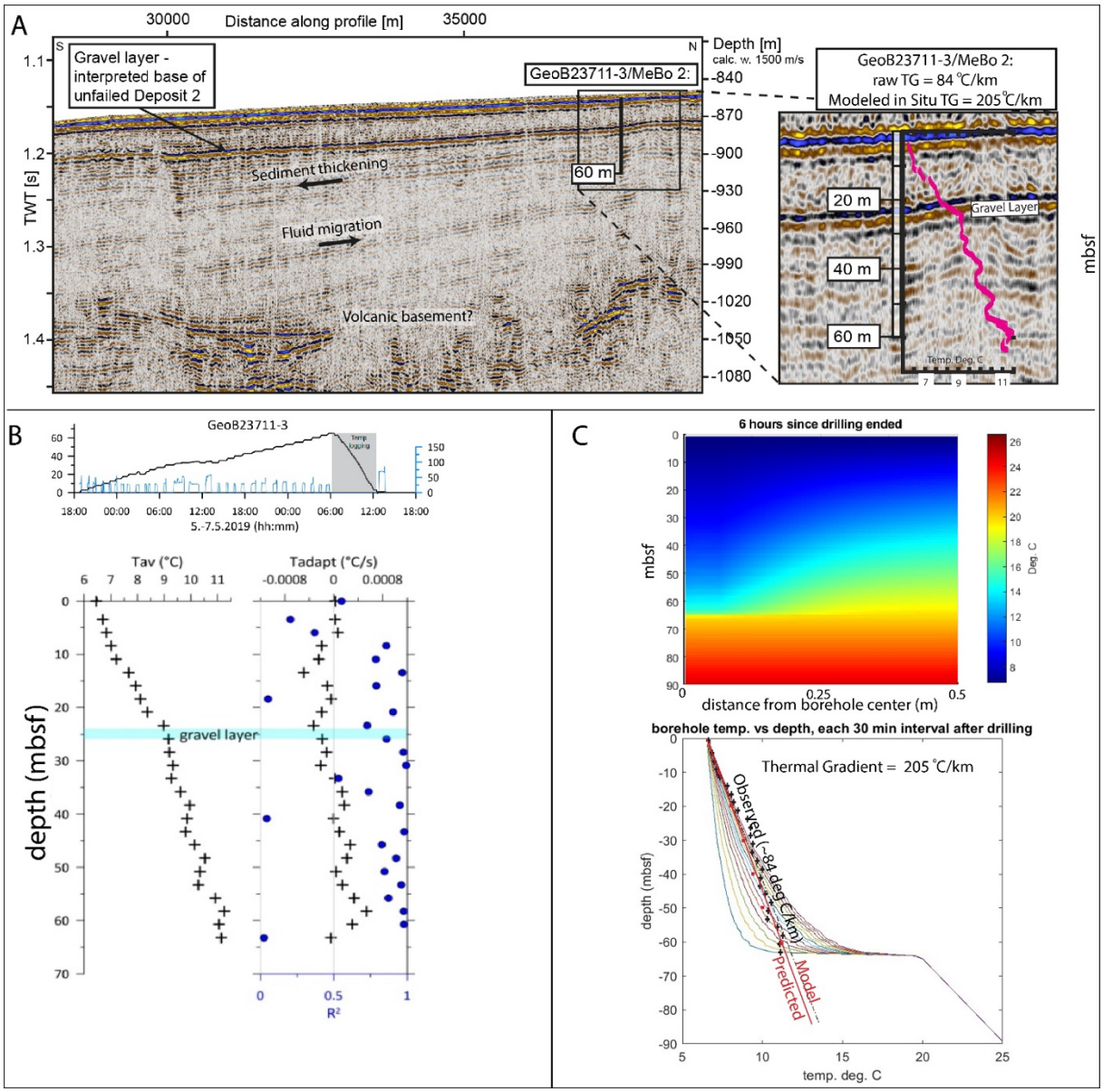

Figure 5.6: *(A) Raw heat flow temperature depth profile at GeoB23711-3/MeBo Site 2 overlain on seismic line P6002 (A, inset on right). The minimum thermal gradient estimated from the raw temperature-depth profile at the site is 84 °C/km. The drill site is located along the southern flank of a bathymetric high. To the south, strata thickens towards an active normal fault. The thicker the sediment, the higher the sedimentation rate and more likely the chances of underconsolidation and overpressure development. These sediments also experience increased relative overburden compared to sediments north due to increased sedimentation above them. We note with arrows the direction of increased sedimentation and potential fluid flow caused by possible differential loading. (B) (top) shows the timing of fluid circulation versus drilling depth and (bottom) both average temperature at stationary phases and associated* T_{adapt} *(+),* R^2 *values (blue dots) versus depth. Note the step-wise change in temperature gradient at a depth*

of ~25 m - the depth where a strong seismic reflection associated with a gravel-rich layer and the base of failure for submarine slide Deposit 2 exists. Model predictions (C) indicate a best fit if the true in situ thermal gradient is 205 +/- 20 ˚C/km.

5.5.2.4 GeoB23725-1/MeBo Site 4 heat flow results

GeoB23725-1/MeBo Site 4 was drilled in the middle of the Bouillante-Montserrat half-graben, ~3.5 km east of the arc, to a depth of ~28 m below the sea floor (Figure 5.1). Temperature was measured to a depth of ~26 mbsf at this site. The drill string was flushed for cleaning immediately before the tool was dropped to the base of the hole in an attempt to clear the borehole, however, pressure in the bottom of the well injected fluids upward into the drill pipe. We know this because the acoustic tool data indicate acoustic velocities of steel for the first ~5 meters, indicating that the probe didn't fall completely to the base of the drill pipe due to sediment likely flowing up the borehole. Temperatures at depths greater than ~15 mbsf therefore have high uncertainty and generally low R^2 values due to lack of depth control and unclear borehole conditions. Furthermore, at depths greater than ~15m, we observe anomalous negative T_{adapt} values consistent with advection. Shallower than 15 mbsf, however, T_{adapt} values are positive, consistent with diffusion dominated heat flow (Figure 5.7). It is remarkable that, even after significant flushing with colder ocean bottom data (Figure 5.7) for sometimes several hours, we observe anomalously warm temperatures at depth from 15-20 mbsf compared to shallower depths in the same zone where we also observe negative T_{adapt} values. In general, we observe low, normal (positive, conductive) temperature adaption rates in the upper ~15 m of sediment and warmer temperatures but, more chaotic, negative T_{adapt} values below. The apparent temperature-depth profile in the upper 15 m of sediment increases approximately linearly with depth and is low, averaging ~25 ˚C/km (Figure 5.7). Deeper then 15 mbsf, however, the temperature increases abruptly by ~0.5 ºC. This increase in temperature coincides with a strong seismic reflection, negative T_{adapt} values, and the existence of a known sand-rich slope failure event (Figure 5.7). At depths greater than 15 m, the temperature appears approximately isothermal, maintaining a near constant value of ~5.8 ºC. Notably, the isothermal zone is coincident with low seismic reflectivity, consistent with homogenous sediment character often associated with slope failures, and implying little change in sediment density or velocity.

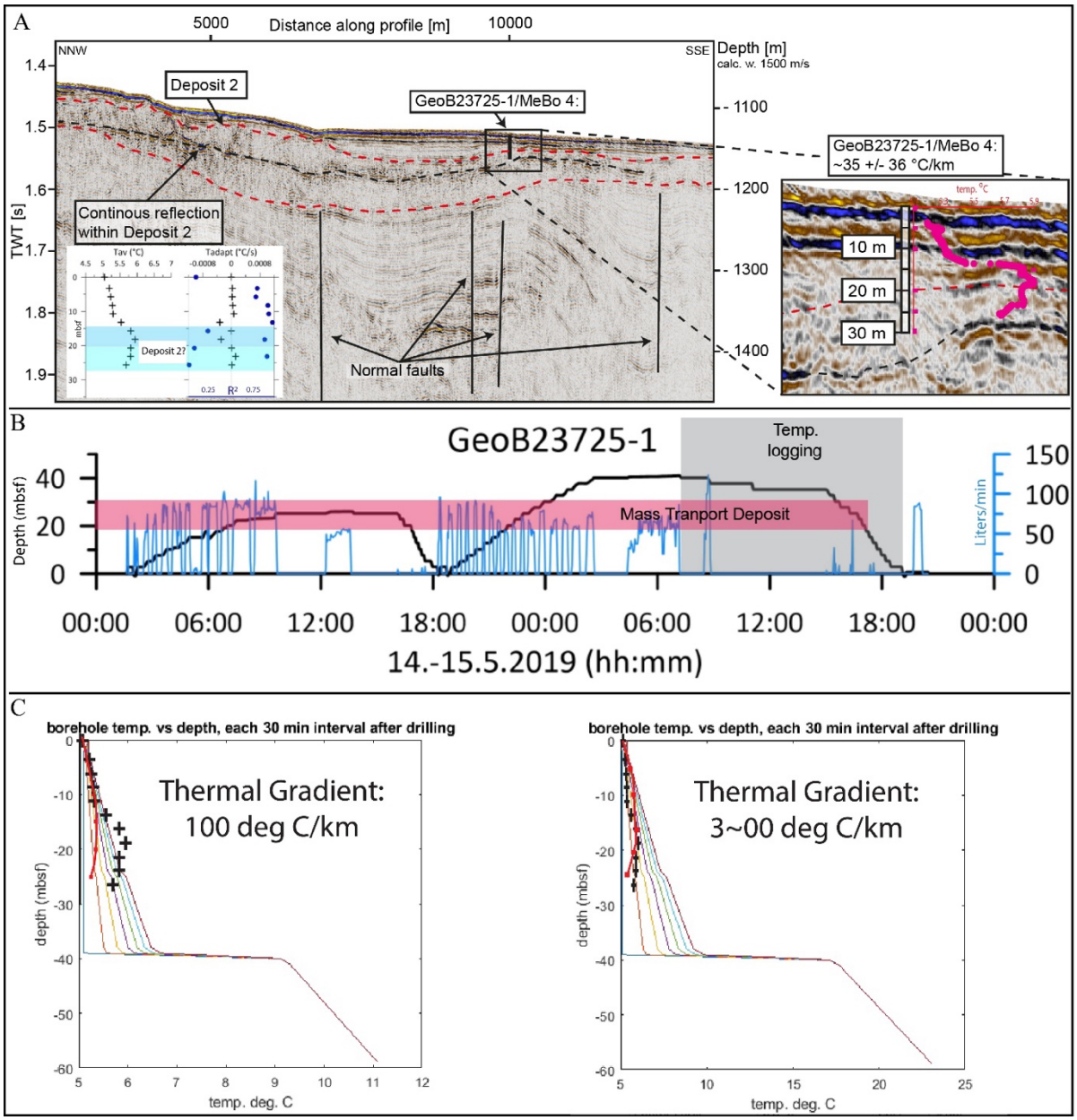

Figure 5.7: *(A) Raw heat flow temperature-depth profile at GeoB23725-1/MeBo Site 4 overlain on seismic line P5003 (pink dots, right), with average temperature depth profile and associated* T_{adapt} *and* R^2 *values with depth (inset).* T_{adapt} *is positive and consistent with diffusive heat flow in the upper 15 mbsf, but negative at greater depth where a mass transport deposit exists. (B) the drilling and fluid circulation log for MeBo site 4. Note drilling halted at ~20 m and time of ~16:00 followed by drill string recovery. Re-entry and continued circulation/drilling commenced again at 18:00. The timing of this and circulation are accounted for in the numerical model. (C) model predictions (red) compared to observed values (black) for thermal gradients of 100 (left) versus 300 °C/km. Model result best fit observations in the upper 15 mbsf for 100 ˚C/km, but best fit observation at depths greater than 15 mbsf with much higher gradients (but with poorer fit to shallower measurements). We suggest advection at depths >15*

mbsf and diffusion above based on both model results and T_{adapt} values and suggest that drilling may have induced upward flow.

5.5.2.5 GeoB23730-1/MeBo Site 5 heat flow results

GeoB23730-1/MeBo Site 5 was drilled ~10 km east of the arc, in sediment onlapping the Kahouanne Seamount at the eastern edge of the Bouillante-Montserrat half-graben. Drilling occurred to a depth of 25.3 mbsf in a water depth of 1088 m (Figure 5.8) and temperature was measured to a depth of ~23 m below the sea floor at this site. This site, like MeBo Site 6, had relatively steady drilling progression with depth, and flushing occurred during logging-while-drilling only at a depth of 3.26 mbsf. As a result, it shows a more linear temperature-depth profile, also similar to MeBo site 6, however, with a much higher initial thermal gradient. Although possibly minor isothermal zones exist between 3-5 m, 10-13 mbsf and 14-17 mbsf - where we also again observe slightly negative T_{adapt} values - the temperature-depth profile at the site appears approximately linear with an initial (minimum end-member estimated) thermal gradient of 94 +/- 22 ˚C/km. Seismic data indicate sediments have an apparent dip westward toward the basin and the active volcanic arc (Figure 5.8). Numerical modeling results indicate a best fit occurs if the true background thermal gradient is 270 +/- 20 ˚C/km. A high value that is similar to values measured with the HyLO probe on the eastern side of the basin. The location of MeBo drill site near the basin edge where bounding faults and possible upward/lateral fluid flow occurs might explain why we observe such a high heat flow at this site (Figure 5.8).

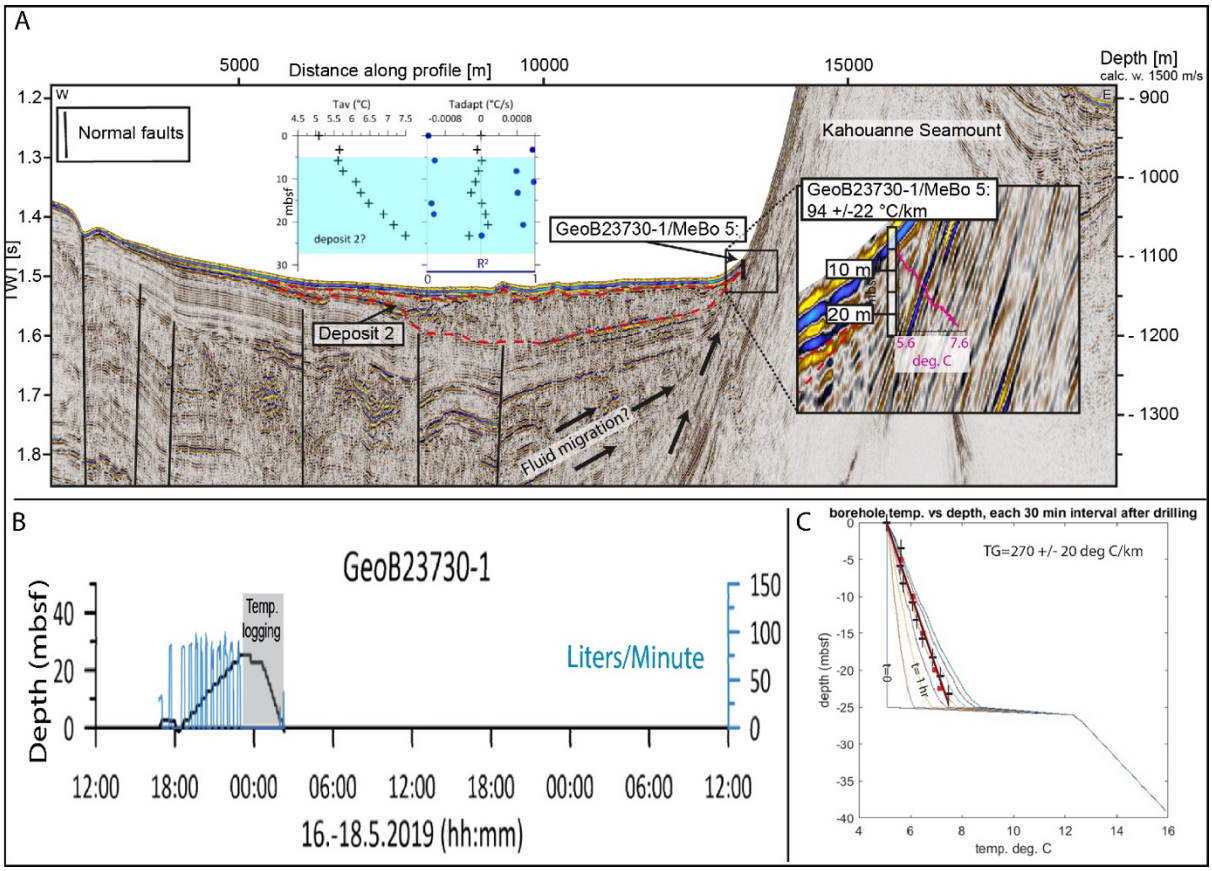

Figure 5.8: *(A) seismic line showing the location of MeBo 5, including the raw temperature-depth profiles (right inset, pink points), the T_{av} values, and the T_{adapt}/R2 values (left inset). (B) the fluid circulation and drilling depth history at this site is one of the simplest compared to other sites, resulting in a nearly linear initial (minimum) thermal gradient of ~94 °C/km, and only very small negative T_{adapt} values (<0.0002) that only occur at depths of 8-12 mbsf. Numerical modelling results indicate a best fit occurs for a true thermal gradient of 270 °C/km.*

5.5.3 Comparing New Heat Flow Measurements to Previous Studies

To assess heat flow in two dimensions across the Lesser Antilles arc, we apply a thermal conductivity of 1.04 W/m*k consistent with sediments in this area (Manga et al., 2012), and calculate heat flow at each site using the average thermal gradient estimate. Comparison of the new heat flow estimates with a 2D seismic profile perpendicular to the arc indicates the highest heat flow values (>250 mW/m^2) occur at the edges of the basin, either within 2-3 km of the MBS fault system near the arc apex or the flanks of the basin, where the most heavily faulted regions are imaged in seismic data (Figure 5.9). Outside this basin and away from the faults (MeBo sites 2, 6) heat flow is lower (less 250 mW/m^2) The analysis implies that the highest heat flow across the Lesser Antilles is focused at or near faults. One possible explanation for

the observed high heat flow at the MBS fault system west of the graben is that hot fluids migrate up and along fractures into more permeable aquifers below. The lower heat flow measurements distal to this fault zone may also represent recharge zones, similar to, and consistent with, observations at ridge-flank crustal hydrothermal systems where anomalously low heat flow adjacent to upwardly advection zones exist (e.g., Davis et al., 1992, 1999; Hutnak et al., 2006).

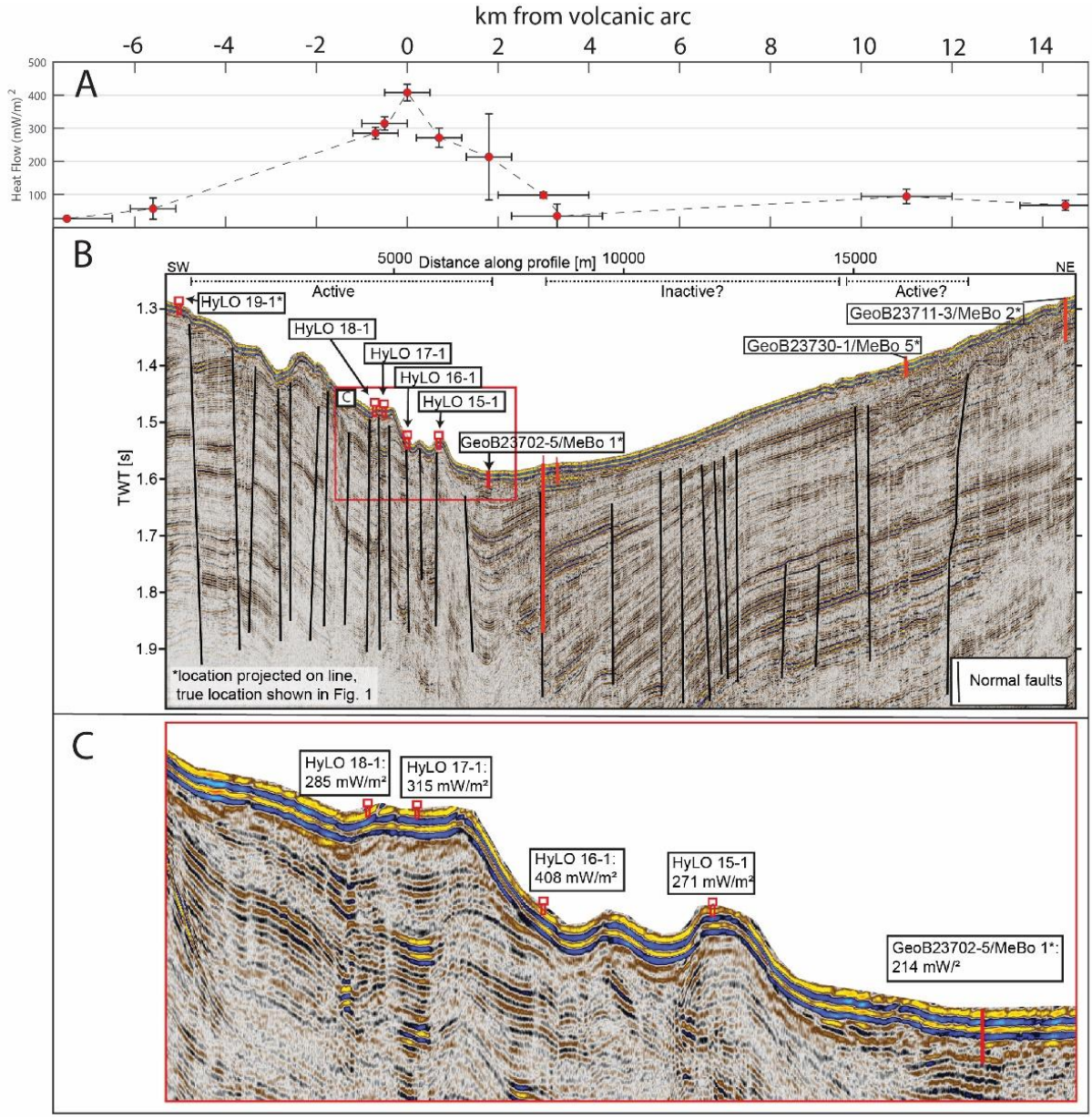

Figure 5.9: *(A) Heat flow versus estimated approximate distance from the axis of the volcanic arc obtained from new HyLO and MeBo measurements, with IODP Site 1395 heat flow included as an additional reference. Here, we assume the MBS fault system, which extends between active volcanic centers between Montserrat and Guadeloupe and shows evidence of submarine volcanism (Figure 5.1) and active faulting, represents the approximate position of the arc at*

this site. (B) Seismic line P5008 along an East-West profile across the arc, approximately coincident with the HyLO heat flow measurements, with additional MeBo heat flow measurements projected on the line. Solid black lines indicate the location of interpreted faults. (C) Zoomed view of subsurface seismically imaged structure for the location of the HyLO heat flow sites representing the red box in (B) showing how the highest heat flow measurements generally coincide with significant seismic reflection variability, faulting, and bathymetry changes in the region.

5.6 Discussion

Measurements in the shallow subsurface of the seabed (upper 5-10 mbsf) using both the HyLO probe and MeBo indicate near-linear temperature-depth profiles consistent with diffusive heat flow. However, deeper temperature-depth MeBo measurements suggest a more complex heat flow environment with depth, particularly in more permeable, sand-rich sediments associated with slope failure deposits. Below, we first assess possible causes of the non-linear temperature-depth measurements and unusual T_{adapt} values observed at 3 of the 5 MeBo sites (i.e., MeBo sites 1, 2, 4). We then use this information to provide a broader context for these measurements. Arguably, the most important implication of this study is that the new MeBo results provide new insight into the underpinnings of heat and fluid transport in marine convergent margins often not captured by traditional Lister or more sparsely sampled scientific ocean drilling heat flow measurements. We suggest subsurface geology, and in particular, buried mass transport deposits, play a fundamental role in heat and fluid transport in marine environments.

5.6.1 Assessing the cause of anomalous MeBo temperature-depth profiles and negative T_{adapt} values

Previous MeBo temperature-depth studies using the acoustic logging tool thermometer demonstrate that, in clay-rich diffusion-dominated heat flow settings, the temperature gradient with depth estimated using the T_{adapt} approach matches steady-state heat flow conditions in the shallow part of the well but under-predicts heat flow at greater (~>20mbsf) depths. (Freudenthal et al., 2022). The true steady-state thermal gradient is anomalously low with depth in these conditions because (1) the deepest measurements are where the largest temperature contrast between circulated bottom water and formation temperature exist and (2) the least amount of time between drilling and flushing has passed. As a result, we typically predict and observe

positive T_{adapt} values increasing with depth, with the largest values at the greatest depth in diffusive heat flow environments (Freudenthal et al., 2022).

In rare instances, particularly where core recovery is poor and turbidites exist, however, we sometimes observe negative T_{adapt} values, where, instead of warming, temperature cools rapidly during temperature logging (Freudenthal et al., 2022; Riedel et al., 2020). Negative T_{adapt} values are not predicted in borehole models where diffusive heat flow dominates (Freudenthal et al., 2022); why rapid cooling occurs in these zones is currently unclear. Possible causes of rapid cooling of sediments in the borehole may include, but are not limited to, (1) exposure to colder borehole temperatures during temperature logging due to downward fluid advection, (2) exposure to warmer temperatures just prior to logging do to upward injection of warm fluid, and (3) possible endothermic chemical reactions (such as hydrate destabilization due to recent temperature or pressure changes in the sediment). Although deciphering which of these explanations, or combinations of these explanations, are most plausible is difficult - all three scenarios above require dynamic thermal conditions associated with advection.

Before addressing the most plausible cause of the negative T_{adapt} values, we consider the following: (1) in all instances where T_{adapt} is negative, the initial starting temperature is anomalously high compared to shallower measurements, consistent with recent, rapid warming at the measurement depth; (2) in most instances where flushing of cold seawater occurs at the beginning of stationary temperature measurements to free the tool, temperature measurements remain warm and T_{adapt} after flushing is negative, implying flushing colder water has minimal influence on cooling the system at the flushing depth; (3) negative T_{adapt} values are usually located in or immediately above low core recovery zones where sand-rich, potentially higher permeability sediment - often associated with slope failure events - exists, (4) in nearly all instances where positive T_{adapt} values occur, we observe clay-rich, lower permeability (higher recovery) sediments, and (5) no evidence of elevated methane concentrations or methane hydrate were observed in any sediments recovered at the site either during MeBo drilling or prior IODP Expedition 340 drilling (e.g. Le Friant et al. 2019), implying no significant endo/exothermic reactions occurred at these sites during drilling.

Based on these observations, it seems implausible that negative T_{adapt} values are caused by downwelling of colder water or methane hydrate dissociation. The clay-rich sediments within and above these zones have inherently a low permeability and are prone to swelling, thereby impeding flow both in sediment and along the outer wall of the borehole. Additionally, cores

collected in this area appear devoid of organic carbon needed to form methane and methane hydrates (e.g., Subramanyam et al., 2020). We therefore suggest that both downwelling and methane hydrate dissociation are unlikely mechanisms for causing negative T_{adapt} observations at these site.

In contrast, if upward fluid flow occurs at, near, or into the base of the drill pipe, we would anticipate sharply higher temperatures at the thermistor, especially at depths closest to the source of the upwelling deeper (and therefore presumably warmer) fluid. Removal of the drill pipe section - where the tool is pulled up 2.5 m after each pipe racking - could further facilitate upward flow, as either suction or potentially overpressured fluids and sediment flow inward and upward into the void space left by the wider drill pipe into the narrower space of the tool string (Figure 5.10). In such instances where higher permeability, or potentially pressurized formations exist, flushing may have minimal impact on reducing temperature since fluids injected from the seafloor could rapidly flow away from the tool out into the higher permeability sediment, get flushed back up the borehole, or even push warmer fluid upward against the side of the borehole. The hypothesis of upward fluid flow caused by overpressured sediments causing negative T_{adapt} values is also supported by observations of “borehole smoking” - that is, water with suspension load evading out of the drill pipe as soon as the drill head or a drill rod is disconnected - that was frequently observed and recorded by the MeBo video footage at the sea floor when drilling into or tripping out of sandy sediments.

We therefore suggest that the simplest explanation for the high average temperatures and negative T_{adapt} values observed at several depth intervals results from upward flow of fluids from deeper buried, higher permeability sediments into the borehole during drill string recovery (Figure 5.10). Higher permeability, poorly consolidated sediments are well recognized for their ability to facilitate fluid flow (e.g., Taheri et al., 2017) and our suggestion is that sand-rich turbidites associated with slope failures may have elevated fluid pressures capable of injecting fluid upward into overlying lower permeability formations, consistent with previous studies in this region (e.g., Lafuerza et al., 2014; Hornbach et al., 2015). Negative T_{adapt} zones may therefore represent important indicators for upward advective heat transport during MeBo drilling. Step-like changes in temperature at the boundary of these high-permeability zones (e.g., Figure 5.7) indicate that dynamic non-steady fluid flow likely occurs in these higher permeability zones, and that they may act as important fluid and heat conduits on margins as well as potential zones of fluid flow, elevated pressure, and mechanical weakness. Heat and fluid transport in these higher permeability zones associated with mass transport deposits may

be very difficult or even impossible to detect using only shallow Lister-type heat flow measurements that typically fail to penetrate into these sand-rich formations, and if flow in these deeper zones occurs, shallowly penetrating Lister probes will generate apparently conductive heat flow measurements that are significantly influenced by deeper advective processes.

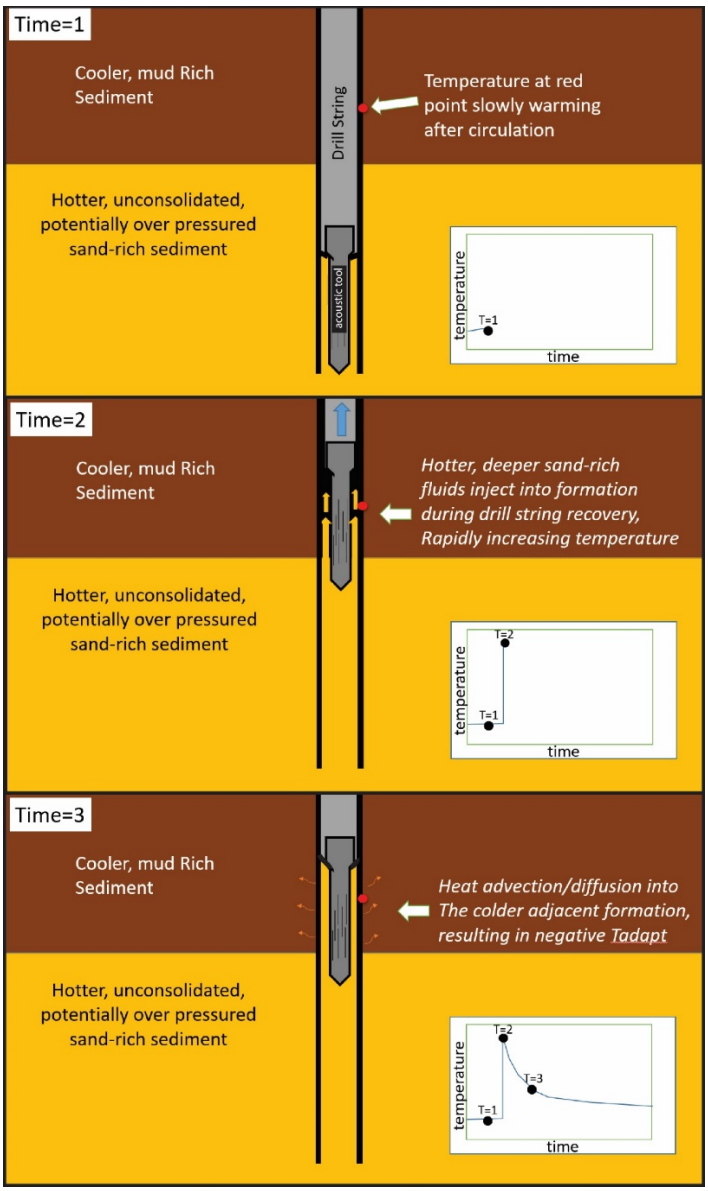

Figure 5.10: *Schematic diagram demonstrating how we might observe negative* T_{adapt} *values during temperature measurement. The top, at time T=1, shows a cross section of the acoustic tool located at the bottom of the drill pipe, initially located in warmer, higher permeability, potentially over pressured sediment associated with a mass transport deposit. The red dot shows the location where a future temperature measurement will be taken when 2.5 m of pipe at the*

top of the drill string are pulled up. Initially, at time T=1 the temperature in the borehole is slowly warming following thermal recovery from cold water circulation. Time T=2 shows the borehole during tool mobilization upward 2.5 m. Note that if the sediment below is overpressured, there is the possibility of fluid injection upward into the borehole, causing initial heating at the red dot. Time T=3 shows subsequent cooling during pipe wracking due to heat dissipation into the cooler-clay-rich formation, resulting in negative T_{adapt} values. As the tool continues to be removed, more clay will likely mix with the sand, resulting perhaps in less upward fluid injection with time, and more stable, positive T_{adapt} values.

5.6.2 Unique insight into heat and fluid transport provided by MeBo measurements

The high vertical resolution of temperature measurements obtained from MeBo70 acoustic-temperature logs provide important new insights into heat and fluid flow near Montserrat that demonstrate the potential complexity of quantifying the thermal gradient at volcanic arcs, as well as the complexity of assessing heat flow using logging-while-tripping. At three of the five MeBo sites, we observe non-linear temperature-depth profiles indicating temperature with depth may be controlled by advection. For example, there is evidence from temperature-depth measurements at MeBo site 1 that advective flow occurs, and is perhaps long-lived, since the temperature gradient in the upper 10 m of the seafloor is similar to the thermal gradient measurements obtained from nearby HyLO probe measurements, yet deeper (>10 mbsf) MeBo temperature measurements indicate that the shallow (<10 mbsf) thermal gradient at this site may be artificially elevated by a warm isothermal zone where lateral advection seems to occur in deeper, more permeable layers associated with a mass transport deposit. The consistency of the temperature depth profile in the upper 10 meters between the adjacent MeBo site 1 and HyLO site 15-1 supports the conclusion that heat transfer in the deeper isothermal zone measured by MeBo is longer lived (>5 years), as it would take several years for a linear-temperature-depth profile to evolve over this depth interval (e.g., Figure 5.2 and 5.5). The MeBo measurements, particularly at MeBo site 1, therefore demonstrate how shallower, Lister-type heat flow probe measurements may often be heavily (yet unknowingly) influenced by deeper advection-dominated heat flow processes. The MeBo measurements - though limited at times by drilling induced thermal effects - represents a valuable tool for not only providing meter-scale temperature-depth information, but also the role of lithology in heat and fluid transfer in complex geologic settings like volcanic arcs.

In some instances, however, anomalous temperatures measured via MeBo drilling may be associated with the drilling itself. For example, at depths greater than ~10 mbsf at MeBo site 4 (Figure 5.7), the estimated thermal gradient is nearly 100% higher than what might be predicted using a standard more-shallow penetrating Lister type probe at this site. The sharp change in temperature below 10 m depth is consistent with the hypothesis of recent - perhaps drilling induced - advective heat transport (e.g., Figure 5.11), since the temperature-depth profile increases step-wise to ~0.5 ºC over a narrow (3-5 m) depth interval between ~10-15 mbsf. At this depth interval, the thermistor passes through a sediment transition from hemipelagic sediment above to a mass transport deposit below. Based on first-order 1D heat flow modeling, we estimate that fluid flow began recently and is likely associated with drilling itself.

An important question, therefore, regarding the future use of MeBo acoustic log temperature measurements for heat/fluid flow studies is whether the isothermal sections the logs record in mass transport deposits are truly indicative of long-lived advection as opposed to drilling disturbance. The analysis we present at MeBo Site 4 (Figure 5.11) supports the hypothesis that temperature changes at this specific site are recent, sudden, and therefore, likely caused by drilling itself. MeBo Site 4, however, is the only location where we have high confidence that drilling-induced advection occurred. This is because the temperature-depth profile at MeBo Site 4 increases abruptly with depth, whereas the temperature-depth profile at other MeBo sites increase continuously and nearly linearly (to within our thermal gradient uncertainties) towards isothermal zones. For example, at MeBo site 1, we observe a significant, yet approximately linear, temperature increase with depth from the seabed to the isothermal zone (~10 mbsf). Like MeBo Site 4, the isothermal zone at MeBo Site 1 also occurs at a depth where higher permeability sediment exist. Nonetheless, the shallow thermal gradient at MeBo site 1 is consistent with values obtained from the nearby HyLO probe site 15-1 and the steady increase in temperature with depth at MeBo site 1 to the isothermal zone further suggests a stable thermal regime. The observations of similar shallow thermal gradients at HyLO site 15-1 and MeBo Site 1 support the hypothesis that the shallow thermal gradient observed at MeBo site 1 is near quasi-steady state, and fluid flow along the isothermal zone at MeBo site 1 is long-lived, implying that temperature-depth measurements at MeBo Site 1 are less influenced by drilling. Although we are not able to compare thermal gradient measurements at MeBo Sites 2 and 3 to other shallow measurements (since no HyLO or previous heat flow measurements were collected near these sites), we observe no large (>0.5ºC) discontinuous step in temperature, and the thermal gradients observed in the upper 10 meters of these drill sites are, to within

uncertainty, similar to the gradient we observe at greater depths. These observations, though limited, support the hypothesis that temperature-depth profiles at MeBo Sites 2 and 3 are geologically reasonable (i.e., consistent with what we would expect for thermal gradients in the earth) and may have experienced only limited drilling disturbance. Based on these observations, we suggest only MeBo Site 4 temperature-depth measurements are significantly influenced by drilling. The drilling disturbance at MeBo Site 4 provides insight into subsurface physical properties, since the temperature spike we observe at ~15 mbsf supports the hypothesis for rapid fluid migration from a significantly hotter (and likely deeper) source. This information is itself useful hydrogeological information. Although the source of the fluid and lateral extent of this higher permeability zone is unclear, future integration of these data with 3D seismic data and subsurface flow/pressure models may provide further insight into the potential source of these warmer fluids.

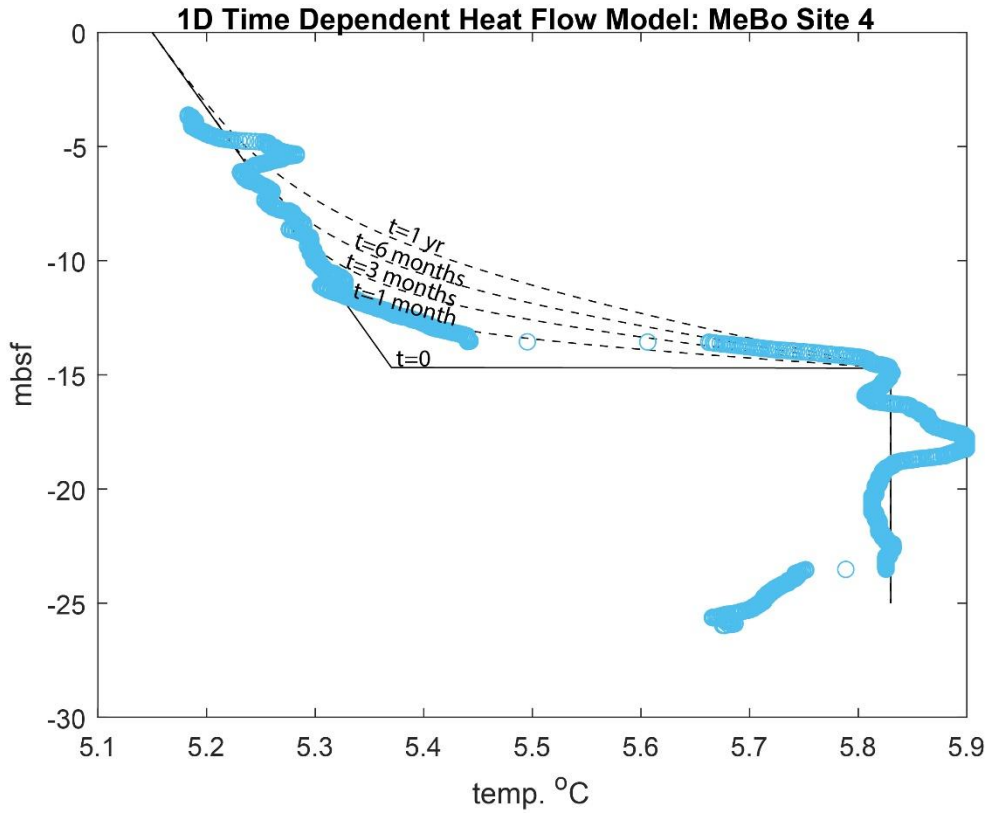

Figure 5.11: *Evidence of possible drilling-triggered upward fluid flow: Comparison of a 1D time-dependent heat flow model (black dashed lines) with observed raw temperature-depth values (blue circles) at MeBo Site 4. Note that the raw temperature-depth values suggest a dynamic thermal state, since the sharp increase in temperature between 10 and 15 m depth should appear near linear if steady-state conditions exist. The model at time=0 assumes a 15 °C/km thermal gradient from zero to 15 mbsf, and a jump in temperature of 0.5 oC at greater*

depths due to an injection of warm fluids from greater depth caused perhaps by drilling. Dashed lines indicate the temperature response with time assuming diffusive heat flow, a conductivity of 1.1 W/m-K, and thermal diffusivity of 3.2x10-7 m^2/s. The best fit between the model and observations occurs at short time scales and is consistent with the onset of warming during the past 1-3 months, assuming no advective heat transport above 15 mbsf. A potential explanation for the observation is that drilling increased subsurface permeability or that drilling penetration into an overpressured formation allowed upward fluid flow along a fault or borehole.

The vertical resolution of MeBo temperature measurements is also insightful for understanding the role of geology in transporting heat compared to traditional heat flow measurements (such as standard IODP ocean drilling heat flow measurements). Though IODP heat flow measurements are invaluable for assessing broad-scale thermal gradients and heat flow at greater depth (>70 mbsf), most IODP measurements consist of only 4-8 temperature-depth measurements over a depth interval of ~100 m, or on average, 1 measurement every 10-20 m, making it difficult if not impossible to resolve or quantify smaller-scale advection or links between heat flow, fluid flow, and lithology at these sites. For example, IODP Expedition 340 measurements (where temperature was measured at 10-20 m vertical spacing) have the potential to entirely miss the advective zones that we observe at several of the MeBo sites. Manga et al. (2012) note that horizontal advection, and advection in higher-permeability sediments where temperature-depth measurements could not be made, are very difficult to detect using standard IODP heat flow measurement approaches, and that lateral heat flow at these sites could not be ruled out, despite the roughly linear temperature-depth profile at these sites. The limited vertical spatial resolution of temperature with depth using traditional IODP temperature depth measurements therefore makes detecting fluid flow difficult. Nonetheless evidence for possible isolated advection as well as drilling related disturbance at Expedition 340 sites also exists: at least three IODP Expedition 340 Sites (U1395, U1397 and U1398) show 1 ^oC or more differences in measured versus estimated steady-state temperature at multiple depth intervals (in some instances with repeat measurements in adjacent boreholes made within 5 meters depth of each other--see for example site U1397, 35 mbsf, in Manga et al., 2012). Since IODP temperature-depth measurements are typically 3-to-6 times lower spatial resolution than MeBo T_{av} depth measurements, thermal effects potentially associated with advection may often be unresolvable and associated with measurement errors, uncertainty, or advection (Manga et al., 2012). MeBo provides the first meter-scale vertical temperature resolution that can be used to

address some of these uncertainties, although at the expense of significant temperature uncertainty associated with fluid circulation and non-steady temperature measurement. Despite these limitations, our study suggests isolated advection is likely detectable and occurs primarily along sand rich layers (as hypothesized by Manga et al., 2012 in this region) and that these zones may play an important role in explaining these anomalous IODP temperature measurements. The MeBo measurements therefore provide unique first-order insight into both heat and fluid transport properties of the subsurface.

5.6.3 Driving mechanisms for advection in sand-rich sediments

Several mechanisms, acting individually or in concert, might explain why fluid flow occurs along higher permeability slope failure deposits offshore Montserrat. Hypotheses include (1) buoyancy or pressure-driven upward fluid flow of warmer fluids along the MBS fault system that intersect and flow along higher-permeability slope failure deposits, (2) lateral flow driven by the higher hydraulic head and a recharge zone on Montserrat, and (3) differential compaction where higher rates of sedimentation near Montserrat result in greater dewatering and injection of fluids into the higher permeability slope failure deposits near Montserrat. For all three hypotheses, we expect progressively warmer fluids found westward, towards Montserrat, since in each instance, the groundwater would flow over, near, or source just above the volcanic arc. Of these three hypotheses, we view the first and third scenario most likely. We believe the second scenario - shallow water aquifer flow driven by a hydraulic head at Montserrat as the least likely since the stratigraphy both onshore and immediate adjacent to Montserrat appears heavily disturbed and frequently reworked by volcanism. The seismic data - though limited - reveal no clearly recognizable, broad, or continuous stratigraphic source unit that we can link to offshore deposits. Additionally, we would expect groundwater freshening in submarine aquifers if Montserrat is indeed the source, and we see no clear evidence of this in the limited drilling data or previous IODP Expedition 340 data. We therefore suggest that fluid flow sourced from MBS faults working perhaps in concert with differential compaction of fine-grained sediments represents the most likely mechanisms for driving fluid flow in this region. Ongoing analysis of 3D seismic data collected in this region may provide additional insight into the source of these fluids.

Determining the rate of fluid flow necessary to explain subsurface temperature observations requires understanding not only subsurface permeability, stratigraphy and structure (ideally in 3D), but also the location, age, and magnitude of both the heat source and the pressure regime.

If the fluid source derives directly from MBS faults found above subsurface volcanic centers, flow rates of ~10 m/yr might generate heat flow values two orders of magnitude greater than current observations (Bredehoeft & Papadopoulos, 1965). This is because heat flow above volcanic centers is often very high (>>1000 W/m^2), with faults located over volcanic centers efficiently transporting significant amounts of heat (Hurwitz et al., 2012). We therefore suggest relatively low ground water flow rates (<<10 m/yr) may be all that is necessary to explain our observations. Although a detailed assessment of fluid flow rates, subsurface pressures, and driving mechanisms extends beyond the scope of this current work, it is the subject of on-going research and will be addressed in a future study that integrates recently collected active source 3D P-cable seismic data with IODP/MeBo drilling and HyLO heat flow results.

5.6.4 Implications of higher permeability and advection along mass transport deposits.

The isothermal zones observed in MeBo temperature-depth data generally correlate with locations of known or inferred mass transport deposits (e.g., Watt et al., 2012a, Lafuerza et al., 2014; Hornbach et al., 2015; Koehn et al., 2022). It is intriguing that nearly all isothermal zones observed in the MeBo temperature depth data correlate with acoustically transparent seismic zones. These “acoustically blank” zones are usually caused by either low seismic impedance contrast or high acoustic scattering often associated with slope failure deposits (e.g., Scholz et al., 2012). Here, several of the acoustically blank isothermal zones observed also occur at depths where known mass transport deposits exist or have been interpreted (e.g., Deplus et al., 2001; Lebas et al., 2011; Watt et al., 2012a; Le Friant et al., 2019) (e.g., Figures 5.5 and 5.7). We interpret these isothermal zones as evidence for fluids preferentially flowing laterally along higher permeability stratigraphy. Anomalously warm isothermal zones have previously been associated with warm fluid migrating upwards and laterally along higher permeability boundaries (e.g., Blackwell et al., 1990). MeBo sites 1, 2, 4, and 5 highlight this phenomenon and show how higher than average heat flow might exist when adjacent beds intersect deeper-seated faults, and we suggest the observed high heat flow at several sites results from perhaps both fluid migration up faults associated with the MBS system and lateral migration along mass transport deposits. The implication is that turbidites associated with mass transport deposits likely play a significant, previously unrecognized role in transporting heat and fluids along volcanic arcs. Given that mass transport deposits are ubiquitous on convergent margins, it is possible that the significant variability in heat flow observed at other volcanic arcs is the direct result of subsurface fluid transport in buried higher permeability mass transport deposits at these sites. Deposit 2 offshore Montserrat appears to facilitate lateral fluid flow in the graben and

covers ~200 km^2 - twice the area of Montserrat and three times that of Manhattan - yet this slide deposit is neither unique or particularly large for the region: order-of-magnitude larger slides are already well documented at the Lesser Antilles convergent margin as well as other volcanic arcs (e.g., Deplus et al., 2001). It therefore seems highly probable that such widespread mass transport deposits play a fundamental - yet currently overlooked - role in fluid and heat transport at these sites.

5.7 Conclusions

New heat flow measurements acquired using a HyLO probe and MeBo70 acoustic-temperature log measurements indicate highly variable heat flow across the Lesser Antilles arc, with the highest values in heavily faulted regions and anomalously warm isothermal zones associated with higher permeability mass transport deposits. Negative T_{adapt} values observed at the upper boundary of these mass transport deposits are best explained by upward injection of fluid from over-pressured mass transport deposits into overlying lower permeability hemipelagic sediments.

The MeBo thermistor tool provides the first *in situ* meter to cm-scale approach for assessing heat and fluid transport along discrete geologic formations, and represents a potentially powerful tool for assessing small-scale fluid and heat transport variations in marine sediments.

Heat transport along the Lesser Antilles is dynamic, exhibiting non-steady temperatures in space and time that depend on submarine sediment physical properties. Advective heat flow observed along the Lesser Antilles - particularly within higher permeability slope failure deposits may represent a more widespread and fundamental phenomenon than previously recognized, as slope failures and buried mass transport deposits are ubiquitous on continental margins.

Acknowledgements

The authors thank Captain Hambacher and crew of the R/V Meteor for their support during instrument sea trials. We especially thank Klaus Dehning, Christian Hilgenfeld, and Birgit Meyer-Schack for their expertise and professionalism with gravity coring, outrigging, and deployment. Funding for HyLO work was provided by the United States National Science Foundation, Division of Ocean Sciences Grant no. 1926729. Funding for ship time and MeBo testing/calibration was provided by Deutsche Forschungsgemeinschaft (The German Research Foundation). Funding for researchers to conduct integrated analysis of the MeBo and HyLO

dataset with global machine learning models was provided by the U.S. Office of Naval Research & The Naval Research Lab Faculty Sabbatical Support Program.

Data Availability Statement

Raw MeBo heat flow data and bathymetry data are all freely and publicly available at the PANGAEA data publisher for earth and environmental science (https://www.pangaea.de/) under the following DOIs: borehole temperatures: https://doi.pangaea.de/10.1594/PANGAEA.961273; bathymetry data: https://doi.org/10.1594/PANGAEA.935598. The seismic data is under a moratorium until April 2025; after this date the data will be freely available for download from Kühn et al. (2023) (DOI: https://doi.pangaea.de/10.1594/PANGAEA.957490). Additionally, we have included raw data as supporting information associated with this manuscript.

References

Beardsmore, G. R., & Cull, J. P. (2001). *Crustal heat flow: a guide to measurement and modelling*. Cambridge university press.

Berndt, C., Böttner, C., Elger, J., Kontradowitz, S., Kühn, M., Müller, S., Schramm, B., & Stelzner, M. (2019). *Sector collapse kinematics and tsunami implications - SEKT, Cruise No. M154/1, April 3 - April 25, 2019, Mindelo (Cape Verde) - Point-á-Pitre (Guadeloupe). METEOR-Berichte, M154/1. Gutachterpanel Forschungsschiffe, Bonn, 47 pp.* https://doi.org/10.2312/cr_m154_1

Berndt, C., Böttner, C., & Wölfl, A.-C. (2021). *Multibeam bathymetry raw data (Kongsberg EM 122 entire dataset) of RV METEOR during cruise M154/1*. PANGAEA. https://doi.org/10.1594/PANGAEA.935598

Blackwell, D. D., Steele, J. L., Frohme, M. K., Murphey, C. F., Priest, G. R., & Black, G. L. (1990). Heat flow in the Oregon Cascade Range and its correlation with regional gravity, Curie point depths, and geology. *Journal of Geophysical Research: Solid Earth*, *95*(B12), 19475–19493.

Bouysse, P., & Westercamp, D. (1990). *Subduction of Atlantic aseismic ridges and Late Cenozoic evolution of the Lesser Antilles island arc* (Vol. 175).

Bredehoeft, J. D., & Papaopulos, I. S. (1965). Rates of vertical groundwater movement estimated from the Earth's thermal profile. *Water Resources Research*, *1*(2), 325–328.

Carslaw, H. S., Jaeger, J. C., & Feshbach, H. (1962). Conduction of heat in solids. *Physics Today*, *15*(11), 74–76.

Cassidy, M., Trofimovs, J., Palmer, M. R., Talling, P. J., Watt, S. F. L., Moreton, S. G., & Taylor, R. N. (2013). Timing and emplacement dynamics of newly recognised mass flow deposits at ~8-12ka offshore Soufrière Hills volcano, Montserrat: How submarine stratigraphy can complement subaerial eruption histories. *Journal of Volcanology and Geothermal Research*, *253*, 1–14. https://doi.org/10.1016/j.jvolgeores.2012.12.002

Coussens, M., Cassidy, M., Watt, S. F. L., Jutzeler, M., Talling, P. J., Barfod, D., Gernon, T. M., Taylor, R., Hatter, S. J., & Palmer, M. R. (2017). Long-term changes in explosive and effusive behaviour at andesitic arc volcanoes: Chronostratigraphy of the Centre Hills Volcano, Montserrat. *Journal of Volcanology and Geothermal Research*, *333–334*, 15–35. https://doi.org/10.1016/j.jvolgeores.2017.01.003

Crutchley, G. J., Karstens, J., Berndt, C., Talling, P. J., Watt, S. F. L., Vardy, M. E., Hühnerbach, V., Urlaub, M., Sarkar, S., Klaeschen, D., Paulatto, M., Le Friant, A., Lebas, E., & Maeno, F. (2013). Insights into the emplacement dynamics of volcanic landslides from high-resolution 3D seismic data acquired offshore Montserrat, Lesser Antilles. *Marine Geology*, *335*, 1–15. https://doi.org/10.1016/j.margeo.2012.10.004

Davis, E. E., Chapman, D. S., Mottl, M. J., Bentkowski, W. J., Dadey, K., Forster, C., Harris, R.,

Nagihara, S., Rohr, K., & Wheat, G. (1992). FlankFlux: An experiment to study the nature of hydrothermal circulation in young oceanic crust. *Canadian Journal of Earth Sciences*, *29*(5), 925–952.

Davis, E. E., Chapman, D. S., Wang, K., Villinger, H., Fisher, A. T., Robinson, S. W., Grigel, J., Pribnow, D., Stein, J., & Becker, K. (1999). Regional heat flow variations across the sedimented Juan de Fuca Ridge eastern flank: Constraints on lithospheric cooling and lateral hydrothermal heat transport. *Journal of Geophysical Research: Solid Earth*, *104*(B8), 17675–17688.

Deplus, C., Le Friant, A., Boudon, G., Komorowski, J. C., Villemant, B., Harford, C., Ségoufin, J., & Cheminée, J. L. (2001). Submarine evidence for large-scale debris avalanches in the Lesser Antilles Arc. *Earth and Planetary Science Letters*, *192*(2), 145–157. https://doi.org/10.1016/S0012-821X(01)00444-7

Fetter, C. W. (2018). *Applied hydrogeology*. Waveland Press.

Feuillet, N., Leclerc, F., Tapponnier, P., Beauducel, F., Boudon, G., Le Friant, A., Deplus, C., Lebrun, J. F., Nercessian, A., Saurel, J. M., & Clément, V. (2010). Active faulting induced by slip partitioning in montserrat and link with volcanic activity: New insights from the 2009 GWADASEIS marine cruise data. *Geophysical Research Letters*, *37*(19), 1–6. https://doi.org/10.1029/2010GL042556

Fisher, A. T., & Hounslow, M. W. (1990). Transient fluid flow through the toe of the Barbados accretionary complex: constraints from ocean drilling program leg 110 heat row studies and simple models. *Journal of Geophysical Research: Solid Earth*, *95*(B6), 8845–8858.

Freudenthal, T., Villinger, H., Riedel, M., & Pape, T. (2022). Heat flux estimation from borehole temperatures acquired during logging while tripping: a case study with the sea floor drill rig MARUM-MeBo. *Marine Geophysical Research*, *43*(3). https://doi.org/10.1007/s11001-022-09500-1

Freudenthal, T., & Wefer, G. (2013). Drilling cores on the sea floor with the remote-controlled sea floor drilling rig MeBo. *Geoscientific Instrumentation, Methods and Data Systems*, *2*(2), 329–337. https://doi.org/10.5194/gi-2-329-2013

Graw, J. H., Wood, W. T., & Phrampus, B. J. (2023). Predicting Marine In Situ Heat Flow Using a Geospatial Machine Learning Conformal Prediction. *Geochemistry, Geophysics, Geosystems*, *24*(6). https://doi.org/10.1029/2023GC010913

Heesemann, M., Villinger, H., Fisher, A. T., Tréhu, A. M., & White, S. (2008). Data report: testing and deployment of the new APCT-3 tool to determine in situ temperatures while piston coring. *Advances in the Acquisition and Processing of Subseafloor Temperature and Pressure Data and Their Interpretation in the Context of Convergent Margin Processes*, 21.

Hornbach, M. J., Manga, M., Genecov, M., Valdez, R., Miller, P., Saffer, D., Adelstein, E., Lafuerza, S., Adachi, T., Breitkreuz, C., Jutzeler, M., LeFriant, A., Ishizuka, O., Morgan, S., Slagle, A., Talling,

P. J., Fraass, A., Watt, S. F. L., Stroncik, N. A., … Wang, and F. (2015). Permeability and pressure measurements in Lesser Antilles submarine slides: Evidence for pressure-driven slow-slip failure. *Journal of Geophysical Research: Solid Earth*, *120*, 7986–8011. https://doi.org/10.1002/2015JB012061

Hornbach, M. J., Sylvester, J., Hayward, C., Kühn, M., Huhn-Frehers, K., Freudenthal, T., Watt, S. F. L., Berndt, C., Kutterolf, S., Kuhlmann, J., Sievers, C., Rapp, S., Pallapies, K., Gatter, R., & Hoenekopp, L. (2021). A Hybrid Lister-Outrigger Probe for Rapid Marine Geothermal Gradient Measurement. *Earth and Space Science*, *8*(1). https://doi.org/10.1029/2020EA001327

Huhn, K., Freudenthal, T., Dehning, K., Gatter, R., Hilgenfeldt, C., Hönekopp, L., Hornbach, M., Kühn, M., Kuhlmann, J., Kutterolf, S., Meyer-Schack, B., Pallapies, K., Rapp, S. K., Sievers, C., Watt, S., & Stelzner, M. (2019). *Sector collapse kinematics and tsunami implications - SEKT, Cruise No. M154-2, April 29 - Mai 23, 2019, Pointe-à-Pitre (Guadeloupe) - Pointe-à-Pitre (Guadeloupe)*.

Hurwitz, S., Harris, R. N., Werner, C. A., & Murphy, F. (2012). Heat flow in vapor dominated areas of the Yellowstone Plateau Volcanic Field: Implications for the thermal budget of the Yellowstone Caldera. *Journal of Geophysical Research: Solid Earth*, *117*(B10).

Hutnak, M., Fisher, A. T., Zühlsdorff, L., Spiess, V., Stauffer, P. H., & Gable, C. W. (2006). Hydrothermal recharge and discharge guided by basement outcrops on 0.7–3.6 Ma seafloor east of the Juan de Fuca Ridge: Observations and numerical models. *Geochemistry, Geophysics, Geosystems*, *7*(7).

Koehn, L., Kyritz, T., Hornbach, M., Berry, J., Betz, P., White, M., Martinez, A., Martinez-Camacho, J. M., McCracken, C., Renzaglia, J., Sylvester, J., & O'Toole, T. (2022). *Data report: permeability measurements inside and outside submarine landslides at IODP Expedition 340 sites*. https://doi.org/10.2204/iodp.proc.340.208.2022

Kokelaar, B. P. (2002). *Setting, chronology and consequences of the eruption of Soufri6re Hills Volcano, Montserrat (1995-1999) In 1997 the House of Commons Select Committee on International*. https://www.lyellcollection.org

Kühn, M., Berndt, C., & Krastel, S. (2023). *2D multichannel seismic reflection processed data (GI Gun entire dataset) of RV METEOR during cruise M154/1*. PANGAEA. https://doi.org/10.1594/PANGAEA.957490

Kühn, M., Berndt, C., Watt, S. F. L., Hornbach, M. J., Krastel, S., Sass, K., Kutterolf, S., Freudenthal, T., Huhn, K., Karstens, J., Schramm, B., Elger, J., Böttner, C., & Klaeschen, D. (2024). Volcanic Flank Collapse, Secondary Sediment Failure and Flow-Transition: Multi-Stage Landslide Emplacement Offshore Montserrat, Lesser Antilles. *Geochemistry, Geophysics, Geosystems*, *25*(6), e2024GC011564. https://doi.org/https://doi.org/10.1029/2024GC011564

Kunde, D. (2020). *Seismic velocity of sector collapse deposits off Montserrat* [Master's thesis]. Christian-Albrechts-Universität zu Kiel.

Lafuerza, S., Le Friant, A., Manga, M., Boudon, G., Villemant, B., Stroncik, N., Voight, B., Hornbach, M., & Ishizuka, O. (2014). Geomechanical characterization of submarine volcano-flank sediments, Martinique, Lesser Antilles Arc. *Submarine Mass Movements and Their Consequences: 6th International Symposium*, 73–81.

Le Friant, A., Ishizuka, O., Boudon, G., Palmer, M. R., Talling, P. J., Villemant, B., Adachi, T., Aljahdali, M., Breitkreuz, C., Brunet, M., Caron, B., Coussens, M., Deplus, C., Endo, D., Feuillet, N., Fraas, A. J., Fujinawa, A., Hart, M. B., Hatfield, R. G., … Watt, S. F. L. (2015). Submarine record of volcanic island construction and collapse in the Lesser Antilles arc: First scientific drilling of submarine volcanic island landslides by IODP Expedition 340. *Geochemistry, Geophysics, Geosystems*, *16*(2), 420–442. https://doi.org/10.1002/2014GC005652

Le Friant, A., Lebas, E., Brunet, M., Lafuerza, S., Hornbach, M., Coussens, M., Watt, S., Cassidy, M., Talling, P. J., & Party, I. 340 E. S. (2019). Submarine landslides around volcanic islands: A review of what can be learned from the Lesser Antilles Arc. *Submarine Landslides: Subaqueous Mass Transport Deposits from Outcrops to Seismic Profiles*, 277–297.

Le Friant, A., Lock, E. J., Hart, M. B., Boudon, G., Sparks, R. S. J., Leng, M. J., Smart, C. W., Komorowski, J.-C., Deplus, C., & Fisher, J. K. (2008). Late Pleistocene tephrochronology of marine sediments adjacent to Montserrat, Lesser Antilles volcanic arc. *Journal of the Geological Society*, *165*(1), 279–289.

Lebas, E., Le Friant, A., Boudon, G., Watt, S. F. L., Talling, P. J., Feuillet, N., Deplus, C., Berndt, C., & Vardy, M. E. (2011). Multiple widespread landslides during the long-term evolution of a volcanic island: Insights from high-resolution seismic data, Montserrat, Lesser Antilles. *Geochemistry, Geophysics, Geosystems*, *12*(5). https://doi.org/10.1029/2010GC003451

Lister, C. R. B. (1979). The pulse-probe method of conductivity measurement. In *Geophys. J. R. astr. Soc* (Vol. 57). https://academic.oup.com/gji/article/57/2/451/618032

Manga, M., Hornbach, M. J., Le Friant, A., Ishizuka, O., Stroncik, N., Adachi, T., Aljahdali, M., Boudon, G., Breitkreuz, C., Fraass, A., Fujinawa, A., Hatfield, R., Jutzeler, M., Kataoka, K., Lafuerza, S., Maeno, F., Martinez-Colon, M., McCanta, M., Morgan, S., … Wang, F. (2012). Heat flow in the Lesser Antilles island arc and adjacent back arc Grenada basin. *Geochemistry, Geophysics, Geosystems*, *13*(8). https://doi.org/10.1029/2012GC004260

Miller, V., & Calder, E. S. (2020). Site specific risk assessment for Fort Ghaut, Plymouth area of the Soufrière Hills Volcano, Montserrat July 2020. *MVO Open File Report*, 20–24.

Pfender, M., & Villinger, H. (2002). Miniaturized data loggers for deep sea sediment temperature gradient measurements. *Marine Geology*, *186*(3–4), 557–570.

Riedel, M., Freudenthal, T., Bergenthal, M., Haeckel, M., Wallmann, K., Spangenberg, E., Bialas, J., & Bohrmann, G. (2020). Physical properties and core-log seismic integration from drilling at the Danube deep-sea fan, Black Sea. *Marine and Petroleum Geology*, *114*, 104192.

Ryan, W. B. F., Carbotte, S. M., Coplan, J. O., O'Hara, S., Melkonian, A., Arko, R., Weissel, R. A., Ferrini, V., Goodwillie, A., Nitsche, F., Bonczkowski, J., & Zemsky, R. (2009). Global multi-resolution topography synthesis. *Geochemistry, Geophysics, Geosystems*, *10*(3). https://doi.org/10.1029/2008GC002332

Scholz, N. A., Riedel, M., Bahk, J.-J., Yoo, D.-G., & Ryu, B.-J. (2012). Mass transport deposits and gas hydrate occurrences in the Ulleung Basin, East Sea–Part 1: Mapping sedimentation patterns using seismic coherency. *Marine and Petroleum Geology*, *35*(1), 91–104.

Sclater, J., Jaupart, C., & Galson, D. (1980). The heat flow through oceanic and continental crust and the heat loss of the Earth. *Reviews of Geophysics*, *18*(1), 269–311.

Shapiro, N. M., & Ritzwoller, M. H. (2004). Inferring surface heat flux distributions guided by a global seismic model: particular application to Antarctica. *Earth and Planetary Science Letters*, *223*(1–2), 213–224.

Subramanyam, K. S. V, Balaram, V., Manikyamba, C., Roy, P., Krishna, A. K., Sawant, S. S., Narshimha, C., & Scientists, I. E. 340. (2020). Geochemistry of marine carbonates from hole 1394, off the coast of Montserrat, IODP expedition-340; implications on provenance, paleoenvironment and lesser Antilles Arc Migration. *Dynamics of the Earth System: Evolution, Processes and Interactions: Contributions from Scientific Ocean Drilling*, 101–140.

Taheri, S., Ghomeshi, S., & Kantzas, A. (2017). Permeability calculations in unconsolidated homogeneous sands. *Powder Technology*, *321*, 380–389.

Vacquier, V., & Von Herzen, R. P. (1964). Evidence for connection between heat flow and the mid-Atlantic ridge magnetic anomaly. *Journal of Geophysical Research*, *69*(6), 1093–1101.

Villinger, H., & Davis, E. E. (1987). A new reduction algorithm for marine heat flow measurements. *Journal of Geophysical Research: Solid Earth*, *92*(B12), 12846–12856.

Vogt, P. R., & Sundvor, E. (1996). Heat flow highs on the Norwegian-Barents-Svalbard continental slope: Deep crustal fractures, dewatering, or "memory in the mud"? *Geophysical Research Letters*, *23*(24), 3571–3574.

Wadge, G., Voight, B., Sparks, R. S. J., Cole, P. D., Loughlin, S. C., & Robertson, R. E. A. (2014). An overview of the eruption of Soufrière Hills Volcano, Montserrat from 2000 to 2010. *Geological Society Memoir*, *39*(1), 1–39. https://doi.org/10.1144/M39.1

Wall-Palmer, D., Coussens, M., Talling, P. J., Jutzeler, M., Cassidy, M., Marchant, I., Palmer, M. R., Watt, S. F. L., Smart, C. W., Fisher, J. K., Hart, M. B., Fraass, A., Trofimovs, J., Le Friant, A., Ishizuka, O., Adachi, T., Aljahdali, M., Boudon, G., Breitkreuz, C., … Wang, F. (2014). Late Pleistocene stratigraphy of IODP Site U1396 and compiled chronology offshore of south and south west Montserrat, Lesser Antilles. *Geochemistry, Geophysics, Geosystems*, *15*(7), 3000–3020. https://doi.org/10.1002/2014GC005402

Watt, S. F. L., Jutzeler, M., Talling, P. J., Carey, S. N., Sparks, R. S. J., Tucker, M., Stinton, A. J., Fisher, J. K., Wall-Palmer, D., Hühnerbach, V., & Moreton, S. G. (2015). New insights into landslide processes around volcanic islands from Remotely Operated Vehicle (ROV) observations offshore Montserrat. *Geochemistry, Geophysics, Geosystems*, *16*(7), 2240–2261. https://doi.org/10.1002/2015GC005781

Watt, S. F. L., Talling, P. J., Vardy, M. E., Heller, V., Hühnerbach, V., Urlaub, M., Sarkar, S., Masson, D. G., Henstock, T. J., Minshull, T. A., Paulatto, M., Le Friant, A., Lebas, E., Berndt, C., Crutchley, G. J., Karstens, J., Stinton, A. J., & Maeno, F. (2012). Combinations of volcanic-flank and seafloor-sediment failure offshore Montserrat, and their implications for tsunami generation. *Earth and Planetary Science Letters*, *319–320*, 228–240. https://doi.org/10.1016/j.epsl.2011.11.032

Watt, S. F. L., Talling, P. J., Vardy, M. E., Masson, D. G., Henstock, T. J., Hühnerbach, V., Minshull, T. A., Urlaub, M., Lebas, E., Le Friant, A., Berndt, C., Crutchley, G. J., & Karstens, J. (2012). Widespread and progressive seafloor-sediment failure following volcanic debris avalanche emplacement: Landslide dynamics and timing offshore Montserrat, Lesser Antilles. *Marine Geology*, *323–325*, 69–94. https://doi.org/10.1016/j.margeo.2012.08.002

Young, S. R., Sparks, R. S. J., Aspinall, W. P., Lynch, L. L., Miller, A. D., Robertson, R. E. A., & Shepherd, J. B. (1998). Overview of the eruption of Soufriere Hills Volcano, Montserrat, 18 July 1995 to December 1997. *Geophysical Research Letters*, *25*(18), 3389–3392. https://doi.org/10.1029/98GL01405

Supplementary Information

Raw temperature data will be available online after publication. Heat flow modelling script example (MATLAB):

```
%%% 5/16/2024
%%% this is a cylindrical borehole heat flow model to assess how
%%% fluid circulation and tool recovery during mebo impact the
%%% the thermal regime
%%%%. Here, we assume variable conductivity with depth, but no
%%%% variability with angle around the borehole (ie no horizontal
%%%% variability). this eliminates the angle term, so that the HF equation
%%%% depends only on radial distance and depth.
clear all
run_time=60*60*16.2;% maximum time to run model, seconds
max_drill_depth=24.5;% meters, apply 1 m offset from true value (23.5 m),
since first cell starts at 1 not zero.
SFT=5.95;%seafloor temperature, deg. C
TG=75;% thermal gradient, deg. C/km
PR=max_drill_depth/run_time;% penetration rate, m/s
%defining radial dimensions
dr=.0025;% m
numcells_r = 200;
r= numcells_r*dr;% m
%defining vertical (z) dimensions
dz=1;% m
numcells_z = 100;
totallength_z= numcells_z*dz;% m
%%%% defining diffusivity %%%%%%%%
Dsed=3.3*10^-7;%m^2/s, sediment from freudenthal et al., 2022
Dm=381*10^-7;%m^2/s, metal in drill string from freudenthal et al., 2022
Dh=1.46*10^-7;% m^2/s, fluid in drill hole, from freudenthal et al., 2022
bhd=1;% cell number where bottom hole depth currently exists--we will
update with time
D(1:numcells_r,1:numcells_z)=Dsed;
M(1:numcells_r,1:numcells_z)=2;%designate sediment at 2
D(1:20,1:bhd)=Dh;% creating borehole
M(1:20,1:bhd)=1;% designate water in borehole as 1
D(16:19,1:bhd)=Dm;% creating borehole
M(16:19,1:bhd)=3;% designate water in borehole as 3
f1=3;
f2=10;
vvv=0
while vvv<f2
   D(1:25,1:bhd)=smoothdata2(D(1:25,1:bhd),'movmean',f1);% filters are
either "gaussian" or "box"
   M(1:25,1:bhd)=smoothdata2(M(1:25,1:bhd),'movmean',f1);% filters are
either "gaussian" or "box"
   vvv=vvv+1;
end
%%%%%%%%%%%%%%%%%%%%%%%%%%%%%%%%%%%%%%%%%%%%%%%%%%%%%%%%%%%%%%%%%%%%%%%
% Define time step for stability of calculation
%%%%%%%%%%%%%%%%%%%%%%%%%%%%%%%%%%%%%%%%%%%%%%%%%%%%%%%%%%%%%%%%%%%%%%%
ms=min([dr dz]);
dt = 0.125*ms^2/max(max(D))*.9;% this should ensure the time step always
fulfills currant conditions
d_tstep=dz/PR;% time required to move drill down a cell
t_deepen=d_tstep; %time to deepen drilling
```

```
%% Defining Initial Temperature Conditions
for j=1:numcells_z
T(1:numcells_r,j)=SFT+TG*dz*j/1000;
end
t=0
plot_inc=60*15;% in seconds
plot_t=0
T_new=T;
aa=1;%figure counter
while t<run_time
    for i=3:1:(numcells_r-2)
    for j=3:1:(numcells_z-2)
        % % % % %%%%% 4th order, variable conductivity %%%%%
        dDdr=(D(i-2,j)-8*D(i-1,j)+8*D(i+1,j)-D(i+2,j))/(12*dr);
        dTdr=(T(i-2,j)-8*T(i-1,j)+8*T(i+1,j)-T(i+2,j))/(12*dr);
        d2Tdr2=1/(12*dr^2)*(-T(i+2,j)+16*T(i+1,j)-30*T(i,j)+16*T(i-1,j)-
T(i-2,j));
        dDdz=(D(i,j-2)-8*D(i,j-1)+8*D(i,j+1)-D(i,j+2))/(12*dz);
        dTdz=(T(i,j-2)-8*T(i,j-1)+8*T(i,j+1)-T(i,j+2))/(12*dz);
        d2Tdz2=1/(12*dz^2)*(-T(i,j+2)+16*T(i,j+1)-30*T(i,j)+16*T(i,j-1)-
T(i,j-2));
        alpha=dDdr*dTdr+D(i,j)/(i*dr)*dTdr+D(i,j)*d2Tdr2 + dDdz*dTdz+
D(i,j)*d2Tdz2;
        T_new(i,j)=T(i,j) + alpha*dt;
    end
    end
    T =T_new ;
    %% resetting all borehole and fluids to seabed temperature when
circulation occurs
    if (t>0 & t<(60*60*.33)) | (t>60*60*1 & t<(60*60*1.5)) | (t>60*60*2 &
t<(60*60*2.5))...
       | (t>60*60*3.5 & t<(60*60*4.7)) | (t>60*60*5.7 & t<(60*60*6.8)) |
(t>60*60*7.8 & t<(60*60*8.3))...
       | (t>60*60*9.4 & t<(60*60*9.7)) | (t>60*60*10.8 & t<(60*60*11.1)) |
(t>60*60*14.4 & t<(60*60*14.8))...
       | (t>60*60*16.0 & t<(60*60*16.2))
    for i=1:(numcells_r)
    for j=1:(numcells_z)
        if M(i,j)~=2
            T(i,j)=SFT;
        end
    end
    end
    end
    %%%%%% keeping bottom boundary open %%%%
    T(:,numcells_z-1)=T(:,numcells_z-2);
    T(:,numcells_z)=T(:,numcells_z-2);
    %%%%%% keeping top boundary constant %%%%
    T(:,2)=(T(:,1)+T(:,3))/2;
    %%%%%%Keeping left side of boundary open
    T(1,:)=T(3,:);
    T(2,:)=T(3,:);
    if t>=plot_t
    model_time_hours=t/3600
    subplot(1,3,1)
    p1=surf(M,'EdgeColor','none')
    colorbar
    colormap jet
    ylabel('2.5 mm/cell')
    xlabel('1 m/cell')
```

```
    xlim([0 30])
    view(90,90)
    title("Material (1=drill fluid,2=sediment, 3=pipe)")
    p2=subplot(1,3,2)
    surf(T,'EdgeColor','none')
    ylabel('2.5 mm/cell')
    xlabel('1 m/cell')
    caxis([6 9])
    acb=colorbar;
    acb.Label.String = 'Deg. C';
    view(90,90)
    title(+ model_time_hours + " hours since start drilling, temp")
    clim([6 T(numcells_r,30)])
    xlim([0 30])
    set(gcf,'Color','w');
    set(gcf, 'Position',  [100, 100, 1600, 400])
    drawnow
    plot_t=plot_t+plot_inc;
    saveas(p2,num2str(aa),'jpg');% use to save each image to file for
making movie
    aa=aa+1;
    end
    t= t + dt;
    %%%% deepening the borehole if time is long enough
     if t>t_deepen
         t_deepen=t_deepen+ d_tstep;
         bhd=bhd+1;%deepen the bottom hole depth by 1 cell
         D(1:numcells_r,1:numcells_z)=Dsed;
         M(1:numcells_r,1:numcells_z)=2;%designate sediment at 2
            D(1:20,1:bhd)=Dh;% creating borehole
            M(1:20,1:bhd)=1;% designate water in borehole as 1
            D(16:19,1:bhd)=Dm;% creating borehole
            M(16:19,1:bhd)=3;% designate water in borehole as 3
        vvv=0
            while vvv<f2
                D(1:25,1:bhd)=smoothdata2(D(1:25,1:bhd),'movmean',f1);%
filters are either "gaussian" or "box"
                M(1:25,1:bhd)=smoothdata2(M(1:25,1:bhd),'movmean',f1);%
filters are either "gaussian" or "box"
                vvv=vvv+1;
            end
     end
end
T_end_of_drilling=T;%
D_end_of_drilling=D;%
M_end_of_drilling=M;%
save('T_end_of_drilling.mat','T');% save the temperature at end of drilling
%%%% Calculating Downhole Temperature During Logging and Recovery
recovery_time=60*60*3.5;% assess how temperature changes over period of
logging
tr=0
plot_t=0
plot_inc=60*30;% in seconds
plot_t=0
T=T_end_of_drilling;%
T_new=T;
%%%%%%%%%%% smooth over diffusivity in borehole or it will blow up%%%%%
D=D_end_of_drilling;
M=M_end_of_drilling;
vvv=0
```

```
% while vvv<3
%
%    D(1:45,1:bhd+1)=smoothdata2(D(1:45,1:bhd+1),'movmean',9);% filters are
either "gaussian" or "box"
%    M(1:45,1:bhd+1)=smoothdata2(M(1:45,1:bhd+1),'movmean',9);% filters are
either "gaussian" or "box"
%    vvv=vvv+1;
%
% end
while tr<recovery_time
    for i=3:1:(numcells_r-2)
    for j=3:1:(numcells_z-2)

        %2nd order, constant Conductivity %
      %  dDdr=(D(i+1,j)-D(i-1,j))/(2*dr);
      %  dTdr=(T(i+1,j)-T(i-1,j))/(2*dr);
      %  d2Tdr2=1/(dr^2)*(T(i+1,j)-2*T(i,j)+T(i-1,j));
      %  dDdz=(D(i,j+1)-D(i,j-1))/(2*dz);
      %  dTdz=(T(i,j+1)-T(i,j-1))/(2*dz);
      %  d2Tdz2=1/(dz^2)*(T(i,j+1)-2*T(i,j)+T(i,j-1));
        % % % % %%%%% 4th order, variable conductivity %%%%%
        dDdr=(D(i-2,j)-8*D(i-1,j)+8*D(i+1,j)-D(i+2,j))/(12*dr);
        dTdr=(T(i-2,j)-8*T(i-1,j)+8*T(i+1,j)-T(i+2,j))/(12*dr);
        d2Tdr2=1/(12*dr^2)*(-T(i+2,j)+16*T(i+1,j)-30*T(i,j)+16*T(i-1,j)-
T(i-2,j));
        dDdz=(D(i,j-2)-8*D(i,j-1)+8*D(i,j+1)-D(i,j+2))/(12*dz);
        dTdz=(T(i,j-2)-8*T(i,j-1)+8*T(i,j+1)-T(i,j+2))/(12*dz);
        d2Tdz2=1/(12*dz^2)*(-T(i,j+2)+16*T(i,j+1)-30*T(i,j)+16*T(i,j-1)-
T(i,j-2));
        alpha=dDdr*dTdr+D(i,j)/(i*dr)*dTdr+D(i,j)*d2Tdr2 + dDdz*dTdz+
D(i,j)*d2Tdz2;
        T_new(i,j)=T(i,j) + alpha*dt;
    end
    end
    T =T_new ;
    %%%%%% keeping bottom boundary open %%%%
    T(:,numcells_z-1)=T(:,numcells_z-2);
    T(:,numcells_z)=T(:,numcells_z-2);
    %%%%%% keeping top boundary constant %%%%
    T(:,2)=(T(:,1)+T(:,3))/2;
    %%%%%%Keeping left side of boundary open
    T(1,:)=T(3,:);
    T(2,:)=T(3,:);
    if tr>=plot_t
    model_time_hours=tr/3600
    subplot(1,3,1)
    p1=surf(M,'EdgeColor','none')
    colorbar
    colormap jet
    ylabel('2.5 mm/cell')
    xlabel('1 m/cell')
    xlim([0 30])
    view(90,90)
    title("Material (1=drill fluid,2=sediment, 3=pipe)")
    p2=subplot(1,3,2)
    surf(T,'EdgeColor','none')
    acb=colorbar;
    acb.Label.String = 'Deg. C';
    view(90,90)
    title(+ model_time_hours + " hours since drilling ended")
```

```
    %clim([6 T(numcells_r,30)])
    clim([6 9])
    xlim([0 30])
    drawnow
    p3=subplot(1,3,3)
    title('borehole temp. vs depth, each 30 min interval after drilling')
    plot(T(20,1:30)',0:-1:-29)
    hold on
    %%%% adding apparent thermal conductivity line%
    plot(((0:1:29)*27/1000+SFT),0:-1:-29,'-.k')
    xlabel('temp. deg. C')
    ylabel('depth (mbsf)')
    hold on
    drawnow
    plot_t=plot_t+plot_inc;
    td_profile(aa,20,1:30)=T(20,1:30)';
    saveas(p2,num2str(aa),'jpg');% use to save each image to file for
making movie
    aa=aa+1;
    end
    tr= tr + dt;
end
```

6. Loaded to fail - Excess pore fluid pressure by stacking of mass transport deposits offshore Montserrat

M. Kühn[1], M. J. Hornbach[2,3], C. Berndt[1], S.F.L. Watt[4], M. Urlaub[1]

[1]GEOMAR Helmholtz Centre for Ocean Research Kiel, Kiel, Germany
[2]United States Naval Research Laboratory, Stennis Space Center, MS, USA
[3]Huffington Department of Earth Sciences, Southern Methodist University, Dallas, TX, USA
[4]School of Geography, Earth and Environmental Sciences, University of Birmingham, Birmingham, United Kingdom

Manuscript in preparation

Abstract

Repeated slope failures have been observed in many geological settings, but the explanations proposed so far are not generally applicable. Excess pore fluid pressure plays a crucial role for slope stability and rapid loading by the emplacement of mass transport deposits may lead to a transient increase in pore pressure. However, it has generally been assumed that overpressures due to an individual slide dissipate quickly. Here, we demonstrate that the emplacement of a volcaniclastic submarine landslide off Montserrat caused nearly-instantaneous excess pore fluid pressure within adjacent and underlying sedimentary units for up to hundreds of kiloyears. We calculate pore fluid pressure changes due to the rapid loading of a MTD on hemipelagic sediments interbedded with two previously deposited MTDs. Results show that permeability contrasts significantly impact pressurization patterns (focused pressurization vs. diffusion) and subsequent sediment stability and that end members of the sediments specific storage (mainly controlled by the compressibility of the sediment) define a time scale of pressurization up to hundred thousands of years. These findings imply that past slope failures change the physical conditions of slopes for thousands of years constraining their propensity to fail in the future. The findings should apply to a wide range of slope failures both in volcanic and sedimentary environments providing a unifying explanation for the observation of stacked MTDs.

Main Text

Submarine landslides, especially those resulting from volcanic island flank collapses, are known to cause significant geological hazards, including (but not limited to) the generation of destructive tsunamis (Day, 2015). Hazard assessments for such disastrous events require a good understanding of mechanisms active before, during, and after failure. Stacked mass transport deposits (MTD) are common observation indicating that slopes failed multiple times in the

same place (Masson et al., 2006). In the past this repetition of landslides has variably been explained with repetitive glaciation processes (Bryn et al., 2003), fluid migration (Bünz et al., 2005; Berndt et al., 2012), gas hydrate dissociation induced by climate cycles (Sultan et al., 2004b), or rapid loading due to high sedimentation from a point source (Omeru and Cartwright, 2015). In the past it has been generally assumed that the excess pore pressure generated by the shallow deposition of a slope failure would dissipate quickly and slope failures have not been considered as a pre-conditioning factor for subsequent failure.

Here, we demonstrate that the deposition of a submarine landslide may actually lead itself to instability because rapid loading causes nearly-instantaneous excess pore fluid pressure to build up within the surrounding sediments. This means that once a slope or volcanic flank failure occurs, the risk of future failure events increase.

Evidence for elevated pore pressures in the MTDs off Montserrat

Elevated pore fluid pressure is a crucial parameter in the destabilization of slope sediments (King Hubbert and Rubey, 1959; Hampton et al., 1996; Dugan and Flemings, 2000) and volcanic edifices (Moore and Normark, 1994; Day, 1996). Here, we show evidence for excess pore fluid pressure in the buried MTD ‘Deposit 2a’ offshore Montserrat, Lesser Antilles (Fig. 6.1) that has been dated 318 ka minimum (Kühn et al., 2024) based on sedimentation rates from International Ocean Discovery Program (IODP) Expedition 340 (Le Friant et al., 2015). Cone penetration tests during drilling operations provide direct evidence for excess pore fluid pressure of 200 to 400 kPa above hydrostatic (Fig. 6.2). The depth of the pore pressure increase is consistent with the previously interpreted top boundary of the MTD, indicated by a structural change from undeformed to deformed hemipelagic sediments in the distal toe of the deposit (Kühn et al., 2024). The peak of excess pore pressure is located directly below an impermeable layer of hemipelagic clays (Fig. 6.2).

This is consistent with a recent study that finds indications for advective heat flow within the MTD, manifested e.g., in an isothermal zone of elevated temperature (~1.5 °C above the surroundings) that cannot be explained with diffusive heat flux, indicating fluid flow and thus high pore fluid pressure gradients within the deposit (Hornbach et al., submitted).

Potential overpressure also manifested sediment gushing out of drill holes once the MTD was hit during drilling operations (Hornbach et al., submitted). Another indication for overpressure are seismic amplitude reductions at the top of the MTD (Kühn et al., 2024) that likely represent

fluid migration structures. Such structures might be the result of hydrofracturing due to critical pore fluid overpressure (Cartwright, 1994; Cartwright and Santamarina, 2015; Elger et al., 2018). Hydrofracturing occurs when the excess pore fluid pressure becomes as high as the least principle (confining) stress in the system plus the cohesion of the sediments (Cartwright, 1994; Sultan et al., 2004a). Comparable fluid migration structures have been observed in other MTD worldwide (e.g., Brunei Slide, Gee et al., 2007 or Sakar Island, Kühn et al., 2021).

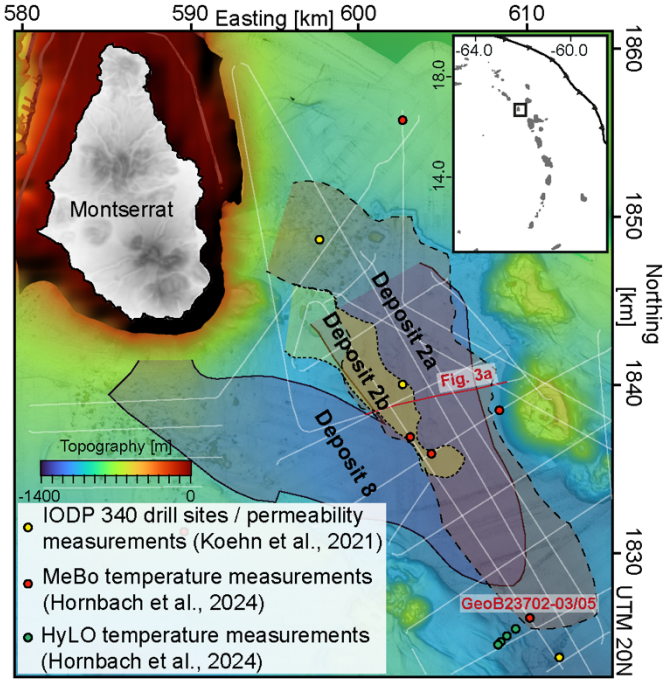

Figure 6.1: *Overview map of Montserrat and the seafloor west and south of the island with the outlines of Deposit 2a, 2b (from Kühn et al., 2024) and 8 (from Watt et al., 2012). White lines mark high-resolution 2D seismic profiles. Inset: Location of Montserrat on the northern Lesser Antilles Arc.*

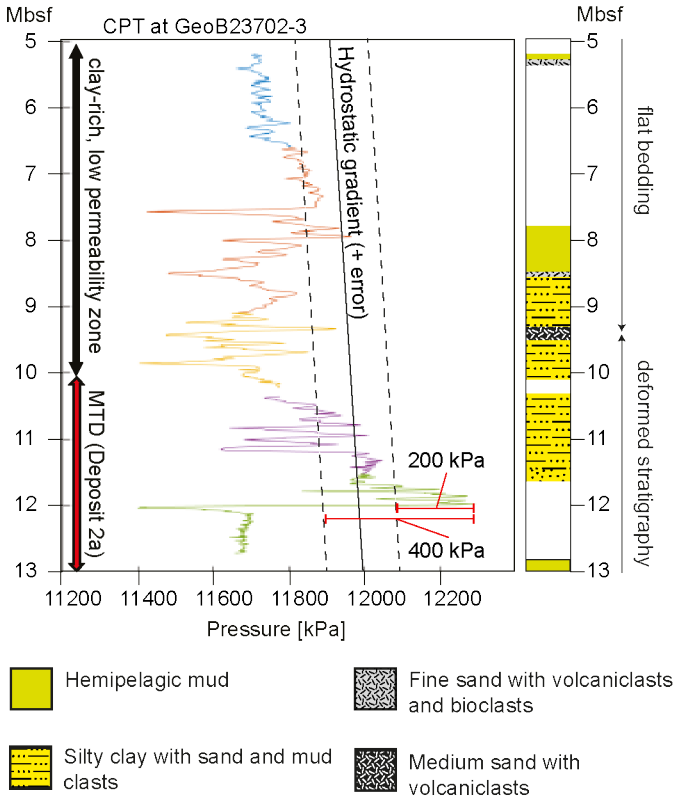

Figure 6.2: *Pore fluid pressure from CPT at MeBo Site GeoB23702-03 (modified after Huhn et al., 2019) and drill core lithology from MeBo Site 230702-05 (~50 m east of GeoB23702-03) (modified after Kühn et al., 2024). The black line marks the hydrostatic gradient assuming a water depth of 1081 m. Black dashed lines mark range of uncertainty of +/- 10 m of water depth.*

Excess pore fluid pressure simulations

We calculate the pore fluid pressure changes due to the rapid loading (+ ~213 kPa) by a MTD (Deposit 2b, Fig. 6.2a) on previously deposited, buried MTDs (Deposit 2a and Deposit 8, Fig. 2a) and the surrounding slope sediments offshore Montserrat (Fig. 6.1). To this end, we use a 2D finite difference modelling approach (see Methods) constrained by seismic interpretations (Watt et al., 2012; Kühn et al., 2024) and physical sediment property measurements from International Ocean Discovery Program (IODP) Expedition 340 (Hornbach et al., 2015b; Koehn et al., 2022). Based on the end members of permeability (Hornbach et al., 2015b; Koehn et al., 2022, Fig. 6.3b) and specific storage capacity we define six scenarios with a) low permeability contrasts of two orders of magnitude (M1, M2), b) medium permeability contrasts of four orders of magnitude (M3, M4) and c) high permeability contrast of six orders of magnitude (M5, M6).

Pressure distribution and time scales

Where the permeability contrast is low (i.e., two orders of magnitude), the whole sediment system is rapidly pressurized (Fig. 6.3c-f), but the pressure diffuses within several years to tens of years (Fig. 6.4a, b). Higher contrasts of four to six orders of magnitude in permeability between MTDs and the background sediments always lead to an initially focused pressurization of the buried high-permeable MTDs (Fig. 6.3g-n) that may lead to slow-slip failure of sediments adjacent to the MTD (Hornbach et al., 2015b). The pressurization of these systems beyond hydrostatic conditions lasts up to ~300 Kyrs (Fig. 6.4a, c). Steep pressure gradients exist in all models where a MTD protrudes through the seafloor and where the topography is complex (e.g., Fig. 6.3g, h, k, l). The rapid pressurization of the volcanic flank reduces the effective stress implying that less ground acceleration would be necessary for failure.

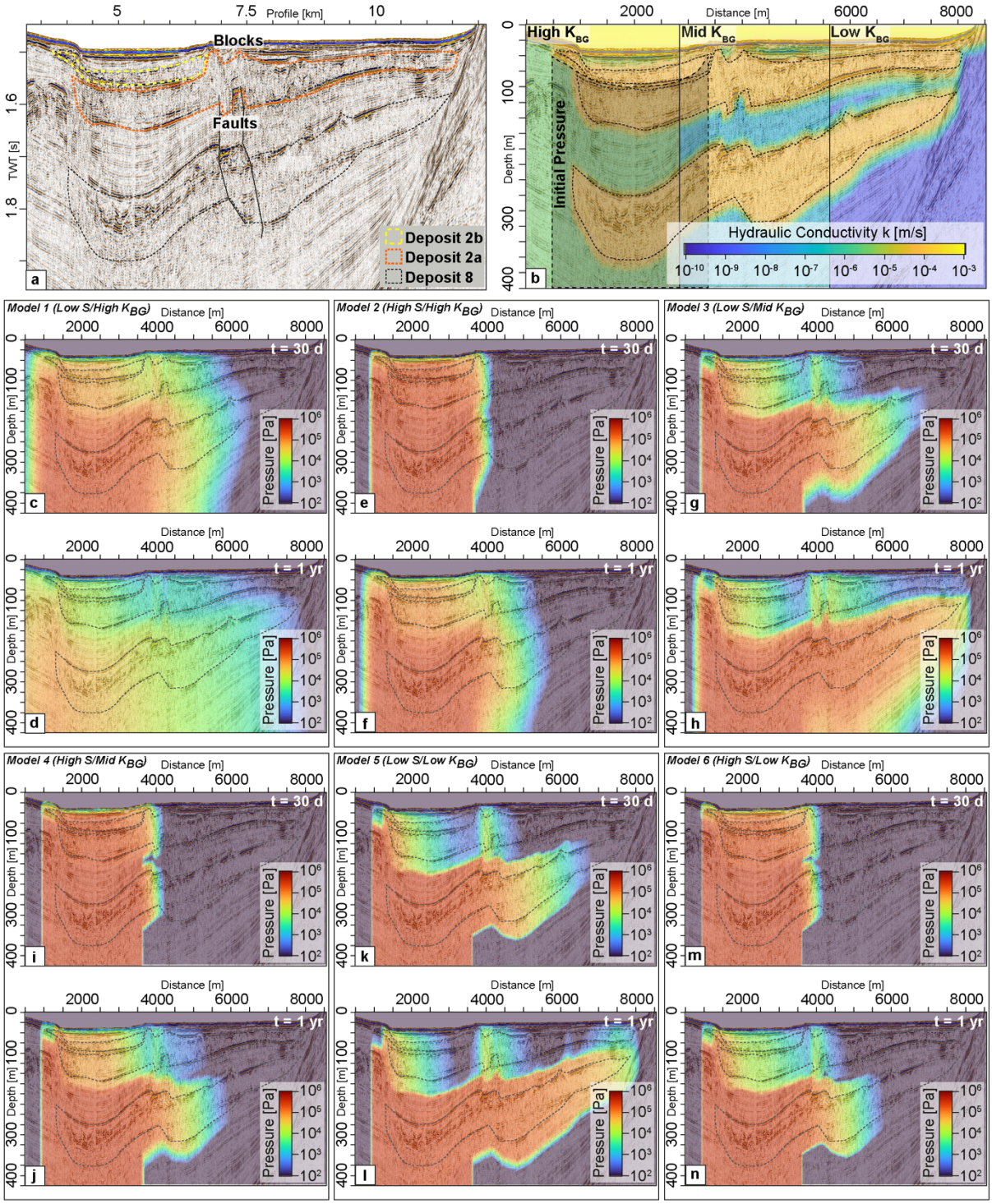

Figure 6.3: *a: Interpretation on MCS line 5016 offshore Montserrat showing three MTDs interbedded with hemipelagic background sediments. b: Three permeability end-member models overlain on MCS data. c – n: Pressure models M1 to M6 at t=30 days and t = 1 yr.*

The pressure distribution in M1 (Low S/High K_{BG}) is diffusive (Fig. 6.3c) and decays rapidly Fig. 6.3a). The maximum pressure is below 1 Pa after approximately 5 years (Fig. 6.4b). To estimate when the pore fluid pressure conditions are back to hydrostatic, we modelled or

extrapolated the pressure decay to the point where the pressure drops below 1 Pa by fitting exponential decay functions to the modelled time series (Fig. 6.4). As an exponential decay function will never reach zero, we chose 1 Pa as reference value where the system is back to quasi-hydrostatic. The initial pressure cell is visible for at least 30 days (Fig. 6.3d), with the fastest depressurization observed among all models. M2 also shows a diffusive pressure distribution (Fig. 6.3e), though it diffuses more slowly than M1 (Fig. 6.3f). The maximum pressure is below 1 Pa after 152 years (Fig. 6.4), with the initial pressure cell visible for about 2 years. These two simulations used high permeable background sediments (only two orders of magnitude lower than the MTDs) that were measured in hemipelagic sands offshore Montserrat. This sandy lithology of the background sediments appears to favor a rapid, diffusive pressurization of the whole slope in the model space, but also a quick decay of effective pressure. This indicates that in settings where sand-rich sediments dominate the lithology of background sedimentation, the risk of failure is highly increased, but only on a short time scale of days to a few years maximum. The pressure distribution in M3 is initially focused in Deposit 8 and lower in Deposits 2a and 2b (Fig. 6.3g). After ~90 days, pressure starts to increase outside of the MTDs as well, diffusing over the entire system within a year (Fig. 6.3h). The maximum pressure drops below 1 Pa after approximately 258 years (Fig. 6.4a), with the initial pressure cell visible for 2-3 years. High pressure gradients are noted at the blocky center of Deposit 2a, the eastern boundary of Deposit 2b, and where faults create complex deposit boundaries (Fig. 6.3g,h). M4 shows a focused pressure distribution in Deposits 2a, 2b, and 8, too (Fig. 6.3i). The maximum pressure decays below 1 Pa after around 6.9 Kyrs (Fig. 6.4a,b), with the initial pressure cell visible for about 50 years, indicating a prolonged period of maximum excess pore pressure. For M3 and M4 we assumed lower permeable background sediments (four orders of magnitude lower than the MTDs) that were measured in hemipelagic mud off Montserrat, with a decreased sand content and an increased clay content in the background sediments. The pressure distribution in M5 is focused in Deposits 2a, 2b, and 8 (Fig. 6.3k), with high pressure gradients where faults create complex boundaries (Fig. 6.3l). The prediction indicates pressure will fall below 1 Pa after 11.5 Kyrs (Fig. 6.4c). Similar to M5, M6 shows a focused pressure distribution in Deposits 2a, 2b, and 8 (Fig. 6.3m,n), with high pressure gradients at fault-created complex boundaries. The prediction indicates that the maximum pressure will fall below 1 Pa after 316 Kyrs (Fig. 6.4c). The simulations M5 and M6 used low permeable background sediments (six orders of magnitude lower than the MTDs) that were measured in hemipelagic clays offshore Martinique. This means that settings where low-permeable clays dominate the

background sedimentations, excess pore pressure might be maintained up to several hundred kiloyears.

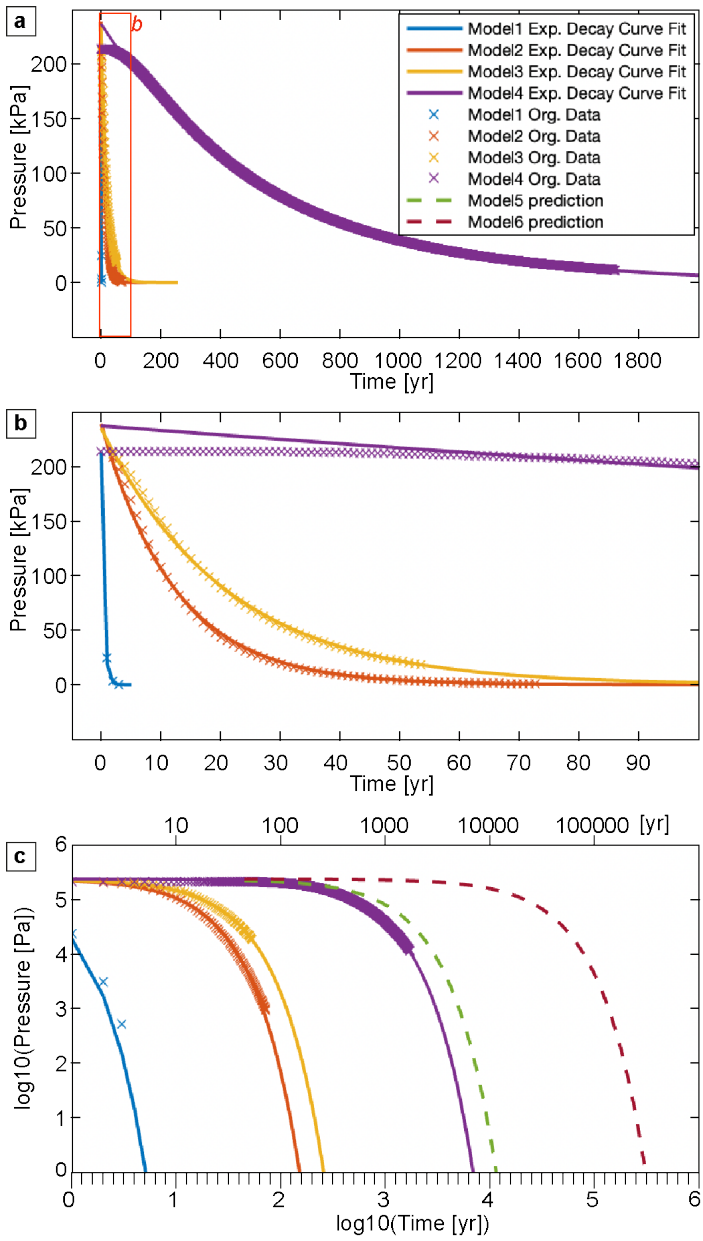

Figure 6.4: *Excess pore pressure decay over time. a: Pressure decay of modelled data (crosses) and fitted exponential decay functions to estimate when the pressure drops below 1 Pa in Models 1 – 4. b: Zoom into a. c: Logarithmic pressure-time diagram showing the pressure decay predictions for Model 5 and Model 6.*

Consequences for slope failure

Much of earth's crust is critically stressed (Zoback et al., 1989) and minor changes in stress of a few kilopascals can already lead to failure. This is exemplified by multiple studies that show how induced seismicity in the US has been triggered by pressure changes of only a few kilopascals (Hornbach et al., 2015a, 2016; Smye et al., 2024). Our end-member models show that the time scale on which excess pore fluid pressure exists within the sedimentary units as response to rapid loading spans from several years to up to several hundred thousand of years, depending on the specific storage and permeability of the sediments, i.e., the lithology of the background sediments. While sand-rich background sediments respond with a rapid excess pore fluid pressure development on the whole slope decaying within days to years, clay-rich sediments favor a more focused pressurization of high-permeable MTDs than the surrounding background sediments, keeping buried MTD's pressurized for hundred thousands of years. Sustained overpressures for several thousands of years imply that there is a high likelihood that not only large earthquakes, but also other geological processes may interact with the pressurized slopes, e.g., unrelated slope failures that deposit MTDs on top of the pressurized MTD may further increase subsurface pressure and sea level will oscillate due to climate cycles changing the hydrostatic pressure (Hermanrud et al., 2013). In consequence, slope failures change the boundary conditions for future slope failures for thousands of years. In sand-rich lithological settings, this may lead to an immediate increase of risk of subsequent failure events on a short time scale, while in clay-rich settings the risk of subsequent failure persist on a geological time scale.

Although this study focuses on slope failures from volcanic ocean islands the results should also be applicable for slope failures on non-volcanic sedimentary slopes, e.g., continental margins. This would explain the observed repetition of slope failures at many well investigated sites such as the Storegga Slide (Berg et al., 2005), the Ana Slide (Berndt et al., 2012), the Cape Fear Slide (Hornbach et al., 2007), or the Fram Slide (Elger et al., 2015). While in the case of the Storegga Slide the recurrence interval fits well with cycles of increased glacial sediment accumulation due to climate cycles (Bryn et al., 2003), this does not apply to many other repeated failure sites. Instead, failure mechanisms related to gas hydrate dissociation (Elger et al., 2015; Hornbach et al., 2007) and fluid migration have been proposed to decrease the stability of sediments to a point where seismic shaking could ultimately trigger slope failure. Overpressure due to loading by previous slope failures has been neglected in the analyses of failure mechanisms at these events. The main reason for this is that the required physical

properties (mainly permeability and compressibility) to calculate pressures and in situ pore fluid pressures are rarely measured during drilling operations. This study indicates that overpressure due to loading of previous slope failures might be in fact the most important control on repeated slope failure. This needs to be included in future hazard assessments of slope failure events.

Methods

The seafloor around Montserrat, Lesser Antilles, hosts more than ten buried or surficial MTDs (Lebas et al., 2011), including failed seafloor sediments (Crutchley et al., 2013) and transported blocks of failed volcanic edifice (Watt et al., 2015). One deposit that combines both, volcanic flank collapse material and failed pre-existing seafloor, is Deposit 2 (Watt et al., 2012). Deposit 2 is composite deposit formed by at least two major volcanic flank collapse events separated by up to 20 m of background sedimentation that differentiate the deposit into two subunits, 2a and 2b (Kühn et al., 2024; Watt et al., 2012). Deposit 2b and 2a are dated 138 and 318 ka., respectively (Kühn et al., 2024; Le Friant et al., 2015). Another MTD, Deposit 8, is located ~100 m below Deposit 2a (Watt et al., 2012).

We use 2D multichannel seismic (MCS) (Kühn et al., 2023) and bathymetry data (Berndt et al., 2021) to constrain the dimensions and thicknesses of the buried MTDs Deposit 2a, Deposit 2b and Deposit 8 (Fig. 6.3a) based on previous interpretations (e.g., Kühn et al., 2024; Lebas et al., 2011, Watt et al., 2012). Two-way-travel times were converted to depth with a constant velocity of 1700 m/s derived from OBS experiments (Kunde, 2020).

We calculate subsurface pressure changes in both space and time using the non-steady two-dimensional pore pressure diffusion equation for porous media with spatially variable hydraulic conductivity:

$$(1)\ \frac{dP}{dt} = \frac{1}{S}\nabla * (k\ \nabla P)$$

where P is the fluid pressure (in space and time) above hydrostatic (Pa), k is the hydraulic conductivity (m/s) variable in space, and S, the specific storage coefficient (1/m), is treated as constant. $\frac{dP}{dt}$ is the change in pressure at a particular location with respect to time, ∇ is the gradient operator, and ∇P is the change in pressure with respect to space. Here, hydraulic conductivity—the ease at which a fluid can moved through pore space—is defined in space for different sedimentary units by direct measurements of drilling samples collected from offshore of the Lesser Antilles (Hornbach et al., 2015b; Koehn et al., 2022). The highest permeability

sediment (sand-rich volcaniclastic turbidites) is assigned a permeability of $1.11e^{-11}$ m^2 (averaged from Koehn et al., 2022), and the lower-permeability hemipelagic sediments are assigned end member minimum values of $9.92e^{-17}$ m^2 (hemipelagic clay, Hornbach et al., 2015b), a mid-range $9.14e^{-15}$ m^2 (minimum hemipelagic sand from Koehn et al., 2022), and a maximum of $3.81e^{-13}$ m^2 (hemipelagic silt/silty sand, averaged from Koehn et al., 2022). For the pressure calculations we converted permeabilities to hydraulic conductivity. The specific storage coefficient S - the amount of water per unit volume an aquifer releases from storage for a given drop in pressure (due to aquifer compressibility) - is assigned minimum end member values of 0.001 m^{-1} for turbidites (Urgeles et al., 2010) and maximum end member values of 0.027 m^{-1} for hemipelagic sediments (Mencaroni et al., 2020) consistent with measurements for unconsolidated sediments (e.g., Domenico and Mifflin, 1965).

We assume the landslide associated with Deposit 2b is emplaced initially at time t=0, and that all sediments not buried by the landslide exhibit hydrostatic pressure conditions (i.e., no overpressure) at this time. For sediments located directly below the landslide, we assume at t=0 an instantaneous increase in pore fluid pressure equal to the weight per unit area of the submerged landslide deposit:

$$(2)\ P_i = (\rho_b - \rho_w)gh$$

where P_i is the initial fluid pressure (Pa) at t=0 above hydrostatic for all sediments located directly below the landslide that feel the initial weight of the deposited landslide, ρ_b is the bulk sediment density (assumed to be, on average, 1750 kg/m^3 based on IODP Expedition 340 measurements (Expedition 340 Scientists, 2013), ρ_w is seawater density (1025 kg/m^3), g is gravitational acceleration, and h is the vertical thickness of the landslide deposit at a particular location (m). This results in an initial pressure of ~0.2134 MPa at t=0. End members for the bulk density of the sediments of 1650 kg/m^3 and 2080 kg/m^3 results in an uncertainty of 0.03 - 0.09 MPa for this initial pore fluid pressure. We model change in pressure in space and time using an explicit (forward in time, center in space), 4^{th} order 2D finite difference methods consistent with previously published pressure and groundwater flow models (e.g., McDonald and Harbaugh, 1988; Fetter, 2018). Model dimensions are 8500 m x 425 m with cell dimensions of 30 m^2 (10 m horizontal and 3 m vertical resolution). To maintain numerical stability, vertical permeability interfaces at sediment boundaries are smoothed with a moving average filter over 3 cells. We assume open (Neuman) side and bottom boundary conditions that allow for pressure to flow out of the model domain, and a constant (Dirichlet) boundary condition at the seabed

of hydrostatic fluid pressure. With the end-member values for the permeability of the background sediments and the specific storage we define six different models (M1 – M6) for pore fluid pressure evolution (Table 6.1). Due to the low deviation (within one order of magnitude) of the measured permeabilities of volcaniclastic deposits in Koehn et al. (2022) we use a constant, averaged permeability of $1.11e^{-11}$ m^2 ($9.90e^{-5}$ m/s hydraulic conductivity) for the MTDs.

Table 6.1: *Modelling parameter values and model names.*

	Permeability of Background Sediments (K_{BG})	Hydraulic Conductivity of Background Sediments	Specific Storage (S)
Model 1	$3.81e^{-13}$ m^2	$3.40e^{-6}$ m/s	0.001 m^{-1}
Model 2	$3.81e^{-13}$ m^2	$3.40e^{-6}$ m/s	0.027 m^{-1}
Model 3	$9.14e^{-15}$ m^2	$8.15e^{-8}$ m/s	0.001 m^{-1}
Model 4	$9.14e^{-15}$ m^2	$8.15e^{-8}$ m/s	0.027 m^{-1}
Model 5	$9.92e^{-17}$ m^2	$8.85e^{-10}$ m/s	0.001 m^{-1}
Model 6	$9.92e^{-17}$ m^2	$8.85e^{-10}$ m/s	0.027 m^{-1}

Uncertainties

We assume isotropy of permeability and specific storage in the perpendicular to the modeling transect which is reasonable for a directed slide that is much wider than thick.

The vertical resolution of the model is 3 m. Thinner impermeable layers may further hinder fluid migration and result in an underestimation in pressure bleed off times.

The seismic data have been converted with a constant velocity of 1700 m/s that is consistent with the core and logging data. Laterally, these velocities may vary by up to 50 m/s resulting in a 3% uncertainty in layer thicknesses.

The used permeabilities and specific storages are variable in space, but not in time. Sediments should slowly consolidate and thus become more impermeable and specific storage should

decrease with time due to contraction. However, the parameter tests with different specific storage should account for this.

We model only the pressure effect of the deposition of one collapse event and neglect the effect of subsequent flank collapses that formed deposits further upslope (e.g., Deposit 1 and pyroclastic flow deposits (Crutchley et al., 2013; Karstens et al., 2013)). However, these deposits do not overly Deposit 2a and should have a neglibel effect on the measurements. Ground acceleration might lead to liquefaction and fluid flow during earthquake events. This may be another explanation for the observed fluid migration structures, but we propose that this is unlikely as they directly connect to the deposit and are absent elsewhere.

Normal faults of the Montserrat Bouillante Graben offset the central part of deposits 2a and 2b. There are no geophysical or geotechnical constraints on the hydraulic permeability of these faults and it is possible that they act as fluid pathways or fluid obstacles. Thus, the results may not be applicable in the direct vicinity of the faults.

References

Berg, K., Solheim, A., and Bryn, P., 2005, The Pleistocene to recent geological development of the Ormen Lange area: Marine and Petroleum Geology, v. 22, p. 45–56, doi:10.1016/j.marpetgeo.2004.10.009.

Berndt, C., Böttner, C., and Wölfl, A.-C., 2021, Multibeam bathymetry raw data (Kongsberg EM 122 entire dataset) of RV METEOR during cruise M154/1:, doi:10.1594/PANGAEA.935598.

Berndt, C., Costa, S., Canals, M., Camerlenghi, A., De Mol, B., and Saunders, M., 2012, Repeated slope failure linked to fluid migration: The Ana submarine landslide complex, Eivissa Channel, Western Mediterranean Sea: Earth and Planetary Science Letters, v. 319–320, p. 65–74, doi:10.1016/j.epsl.2011.11.045.

Bryn, P., Solheim, A., Berg, K., Lien, R., Forsberg, C.F., Haflidason, H., Ottesen, D., and Rise, L., 2003, The Storegga Slide complex; repeated large scale sliding in response to climatic cyclicity, *in* Submarine Mass Movements and Their Consequences: 1 st International Symposium, Springer, p. 215–222.

Bünz, S., Mienert, J., Bryn, P., and Berg, K., 2005, Fluid flow impact on slope failure from 3D seismic data: a case study in the Storegga Slide: Basin Research, v. 17, p. 109–122.

Cartwright, J.A., 1994, Episodic basin-wide hydrofracturing of overpressured Early Cenozoic mudrock sequences in the North Sea Basin: Marine and Petroleum Geology, v. 11, p. 587–607.

Cartwright, J., and Santamarina, C., 2015, Seismic characteristics of fluid escape pipes in sedimentary basins: Implications for pipe genesis: Marine and Petroleum Geology, v. 65, p. 126–140, doi:10.1016/j.marpetgeo.2015.03.023.

Crutchley, G.J. et al., 2013, Insights into the emplacement dynamics of volcanic landslides from high-resolution 3D seismic data acquired offshore Montserrat, Lesser Antilles: Marine Geology, v. 335, p. 1–15, doi:10.1016/j.margeo.2012.10.004.

Day, S.J., 1996, Hydrothermal pore fluid pressure and the stability of porous, permeable volcanoes: Geological Society, London, Special Publications, v. 110, p. 77–93.

Day, S.J., 2015, Volcanic Tsunamis, *in* The Encyclopedia of Volcanoes, Elsevier, p. 993–1009, doi:10.1016/B978-0-12-385938-9.00058-4.

Domenico, P.A., and Mifflin, dan M.D., 1965, Water from low-permeability sediments and land subsidence: Water Resources Research, v. 1, p. 563–576.

Dugan, B., and Flemings, P.B., 2000, Overpressure and fluid flow in the New Jersey continental slope: Implications for slope failure and cold seeps: Science, v. 289, p. 288–291.

Elger, J., Berndt, C., Krastel, S., David, D.J., Gross, F., Spielhagen, R.F., and Meyer, S., 2015, The fram slide off svalbard: A submarine landslide on a lowsedimentation- rate glacial continental margin:

Journal of the Geological Society, v. 172, p. 153–156, doi:10.1144/jgs2014-055.

Elger, J., Berndt, C., Rüpke, L., Krastel, S., Gross, F., and Geissler, W.H., 2018, Submarine slope failures due to pipe structure formation: Nature communications, v. 9, p. 715.

Expedition 340 Scientists, 2013, Expedition 340 summary, *in* Le Friant, A., Ishizuka, O., Stroncik, N.A., and the Expedition 340 Scientists, Proc. IODP, 340: Tokyo (Integrated Ocean Drilling Program Management International, Inc.), doi:10.2204/iodp.proc.340.101.2013.

Fetter, C.W., 2018, Applied hydrogeology: Waveland Press.

Le Friant, A. et al., 2015, Submarine record of volcanic island construction and collapse in the Lesser Antilles arc: First scientific drilling of submarine volcanic island landslides by IODP Expedition 340: Geochemistry, Geophysics, Geosystems, v. 16, p. 420–442, doi:10.1002/2014GC005652.

Gee, M.J.R., Uy, H.S., Warren, J., Morley, C.K., and Lambiase, J.J., 2007, The Brunei slide: A giant submarine landslide on the North West Borneo Margin revealed by 3D seismic data: Marine Geology, v. 246, p. 9–23, doi:10.1016/j.margeo.2007.07.009.

Hampton, M.A., Lee, H.J., and Locat, J., 1996, Submarine landslides: Reviews of Geophysics, v. 34, p. 33–59, doi:10.1029/95RG03287.

Hermanrud, C., Venstad, J.M., Cartwright, J., Rennan, L., Hermanrud, K., and Nordgård Bolås, H.M., 2013, Consequences of Water Level Drops for Soft Sediment Deformation and Vertical Fluid Leakage: Mathematical Geosciences, v. 45, p. 1–30, doi:10.1007/s11004-012-9435-0.

Hornbach, M.J. et al., 2015a, Causal factors for seismicity near Azle, Texas: Nature Communications, v. 6, doi:10.1038/ncomms7728.

Hornbach, M.J. et al., 2015b, Permeability and pressure measurements in Lesser Antilles submarine slides: Evidence for pressure-driven slow-slip failure: Journal of Geophysical Research: Solid Earth, v. 120, p. 7986–8011, doi:10.1002/2015JB012061.

Hornbach, M.J., Jones, M., Scales, M., DeShon, H.R., Magnani, M.B., Frohlich, C., Stump, B., Hayward, C., and Layton, M., 2016, Ellenburger wastewater injection and seismicity in North Texas: Physics of the Earth and Planetary Interiors, v. 261, p. 54–68, doi:10.1016/j.pepi.2016.06.012.

Hornbach, M.J., Lavier, L.L., and Ruppel, C.D., 2007, Triggering mechanism and tsunamogenic potential of the Cape Fear Slide complex, U.S. Atlantic margin: Geochemistry, Geophysics, Geosystems, v. 8, doi:10.1029/2007GC001722.

Huhn, K. et al., 2019, Sector collapse kinematics and tsunami implications - SEKT, Cruise No. M154-2, April 29 - Mai 23, 2019, Pointe-à-Pitre (Guadeloupe) - Pointe-à-Pitre (Guadeloupe).:

Karstens, J., Crutchley, G.J., Berndt, C., Talling, P.J., Watt, S.F.L., Hühnerbach, V., Friant, A. Le, Lebas, E., and Trofimovs, J., 2013, Emplacement of pyroclastic deposits offshore Montserrat: Insights from 3D seismic data: Journal of Volcanology and Geothermal Research, v. 257, p. 1–11,

doi:10.1016/j.jvolgeores.2013.03.004.

King Hubbert, M., and Rubey, W.W., 1959, Role of fluid pressure in mechanics of overthrust faulting: I. Mechanics of fluid-filled porous solids and its application to overthrust faulting: Bulletin of the Geological Society of America, v. 70, p. 115–166, doi:10.1130/0016-7606(1959)70[115:ROFPIM]2.0.CO;2.

Koehn, L. et al., 2022, Data report: permeability measurements inside and outside submarine landslides at IODP Expedition 340 sites, doi:10.2204/iodp.proc.340.208.2022.

Kühn, M. et al., 2024, Volcanic Flank Collapse, Secondary Sediment Failure and Flow-Transition: Multi-Stage Landslide Emplacement Offshore Montserrat, Lesser Antilles: Geochemistry, Geophysics, Geosystems, v. 25, p. e2024GC011564, doi:https://doi.org/10.1029/2024GC011564.

Kühn, M., Berndt, C., and Krastel, S., 2023, 2D multichannel seismic reflection processed data (GI Gun entire dataset) of RV METEOR during cruise M154/1:, doi:10.1594/PANGAEA.957490.

Kühn, M., Karstens, J., Berndt, C., and Watt, S.F.L., 2021, Seismic reconstruction of seafloor sediment deformation during volcanic debris avalanche emplacement offshore Sakar, Papua New Guinea: Marine Geology, v. 439, doi:10.1016/j.margeo.2021.106563.

Kunde, D., 2020, Seismic velocity of sector collapse deposits off Montserrat [Master's thesis]: Christian-Albrechts-Universität zu Kiel.

Lebas, E., Le Friant, A., Boudon, G., Watt, S.F.L., Talling, P.J., Feuillet, N., Deplus, C., Berndt, C., and Vardy, M.E., 2011, Multiple widespread landslides during the long-term evolution of a volcanic island: Insights from high-resolution seismic data, Montserrat, Lesser Antilles: Geochemistry, Geophysics, Geosystems, v. 12, doi:10.1029/2010GC003451.

Masson, D.G., Harbitz, C.B., Wynn, R.B., Pedersen, G., and Løvholt, F., 2006, Submarine landslides: processes, triggers and hazard prediction.: Philosophical transactions. Series A, Mathematical, physical, and engineering sciences, v. 364, p. 2009–2039, doi:10.1098/rsta.2006.1810.

McDonald, M.G., and Harbaugh, A.W., 1988, A modular three-dimensional finite-difference ground-water flow model: US Geological Survey.

Mencaroni, D., Llopart, J., Urgeles, R., Lafuerza, S., Gràcia, E., Friant, A. Le, and Urlaub, M., 2020, From gravity cores to overpressure history: The importance of measured sediment physical properties in hydrogeological models, *in* Geological Society Special Publication, Geological Society of London, v. 500, p. 289–300, doi:10.1144/SP500-2019-176.

Moore, J.G., and Normark, W.R., 1994, Giant Hawaiian Landslides: Annual Review of Earth and Planetary Sciences, v. 22, p. 119–144.

Omeru, T., and Cartwright, J.A., 2015, Multistage, progressive slope failure in the Pleistocene pro-deltaic slope of the West Nile Delta (Eastern Mediterranean): Marine Geology, v. 362, p. 76–92, doi:10.1016/j.margeo.2015.01.012.

Smye, K.M., Ge, J., Calle, A., Morris, A., Horne, E.A., Eastwood, R.L., Darvari, R., Nicot, J.P., and Hennings, P., 2024, Role of Deep Fluid Injection in Induced Seismicity in the Delaware Basin, West Texas and Southeast New Mexico: Geochemistry, Geophysics, Geosystems, v. 25, doi:10.1029/2023GC011260.

Sultan, N. et al., 2004a, Triggering mechanisms of slope instability processes and sediment failures on continental margins: A geotechnical approach: Marine Geology, v. 213, p. 291–321, doi:10.1016/j.margeo.2004.10.011.

Sultan, N., Cochonat, P., Foucher, J.P., and Mienert, J., 2004b, Effect of gas hydrates melting on seafloor slope instability: Marine Geology, v. 213, p. 379–401, doi:10.1016/j.margeo.2004.10.015.

Urgeles, R., Locat, J., Sawyer, D.E., Flemings, P.B., Dugan, B., and Binh, N.T.T., 2010, History of pore pressure build up and slope instability in mud-dominated sediments of Ursa Basin, Gulf of Mexico continental slope: Submarine mass movements and their consequences, p. 179–190.

Watt, S.F.L. et al., 2015, New insights into landslide processes around volcanic islands from Remotely Operated Vehicle (ROV) observations offshore Montserrat: Geochemistry, Geophysics, Geosystems, v. 16, p. 2240–2261, doi:10.1002/2015GC005781.

Watt, S.F.L. et al., 2012, Widespread and progressive seafloor-sediment failure following volcanic debris avalanche emplacement: Landslide dynamics and timing offshore Montserrat, Lesser Antilles: Marine Geology, v. 323–325, p. 69–94, doi:10.1016/j.margeo.2012.08.002.

Zoback, M. Lou, Zoback, M.D., Adams, J., Assumpcao, M., Bell, S., Bergman, E.A., Blümling, P., Brereton, N.R., Denham, D., and Ding, J., 1989, Global patterns of tectonic stress: Nature, v. 341, p. 291–298.

7. Conclusion and Outlook

7.1 Conclusion

Reliable hazard assessment for volcanic island flank collapse requires precise information on the geological and physical processes before, during and after the failure event. In volcanic island settings, where collapse scars can be quickly overprinted by subsequent volcanism and erosion, offshore mass transport deposits often represent the only available constraints. However, these deposits cannot be easily accessed from the land side, complicating research endeavors. High-resolution 3D and 2D seismic and hydroacoustic data, combined with drill cores, and physical sediment properties allow a detailed reconstruction of the processes involved in the emplacement of the associated submarine mass transport deposits.

The potential of seismic analyses has been demonstrated in Chapter 3 of this thesis (Kühn et al., 2021) by analyzing two previously unknown volcanic flank collapse deposits (SLD1 and SLD2) offshore Sakar Island, Papua New Guinea. Although originating from the same source and deposited on the same slope, SLD2 has an elongated shape and consists to more than half of seafloor sediments that were deformed by the proximal incision of an initial, blocky volcanic debris avalanche and an overrunning debris flow associated with the initial collapse event. SLD1 in contrast, was deposited in a sub-circular shape showing no clear evidence of large-scale seafloor sediment incorporation or deformation. We explain this different style of emplacement with the nature of the substrate: the slide mass associated with SLD2 slid on relatively homogeneous hemipelagic sediments that could easily be eroded into by the initial debris avalanche. The slide mass associated with SLD1 slid on a comparably inhomogeneous substrate, the proximal SLD2. Chapter 3 highlights that the nature of the substrate is a crucial factor for the evolution of a submarine landslide and its tsunami hazard.

However, the analyses of the Sakar Island debris avalanche deposits were solely based on seismic data as no sediment core or drill data was available, which could have allowed constraining the nature of the slide material and the underlying sediment inn detail. The significant benefit of including such data in the analysis is illustrated by Chapter 4 (Kühn et al., 2024), which investigates the geological processes that have been involved in the emplacement of an ancient mass transport deposit (subdivided in Deposit 2a and Deposit 2b) offshore Montserrat, Lesser Antilles. Our combined high-resolution seismic and drill core analyzes revealed that Deposit 2a and Deposit 2b are separated by up to 20 m of hemipelagic sediments

implying a minimum time gap of 180 kyrs between their deposition. Both deposits originate from volcanic flank collapse events at Soufrière Hills volcano on Montserrat, but the event associated with Deposit 2a also triggered secondary seafloor failure of the norther flank of the Montserrat-Bouillante-Graben and incised into the preexisting seafloor and caused large-scale sediment deformation. It is therefore essential for accurate tsunami simulations to consider the possibility of multiple stages in the formation of mass transport deposits. Despite advancements in 3D seismic-reflection datasets and core sampling, uncertainties about the timing and nature of events, such as those forming Deposit 2, persist. We show that the topography influences the transport evolution of blocky volcanic mass transport deposits. Features like graben structures or pre-existing deposits can direct the movement of avalanches along slopes rather than a free spreading of the slide mass. This topographic control must be considered in landslide modeling. While these complexities may not have a significant impact on tsunami generation at Montserrat due to the water depth of more than 1 km, they are likely critical in shallower water settings such as Anak Krakatau or Ritter Island. Additionally, we report the late-stage occurrence of a highly-mobile, erosive density flow that incised a channel-system on top of the blocky central part of Deposit 2a. As this is the second time that such erosive flow preceding a flank collapse event is observed, this might be a common process in the depositional sequence of volcanic flank collapses.

While the analysis of seismic data can provide indications for fluid migration, which is critical for assessing slope stability and highly relevant for the potential of secondary seafloor failures and entrapment, only direct measurements of pore fluid parameters such as temperature and pressure allow quantification of fluid migration associated with mass movement. The potential of such analyses are explored in Chapters 5 and 6. Chapter 5 (Hornbach et al., in review) investigates temperature data measured in buried mass transport deposits offshore Montserrat. Temperature data were acquired with a HyLO probe and MeBo70 acoustic-temperature log measurements and indicate highly variable heat flow across the Lesser Antilles arc. Our approach provides the first high-resolution (cm-scale) temperature-depth measurements in the area. We find the highest temperature values in heavily faulted regions and anomalously warm isothermal zones associated with higher permeability mass transport deposits. Thermal gradient models based on this data indicate advective heat flow, suggesting an upward injection of warm fluid from overpressured mass transport deposits into overlying low-permeable hemipelagic background sediments.

Based on the results of this analyses, Chapter 6 deals with the evolution of excess pore fluid pressure after the rapid loading due to volcanic flank collapse emplacement. We used a 2D finite difference modelling approach to solve the diffusive pressure equation derived from Darcy's Law and the Conservation of Mass. My co-authors and I show that excess pore fluid pressure due to loading of a previous slope failure/flank collapse can persist over hundreds of thousands of years, if the background sediments are mostly clay-rich and thus highly impermeable and the pressure distribution is focused in buried mass transport deposits. In settings that are dominated by sand-rich background sediments, pore pressure diffuses within years, but pressurizes the whole slope due to a very low permeability contrast of the high-permeable mass transport deposits and the only slightly more impermeable sand-rich background sediments. We show that overpressure due to previous slope failure events is far more important for slope stability than previously anticipated.

The main aim of this thesis is to identify processes that are involved in the emplacement of volcanic flank collapses, to analyze how these processes interact with each other and how they affect tsunami magnitudes. Chapter 3 highlights that volcanic flank collapse deposition offshore Sakar Island included two initial volcanic flank collapses, the proximal incision of the first slide mass into the substrate and wide-spread sediment deformation with a main axis following the general slide direction. Chapter 4 identifies two distinct volcanic flank collapse events forming a large-scale mass transport deposit as well. In the chain of events that preceded the first initial flank collapse, secondary sediment failure was triggered and the slide mass incised into substrate, causing again wide-spread deformation of seafloor sediments. We find indications that highly-erosive flows are common late-stage phenomena during flank collapse events. Chapters 3 and 4 indicate two major controls on the deposit's shape and morphology: the nature of the substrate defines if a slide incises into the substrate. The more homogenous the substrate is, the more likely is an incision. These proximal incisions are the main driver for deformation of adjacent seafloor sediments. The second control on the deposit's shape and morphology is the pre-existing topography. A channelization of the slide mass by a tectonic graben or a narrowed topography by pre-existing mass transport deposits or other morphological features on the slope facilitate a longer runout and more elongated shape of the deposits, while a freely-spreading slide is mostly deposited in a sub-circular shape and with a shorter runout. The deposition of a volcanic flank collapse is far more complex than a simple, constant volume of a slide mass travelling down a homogenous slope. Landslide and tsunami models need to include this complexity for accurate hazard assessment. Setting up an individual landslide and

tsunami model for Sakar Island and Montserrat could not be achieved within the framework of this thesis, but might be part of future work with the associated datasets.

Another major aim of this thesis is to investigate the influence of rapid loading by a volcanic mass transport deposit on subsurface pore fluid pressure and what consequences for the stability of the sediments on the volcanic flank arise from this. We show that buried mass transport deposits offshore Montserrat are in fact overpressured (Chapters 5 and 6) and the rapid emplacement of a mass transport deposit can cause excess pore pressure in the underlying and adjacent sediments for up to hundreds of thousands of years. This is a previously neglected explanation for repeated slope failures at the same sites in different settings and locations around the world. Slope failures are a crucial factor for future slope stability.

7.2 Outlook

Chapters 4, 5, and 6 clearly illustrate that drilling data is crucial to ground-truth seismic interpretations and to extract insights on flank collapse processes from ancient flank collapse deposits. As of today, global seafloor drilling campaigns within the framework of IODP using dedicated drill vessels like D/V *JOIDES Resolution* will not be continued. Consequently, marine research and especially volcano collapse research will lose a powerful tool to obtain *in situ* information of volcanic flank collapse deposits, e.g., lithology, physical properties, temperature, and pressure. As I have shown in the Chapters 4, 5, and 6 of this thesis, these parameters are crucial to understand the processes and mechanisms that lead to failure and tsunami generation. Alternatives to IODP are mission-specific platforms (Daigle et al., 2023) or robotic seafloor drill rigs like MeBo70 and MeBo200 (Freudenthal and Wefer, 2013). Offshore Montserrat, MeBo70 has proven to be a drilling platform capable of not only drilling into volcanic flank collapse deposits, but also retrieve core sections, core logs, physical properties, seismic velocities, and *in situ* pressures (Huhn et al., 2019; Kühn et al., 2024). This is remarkable given the fact, that the - in orders of magnitude more expensive - IODP Expedition 340 on D/V *JOIDES Resolution* was less successful in achieving this in the same area (c.f. Le Friant et al., 2015). Robust tsunami simulations rely on differentiating between initially failed volcanic edifice material and secondarily failed seafloor (Karstens et al., 2020). As shown in Chapter 5, this cannot be achieved by using seismic data alone, but requires lithological analyses of drill cores. The combination of high-resolution 3D P-Cable MCS data with MeBo drill data has proven to be a successful combination of tools to target this. However, the large volcanic flank collapse deposits offshore Montserrat have been deposited thousands

to hundred thousands of years ago and have likely been affected by erosional processes. A 'fresh' example, likely undisturbed by major erosional processes, are the deposits associated with the 2018 collapse of Anak Krakatau, Indonesia. This undisturbed nature makes Anak Krakatau an ideal target for future research. In consequence, I recommend a proposal of a two-stage research expedition to Anak Krakatau. The first stage involves the acquisition of a 3D P-Cable MCS over the extent of the 2018 deposits to determine its shape, volume, morphology, and internal architecture. The second stage involves a drilling campaign with the MeBo70 or MeBo200 seafloor drill rig to acquire drill data from above, within, below, and adjacent to the deposit, including in situ pressure measurements via CPT and the MeBo70-CORK (Circulation Obviation Retrofit Kits) (Kopf et al., 2015). This expedition would deliver key information to better understand volcanic flank collapses and their deposition.

Previous tsunami simulations have shown that the tsunami magnitude is mainly controlled by the initial slide volume of the collapsing flank and the initial velocity of the slide mass as it breaks through the sea surface (Karstens et al., 2020). Chapter 4 of this thesis delivers the first parameter, as I mapped out two distinct volcanic flank collapse deposits differentiated from an adjacent and underlying apron of deformed seafloor sediments. The consequential next step for the Montserrat data will be to use this (combined with the physical properties from the MeBo70 campaign) as input for numerical landslide models to constrain the slide velocity of the landslides associated with the flank failures of Soufriére Hills volcano. Several numerical landslide models have been developed in the past (e.g., Carlton et al., 2019; Løvholt et al., 2017). The resulting landslide velocities could then be used for tsunami hazard assessments at Montserrat, but will also be applicable to other volcanic islands.

Our study on pore fluid pressure development in response to rapid loading by mass transport deposits (Chapter 7) has shown that overpressure due to previous slope failures may sustain for hundred thousands of years, increasing the risk for subsequent failure. The role of previous failure events in overpressure development in slope sediments has been underestimated in the past. I propose to conduct a generic pore pressure 3D modelling study to model pore pressure evolution due to loading by previous failure events in different environments, from arc-island settings, via intraplate ocean islands, to continental margins. These models could be used to further analyze the influence of critical parameters like permeability and specific storage, but also the influence of slide volumes and slope angles. The plausibility of these models could then be tested with water tank experiments. This composite modelling/water tank experiment study will deliver important constraints for slope stability assessments.

Volcanic flank collapse and associated tsunami hazard assessments require direct monitoring of subaerial volcanoes and their flanks, as well as the submerged part of the flank and associated sedimentary slopes. A crucial parameter for this is the deformation of the volcanic flank. Subaearial flank monitoring, focused on deformation and flank movement can be cost-efficiently achieved by satellite-based techniques, e.g., GPS/GNSS and InSAR (Bonforte et al., 2011; Bonforte and Puglisi, 2006) or approaches combining satellite data with onshore seismicity data (e.g., Di Traglia et al., 2023). However, satellite-based geodetic measurements are not usable to detect movement in submarine environments, as seawater has a very high opacity to electromagnetic waves. Several methods have been developed over the past decades to address this problem by measuring seafloor deformation and displacement with devices deployed at the seafloor (c.f. Urlaub and Villinger, 2018; references therein). A practical and cost-efficient solution for this is the use of seafloor geodetic devices equipped with pressure sensors and acoustic direct path transponders to measure absolute vertical displacements (pressure sensors) and relative horizontal displacements (acoustic ranging) (Bürgmann and Chadwell, 2014; McGuire and Collins, 2013; Petersen et al., 2019). This method was successfully applied at Mt. Etna, Italy, where an array of seafloor geodetic instruments for the first time detected rapid movement of the volcanos submarine flank (Urlaub et al., 2018). Another instrumentation to measure seafloor displacement are fiber optic cables: in this approach, laser reflectometry is used to optically measure strain in a fiber optic cable deployed at the seafloor (Gutscher et al., 2023). This is currently tested as part of the ongoing European Research Council (ERC) Project FOCUS (Fiber Optic Cable Use for Seafloor studies of earthquake hazard and deformation) offshore Mt. Etna (Gutscher et al., 2019). As volcanic flank collapses are often linked to volcanic eruptions (e.g., Anak Krakatau, Walter et al., 2019), eruption forecasting is an important tool to assess the risk of volcanic flank collapse as well. Over the past decades, the research of eruption forecasts has slowly shifted from description-based models that rely on historically reported eruptions of specific volcano towards physics-based models, focusing on understanding pre-eruptive processes (Acocella et al., 2024). A successful eruption forecast at a submarine volcano by inflation detection has been made at Axial Seamount, where water-pressure sensors measuring vertical displacement of the seafloor could be used to forecast an eruption of the volcano in 2015 (Nooner and Chadwick Jr, 2016). The instruments use for this were part of a large array of instruments and cables spanning the Juan-de-Fuca-Plate in the East Pacific Ocean (Kelley et al., 2014). Observatories that enable live monitoring of volcanos and the seafloor are in operation at several locations worldwide (e.g., Howe et al., 2011; Kauahikaua and Poland, 2012). An example for a more recently

initiated holistic monitoring approach is the SANTORY project (Nomikou et al., 2022) that aims to monitor the seafloor around Santorini and Kolumbo in Aegean Sea with multiple chemical and geophysical methods, including hyperspectral imaging, temperature sensors, a radiation spectrometer, fluid/gas samplers, and pressure gauges (Nomikou et al., 2022). A similar approach is used in the recently started joint project MULTI-MAREX by the *Deutsche Allianz Meeresforschung* with several international partners that aims to set up an observatory for investigating extreme geological events and associated hazards (see https://www.geomar.de/en/multi-marex).

As stated earlier, no tsunami warning was issued in the event chain of the 2018 Anak Krakatau flank collapse, because the regional tsunami early warning system was responsive to earthquake-related tsunamis only (Zorn et al., 2023). However, over the last years a new tsunami early warning system based on continuous tide gauge and CCTV observations was successfully installed around the remnants Krakatau archipelago to fill this gap (Annunziato et al., 2019).

Volcanic flank collapse hazard assessments require both, the study of ancient and historic flank collapse deposits to understand processes and controlling parameters pre-, syn-, and post-collapse, as well as the active monitoring of volcanic flanks as part of early warning systems (Kopp et al., 2021). Recent studies indicate that the rapid anthropogenic climate change and the resulting increase in the frequency of extreme weather events (e.g., heavy rainfalls) may increase the frequency of future flank collapse events (Aubry et al., 2022; Farquharson and Amelung, 2022). In consequence, we need to facilitate our efforts to develop robust hazard assessments to reduce the risk for life and infrastructure in the vicinity of marine volcanoes.

In summary I propose four next steps to continue the research of this doctoral thesis:

- I propose a combined 3D MCS/drilling expedition to Anak Krakatau – the latest historic example of a tsunamigenic volcanic flank collapse
- Landslide modelling of the flank collapses associated with Deposit 2a and Deposit 2b to constrain landslide velocities
- A generic pore pressure evolution modelling study combined with water tank experiments to further analyze the role of overpressure in destabilizing slopes in different volcanic and sedimentary settings
- Acceleration of the development of active monitoring systems due to a potentially increased risk of volcano collapses by climate change

References

Acocella, V., Ripepe, M., Rivalta, E., Peltier, A., Galetto, F., Joseph, E., 2024. Towards scientific forecasting of magmatic eruptions. Nat Rev Earth Environ. https://doi.org/10.1038/s43017-023-00492-z

Annunziato, A., Prasetya, G., Husrin, S., 2019. Anak Krakatau volcano emergency tsunami early warning system. Science of Tsunami Hazards 38, 68–95.

Aubry, T.J., Farquharson, J.I., Rowell, C.R., Watt, S.F.L., Pinel, V., Beckett, F., Fasullo, J., Hopcroft, P.O., Pyle, D.M., Schmidt, A., Sykes, J.S., 2022. Impact of climate change on volcanic processes: current understanding and future challenges. Bull Volcanol 84. https://doi.org/10.1007/s00445-022-01562-8

Bonforte, A., Guglielmino, F., Coltelli, M., Ferretti, A., Puglisi, G., 2011. Structural assessment of mount Etna volcano from permanent scatterers analysis. Geochemistry, Geophysics, Geosystems 12. https://doi.org/10.1029/2010GC003213

Bonforte, A., Puglisi, G., 2006. Dynamics of the eastern flank of Mt. Etna volcano (Italy) investigated by a dense GPS network. Journal of Volcanology and Geothermal Research 153, 357–369. https://doi.org/10.1016/j.jvolgeores.2005.12.005

Bürgmann, R., Chadwell, D., 2014. Seafloor geodesy. Annu Rev Earth Planet Sci. https://doi.org/10.1146/annurev-earth-060313-054953

Carlton, B., Vanneste, M., Forsberg, C.F., Knudsen, S., Løvholt, F., Kvalstad, T., Holm, S., Kjennbakken, H., Mazhar, M.A., Degago, S., 2019. Geohazard assessment related to submarine instabilities in Bjørnafjorden, Norway. Geological Society, London, Special Publications 477, 549–566.

Daigle, H., Duarte, J.C., Fagereng, A., Paris, R., Persaud, P., Gómez-García, Á.M., 2023. MagellanPlus Workshop: mission-specific platform approaches to assessing natural hazards that impact society.

Di Traglia, F., Bruno, V., Casu, F., Cocina, O., De Luca, C., Giudicepietro, F., Macedonio, G., Mattia, M., Monterroso, F., Privitera, E., Lanari, R., 2023. Multi-Temporal InSAR, GNSS and Seismic Measurements Reveal the Origin of the 2021 Vulcano Island (Italy) Unrest. Geophys Res Lett 50. https://doi.org/10.1029/2023GL104952

Farquharson, J.I., Amelung, F., 2022. Volcanic hazard exacerbated by future global warming-driven increase in heavy rainfall. R Soc Open Sci 9. https://doi.org/10.1098/rsos.220275

Freudenthal, T., Wefer, G., 2013. Drilling cores on the sea floor with the remote-controlled sea floor drilling rig MeBo. Geoscientific Instrumentation, Methods and Data Systems 2, 329–337. https://doi.org/10.5194/gi-2-329-2013

Gutscher, M.A., Quetel, L., Murphy, S., Riccobene, G., Royer, J.Y., Barreca, G., Aurnia, S., Klingelhoefer, F., Cappelli, G., Urlaub, M., Krastel, S., Gross, F., Kopp, H., 2023. Detecting strain with a fiber optic cable on the seafloor offshore Mount Etna, Southern Italy. Earth Planet Sci Lett

616. https://doi.org/10.1016/j.epsl.2023.118230

Gutscher, M.-A., Royer, J.-Y., Graindorge, D., Murphy, S., Klingelhoefer, F., Aiken, C., Cattaneo, A., Barreca, G., Quetel, L., Riccobene, G., Petersen, F., Urlaub, M., Krastel, S., Gross, F., Kopp, H., Margheriti, L., Beranzoli, L., 2019. Fiber optic monitoring of active faults at the seafloor: the FOCUS project. Photoniques 32–37. https://doi.org/10.1051/photon/2019s432

Howe, B.M., Lukas, R., Duennebier, F., Karl, D., 2011. ALOHA cabled observatory installation, in: OCEANS'11 MTS/IEEE KONA. IEEE, pp. 1–11.

Huhn, K., Freudenthal, T., Dehning, K., Gatter, R., Hilgenfeldt, C., Hönekopp, L., Hornbach, M., Kühn, M., Kuhlmann, J., Kutterolf, S., Meyer-Schack, B., Pallapies, K., Rapp, S.K., Sievers, C., Watt, S., Stelzner, M., 2019. Sector collapse kinematics and tsunami implications - SEKT, Cruise No. M154-2, April 29 - Mai 23, 2019, Pointe-à-Pitre (Guadeloupe) - Pointe-à-Pitre (Guadeloupe).

Karstens, J., Kelfoun, K., Watt, S.F.L., Berndt, C., 2020. Combining 3D seismics, eyewitness accounts and numerical simulations to reconstruct the 1888 Ritter Island sector collapse and tsunami. International Journal of Earth Sciences. https://doi.org/10.1007/s00531-020-01854-4

Kauahikaua, J., Poland, M., 2012. One hundred years of volcano monitoring in Hawaii. Eos (Washington DC) 93, 29–30. https://doi.org/10.1029/2012EO030001

Kelley, D.S., Delaney, J.R., Juniper, S.K., 2014. Establishing a new era of submarine volcanic observatories: Cabling Axial Seamount and the Endeavour Segment of the Juan de Fuca Ridge. Mar Geol 352, 426–450. https://doi.org/10.1016/j.margeo.2014.03.010

Kopf, A., Freudenthal, T., Ratmeyer, V., Bergenthal, M., Lange, M., Fleischmann, T., Hammerschmidt, S., Seiter, C., Wefer, G., 2015. Simple, affordable, and sustainable borehole observatories for complex monitoring objectives. Geoscientific Instrumentation, Methods and Data Systems 4, 99–109. https://doi.org/10.5194/gi-4-99-2015

Kopp, H., Chiocci, F.L., Berndt, C., Çağatay, M.N., Ferreira, T., Fortes, C.J.E.M., Gràcia, E., González Vega, A., Kopf, A.J., Sørensen, M.B., 2021. Marine geohazards: Safeguarding society and the Blue Economy from a hidden threat. European Marine Board IVZW.

Kühn, M., Berndt, C., Watt, S.F.L., Hornbach, M.J., Krastel, S., Sass, K., Kutterolf, S., Freudenthal, T., Huhn, K., Karstens, J., Schramm, B., Elger, J., Böttner, C., Klaeschen, D., 2024. Volcanic Flank Collapse, Secondary Sediment Failure and Flow-Transition: Multi-Stage Landslide Emplacement Offshore Montserrat, Lesser Antilles. Geochemistry, Geophysics, Geosystems 25, e2024GC011564. https://doi.org/https://doi.org/10.1029/2024GC011564

Kühn, M., Karstens, J., Berndt, C., Watt, S.F.L., 2021. Seismic reconstruction of seafloor sediment deformation during volcanic debris avalanche emplacement offshore Sakar, Papua New Guinea. Mar Geol 439. https://doi.org/10.1016/j.margeo.2021.106563

Le Friant, A., Ishizuka, O., Boudon, G., Palmer, M.R., Talling, P.J., Villemant, B., Adachi, T., Aljahdali,

M., Breitkreuz, C., Brunet, M., Caron, B., Coussens, M., Deplus, C., Endo, D., Feuillet, N., Fraas, A.J., Fujinawa, A., Hart, M.B., Hatfield, R.G., Hornbach, M., Jutzeler, M., Kataoka, K.S., Komorowski, J.C., Lebas, E., Lafuerza, S., Maeno, F., Manga, M., Martínez-Colõn, M., McCanta, M., Morgan, S., Saito, T., Slagle, A., Sparks, S., Stinton, A., Stroncik, N., Subramanyam, K.S.V., Tamura, Y., Trofimovs, J., Voight, B., Wall-Palmer, D., Wang, F., Watt, S.F.L., 2015. Submarine record of volcanic island construction and collapse in the Lesser Antilles arc: First scientific drilling of submarine volcanic island landslides by IODP Expedition 340. Geochemistry, Geophysics, Geosystems 16, 420–442. https://doi.org/10.1002/2014GC005652

Løvholt, F., Bondevik, S., Laberg, J.S., Kim, J., Boylan, N., 2017. Some giant submarine landslides do not produce large tsunamis. Geophys Res Lett 44, 8463–8472. https://doi.org/10.1002/2017GL074062

McGuire, J.J., Collins, J.A., 2013. Millimeter-level precision in a seafloor geodesy experiment at the Discovery transform fault, East Pacific Rise. Geochemistry, Geophysics, Geosystems 14, 4392–4402. https://doi.org/10.1002/ggge.20225

Nomikou, P., Polymenakou, P.N., Rizzo, A.L., Petersen, S., Hannington, M., Kilias, S.P., Papanikolaou, D., Escartin, J., Karantzalos, K., Mertzimekis, T.J., Antoniou, V., Krokos, M., Grammatikopoulos, L., Italiano, F., Caruso, C.G., Lazzaro, G., Longo, M., Sciré Scappuzzo, S., D'Alessandro, W., Grassa, F., Bejelou, K., Lampridou, D., Katsigera, A., Dura, A., 2022. SANTORY: SANTORini's Seafloor Volcanic ObservatorY. Front Mar Sci 9. https://doi.org/10.3389/fmars.2022.796376

Nooner, S.L., Chadwick Jr, W.W., 2016. Inflation-predictable behavior and co-eruption deformation at Axial Seamount. Science (1979) 354, 1399–1403.

Petersen, F., Kopp, H., Lange, D., Hannemann, K., Urlaub, M., 2019. Measuring tectonic seafloor deformation and strain-build up with acoustic direct-path ranging. J Geodyn. https://doi.org/10.1016/j.jog.2019.01.002

Urlaub, M., Petersen, F., Gross, F., Bonforte, A., Puglisi, G., Guglielmino, F., Krastel, S., Lange, D., Kopp, H., 2018. Gravitational collapse of Mount Etna's southeastern flank, Sci. Adv.

Urlaub, M., Villinger, H., 2018. Combining in situ monitoring using seabed instruments and numerical modelling to assess the transient stability of underwater slopes, in: 8th International Symposium on Submarine Mass Movements and Their Consequences, ISSMMTC 2018. The Geological Society of London, pp. 511–521. https://doi.org/10.1144/SP477.8

Walter, T.R., Haghshenas Haghighi, M., Schneider, F.M., Coppola, D., Motagh, M., Saul, J., Babeyko, A., Dahm, T., Troll, V.R., Tilmann, F., Heimann, S., Valade, S., Triyono, R., Khomarudin, R., Kartadinata, N., Laiolo, M., Massimetti, F., Gaebler, P., 2019. Complex hazard cascade culminating in the Anak Krakatau sector collapse. Nat Commun 10. https://doi.org/10.1038/s41467-019-12284-5

Zorn, E.U., Vassileva, M., Walter, T.R., Darmawan, H., Röhler, L., Amelung, F., 2023. Interactions of

magmatic intrusions with the multiyear flank instability at Anak Krakatau volcano, Indonesia: Insights from InSAR and analogue modeling. Geology 51, 340–344. https://doi.org/10.1130/G50693.1

Acknowledgements

First and foremost, I would like to thank **Christian Berndt** for his supervision over the last years. Thanks for mentoring me through this work and for your tireless support. You once told me that one of your main aspirations is that your doctoral students are ready to be released into the scientific world at the end of their doctorates. I don't know if that applies in my case, but we certainly had a lot of fun along the way. I would also like to thank **Sebastian Krastel** for his co-supervision and support. Thanks for hosting me in your research group.

My special thanks go to **Matthew J. Hornbach**, the Ricky Bobby of Marine Geophysics. Working with you and your group, especially your attitude and your approach to science has had lasting impact on me. Thank you for your mentoring, your support, your hospitality, and for letting me drive a golf cart through East Texas. I really appreciate it.

Special thanks to **Bettina Schramm**, for proofreading this thesis, your relentless support, and for everything else.

Special thanks also to **Rebecca Kühn** for proofreading this thesis and for awakening my interest in Earth Sciences many years ago.

Big thanks also to **Jens Karstens**, **Morelia Urlaub**, **Gareth Crutchley**, **Dirk Klaeschen**, and **Michael Riedel** for your support and for all the discussions on various geological and geophysical problems. And thanks to **Heidrun Kopp** for your trust in giving me responsibility at sea and your advices regarding my career. Many thanks to **Anne Völsch** for your constant support over the last years and of course for all the coffee. Many thanks also to **Jette Schätzel**, **Jasmin Mögeltönder**, **Thies Bartels**, and **Lea Rohde**.

Many thanks to the entire **Geodynamics group** for the nice atmosphere, the support, and all fun we had on our research expeditions to all the world's oceans. This work would not have been possible without the great scientists, technicians, and crews of the research expeditions SO252 and M154. I appreciate your work and efforts. I thankfully acknowledge the funding of my work by the DFG as part of the "SEKT" project.

And of course, many thanks to my family for your support. Thank you, **Beate**, **Ebi**, **Rebecca**, **David**, and **Kassia**.

Thanks to all of you. The next round is on me.

Curriculum Vitae

Removed in online version.

Publication list

The following publications can be found online and accessed via:
https://oceanrep.geomar.de/view/creators/1309d47b-0958-4c6b-bcd6-8e3e7abfb534.default.html and via ORCID: https://orcid.org/0000-0002-6323-896X.

Peer-reviewed articles

Kühn, M., Hornbach, M. J., Berndt, C., Watt, S. F. L., and Urlaub, M. (in preparation). *Loaded to fail - Excess pore fluid pressure by stacking of mass transport deposits offshore Montserrat.*

Hornbach, M. J., **Kühn, M.**, Freudenthal, T., Graw, J., Berndt, C., Huhn, K., Watt, S.F.L., Phrampus, B. J. and Wood, W. T. (submitted). *New Heat Flow Measurements Offshore Montserrat: Advective Heat Flow Detected via MeBo Borehole Temperature Logging.* Journal of Geophysical Research – Solid Earth.

Kühn, M., Berndt, C., Watt, S. F. L., Hornbach, M. J., Krastel, S., Sass, K., Kutterolf, S., Freudenthal, T., Huhn, K., Karstens, J., Schramm, S., Elger, J., Böttner, C., and Klaeschen, D. (2024). *Volcanic flank collapse, secondary sediment failure and flow-transition: Multi-stage landslide emplacement offshore Montserrat, Lesser Antilles.* Geochemistry, Geophysics, Geosystems, 25(6), e2024GC011564.

Karstens, J., Crutchley, G. J., Hansteen, T. H., Preine, J., Carey, S., Elger, J., **Kühn, M.**, Nomikou, P., Schmid, F., Dalla Valle, G., Kelfoun, K. and Berndt, C. (2023). *Cascading events during the 1650 tsunamigenic eruption of Kolumbo volcano.* Nature Communications, 14. Art.Nr. 6606. DOI 10.1038/s41467-023-42261-y.

Crutchley, G. J., Karstens, J., Preine, J., Hübscher, C., Fossen, H. and **Kühn, M.** (2023). *Extensional Faulting Around Kolumbo Volcano, Aegean Sea — Relationships Between Local Stress Fields, Fault Relay Ramps, and Volcanism.* Tectonics, 42 (10). e2023TC007951. DOI 10.1029/2023TC007951.

Karstens, J., Preine, J., Crutchley, G. J., Kutterolf, S., van der Bilt, W. G., Hooft, E. E., Druitt, T. H., Schmid, F., Cederstrøm, J. M., Hübscher, C., Nomikou, P., Carey, S., **Kühn, M.**, Elger, J., & Berndt, C. (2023). *Revised Minoan eruption volume as benchmark for large volcanic eruptions.* Nature communications, *14*(1), 2497.

Karstens, J., Schneider von Deimling, J., Berndt, C., Böttner, C., **Kühn, M.**, Reinardy, B. T. I., Ehrhardt, A., Gros, J., Schramm, B., Klaeschen, D., Elger, J., Haeckel, M., Schmidt, M., Heinrich, S., Müller, P., & Bense, F. (2022). *Formation of the Figge Maar Seafloor Crater During the 1964 B1 Blowout in the German North Sea.* Earth Science, Systems and Society, 2. https://doi.org/10.3389/esss.2022.10053.

Kühn, M., Karstens, J., Berndt, C. and Watt, S. F. L. (2021) *Seismic reconstruction of seafloor sediment deformation during volcanic debris avalanche emplacement offshore Sakar, Papua New Guinea.* Marine Geology, 439. Art.Nr. 106563. DOI 10.1016/j.margeo.2021.106563.

Haroon, A., Micallef, A., Jegen, M., Schwalenberg, K., Karstens, J., Berndt, C., Garcia, X., **Kuehn, M.**, Rizzo, E., Fusi, N. C., Ahaneku, C. V., Petronio, L., Faghih, Z., Weymer, B. A., De Biase, M. and Chidichimo, F. (2021) *Electrical resistivity anomalies offshore a carbonate coastline: Evidence for freshened groundwater?.* Geophysical Research Letters, 48 (14). e2020GL091909. DOI 10.1029/2020GL091909.

Hornbach, M. J., Sylvester, J., Hayward, C., **Kühn, M.**, Huhn-Frehers, K., Freudenthal, T., Watt, S. F. L., Berndt, C., Kutterolf, S. , Kuhlmann, J., Sievers, C., Rapp, S., Pallapies, K., Gatter, R. and Hoenekopp, L.

(2021) *A Hybrid Lister-Outrigger Probe for Rapid Marine Geothermal Gradient Measurement.* Earth and Space Science, 8 (1). e2020EA001327. DOI 10.1029/2020EA001327.

Karstens, J., Berndt, C., Urlaub, M., Watt, S. F. L., Micallef, A., Ray, M., Klaucke, I., Muff, S., Klaeschen, D., **Kühn, M.**, Roth, T., Böttner, C., Schramm, B., Elger, J. and Brune, S. (2019) *From gradual spreading to catastrophic collapse - Reconstruction of the 1888 Ritter Island volcanic sector collapse from high-resolution 3D seismic data.* Earth and Planetary Science Letters, 517 pp. 1-13. DOI 10.1016/j.epsl.2019.04.009.

Watt, S. F. L. , Karstens, J., Micallef, A., Berndt, C., Urlaub, M., Ray, M., Desai, A., Sammartini, M., Klaucke, I. , Böttner, C., Day, S., Downes, H., **Kühn, M.** and Elger, J. (2019) *From catastrophic collapse to multi-phase deposition: Flow transformation, seafloor interaction and triggered eruption following a volcanic-island landslide.* Earth and Planetary Science Letters, 517. pp. 135147. DOI 10.1016/j.epsl.2019.04.024.

Conference talks

Crutchley, G. J., Karstens, J., Preine, J., Hübscher, C., Fossen, H. and **Kühn, M.** (2023) *Normal faulting around Kolumbo Volcano - exploring relationships between stress fields and volcanism.* [Talk] In: GeoBerlin 2023. 03.-07.09.2023, Berlin, Germany.

Haroon, A., Micallef, A., Jegen, M., Schwalenberg, K., Karstens, J., Berndt, C., Garcia, X., **Kuehn, M.**, Rizzo, E., Fusi, N. C., Ahanek, C. V., Petronio, L., Faghih, Z., Weymer, B. A., de Biase, M., Chidichimo, F., Pondthai, P. and Everett, M. (2022) *Evidence for OFG in the carbonate margin of Malta? Insights from geophysical investigations.* [Talk] In: International Workshop on Freshened Groundwater Research 2022. 27.-28.07.2022, Valletta, Malta.

Karstens, J., Schmid, F., Elger, J., Berndt, C., Crutchley, G. J., Kutterolf, S., **Kühn, M.**, Preine, J., Van der Bilt, W., Hooft, E., Druitt, T. H., Cederstroem, J. M., Hübscher, C., Nomikou, P. and Carey, S. (2022) *Revising the volume of the Minoan eruption (Santorini) based on new marine geophysical and sedimentological data.* [Talk] In: 11. Conference Cities on Volcanoes (COV11). 12.06.2022-17.06.2022, Heraklion, Greece.

Kühn, M., Karstens, J., Berndt, C. and Watt, S. (2021) *Seismic reconstruction of seafloor sediment deformation during volcanic debris avalanche emplacement offshore Sakar, Papua New Guinea.* [Talk] In: 81. Jahrestagung der Deutschen Geophysikalischen Gesellschaft (DGG), 01.03.-05.03.2021, Kiel (online).

Conference posters

Kühn, M., Berndt, C., Krastel, S., Karstens, J., Watt, S., Kutterolf, S., Huhn, K., and Freudenthal, T. (2023). Flank collapse, sediment failure and flow-transition: the multi-stage deposition of a volcanic sector collapse offshore Montserrat, Lesser Antilles, EGU General Assembly 2023, Vienna, Austria, 24–28 Apr 2023, EGU23-12087, https://doi.org/10.5194/egusphere-egu23-12087, 2023.

Hornbach, M. J., **Kühn, M.**, Huhn, K., Freudenthal, T., Watt, S. F., Berndt, C., Kutterolf, S., Kuhlmann, J., Pallapies, K., Gatter, R., Hoenekopp, L., Sylvester, J., Hayward, C. and Mulone, T. (2019, December). New Submarine Heat Flow Measurements on the Lesser Antilles Volcanic Arc. In AGU Fall Meeting 2019. AGU.

Karstens, J., Crutchley, G., Nomikou, P., Preine, J., **Kühn, M.**, Elger, J., Schmid, F., Dalla Valle, G., Hübscher, C. and Berndt, C. (2021) POS538: High-resolution 2D and 3D reflection seismic analysis of tsunamigenic volcanic eruptions in the Southern Aegean Sea (Greece). [Poster] In: 81. Jahrestagung der Deutschen Geophysikalischen Gesellschaft (DGG), 01.03.-05.03.2021, Kiel (online).

Haroon, A., Micallef, A., Faghih, Z., Jegen, M., Schwalenberg, K., Karstens, J., Berndt, C. , Garcia, X., **Kuehn, M.**, Rizzo, E., Fusi, N. C., Ahaneku, C. V., Petronio, L. and Weymer, B. A. (2021) Controlled source electromagnetic measurements offshore the Maltese Islands: Implications for offshore freshened groundwater in a carbonate shelf. [PICO] In: EGU General Assembly 2021, 19.30.03.2021, Online. DOI 10.5194/egusphere-egu21-5080.

Karstens, J., Urlaub, M., Berndt, C., Watt, S. F. L., Micaleff, A., Klaucke, I., Klaeschen, D. , Brune, S. and **Kühn, M.** (2017) The complex emplacement dynamics and tsunami genesis of the 1888 Ritter Island sector collapse from 3D seismic data. [Poster] In: AGU Fall Meeting 2017, 11.12 - 15.12.2017, New Orleans, USA.

Reports

Lange, D., Kopp, H., Dannowski, A., Klaucke, I., Moreno, M., Diaz, J., **Kühn, M**., Riedel, M. and Contreras-Reyes, E., and Cruise participants SO297 (2023) A high-resolution controlled-source seismic experiment offshore Taltal to elucidate structural controls on megathrust slip, Cruise No. SO297, February 23 - April 11, 2023, Talcahuano (Chile) - Guayaquil (Ecuador). Sonne-Berichte, SO297 . Leitstelle Deutscher Forschungsschiffe, Bonn, Germany, 44 pp. DOI 10.48433/cr_so297.

Berndt, C., Urlaub, M., Jegen, M., Faghih, Z., Reeck, K., Franz, G., Barnscheidt, K. C., Wollatz-Vogt, M., Liebsch, J., Schramm, B., Elger, J., **Kühn, M**., Müller, T., Schmidt, M. , Spiegel, T., Timm, H., Hinz, A. K., Sager, T., Hilbert, H. S., Rohde, L., Korbjuhn, T., Reissmann, S. and Diller, N. (2021) RV SONNE Fahrtbericht / Cruise Report SO277 OMAX: Offshore Malta Aquifer Exploration, Emden (Germany) – Emden (Germany), 14.08. – 03.10.2020. . GEOMAR Report, N. Ser. 057. GEOMAR Helmholtz-Zentrum für Ozeanforschung Kiel, Kiel, Germany, 139 pp. DOI 10.3289/GEOMAR_REP_NS_57_20.

Karstens, J., Crutchley, G. , Elger, J., **Kühn, M**., Schmid, F., Dalla Valle, G., Preine, J. and Nomikou, P. (2020) R/V Poseidon Cruise Report 538 - THESEUS Tsunami hazard of explosive submarine eruptions, 7th October – 28th October 2019, Cartagena (Spain) - Heraklion (Greece) . . GEOMAR Helmholtz Centre for Ocean Research, Kiel, Germany, 106 pp. DOI 10.3289/cr_pos538.

Huhn, K., Freudenthal, T., Dehning, K., Gatter, R., Hilgenfeldt, C., Hönekopp, L., Hornbach, M. J., **Kühn, M**., Kuhlmann, J., Kutterolf, S., Meyer-Schack, B., Pallapies, K., Rapp, S. K., Sievers, C., Watt, S., & Stelzner, M. (2019). Sector collapse kinematics and tsunami implications - SEKT, Cruise No. M154-2, April 29 - Mai 23, 2019, Pointe-à-Pitre (Guadeloupe) - Pointe-à-Pitre (Guadeloupe). In METEOR-Berichte M154/2. Gutachterpanel Forschungsschiffe. Bonn, 16 pp. https://doi.org/10.2312/cr_m154_2.

Berndt, C., Böttner, C., Elger, J., Kontradowitz, S., **Kühn, M.**, Müller, S., Schramm, B. and Stelzner, M. (2019) Sector collapse kinematics and tsunami implications - SEKT, Cruise No. M154/1, April 3 - April 25, 2019, Mindelo (Cape Verde) - Point-á-Pitre (Guadeloupe). In METEOR-Berichte, M154/1. Gutachterpanel Forschungsschiffe, Bonn, 47 pp. DOI 10.2312/cr_m154_1.

Karstens, J., Schneider von Deimling, J., Böttner, C., Elger, J., Hilbert, H. S., **Kühn, M**., Kühn, R., Müller, P., Reinardy, B. and Schramm, B. (2018) RV ALKOR Cruise Report 512 [AL512] - North Sea Blowouts, 15th July - 26th July, 2018, Cuxhaven - Kiel (Germany). Alkor-Berichte, AL512. GEOMAR, Kiel, Germany, 39 pp. DOI 10.3289/CR_AL512.